ISSN 2074-272X

науково-практичний журнал

2023/1

Електротехніка і Електромеханіка

Electrical Engineering & Electromechanics

Інженерна електрофізика.
Техніка сильних електричних та магнітних полів
Електричні машини та апарати
Електротехнічні комплекси та системи
Промислова електроніка
Електричні станції, мережі і системи
Безпека електрообладнання

Журнал включено до найвищої категорії «А»
Переліку фахових видань України

З 2021 р. журнал індексується у Scopus

З 2015 р. журнал індексується
у Web of Science Core Collection:
Emerging Sources Citation Index

Electrical Engineering & Electromechanics

Scientific Journal was founded in 2002
Founder – National Technical University «Kharkiv Polytechnic Institute» (Kharkiv, Ukraine)

From no. 1 2021 Journal «Electrical Engineering & Electromechanics» is indexing in **Scopus** and from no. 1 2015 Journal is indexing in **Web of Science Core Collection: Emerging Sources Citation Index (ESCI)**.

Also included in DOAJ (Directory of Open Access Journals), in EBSCO's database, in ProQuest's databases – Advanced Technologies & Aerospace Database and Materials Science & Engineering Database, in Gale/Cengage Learning databases.

Editorial office address:
National Technical University «Kharkiv Polytechnic Institute», Kyrpychova Str., 2, Kharkiv, 61002, Ukraine
phones: +380 57 7076281, +380 67 3594696, **e-mail:** a.m.grechko@gmail.com (**Grechko O.M.)**

ISSN (print) 2074-272X
ISSN (online) 2309-3404

Printed 05 January 2023. Format 60 × 90 ⅛. Paper – offset. Laser printing. Edition 200 copies.
Printed by Printing house «Madrid Ltd» (18, Gudanova Str., Kharkiv, 61024, Ukraine)

Electrical Engineering & Electromechanics
Scientific Journal

no. 1, 2023

Table of Contents

UDC 621.313 https://doi.org/10.20998/2074-272X.2023.1.01

S. Arslan, H. Mellah

Analysis and testing of internal combustion engine driven linear alternator

Introduction. *Internal combustion engine technology has been considered for the alternator system in the last two decades. Especially when considering fuel diversity, reliability, portability, power density, research studies are increasing day by day. In this respect, interest has been focused on linear generator studies.* ***Purpose***. *The goal of the research is to investigate the performance of a linear generator and its application to generate electrical energy from an internal combustion engine to solve the range problem of small electric powered vehicles. The generator, unlike a traditional generator, consists of a linear generator with a crank mechanism driven by an internal combustion engine.* ***Originality.*** *The configuration of the linear generator with internal combustion engine crank has not previously been reported.* ***Methods***. *The numerical solution of the generator was carried out by the finite element method in the Ansys Maxwell software in a cylindrical coordinate system. The effect of stroke length and frequency on voltage and output power was investigated by monitoring an external electrical load. A prototype linear generator has been designed and produced considering the sizing dimensions. The configuration can be used in power-hungry applications and increase the range of small electric vehicles.* ***Results***. *The results from simulation and practice are largely in agreement.* ***Practical value***. *A practical mechanical system was built comprising a linear generator connected to a 2.2 kW internal combustion engine via a crank connecting rod for analysis.* References 35, table 1, figures 15.

Key words: **linear generator, electric vehicle, hybrid vehicle, internal combustion engine.**

Вступ. *Останні два десятиліття розглядалася техніка двигуна внутрішнього згоряння для системи генератора змінного струму. Особливо з урахуванням різноманітності видів палива, надійності, портативності, питомої потужності кількість досліджень зростає з кожним днем. У зв'язку з цим інтерес був зосереджений на дослідженнях лінійних генераторів.* ***Мета***. *Метою дослідження є аналіз продуктивності лінійного генератора та його застосування для вироблення електроенергії від двигуна внутрішнього згоряння для вирішення проблеми запасу ходу малих електромобілів. Генератор, на відміну від традиційного, складається з лінійного генератора з кривошипно-шатунним механізмом, що рухається двигуном внутрішнього згоряння.* ***Оригінальність***. *Про конфігурацію лінійного генератора з кривошипом двигуна внутрішнього згоряння раніше не повідомлялося.* ***Методи***. *Чисельне рішення генератора проводилося методом скінченних елементів у програмі Ansys Maxwell в циліндричної системі координат. Вплив довжини та частоти ходу на напругу та вихідну потужність досліджували шляхом моніторингу зовнішнього електричного навантаження. З урахуванням габаритних розмірів розроблено та виготовлено прототип лінійного генератора. Конфігурація може використовуватися в енергоємних застосуваннях і збільшувати запас ходу невеликих електромобілів.* ***Результати***. *Результати моделювання та з практики переважно збігаються.* ***Практична цінність***. *Для аналізу було побудовано практичну механічну систему, що складається з лінійного генератора, з'єднаного з двигуном внутрішнього згоряння потужністю 2,2 кВт через шатун кривошипу.* Бібл. 35, табл. 1, рис. 15.

Ключові слова: **лінійний генератор, електромобіль, гібридний автомобіль, двигун внутрішнього згоряння.**

Introduction. Energy has become important for the developing world. Electrical energy has typically been produced using fossil fuels despite the harmful effects to the environment. Vehicles, and the internal combustion engine (ICE), are one of the major users of fossil fuel. Although electric vehicles have zero emissions, they suffer from a range and charging problems. However, with advances in battery and charging technology, the number of electric and electric/hybrid vehicles is increasing. Hybrid vehicles offer an alternative compared to traditional fossil fuel-based vehicles in the short and medium term. In addition, future technology, such as fuel cells, promises to solve the range problem in hybrid vehicles and is emission free. Further advances in battery technology (long life, fast charge-late discharge, high per unit mass capacity, and low cost) will reduce the disadvantages of electric/hybrid vehicles.

Further energy-generating technology can be incorporated in electric vehicles to improve the range and make use of electric or hybrid electric vehicles more attractive. It can be given as regenerative braking, regenerative suspension systems, solar panels, wind generator, thermo-electric generator, respectively.

In hybrid electric vehicles, the role of the ICE can be categorized into series, series-parallel, and parallel classes, according to its purpose in relation to the electrical propulsion. Various forms of ICE have been used in hybrid electric vehicles including two-stroke and four-stroke. The two-stroke engine offers higher power and speed, and lower vibration compared to the four-stroke engine [1]. Vibration is a major problem, especially at high speeds, and studies on the effects of vibration have been conducted between 10 Hz and 30 Hz [2-4]. The stroke length of the linear motion of the ICE equals the length of motion of the ICE piston. For example, in [5] the effective stroke length is 62 mm. In studies [2, 6-10], it has been shown that the free piston mechanism and the crank connecting mechanism exhibit a very similar movement profile. Newer forms of ICE, including the free piston system [11-13], are being investigated as multi-fuel, high efficiency, low emission options.

In the ICE, the linear force of the piston rod is turned into torque and rotational motion through the action of the crank rods and crankshaft. This rotational drive can be applied directly to the shaft a conventional rotating electrical generator. However, the linear motion of the piston rod can be used directly as a free piston mechanism for a linear motion drive [14, 15].

The moving part of a linear generator is arranged so that it moves back and forth freely. In order for a free-piston linear generator to operate with an ICE, the piston has first to be moved to compress the air-fuel mixture. This is difficult on the first stroke. Despite the limited number of studies on the initial state of the linear generator, some methods have been offered as solutions to the starting problem [16-25], including mechanical

resonance [16-18], injection time control [23-26] or special control system [19-26].

Some studies [27, 28] have investigated the Wankel REX [29] and Otto REX [29], as these generate rotational drive directly that can be connected to a conventional electrical generator.

The goal of the paper is to investigate the generation of electrical energy numerically and experimentally by operating the tube type linear generator on an ICE with a crank connecting rod mechanism.

Investigation of linear generator with finite element analysis (FEA). A linear machine converts mechanical energy into electrical energy or converts electrical energy into mechanical energy via linear motion [11]. Designs may vary according to application, with different values of speed, frequency, stroke distance, and force. Different types of linear generator are detailed in [26, 27, 30]. The structure and working principle (induction, synchronous, transverse flux, or longitudinal flux) will determine the parameters for the electric generator. This study investigates the permanent magnet linear generator with longitudinal flux. The stroke length of the generator has been limited to allow use as tubular geometry and be coupled to an ICE. The tube-type geometry has advantages compared to the flat-type linear generators; it minimizes asymmetric forces between the moving magnet and primary windings, and has higher power-to-weight ratio, higher efficiency, and power density. However, having the magnet as the moving part, a deceleration force will occur between the primary windings and the moving magnet. As the flux density of the magnet increases, the generator output voltage and cogging force increase [31]. This force can be reduced by methods such as the geometry of the magnet, pole pitch ratio, split ratio and including slot pitch. This study has taken the design of the tubular generator as 4 magnetic poles and 6 primary windings, as shown in Fig. 1, for analysis.

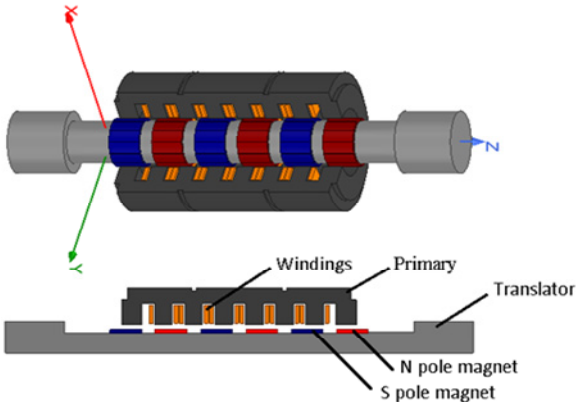

Fig. 1. 3-D and 2-D views of tube-shaped linear generator

Output parameters of circular linear machines can be calculated by using numerical analysis programs such as Ansys Maxwell 2D/3D, MotorSolve [32], Speed, etc.

Generator numerical analysis. The 3-D geometry of the linear generator can be converted to 2-D geometry for analysis by the finite element method, as this reduces computation time. 2-D FEA is often used to help in the design of electric machines, and determine parameters such as current density, magnetic flux distribution, winding inductance changes and electromagnetic force. The design parameters for the linear generator of this study are given in Table 1.

Table 1

Linear generator design parameters

Parameters	Value	Unit
Frequency	50	Hz
Airgap length	1	mm
Primary inner diameter	51	mm
Magnet width	20	mm
Alpha (pole pitch ratio)	0.72	
Beta (slot pitch ratio)	0.5	
Slot / Pole	6/4	
Slot filling factor	0.7	

2-D analysis of the linear generator. Values have been set for the moving force (magneto-static solution and transient solution), and winding inductance (magneto-static solution) for the simulation. In addition, two-dimensional numerical analyzes can be applied to analyze different situations (magnet shift technique [33], different magnet geometries [34], etc.) for reducing cogging force in the machine. The duration of the simulation and time steps were also set. The force on the moving part of the generator (in the seconder), magnetic flux density, magnetic field intensity, flux paths, and current density were determined in the simulation at each time step.

The simulation includes transient state and continuous state analysis of the 2-D plane selected to determine surface conditions. Mesh selection is very important, with a high resolution mesh applied in critical areas. For example, in time-dependent analysis, dense mesh resolution is used in areas of movement to increase the accuracy of the calculation of force.

Increasing working current will increase the current density in the conductive regions. The increase in power will increase losses and heat, which will require the thermal value of the generator to be increased and may require additional cooling.

The effect of variables such as a pole pitch ratio, inner diameter outer diameter ratio, and slot pitch ratio on parameters including cogging force, induced voltage, and losses, can be determined by parametric analysis. Figure 2 shows the electrical equivalent of the linear generator with and without load that is used for the numerical and experimental studies.

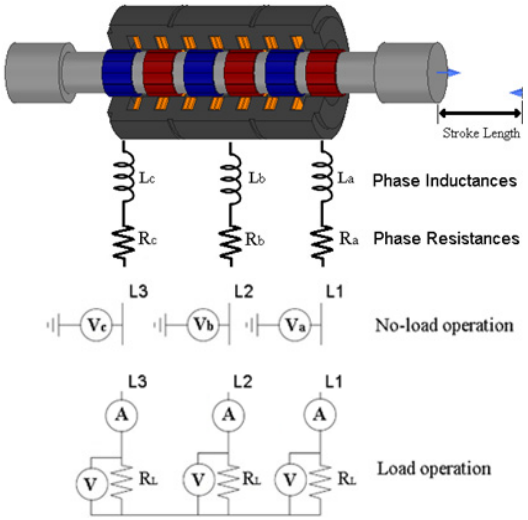

Fig. 2. Wiring diagram of linear generator for no-load and load condition

The phase windings have been configured with no-load in FEA transient state analysis to analyse the no-load condition and investigate the effect of frequency and stroke length on induced voltage.

Figure 3 shows how the induced voltage increases as the stroke length increases at constant frequency. Figure 3 also shows how the induced voltage increases as the frequency increases at constant stroke length. In fixed frequency operation, as the stroke length increases, the induced voltage increases, while in the loaded condition, the iron loss and copper loss increase and the induced voltage decreases at larger stroke lengths. The windings include inductance and so a capacitor of 100 μF has been connected in series with the phase windings and load in order to compensate for the effects [35]. Figure 2 shows the generator with a load connected to investigate the power generated; two load resistances were considered, 10 Ω and 30 Ω.

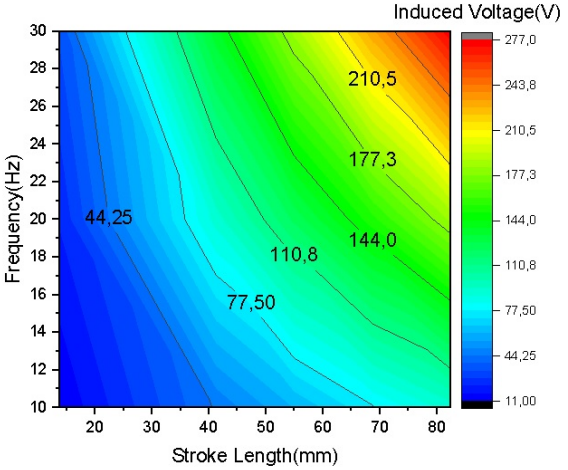

Fig. 3. Induced voltage according to stroke length and frequency in no-load condition.

The output power of the linear generator was investigated for stroke length and frequency for the two loads, with and without series capacitor (Fig. 4,*a*-*d*).

Figure 4 shows that output power increases with stroke length and frequency, and an optimum operating point can be determined. Figure 4 also shows that compensating for the winding reactance increases significantly the power delivered to the load at high frequencies. However, there is no increase in output power at low speeds. It would be important to determine the optimum value for the capacitor for the specific operating condition. This could include use of different capacitors for power compensation at different operating speeds of the generator.

In 2-D analysis, the effect of load resistance changes on the power and efficiency produced in the linear generator can be examined. Thus, maximum power and maximum efficiency are obtained according to the changing external load resistance. The variation of power generation and efficiency performance with different external load values is shown in Fig. 5.

According to the results, the efficiency is 83.7 % at 10 Ω, where the maximum power is obtained. However, one can note that as the external load increases, the efficiency increases significantly and the power decreases. The load value at which the efficiency is maximum (93.87 %) is 70 Ω. At the optimum load value (16 Ω), the power obtained from the generator is 787 W, the efficiency is 88 %.

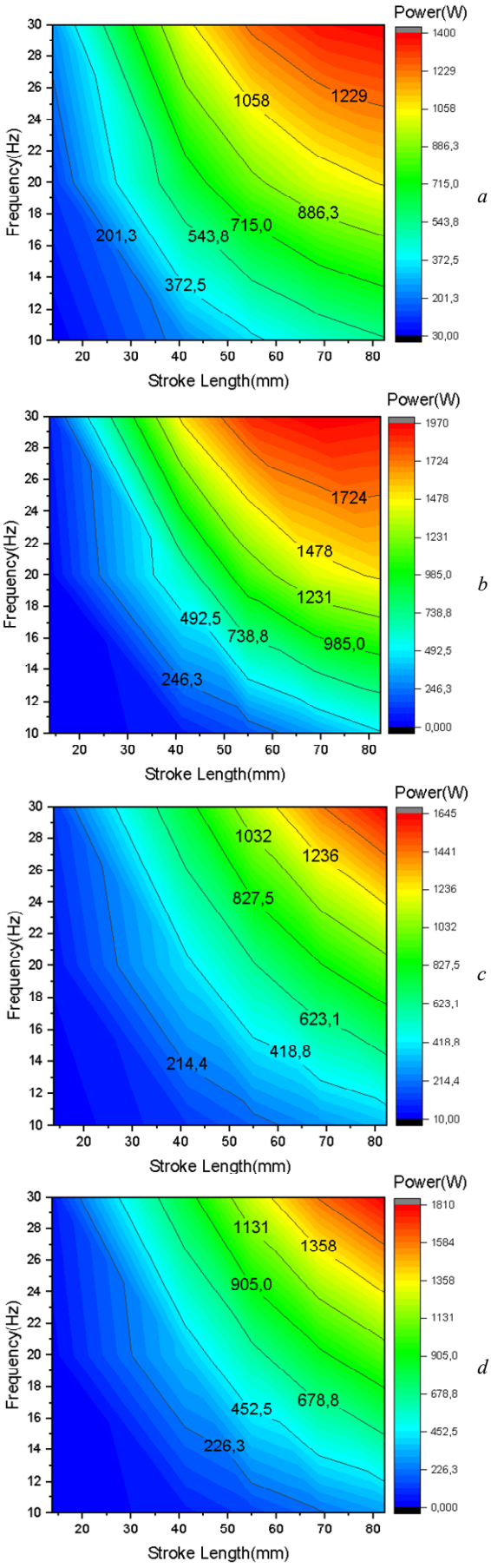

Fig. 4. Output power for stroke length and frequency: 10 Ω (*a*); 10 Ω with 100 μF capacitor (*b*); 30 Ω (*c*); 30 Ω with 100 μF capacitor (*d*)

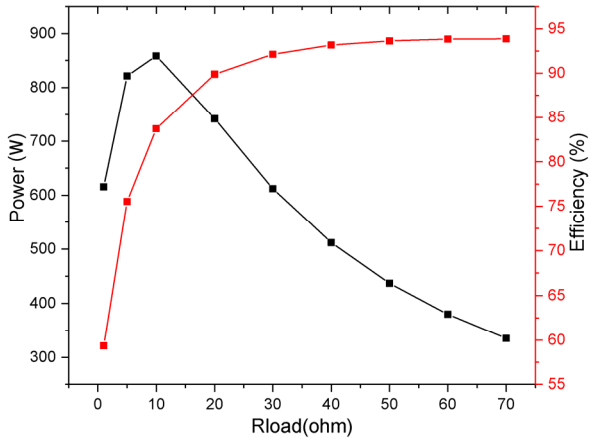

Fig. 5. Power and efficiency variation of the linear generator vs load resistance

Linear generator manufacture and testing. The linear generator in this study has been made in a tubular topology using the dimensions determined from the FEA. The primary laminates are produced from 0.5 mm M43 quality steel using laser cutting. 1020 quality steel is used for the moving secondary shaft, on which the magnets are mounted. The windings are wrapped on a mould made of delrin material. Figure 6 shows the individual components of the linear generator.

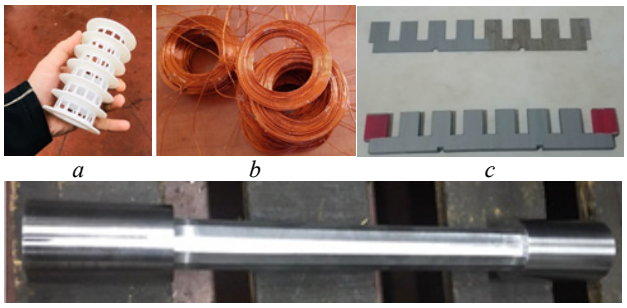

a *b* *c*

d

Fig. 6. Materials: CNC-produced winding mould (*a*); windings (*b*); laser-cut primary laminate (*c*); CNC-produced magnetless shaft (*d*)

Generator drive system. In a free piston system, the linear velocity is close to sinusoidal in form. For this study, an eccentric system with a crank mechanism has been designed to connect to an existing ICE to provide a sinusoidal linear speed profile. The Por-MAX CS-5200 2.2 kW gasoline engine (Fig. 7) has been used as ICE to provide the drive to the linear generator.

Fig. 7. ICE 2.2 kW

The ICE provides a power of 2.2 kW at 4000 rpm, giving a torque as given as (1), giving engine torque as 5.25 N·m. This value is calculated as the torque produced by the ICE:

$$T_m = 9550 \cdot P_m / N_m \,. \tag{1}$$

There was concern that the ICE could cause significant vibration and result in damage to the engine when connected to the linear generator and operated at low speeds. A reducer was therefore used to reduce these effects. The torque at the output of a reducer is proportional to its gear ratio, whereas the output speed of the reducer is inversely proportional to the gear ratio of the input speed, as in (2):

$$T_{rg} / T_{rc} = z_1 / z_2 \,. \tag{2}$$

The gear ratio of the reducer used in this study is 6:1, giving the output torque of the gearbox as 31.5 N·m, with output speed of 666.6 rpm (4000/6). The arrangement of ICE, reducer, linear generator and load is shown in Fig. 8.

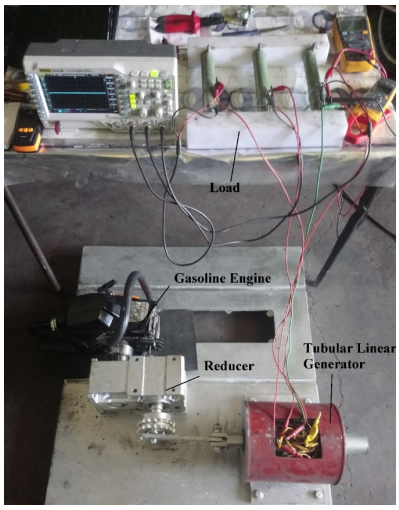

Fig. 8. Linear generator system with ICE drive

Preliminary testing was carried out to eliminate mechanical problems. Different stroke lengths were achieved by placing mount holes in different locations along the length of the crank of the reducer. A laser displacement sensor (Micro-Epsilon ILD 1420 model) was used to measure shaft displacement accurately. The output of the sensor is shown in Fig. 9.

Figure 9 shows the displacement of the shaft and indicates vibration was occurring. After correcting the error, the displacement is seen to have a sinusoidal form. The stroke length is determined from the extremes of displacement, in this instance 102.0965 mm.

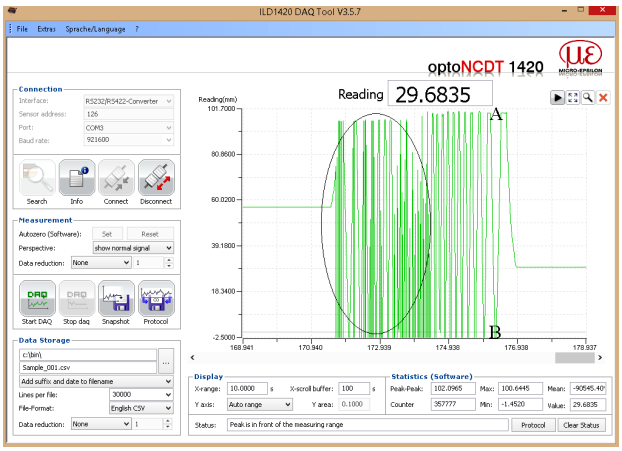

Fig. 9. Displacement of the moving component

Test and experiment results. The speed of the ICE shaft was measured with a laser tachometer and the speed of the linear generator determined from the reducer ratio. The induced voltage of the linear generator versus speed of rotation in the no-load condition is shown in Fig. 10.

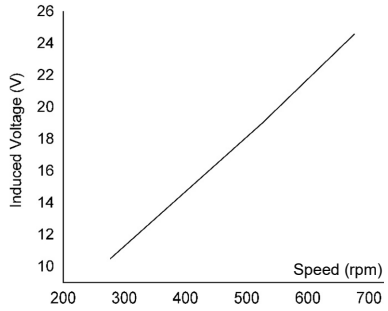

Fig. 10. Induced voltage versus linear generator rotation speed

Figure 10 indicates that the induced voltage increases with rotation speed in the no-load condition, and is 0.0353 V/rpm (2.12 V·s/rad). This would indicate that the results from FEA agree with experiment. The induced voltage at no-load condition for generator rotation speed of 277 rpm (engine speed 1664 rpm) is shown in Fig. 11 and for 525 rpm (engine speed 3150 rpm) in Fig. 12.

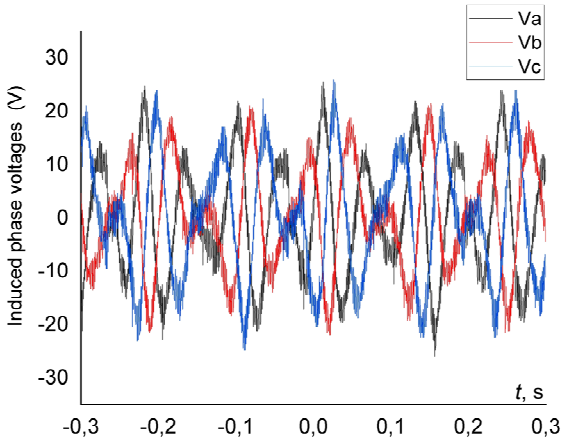

Fig. 11. Phase voltages measured with an oscilloscope at 277 rpm

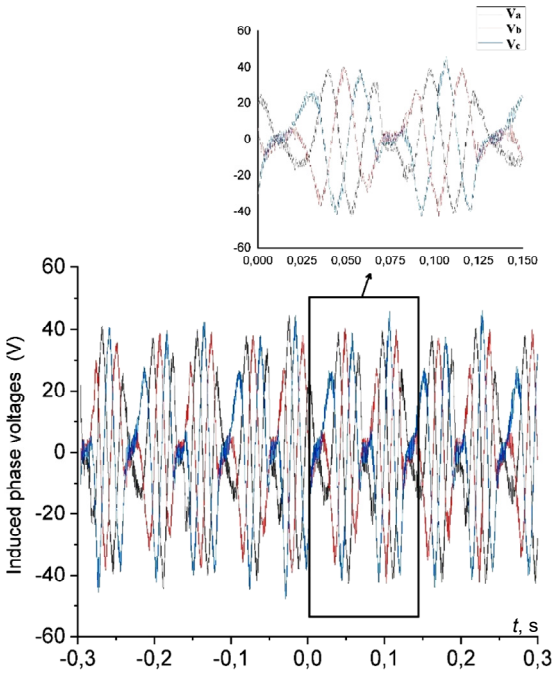

Fig. 12. Phase voltages measured with an oscilloscope at 525 rpm

An expanded version of the induced voltage at generator rotation speed of 528 rpm is given in Fig. 13.

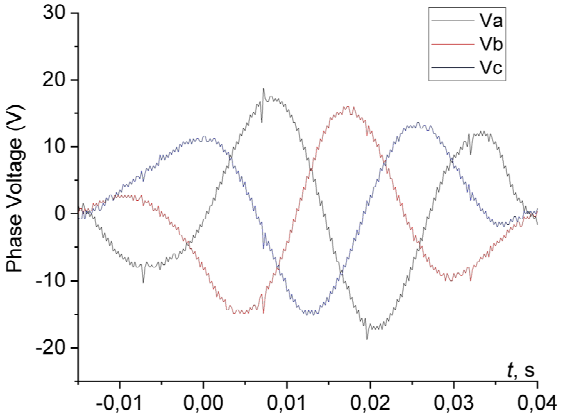

Fig. 13. Phase voltage change according to generator rotation speed of 528 rpm

Figure 13 shows that the phase voltage in each of the three phases. When the shaft is in mid position of travel and magnets pass windings, there will be sinusoidal waveform, but as the shaft approaches extreme of travel, it will slow and reverse direction. This will have the effect of modulating the amplitude of the waveform. At mid travel, the waveform has a higher frequency than at the extremes due to higher speed of the shaft. The waveform inverts when the direction of the shaft changes. The amplitude of V_t (voltage, $V(t)$) in each generator shown in Fig. 13 and Fig. 14 is less than the magnitude of E_f (Fig. 3 and Fig. 10) due to the resistance (R_{phase}) and inductance (L_{phase}) of each winding. Since the linear generator works at a fixed stroke distance, the frequency changes in response to the speed of the engine.

Figure 14 shows how induced voltage increases with generator rotation speed and load resistance. Figure 15 shows how the phase current increases with generator rotation speed and decreases with load resistance.

Conclusions.

1. This study investigates the performance of a linear generator through numerical analysis with finite element analysis and with a practical linear generator driven by an internal combustion engine. Both no-load and loaded conditions were examined by numerical analysis and practical measurement to characterise the linear generator.

2. A tubular type linear generator was produced for test. A reducer was used to connect the crankshaft of the internal combustion engine to the linear generator to match the speed of the engine to the working speed of the linear generator and overcome problems of engine vibration at low engine speed.

3. Stroke length and frequency increase the induced voltage and thus output power. The voltage and power obtained from the linear generator were found to be sufficient for battery charging.

4. If the practical issues of the linear generator, such as bearings and control of the speed of the internal combustion engine can be achieved, then the linear generator can be used in place of the rotating generator. However, as the travel of a piston in the internal combustion engine is limited, the stroke length in the linear generator will likewise be limited. Stroke length can be increased by connecting rod mechanisms.

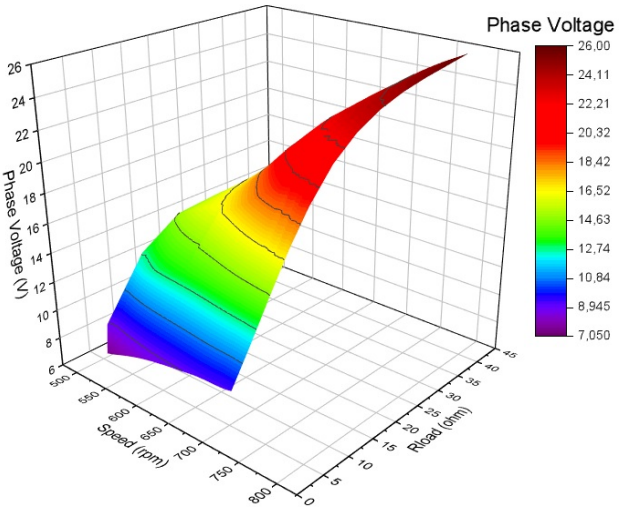

Fig. 14. Phase voltage versus generator rotation speed and load resistance

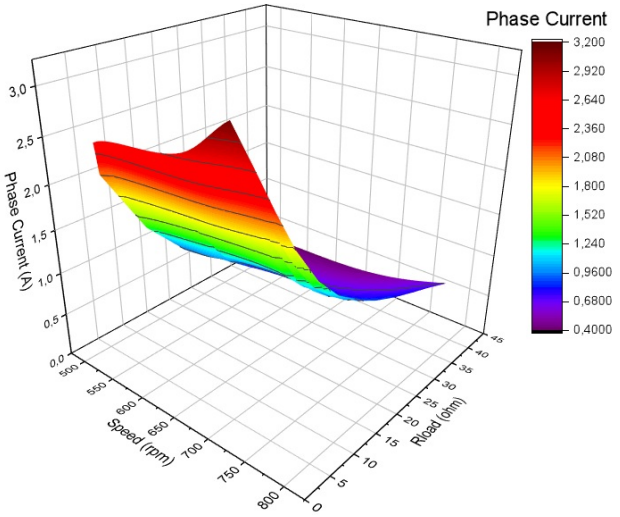

Fig. 15. Phase current versus generator rotation speed and load

Acknowledgements. This work was supported by the Scientific and Technological Research Council of Turkey (TUBITAK 1512) under Grant Number 2180435. Ansys Maxwell software used in this study was provided by Harran University Scientific Research Project Unit (Project No: 18060).

Conflict of interest. The authors declare that they have no conflicts of interest.

REFERENCES

1. Jia B., Smallbone A., Zuo Z., Feng H., Roskilly A.P. Design and simulation of a two- or four-stroke free-piston engine generator for range extender applications. *Energy Conversion and Management*, 2016, vol. 111, pp. 289-298. doi: https://doi.org/10.1016/j.enconman.2015.12.063.

2. Guo C., Feng H., Jia B., Zuo Z., Guo Y., Roskilly T. Research on the operation characteristics of a free-piston linear generator: Numerical model and experimental results. *Energy Conversion and Management*, 2017, vol. 131, pp. 32-43. doi: https://doi.org/10.1016/j.enconman.2016.11.010.

3. Chiang C.-J., Yang J.-L., Lan S.-Y., Shei T.-W., Chiang W.-S., Chen B.-L. Dynamic modeling of a SI/HCCI free-piston engine generator with electric mechanical valves. *Applied Energy*, 2013, vol. 102, pp. 336-346. doi: https://doi.org/10.1016/j.apenergy.2012.07.033.

4. Schneider S., Rinderknecht F., Friedrich H.E. Design of future concepts and variants of The Free Piston Linear Generator. *2014 Ninth International Conference on Ecological Vehicles and Renewable Energies (EVER)*, 2014, pp. 1-8. doi: https://doi.org/10.1109/EVER.2014.6844029.

5. Mao J., Zuo Z., Feng H. Parameters coupling designation of diesel free-piston linear alternator. *Applied Energy*, 2011, vol. 88, no. 12, pp. 4577-4589. doi: https://doi.org/10.1016/j.apenergy.2011.05.051.

6. Miao Y., Zuo Z., Feng H., Guo C., Song Y., Jia B., Guo Y. Research on the Combustion Characteristics of a Free-Piston Gasoline Engine Linear Generator during the Stable Generating Process. *Energies*, 2016, vol. 9, no. 8, art. no. 655. doi: https://doi.org/10.3390/en9080655.

7. Xiao J., Li Q., Huang Z. Motion characteristic of a free piston linear engine. *Applied Energy*, 2010, vol. 87, no. 4, pp. 1288-1294. doi: https://doi.org/10.1016/j.apenergy.2009.07.005.

8. Aichlmayr H.T., Kittlelson D.B., Zachariah M.R. Micro-homogeneous charge compression ignition (HCCI) combustion: Investigations employing detailed chemical kinetic modeling and experiments. *Chemical and Physical Processes in Combustion, Fall Technical Meeting, The Eastern States Section*, 2001, pp. 384-387.

9. Mikalsen R. *An investigation into the free-piston engine concept and its potential for high efficiency and low emissions power generation*. *PhD Thesis*. Newcastle University, United Kingdom, 2008. 192 p. Available at: http://theses.ncl.ac.uk/jspui/handle/10443/3145 (Accessed 16 March 2022).

10. Hong S., Choi H.-Y., Lim J.-W., Lim H.-J., Jung H.-K. Analysis of tubular-type linear generator for free-piston engine. *Renewable Energy and Power Quality Journal*, 2007, vol. 1, no. 05, pp. 719-722. doi: https://doi.org/10.24084/repqj05.365.

11. Hu Y., Xu Z., Sun Y., Liu L. Electromagnetic Characteristics Analysis of a Tubular Moving Magnet Linear Generator System. *Applied Sciences*, 2020, vol. 10, no. 11, art. no. 3713. doi: https://doi.org/10.3390/app10113713.

12. Ahmed T. Raheem, A. Rashid A. Aziz, Saiful A. Zulkifli, Abdalrazak T. Rahem, Wasiu B Ayandotun. Development, Validation, and Performance Evaluation of An Air-Driven Free-Piston Linear Expander Numerical Model. *Evergreen*, 2022, vol. 9, no. 1, pp. 72-85. doi: https://doi.org/10.5109/4774218.

13. Wu L., Feng H., Jia B., Tang Z., Yan X., Wang W. A novel method to investigate the power generation characteristics of linear generator in full frequency operation range applied to opposed-piston free-piston engine generator _ Simulation and test results. *Energy*, 2022, vol. 254, art. no. 124235. doi: https://doi.org/10.1016/j.energy.2022.124235.

14. Hanipah M.R., Mikalsen R., Roskilly A.P. Recent commercial free-piston engine developments for automotive applications. *Applied Thermal Engineering*, 2015, vol. 75, pp. 493-503. doi: https://doi.org/10.1016/j.applthermaleng.2014.09.039.

15. Hung N.B., Lim O. A review of free-piston linear engines. *Applied Energy*, 2016, vol. 178, pp. 78-97. doi: https://doi.org/10.1016/j.apenergy.2016.06.038.

16. Jia B., Zuo Z., Feng H., Tian G., Roskilly A.P. Investigation of the Starting Process of Free-piston Engine Generator by Mechanical Resonance. *Energy Procedia*, 2014, vol. 61, pp. 572-577. doi: https://doi.org/10.1016/j.egypro.2014.11.1173.

17. Zulkifli S.A., Karsiti M.N., Aziz A.R.A. Starting of a free-piston linear engine-generator by mechanical resonance and rectangular current commutation. *2008 IEEE Vehicle Power and Propulsion Conference*, 2008, pp. 1-7. doi: https://doi.org/10.1109/VPPC.2008.4677748.

18. Zulkifli S.A., Karsiti M.N., A-Aziz A.-R. Investigation of linear generator starting modes by mechanical resonance and rectangular current commutation. *2009 IEEE International Electric Machines and Drives Conference*, 2009, pp. 425-433. doi: https://doi.org/10.1109/IEMDC.2009.5075241.

19. Zulkifli S.A., Karsiti M.N., Abd. Rashid Abd. Aziz. Rectangular current commutation and open-loop control for

starting of a free-piston linear engine-generator. *2008 IEEE 2nd International Power and Energy Conference*, 2008, pp. 1086-1091. doi: https://doi.org/10.1109/PECON.2008.4762637.
20. Li Y., Zuo Z., Feng H., Jia B. Parameters matching requirements for diesel free piston linear alternator start-up. *Advances in Mechanical Engineering*, 2015, vol. 7, no. 3, pp. 1-8. doi: https://doi.org/10.1177/1687814015574408.
21. Kim Y.W., Lim J.W., Jung H.K. Starting mode analysis of flat-type linear generator for free-piston engine. *The Transactions of The Korean Institute of Electrical Engineers*, 2008, vol. 57, no. 6, pp. 966-971.
22. Hanipah M.R., Razali A.R. The numerical assessment of motion strategies for integrated linear motor during starting of a free-piston engine generator. *IOP Conference Series: Materials Science and Engineering*, 2017, vol. 257, art. no. 012054. doi: https://doi.org/10.1088/1757-899X/257/1/012054.
23. Song Y., Feng H., Zuo Z., Wang M., Guo C. Comparison Research on Different Injection Control Strategy of CI Free Piston Linear Generator in One-time Starting Process. *Energy Procedia*, 2014, vol. 61, pp. 1597-1601. doi: https://doi.org/10.1016/j.egypro.2014.12.180.
24. Abdulwehab A.I., Ezrann Zharif B. Zainal A., Rashid A.A., Saiful A.Z. Effect of Injection Timing on the Operation of Hydrogen-Fuelled Free-Piston Linear Generator Engine during Starting. *International Journal of Automotive Engineering*, 2013, vol. 4, no. 2, pp. 47-53. doi: https://doi.org/10.20485/jsaeijae.4.2_47.
25. Eid A.M., Suh K. -Y., Choi K. -J., Han H. -D., Lee H. -W., Nakaoka M. A Unique Starting Scheme of Linear-Engine Tubular PM Linear Generator System Using Position Feedback Controlled PWM Inverter. *2006 37th IEEE Power Electronics Specialists Conference*, 2006, pp. 1-5. doi: https://doi.org/10.1109/PESC.2006.1712166.
26. Wang X., Chen F., Zhu R., Yang G., Zhang C. A Review of the Design and Control of Free-Piston Linear Generator. *Energies*, 2018, vol. 11, no. 8, art. no. 2179. doi: https://doi.org/10.3390/en11082179.
27. Arslan S., Gurdal O. Polygonal tubular linear permanent magnet generator analysis and experimental test. *Scientia Iranica*, 2022, vol. 29, no. 1, pp. 168-182. doi: https://doi.org/10.24200/sci.2019.50094.2739.
28. Arslan S., Gurdal O., Akkaya Oy.S. Design and optimization of tubular linear permanent-magnet generator with performance improvement using response surface methodology and multi-objective genetic algorithm. *Scientia Iranica*, 2020, vol. 27, no. 6, pp. 3053-3065. doi: https://doi.org/10.24200/sci.2018.50093.1506.
29. Virsik R., Heron A. Free piston linear generator in comparison to other range-extender technologies. *2013 World Electric Vehicle Symposium and Exhibition (EVS27)*, 2013, pp. 1-7. doi: https://doi.org/10.1109/EVS.2013.6914925.
30. Serdal A., Gurdal O. Hibrit Araçlar İçin Serbest Pistonlu Doğrusal Jeneratör Çeşitlerinin İncelenmesi. *Mesleki Bilimler Dergisi*, 2017, vol. 6, no. 3, pp. 540-552. (Tur).
31. Cheng C.-H., Dhanasekaran S. Numerical Analysis and Parametric Study of a 7 kW Tubular Permanent Magnet Linear Alternator. *Sustainability*, 2021, vol. 13, no. 13, art. no. 7192. doi: https://doi.org/10.3390/su13137192.
32. Rymsha V.V., Radimov I.N., Gulyy M.V., Merkulov I.V. Motorsolve software package: verification of parameters and characteristics of the brushless permanent magnet motor. *Electrical Engineering & Electromechanics*, 2019, no. 5, pp. 20-24. doi: https://doi.org/10.20998/2074-272X.2019.5.03.
33. Bianchi N., Bolognani S., Cappello A.D.F. Back EMF improvement and force ripple reduction in PM linear motor drives. *2004 IEEE 35th Annual Power Electronics Specialists Conference (IEEE Cat. No.04CH37551)*, 2004, vol. 5, pp. 3372-3377. doi: https://doi.org/10.1109/PESC.2004.1355071.
34. Panchal T.H., Patel A.N., Patel R.M. Reduction of cogging torque of radial flux permanent magnet brushless DC motor by magnet shifting technique. *Electrical Engineering & Electromechanics*, 2022, no. 3, pp. 15-20. doi: https://doi.org/10.20998/2074-272X.2022.3.03.
35. Tajdiny A., Monsef H., Lessani H. Design and analysis of a novel yokeless mover permanent magnet linear generator for free piston engine converter. *IET Electric Power Applications*, 2021, vol. 15, no. 10, pp. 1314-1330. doi: https://doi.org/10.1049/elp2.12101.

Received 03.06.2022
Accepted 11.09.2022
Published 06.01.2023

Serdal Arslan[1]*, Assistance Professor,*
Hacene Mellah[2]*, PhD,*
[1] Department of Electrical,
Harran University Organized Industrial Zone Vocational High School,
Harran University, Sanliurfa, Turkey,
e-mail: serdalarslan@harran.edu.tr (Corresponding Author)
[2] Department of Electrical Engineering,
Akhli Mohend Oulhadj University, Bouira, Algeria,
e-mail: has.mel@gmail.com

How to cite this article:
Arslan S., Mellah H. Analysis and testing of internal combustion engine driven linear alternator. *Electrical Engineering & Electromechanics*, 2023, no. 1, pp. 3-9. doi: https://doi.org/10.20998/2074-272X.2023.1.01

UDC 621.3.013 https://doi.org/10.20998/2074-272X.2023.1.02

A. Ibrar, S. Ahmad, A. Safdar, N. Haroon

Efficiency enhancement strategy implementation in hybrid electric vehicles using sliding mode control

Introduction. *Hybrid electric vehicles are offering the most economically viable choices in today's automotive industry, providing best solutions for a very high fuel economy and low rate of emissions. The rapid progress and development of this industry has prompted progress of human beings from primitive level to a very high industrial society where mobility used to be a fundamental need. However, the use of large number of automobiles is causing serious damage to our environment and human life. At present most of the vehicles are relying on burning of hydrocarbons in order to achieve power of propulsion to drive wheels. Therefore, there is a need to employ clean and efficient vehicles like hybrid electric vehicles. Unfortunately, earlier control strategies of series hybrid electric vehicle fail to include load disturbances during the vehicle operation and some of the variations of the nonlinear parameters (e.g. stator's leakage inductance, resistance of winding etc.). The* ***novelty*** *of the proposed work is based on designing and implementing two robust sliding mode controllers (SMCs) on series hybrid electric vehicle to improve efficiency in terms of both speed and torque respectively. The basic idea is to let the engine operate only when necessary keeping in view the state of charge of battery.* ***Purpose****. In proposed scheme, both performance of engine and generator is being controlled, one sliding mode controllers is controlling engine speed and the other one is controlling generator torque, and results are then compared using 1-SMC and 2-SMC's.* ***Method.*** *The series hybrid electric vehicle powertrain considered in this work consists of a battery bank and an engine-generator set which is referred to as the auxiliary power unit, traction motor, and power electronic circuits to drive the generator and traction motor. The general strategy is based on the operation of the engine in its optimal efficiency region by considering the battery state of charge.* ***Results*** *.Mathematical models of engine and generator were taken into consideration in order to design sliding mode controllers both for engine speed and generator torque control. Vehicle was being tested on standard cycle. Results proved that, instead of using only one controller for engine speed, much better results are achieved by simultaneously using two sliding mode controllers, one controlling engine speed and other controlling generator torque.* References 37, figures 11.
Key words: **hybrid electric vehicles, electric vehicles, sliding mode control, efficiency enhancement.**

Вступ*. Гібридні електромобілі пропонують найбільш економічно доцільний вибір у сучасній автомобільній промисловості, надаючи найкращі рішення для дуже високої економії палива та низького рівня викидів. Швидкий прогрес та розвиток цієї галузі підштовхнули людей до переходу від примітивного рівня до дуже високого індустріального суспільства, де мобільність була фундаментальною потребою. Однак використання великої кількості автомобілів завдає серйозної шкоди довкіллю та життю людини. Нині більшість транспортних засобів покладаються на спалювання вуглеводнів задля досягнення потужності руху на провідних колесах. Отже, необхідно використовувати чисті та ефективні транспортні засоби, такі як гібридні електромобілі. На жаль, раніше стратегії управління серійним гібридним електромобілем не враховували збурення навантаження під час роботи автомобіля і деякі зміни нелінійних параметрів (наприклад, індуктивність розсіювання статора, опір обмотки і т.д.).* ***Новизна*** *запропонованої роботи заснована на розробці та реалізації двох надійних контролерів ковзного режиму (SMC) на серійному гібридному електромобілі для підвищення ефективності з точки зору швидкості та моменту, що крутить, відповідно. Основна ідея полягає в тому, щоб дозволити двигуну працювати тільки тоді, коли це необхідно з урахуванням стану заряду акумулятора.* ***Мета****. У пропонованій схемі контролюються характеристики як двигуна, так і генератора, один контролер ковзного режиму регулює швидкість двигуна, а інший регулює крутний момент генератора, а потім результати порівнюються з використанням режимів 1-SMC і 2-SMC.* ***Метод****. Силова установка серійного гібридного електромобіля, що розглядається в даній роботі, складається з акумуляторної батареї та установки двигун-генератор, яка називається допоміжною силовою установкою, тяговим двигуном та силовими електронними схемами для приводу генератора та тягового двигуна. Загальна стратегія заснована на роботі двигуна в області оптимальної ефективності з урахуванням рівня заряду акумуляторної батареї.* ***Результати****. Математичні моделі двигуна та генератора були прийняті до уваги для розробки регуляторів ковзного режиму як для керування частотою обертання двигуна, так і для керування крутним моментом генератора. Транспортний засіб випробовувався за стандартним циклом. Результати показали, що замість використання лише одного регулятора частоти обертання двигуна набагато кращі результати досягаються при одночасному використанні двох регуляторів ковзного режиму, один з яких керує частотою обертання двигуна, а інший - моментом, що крутить, генератора.* Бібл. 37, рис. 11.
Ключові слова: **гібридні електромобілі, електромобілі, керування ковзним режимом, підвищення ефективності.**

1. Introduction. Advent of high pace development of internal combustion engine (ICE) vehicles and invention of automobile industry is contributing so much by satisfying needs of modern society. This prompted progress of human beings from primitive level to a very high industrial level society where mobility used to be a fundamental need (for instance [1-5]). Automotive industry serves as a backbone towards success and development of a nation. However, the use of large number of automobiles is causing serious damage to our environment and human life. It is causing serious problems, which are affecting our eco system badly. Air pollution and global warming are causing us much trouble. At present most of the vehicles are relying on burning of hydrocarbons in order to achieve power of propulsion to drive wheels. Where heat has been used by the engine and combustion byproducts are released in the atmosphere. By products also comprises of harmful gases like nitrogen oxide (NO) and carbon monoxide (CO) and some of the unburned hydro carbons (HC) which are harmful to environment and human health. Global warming is as result of greenhouse effect, which is happening due to presence of harmful gases like carbon dioxide and methane in the atmosphere. The radiations reflected by the earth are trapped by these gases, resulting in increased temperature. As a result, damaging the whole ecosystem and causing natural disasters.

Over last some decades, the need of clean and fast transportation has increased a lot. Keeping in view the time of need hybrid electric vehicles (HEVs) was developed which offers most fuel efficient and emission free transportation these days. The scholars have been researching more and more to bring out best from them. In order to increase efficiency level, researchers have been applying various optimization techniques on hybrid electric vehicles in order to let them operate at their optimum level. Keeping in view pros and cons of different types of HEV's, researches have been digging out on almost every type of hybrid vehicle. All of them have same components like engine/generator set, power converters, fuel tank, batteries, transmission and traction motors along with some auxiliary electrical loads, the difference lies only the way power is transmitted from engine to wheels. Depending upon architecture of drivetrains, HEVs can be divided into 4 major categories i.e. series hybrid electric vehicle (SHEV), parallel hybrid electric vehicle (PHEV), series-parallel hybrid electric vehicles and complex hybrid electric vehicles. Different scholars have proposed various schemes to improve their efficiency. Due to higher battery cost and small driving range of EVs, HEVs came into existence where hybrid electric vehicles use both ICE and electrical machine to work. It has advantages of both EV and HEV. Furthermore, due to their complex structure scholars have been developing various optimization techniques and control strategies on HEVs to get optimum fuel efficiency and reduced level of emission with enhanced battery life. These control strategies were broadly divided into two main types:

1. Rule based strategies of control mainly depend on the modes of operation of vehicle, and these schemes are easily implemented on real time control techniques. Rule based on control schemes mainly based on heuristic based ideas, human intelligence and without prior knowledge of drive cycle [6]. These controllers were usually based on static points of operation of vehicle components like ICE, generator and motor.

2. In optimization based schemes, the basic aim of the controller is to minimize and optimize the cost function. These cost functions depend upon us; it may be fuel consumption or battery life extension or emissions etc. These strategies were not based on real time energy management directly but if we take instantaneous values of cost function, then it is possible to evaluate on real time. Global optimization requires all prior information regarding state of charge (SOC), driving cycle, response of the driver and type of route. Different optimization techniques have been used by researchers like linear programming, dynamic programming, Pontryagin minimum principle, model predictive control, stochastic control strategies, genetic algorithm etc.

Various research has been done for the electric vehicles modeling [7-10], implantation [11-13] and control [14-20]. Control techniques for electric vehicles are significant to evolve the revolution of automotive industry. In [14] authors developed control algorithms for fuel consumption optimization in parallel hybrid automobiles. For full parallel hybrid mode, a mathematical approach is used whereas for torque assist parallel hybrid an approach is designed from optimal sizing was presented in [15]. Energy management strategy in parallel hybrid electric vehicles (PHEV) by using a variable continuous transmission is discussed in [16]. Later on study developed different control schemes for parallel and series hybrid electric vehicles. These schemes basically focus on decreasing fuel consumption and utilizing battery storage capacity as much as possible [17]. In [18], researchers worked on a power management control based strategy for a parallel configuration hybrid electric truck which further includes minimization of a cost function and reduction of emissions. The study has been carried out by using a model of hybrid vehicle in hybrid engine-vehicle simulation (HE-VESIM) which is developed by a research center named as Automotive Research Centre. In [19] authors presented an algorithm for SHEV's to control electricity generation in order to minimize consumption of fuel based on different parameter like SOC of battery etc. In [20] authors proposed efficiency enhancement strategy in PHEV using model predictive control.

In literature several schemes have been proposed for smooth clutch engagement and low jerks having reduced oscillations, like back stepping motor control, optimal control, model predictive control etc. the primary objective of their research was to introduce such control schemes that reduced the transition oscillations while shifting from a pure electric mode to a pure hybrid mode.

Fuel economy of HEV's are majorly affected by their powertrain configurations, powertrain parameters, and energy management strategies. However, catering all three at a time requires large space and exhaustive optimal control strategy like dynamic programming (DP) which is in fact complex and expensive computationally. A faster and computationally efficient optimization strategy rapid dynamic programming (Rapid-DP) is developed in 2019 authors proposed optimization control of a power split hybrid vehicle where all 3 are optimized simultaneously. A combined optimization strategy was employed on Toyota Prius and Prius++ in order to examine fuel savings and increase in operating mode [21]. In [22] authors presented energy management strategy for series hybrid deep tracked electric vehicle (SHETV) by developing deep Q-learning (DQL) algorithm. Robustness of whole model is improved by utilizing two deep Q-networks with some initial weights and identical structure are built and then trained to estimate action-value function.

In [23] was developed a strategy based on model predictive controller for power split hybrid electric vehicles by developing two management schemes for power-split hybrid electric city bus (HECB), incorporating linear time-varying stochastic model predictive control and Pontriagin minimum principle stochastic model predictive control. Both strategies do have real time fast computational response at cost of complex calculations with increased efficiency.

In [24] analysis based on comparison of energy management strategies for HEV'S was introduced. Different schemes like dynamic programming (DP), Pontryagin minimum principle (PMP) and equivalent consumption minimization strategy (ECMS) were

studied. Results revealed that ECMS used to be only implanted in the real time. While, PMP and DP were proved to be more affective energy management strategies in optimal control.

In [25] study presented a point-by-point investigation of the ideal vitality administration issue for plug-in hybrid electric vehicles illuminated utilizing the PMP. In this study, a relation between directions of state and co-state with the battery characteristics has been produced which are not been investigated in a comparative design in earlier writing. A partial area examination is additionally completed demonstrating the partial linearity of the ideal condition of SOC with appreciation to outing length for a mix of certain standard driving cycles. Information picked up from this activity empowers us to build up a versatile vitality administration methodology. Furthermore, a model predictive control (MPC) torque-split system that consolidates diesel motor transient qualities for PHEV was studied to enhance the fuel efficiency of HEV. For most of the HEV applications where the motors continuously experience transient operations, like including start and stop, the impact of the motor transient attributes on the general HEV powertrain mileage turns out to be more declared [26].

In [27] an adjusted SOC estimation calculation is connected here, which incorporates coulomb checking strategy, as well as open circuit voltages, components of weighting and revision variable in order to track the run time SOC productively. Further, nearness of battery and motor together, needs an overall force split plan for their effective usage. In this study, a fuel proficient vitality administration methodology for force split HEV utilizing adjusted SOC estimation technique is produced. Here, the ideal estimations of different overseeing parameters are firstly figured with hereditary calculation and after that nourished to Pontryagin base standard to choose the limit of the power at which motor is turned on. This procedure actually makes the proposed technique a hearty and gives better opportunity to enhance fuel proficiency. The motor effective working area is additionally distinguished which makes the vehicle work in proficient locale and diminish fuel utilization.

In [28] a quantitative investigation of fuel consumption and performance of series hybrid electric vehicle HMMWV (high mobility multi-reason wheeled vehicle) is a vehicle used in military with a routine HMMWV of proportional size is presented. In this paper, a philosophy is displayed by which the efficiency increases because of streamlined motor are separated from the mileage increases due to regenerative braking. In [29] a control based strategy was developed in order to improvise fuel economy and efficiency of engine of series hybrid vehicle using fuzzy logic and sliding mode control. The fuzzy logic controller has two inputs; the vehicle power demand and SOC of the battery and purpose of this controller was to increase engine and battery efficiency levels. Besides, two sliding mode controllers are designed in order to remove uncertainties and disturbances occurred while vehicle is working.

As of late, numerous analysts have been concentrating on the different issues related to control of the SHEV powertrain architectures. In [30] was presented a control scheme for SHEV's based on sliding mode controllers (SMC) with fixed boundary layers. These controllers are aimed to control engine/generator speed and torque, to let them operate in optimal efficiency area. Consequently, affecting fuel economy and also enhanced battery life is expected.

In the previous literature which is related to SHEVs studies are mostly concentrated on control of auxiliary power unit (APU). The work [31] presents a linear adaptive DP, which requires a prior information and knowledge of the plant. In [32] PI controllers were utilized in order to control auxiliary power unit. However highly nonlinear system nature is a great obstacle in getting optimized performance. In order to achieve maximum fuel economy and battery lifetime bi-level energy management strategy for plug-in hybrid electric vehicles with a reference of SOC was achieved by utilizing radial basis function neural networks along with MPC [33]. However, a review papers in [31-35] elaborated vital energy management strategies for various types of HEV's by focusing on both APU control and energy storage system. Pointing various pros and cons of different energy management strategies used to optimize vehicle efficiency. Where all recommendations and suggestions were shared in [33] varying from proportional–integral–derivative controller, operational or state mode, rule-based or fuzzy logic, and equivalent consumption minimization strategies, are explained. Various optimization techniques were discussed including dynamic programming, geometric algorithms (GA's), particular swarm optimization (PSO) etc. Along many other techniques, research on production of hybrid renewable energy has also been done by using fuzzy logic based smart controllers, where improved energy management and optimization was employed by using smart economic strategy based on fuzzy logic. Fuzzy logic was employed efficiently to control hybrid electric energy sources built around solar panels, wind turbine and electric storage system with assistance of electric grid [36]. Efficiencies of HEV's were enhanced by using multiple techniques, and generator torque control is one of the effective ones. Where generator torque was controlled based on second order SMC for three-level inverter-fed permanent magnet synchronous motor [37]. Application of SMC controller helped resolving uncertain noises and ripples, which enhanced torque response.

Nonetheless, these SHEV powertrain control methodologies neglect to adequately address the exceptionally nonlinear parameter varieties and sudden outside aggravations amid the vehicle operation.

Details regarding series hybrid vehicle structure and implementation of sliding mode controllers in order to control engine speed and torque of the generator will be discussed in next section.

The goal of the paper is to study and model series hybrid electric vehicle and implementing two sliding mode controllers; one for controlling engine speed and other one controlling generator torque and as a result they let the series hybrid vehicle to operate only in its optimum efficiency region.

2. Designed scheme. In this research, a series hybrid electric model has been developed on MATLAB/Simulink with additional two SMCs, which helps a lot in catering nonlinearities developed while driving. Both controllers together let the vehicle to optimize performance of vehicle in terms of speed and torque. In this research, the specific control strategy to be proposed aims at to discover the robustness characteristics of SMC against uncertainties of engine/generator set and the power converter. The very basic idea is not let the engine to operate when vehicle is in idle state. When the SOC of battery drops any reference value engine will be turned ON and it will be turned OFF when SOC reaches a maximum reference value. Both two SMCs run at same time to achieve the optimal efficiency of vehicle by controlling speed of engine and. In some recent years, sliding mode control has become hot topic in case of optimization of hybrid vehicles.

Unfortunately, earlier control strategies of SHEV fail to include load disturbances during the vehicle operation and some of the variations of the nonlinear parameters (e.g. stator's leakage inductance, resistance of winding etc.). SMC is very good for applications in automobile industry due to its very basic property of order reduction; also these controllers are less sensitive to all the disturbances during vehicle operation and parameter variation of the plant [4, 5].

The basic aim of this research is to develop two robust and noise free SMCs for speed of engine and generator's torque control. This will eventually increase efficiency of the SHEV. In this research two controllers were applied simultaneously which will actively contribute to increase the efficiency levels of vehicle. These controllers were applied on APU; consisting engine, generator and power converters. Military vehicle HMMWV is also a series hybrid vehicle and this research helps a lot in enhancing its efficiency. The basic idea is to let the engine operate only when necessary keeping in view the SOC of battery. The controllers will help to let the vehicle operate only in their optimum efficiency range.

3. Powertrain components of series HEV. The engine generator set along with AC/DC drivers are connects with the battery pack in series manner with traction motors.

3.1. Vehicle system. The engine used is a diesel engine generating 114 kW at 5000 rpm. A permanent magnet synchronous generator (PMSG) is used with related output of 114 kW with 90 % efficiency. The battery pack of vehicle used is of nickel metal hydride, as they are available commercially also with a voltage of 12V DC. In this project 12 such batteries are connected in series in order to get a voltage of 288 V. Power is being delivered to the wheels using batteries. Two traction motors are used here to deliver power to the load; they are also permanent magnet synchronous motors. One of the motor is directly connected to the rear differential while second one is connected through drive shaft to front one. Figure 1 shows the system including a diesel engine, a PMSG with its respective drive that is AC-DC converter. Motor is connected with their DC/AC converters aims at providing traction power to the wheels. The generator is working both as starter giving starting torque to engine and as an alternator.

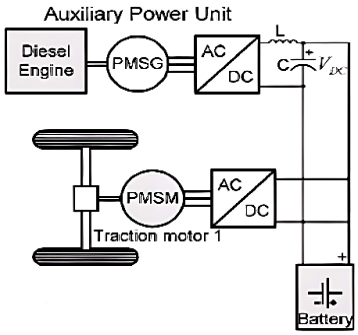

Fig. 1. Schematic diagram of series HEV drivetrain

3.2. Modeling of engine. The modeling of the engine is performed by using torque and speed equations of the engine which are forth order polynomials, found out using least-squares method. Torque T_{es} in terms of speed w_{es} comes out to be:

$$T_{es} = 1.6510 \cdot 10^{-7} \cdot w_e^4 - 0.0002 \cdot w_e^3 + 0.0546 \cdot w_e^2 - \\ - 6.65 \cdot w_e + 361.67 = \sum_{i=0}^{4} \alpha_i w_e^i, \quad (1)$$

where α_i are the polynomial coefficients i = 0,1,2,3,4. It is also possible to derive w_{es} as a function of T_{es} such as

$$w_e = 2.32 \cdot 10^{-6} T_{es}^4 - 0.00114 \cdot T_{es}^3 + 0.1937 \cdot T_{es}^2 - \\ - 11.839 \cdot T + 267.963 = \sum_{i=0}^{4} \alpha_i \cdot \beta_i \cdot T_{es}^j, \quad (2)$$

where β_i are the polynomial coefficients i = 0,1,2,3,4.

Functional block diagram of APU control system is shown in Fig. 2, where 2 control signals are being generated one for control of engine speed and other for generator torque control using information coming from SOC of battery and generator currents.

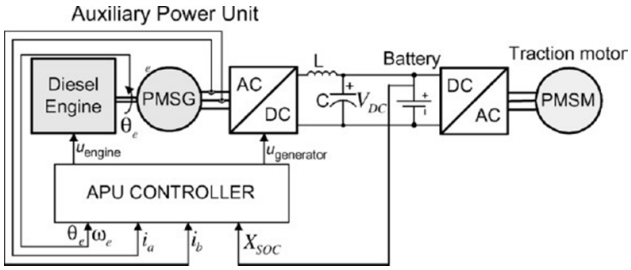

Fig. 2. Functional diagram of APU control system

3.3. Auxiliary power unit (APU). In Fig. 3, Simulink diagram for APU is shown. It comprises of two sliding mode controllers, one PID controller, and two functional blocks are designed in order to calculate reference engine speed and generator torque. In addition, rate limiters and saturation blocks are being employed to let the engine operate in optimum region. A relay is being used to generate ON/OFF signals for auxiliary power unit.

3.4. Modeling of the PMSG. PMSG is used in this research because of its reliability, lower maintenance and more efficiency. The dynamic model of the PMSG is derived reference frame which is synchronous and it is two phase in which with respect to rotation the q-axis is 90° ahead of the d-axis. The dq-axis model of the PMSG is obtained as:

$$\mathrm{d}i_q = -\frac{R}{L_q}\cdot i_q + \frac{w_e \cdot L_d}{L_q}\cdot i_d - \frac{1}{L_q}\cdot v_q + \frac{K_b}{L_q}\cdot w_e; \quad (3)$$

$$\mathrm{d}i_d = -\frac{R}{L_d}\cdot i_q + \frac{w_e \cdot L_q}{L_d}\cdot i_q - \frac{1}{L_d}\cdot v_d; \quad (4)$$

$$T_g = -K_t \cdot i_q + k_1 \cdot \left(L_d - L_q\right)\cdot i_d \cdot i_q \ , \quad (5)$$

where i_d, i_q are the d-q axis axis currents of generator respectively; v_d, v_q are the generator's d-q axis voltages; R is the generator resistance; L_d, L_q are the generator's d-q axis inductances; K_t is the torque constant of generator; K_b is the induced voltage constant of generator; T_g is the generator torque; k_1 is the reluctance torque coefficient; w_e is the speed of the engine.

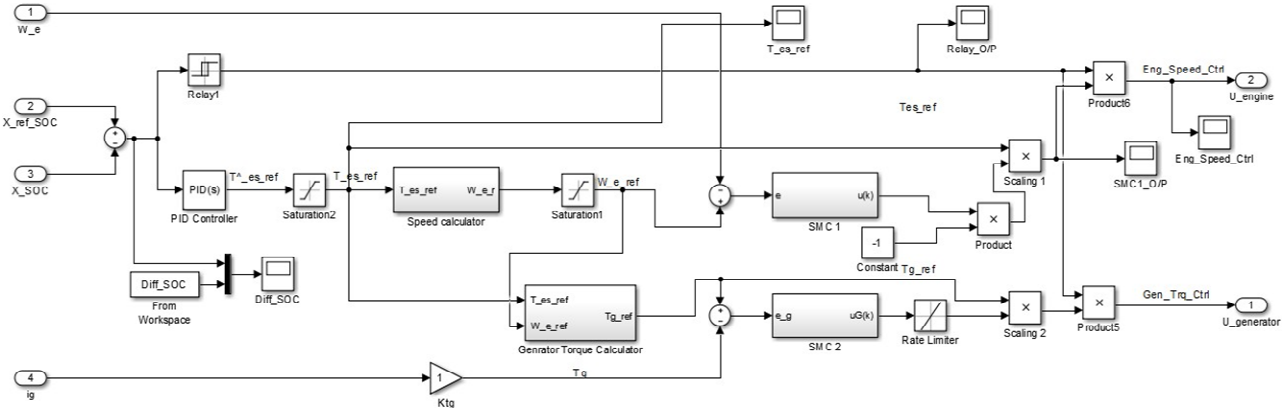

Fig. 3. Schematic diagram of series HEV drivetrain

3.4 Development of control strategy. The control strategy is having the following main aims and objectives. The SOC of the battery is kept between a given minimum and maximum level. When the charge decreases to a certain given lower level ($SOC_{\min}$), the engine will be started or in ON state from idle state EC = 1 and engine is again stopped when SOC reaches a certain maximum level or upper edge ($SOC_{\max}$) then EC = 0:

$$EC = \begin{cases} 1 & SOC_{\min} \geq SOC(t); \\ EC(t-1) & SOC_{\max} > SOC(t) > SOC_{\min}; \\ 0 & SOC_{\max} \leq SOC(t). \end{cases}$$

3.4.1 Parts of APU. (APU) comprises of three parts.

3.4.1.1. Linear PID controller. The basic function of this controller block is to output the reference torque value for the engine, by finding the difference between reference state of charge which is kept 97.7 V here and the actual state of charge of the battery by taking them as its input. After that to assure that the torque value stays in limit, saturation block is placed at the output so that the value stays within a suitable range. Using this optimal region, the speed reference for the optimal efficiency region can be given as:

$$w_e^r = \sum_{j=0}^{4} \beta_j \left(T_{es}^r\right)^j . \quad (6)$$

The speed calculated is again limited via saturator so that it remains in optimal region. After determining the reference torque and speed values, controllers are designed based on sliding mode with aim to control speed and torque.

3.4.1.2. Sliding mode based engine speed control. Overall efficiency improvement of SHEV requires very good control strategies for highly non-linear dynamics of engine. Hence, a robust SMC, which can be able to acquire a high level robustness against non-linear uncertainties and disturbances of the system, is the main aim of the study. For the control strategy under this research, a simple state space representation, using the model of the engine is:

$$\begin{aligned} \frac{\mathrm{d}x_{soc}}{\mathrm{d}t} &= K \cdot i_b; \\ \frac{\mathrm{d}w_e}{\mathrm{d}t} &= \frac{1}{J_{tot}} T_{es} - \frac{1}{n \cdot J_{tot}} \cdot T_g, \end{aligned} \quad (7)$$

where x_{soc} is the state of charge; $i_b = i_q - i_m - i_L$ is the battery current; i_m is the traction motor current; i_L is the parasitic electric load current; i_q is the generator quadrature current; T_g is the generator torque; J_{tot} is the total inertia $J_{tot} = J_g \cdot n^2 + J_e$; J_e is the engine inertia; J_g is the generator inertia; n is the generator speed ratio $w_e/w_g = 1.038$; $K = C_b/3600$, C_b is the battery capacity, Ah.

In (1), the torque function is derived for maximum load in terms of demanded speed; in other words, for maximum throttle level (i.e., 1). The throttle level assumes values between 0 and 1 for engine control. Therefore, the torque of the engine should be rewritten as a function of the throttle level, which takes values from 0 to 1 as follows:

$$T_{es} = u \cdot \left(\alpha_0 + \alpha_1 w_e + \alpha_2 \cdot w_e^2 + \alpha_3 \cdot w_e^3 + \alpha_4 \cdot w_e^4\right), \quad (8)$$

where u is the torque control input (throttle angle 0-100 %).

First, the polynomial approximation in (1) for T_{es}, is substituted in the following equation of motion for the engine:

$$\frac{\mathrm{d}w_e}{\mathrm{d}t} = \frac{1}{J_{tot}} \cdot u \cdot \sum_{i=0}^{4} \alpha_i \cdot w_r^i - \frac{1}{n \cdot J_{tot}} \cdot T_g \ . \quad (9)$$

Then, a sliding surface σ, is chosen as

$$\sigma = T \cdot e, \quad (10)$$

where

$$e = w_e^T - w_e \, . \quad (11)$$

To ensure system's the stability, Lyapunov conditions are used to derive the sliding mode control law:

$$V = \frac{1}{2} \cdot \sigma^2 > 0 \, ; \quad (12)$$

$$\dot{V} = \sigma\dot{\sigma}, \tag{13}$$

which should be equal to $-D\cdot\sigma^2$ to satisfy the condition of negative definiteness of $\dot{V}$. Thus

$$\dot{V} = -D\cdot\sigma^2, \tag{14}$$

where $D>0$.

Consequently

$$\sigma + D\cdot\dot{\sigma} = 0. \tag{15}$$

By taking the derivative of σ and substituting the equation of motion. Inside $\dot{\sigma}$

$$\dot{\sigma} = T^*\cdot\left(\dot{w}_e^t - \dot{w}_e\right) = \\ = T^*\cdot\dot{w}_e^t - T^*\cdot\frac{1}{J_{tot}}\cdot u\cdot\sum_{i=0}^{4}\alpha_i\cdot w_r^i + \frac{1}{n\cdot J_{tot}}\cdot T_g. \tag{16}$$

Now u_{eq}, which is equivalent control input, that makes $\dot{\sigma}=0$ is to be calculated by replacing u with u_{eq}. And it produces

$$u_{eq} = \frac{J_{tot}}{\sum_{i=0}^{4}\alpha_i\cdot w_e^i}\left(\dot{w}_e^t + \frac{1}{n\cdot J_{tot}}T_g\right); \tag{17}$$

$$\dot{\sigma} = T^*\cdot\frac{1}{J_{tot}}\cdot\sum_{i=0}^{4}\alpha_i\cdot w_e^i\cdot\left(u_{eq}-u\right). \tag{18}$$

Substituting in (14) into (18) and discretizing this equation with (18), yields

$$T^*\cdot\frac{1}{J_{tot}}\sum_{i=0}^{4}\alpha_i\cdot w_e^i(k)\cdot\left(u_{eq}(k)-u(k)\right)+D\cdot\sigma(k)=0 \tag{19}$$

and

$$\frac{\alpha(k)-\alpha(k-1)}{T} = T\cdot\frac{1}{J_{tot}}\sum_{i=0}^{4}\alpha_i\cdot w_e^i(k-1)\times \\ \times\left(u_{eq}(k-1)-u(k-1)\right). \tag{20}$$

Assuming that input equivalent control is an average value and nothing else

$$u_{eq}\approx u_{eq}(k-1). \tag{21}$$

Finally generating a chattering free controller named as SMC which is

$$u(k) = u(k-1) + \frac{J_{tot}}{T^*\cdot T\sum_{i-0}^{4}\alpha_i\cdot w_e^i(k)}\times \\ \times\left(\left(1+D\cdot T\right)\sigma(k)-\sigma(k-1)\right), \tag{22}$$

where T^*, D are positive design parameters.

3.4.1.3. Sliding mode based generator torque control. Now, after engine speed controller at this level torque reference values are already being generated using generator torque calculator used in APU model. By using these values a reference torque value is generated using PID controller, optimized values of engine speed and inertia of the generator as

$$T_g^r = T_{es}^r - J_{tot}\cdot\dot{w}^r. \tag{23}$$

A noise free SMC of torque is designed based on PMSG model, and its state space form is

$$\underbrace{\frac{\mathrm{d}}{\mathrm{d}t}\begin{bmatrix} i_d \\ i_q\end{bmatrix}}_{x_g} = \underbrace{\begin{bmatrix} -\frac{R}{L_d} & 0 \\ 0 & -\frac{R}{L_d}\end{bmatrix}}_{A_g}\begin{bmatrix} i_d \\ i_q\end{bmatrix} + \\ + \underbrace{\begin{bmatrix} \frac{L_d}{L_q}w_e i_d + \frac{K_b}{L_q}w_e \\ \frac{L_q}{L_d}w_e i_q\end{bmatrix}}_{\eta} + \underbrace{\begin{bmatrix} -\frac{1}{L_d} & 0 \\ 0 & -\frac{1}{L_d}\end{bmatrix}}_{B_g}\underbrace{\begin{bmatrix} v_d \\ v_q\end{bmatrix}}_{u_g}; \tag{24}$$

$$T_g = K_t\cdot i_q + K_1\cdot\left(L_d - L_q\right)\cdot i_d\cdot i_q.$$

As there is large number of rotor teeth so we assume that $L_d\approx L_q$ the torque of the generator becomes

$$T_g \approx K_t\cdot i_q. \tag{25}$$

In state space form

$$\dot{x}_g = A_g\cdot x_g + B_g\cdot u_g + \eta; \\ y = T_g\cdot x_g = \begin{bmatrix}0 & K_t\end{bmatrix}\begin{bmatrix} i_d \\ i_q\end{bmatrix}. \tag{26}$$

By selecting an error surface based on difference of generator currents and by choosing the Lyapunov function, controller is designed in the same way as done previously. Hence, the law for control can be derived as

$$u_g(k) = u_g(k-1) + \frac{B^{-1}}{T}\left(\left(1+D_g T\right)\sigma_g(k) - \sigma_g(k-1)\right), \tag{27}$$

where

$$u_g = \begin{bmatrix} v_d^r \\ v_q^r\end{bmatrix}. \tag{28}$$

In generator control mechanism, generator output currents are taken and passed through abc/dq, which is converting them to dq state of reference these are being fed into SMCs, after that output voltages of SMC are again being converted to abc state of references which are then passed through ha PWM generator as a control signal further being fed into IGBT's.

4. Simulations and results. In this section simulations are made on MATLAB/Simulink. Where first a series hybrid vehicle is developed and after that SMCs are implemented in order to control engine speed and generator torque. Simulations of different components of series hybrid vehicle are shown in this section.

4.1. Simulation of vehicle system. In Fig. 4 a reference SOC value of 97 V is fed into APU, w_e (actual speed generated by vehicle) is also used as an input to APU, another input is id which is the current generated by the PMSG. APU is generating optimum values of engine speed and generator torque for engine and generator respectively. Next to APU, is engine which is further connected in series to generator, AC-DC-AC converters and battery. And finally a PMSG is connected to the vehicle shaft. Kph demand block is actually based on reference drive signal, which is being fed and used as a standard cycle on which vehicle is being tested.

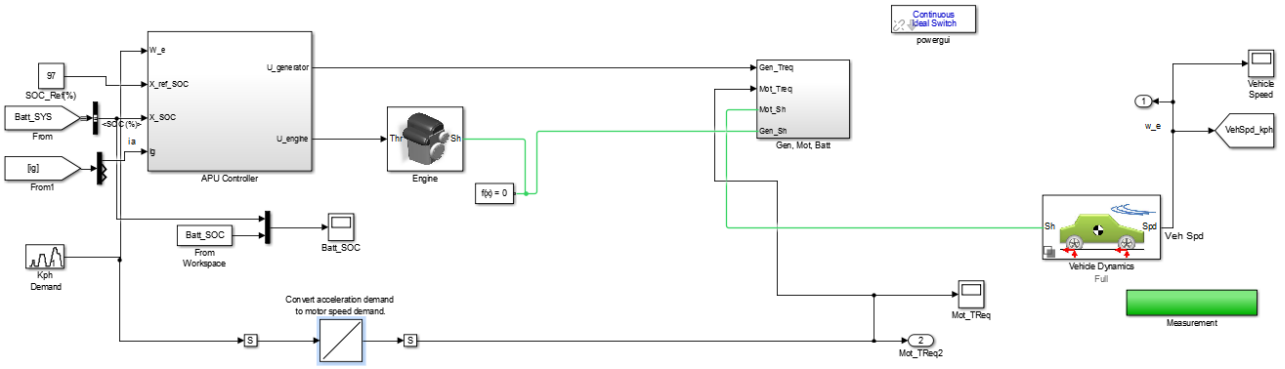

Fig. 4 Overall vehicle system

4.1.1. Simulation of APU. This figure is based on two main parts.

1) A PID controller is used to appropriate reference torque values based on difference between actual SOC and standard SOC value, which is then passed through a saturator to limit the torque value. These torque values are then used as an input by speed calculator block and it output w_{er} speed values by using (2). These speed values are again passed through a saturator in order to limit them. After that w_e coming from actual speed of vehicle and the w_{er} value generated by the speed calculator equation are passed through saturator to get w_{eref}, then passed through a summer to find the error between the two which is then made as an input to SMC 1. Similarly for torque calculation, i_g coming from generator is being multiplied to constant K_{Tg} to get T_g torque and other reference torque value is generated by using previously generated w_{eref} and passing it into torque calculator as an input and output is the respective torque values T_{gref}, now both T_g and T_{gref} are passed into a summer to generate error based on their error SMC 2.

2) Second main part of the APU, are the two sliding mode controllers one is taking error between the speed and generating optimum speed value for engine to be fed into it, and the other one taking error between generator torques and accordingly generating the optimum value for generator torque. The controller designed for engine speed is basically based on (22) and for generator torque is based on (27).

4.1.2 Simulation of engine. The optimum speed u_{engine} is generated by APU is being fed into the engine. A generic spark ignition engine is being used of 114 kW and running at 5000 rpm. Figure 5 is a simulation of engine used in this research. The input speed values are fed into engine as a throttle level between 0 and 1. It is depicting the torque demanded from engine as a fraction of maximum possible torque. If the speed of engine falls below the stall speed, which in this case is 500 rpm, the torque is assumed zero. In this model, F and B are mechanical rotation ports associated with engine shaft. P and FC are output ports via which power of engine and fuel consumption is reported.

4.1.3 Generator, motor and battery. The generator motor and battery of system is connected in series in addition with DC-DC converters (Fig. 6). In this section of simulation, a PMSG of rating 114 kW with related efficiency of 90 % is connected to a DC-DC converter, which is converting AC output of generator to a DC so that is can charge the battery which is next to the converter. The output voltage of DC-DC converter is 500 V. this DC is again converted into AC to be used by synchronous motor. Output is then fed into the vehicle shaft.

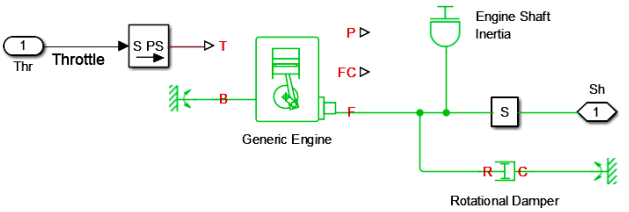

Fig. 5. Speed-torque characteristics of engine

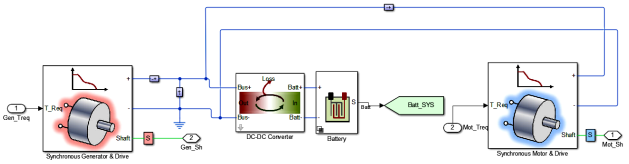

Fig. 6. PMSG, DC-DC converter, battery and motor

In this section of simulation, a PMSG of rating 114 kW with related efficiency of 90 % is connected to a DC-DC converter which is converting AC output of generator to a DC so that is can charge the battery which is next to the converter. The output voltage of DC-DC converter is 500 V. This DC is again converted into AC to be used by synchronous motor. Output is then fed into the vehicle shaft.

4.1.4 Sliding mode based engine speed controller. The simulation model of controller designed for engine speed control based on (29) is basically implemented. Error e is being multiplied with T^* which together makes $\sigma = T^* \cdot e$ the sliding surface. Next this is being multiplied by $(1 + D \cdot T)$ also a delayed signal is introduced making $\sigma(k-1)$ and both the values are subtracted by passing it into a subtracter, where T^* is randomly taken as 15.032, D equals to 7.6 hence $(1 + D \cdot T)$ equals to 32.526. To find out denominator of equation, T^* is multiplied by T and then passed through polynomial equation block to find $\sum_{i=0}^{4} \alpha_i \cdot w_e^i(k)$, is nothing but (1). Then passed through a divider output $u(k)$ is delayed by 1 and passed through adder to complete the equation:

$$u(k) = u(k-1) + \frac{J_{tot}}{T^* \cdot T \sum_{i=0}^{4} \alpha_i \cdot w_e^i(k)} \times \left((1 + D \cdot T) \cdot \sigma(k) - \sigma(k-1) \right) \quad (29)$$

4.1.5 Sliding Mode based Generator Torque Controller. In Fig. 7 equation (27) is implemented in the same way as previous is done.

$$u_g(k) = u_g(k-1) + \\ + \frac{B^{-1}}{T}\left(\left(1 + D_g \cdot T\right)\cdot \sigma_g(k) - \sigma_g(k-1)\right) \quad (30)$$

Target speed. The standard cycle used as a reference over which vehicle is being tested, where initially from 0 to 1 s vehicle is at off state, then afterwards it starts and accelerates up to 50 rpm uptil 2.5 s. After that it again decelerates and comes to 0 rpm at 3.5 s again increased until 10 rpm at 5 s and again decelerated to zero rpm. And finally at 10 s it comes to rest.

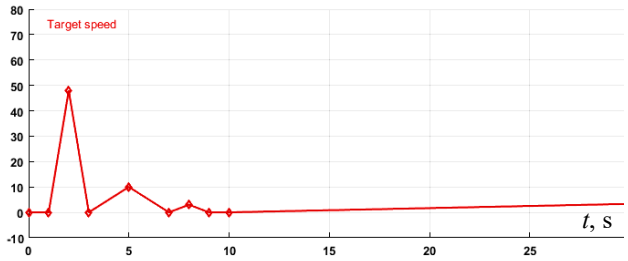

Fig. 7. Standard cycle to test vehicle

4.2 Results. In this section, control methods developed and results are being shown in terms of speed and torque of engine and generator using only one SMC and using both SMC's and their result are compared to see the trend of efficiency.

In the above Fig. 8, SOC is measured versus time. In simulation a reference of 97 V is given below which engine starts shutting down. The graph is showing the trend of battery SOC.

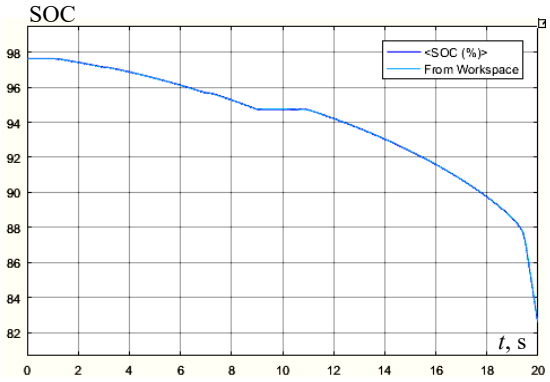

Fig. 8. Battery SOC

In Fig. 9, speed versus time variation of engine is shown. The simulation runs for 20 s over target cycle. First blue graph is using only one controller. For the case when only one controller is applied to the simulation, increase in speed is very less. From zero to 3.5 s speed is negative after that starts increasing and gets maximum upto12 rpm and rests at it until end.

For the case when both controllers are applied, speed graph is more likely following the standard target cycle used. Initially when vehicle is in off state graph is following target cycle and remains at zero rpm until 3.5 s. After that it starts increasing and attains 42 rpm and starts decreasing when vehicle is in deceleration mode. After 10 s speed starts rising and approaching zero.

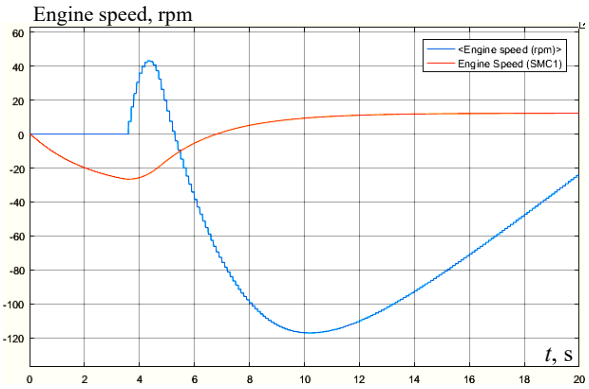

Fig. 9. Engine speed using 1-SMC and 2-SMC's

In Fig. 10, engine torque is shown and there is a great efficiency enhancement in torque also. By using one controller's results seems to be not very satisfactory and maximum gained torque is 0.5 N·m only. While when we implemented both controllers, one controlling engine speed and other controlling generator torque a high torque is added in the system reaching nearly 3 N·m and settling at zero N·m from 10 sec to 20 sec time span.

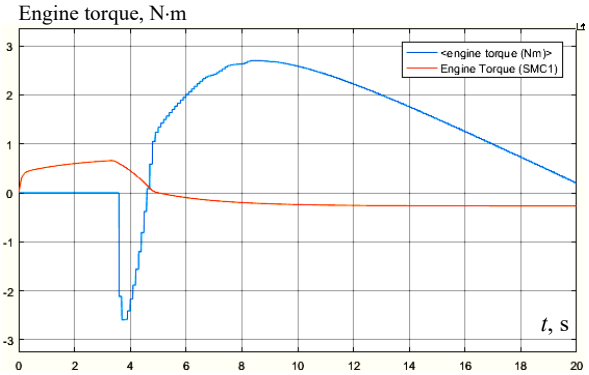

Fig. 10. Engine torque with 1-SMC and 2-SMC's

In Fig. 11, generator torque graphs are shown and compared using 1-SMC and 2-SMC's. while using only one controller, at start it decreases up to 0.6 N·m and then starts increasing at 3.5 s and reach at maximum level of 0.2 N·m. After that approach zero as vehicle comes to rest. As compared to this, a high torque is gained max up to 4.4 N·m in case when both controllers are employed to the system. Hence, results are much better when both controllers are implemented in the system.

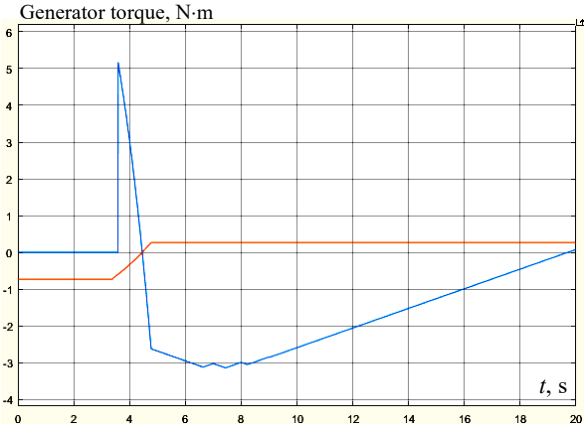

Fig. 11. Generator torque using 1-SMC and 2-SMC's

4.3 Efficiency enhancement. Efficiency enhancement in terms of η is calculated in this section. Using this formula

$$\eta = \frac{\text{obtained speed}}{\text{actual speed}} \cdot 100 .$$

We can easily find out efficiencies in terms of speed by both cased using 1-SMC and 2-SMC's based on their difference we will see how much efficiency is increased by employing second controller to the system.

- **Speed efficiency using 1-SMC.**

Maximum obtained speed is 12 rpm; actual speed needed is 50 rpm:

$$\eta_1 = \frac{12}{50} \cdot 100 = 24\% .$$

- **Speed efficiency using 2-SMC's**.

Maximum obtained speed is 42 rpm; actual speed needed is 50 rpm:

$$\eta_2 = \frac{42}{50} \cdot 100 = 84\% .$$

Hence, increase in efficiency $\eta_2 - \eta_1 = 60$ %.

Therefore, it is very clear that efficiency is increased to a much better extent when both controllers are employed in the system rather than by only using controller for engine generator control enhances the efficiency levels to a much reasonable and acceptable level. SMCs enhanced efficiency level of SHEV to a great extent. These robust controllers helped to reduce noise while vehicle is in operating state. They helped to reduce non-linearities.

5. Conclusion. In this research work, a series hybrid electric model is developed on MATLAB/Simulink and then two robust sliding mode controllers were designed and implemented in order to control engine speed and generator torque so that vehicle would run at maximum possible efficiency level.

As a series hybrid electric vehicle is a highly non-linear system, so a robust controller to be designed is a need of the time. By using two controllers, instead of only one, higher efficiency levels are achieved actually. In past work related to series hybrid electric vehicles, researches mostly focused on control of engine-generator set together called auxiliary power unit. The major development of this research is that two sliding mode controllers have been designed to be used in the system simultaneously, together optimizing speed of the engine and controlling torque of the generator in order to achieve a robust efficiency level in series hybrid electric vehicle.

The results revealed that much higher speed and torque could be achieved by using two controllers simultaneously controlling engine speed and generator torque. By employing both controllers in the system efficiency increases from 24 % to 84 %, hence a net increase of 60 % is observed. Graphs clearly show that by using of two sliding mode controllers a significant amount of speed and torque is added to the system. The basic idea was to not allow the engine to operate outside optimal region. By doing so, fuel consumption is also optimized as vehicle operated only when it is need, while deceleration or idle mode engine shuts off according to control strategy. These sliding mode controllers based control strategies depict the expected robustness via speed and torque. Despite of the load variations and non-linearities, graph tracked the standard cycle to much better level with an efficiency increase of 60 %. The addition of generator torque controller via two sliding mode controllers yields improved performance of series hybrid electric vehicle. The proposed scheme controls all the uncertainties of the system including engine and the generator. When the state of charge of battery drops below a predetermined level engine shuts off, and as engine reaches above the given level engine is stopped.

Conflict of interest. The authors declare that they have no conflicts of interest.

REFERENCES

1. Ding X., Guo H., Xiong R., Chen F., Zhang D., Gerada C. A new strategy of efficiency enhancement for traction systems in electric vehicles. *Applied Energy*, 2017, vol. 205, pp. 880-891. doi: https://doi.org/10.1016/j.apenergy.2017.08.051.

2. Vatsala Ahmad A., Alam M.S., Chaban R.C. Efficiency enhancement of wireless charging for Electric vehicles through reduction of coil misalignment. *2017 IEEE Transportation Electrification Conference and Expo (ITEC)*, 2017, pp. 21-26. doi: https://doi.org/10.1109/ITEC.2017.7993241.

3. Hussain A., Musilek P. Resilience Enhancement Strategies For and Through Electric Vehicles. *Sustainable Cities and Society*, 2022, vol. 80, art. no. 103788. doi: https://doi.org/10.1016/j.scs.2022.103788.

4. Ahmed H., Çelik D. Sliding mode based adaptive linear neuron proportional resonant control of Vienna rectifier for performance improvement of electric vehicle charging system. *Journal of Power Sources*, 2022, vol. 542, art. no. 231788. doi: https://doi.org/10.1016/j.jpowsour.2022.231788.

5. Bouguenna I.F., Azaiz A., Tahour A., Larbaoui A. Robust neuro-fuzzy sliding mode control with extended state observer for an electric drive system. *Energy*, 2019, vol. 169, pp. 1054-1063. doi: https://doi.org/10.1016/j.energy.2018.12.101.

6. Panday A., Bansal H.O. A Review of Optimal Energy Management Strategies for Hybrid Electric Vehicle. *International Journal of Vehicular Technology*, 2014, pp. 1-19. doi: https://doi.org/10.1155/2014/160510.

7. Lekshmi S., Lal Priya P.S. Mathematical modeling of Electric vehicles - A survey. *Control Engineering Practice*, 2019, vol. 92, art. no. 104138. doi: https://doi.org/10.1016/j.conengprac.2019.104138.

8. Patyal V.S., Kumar R., Kushwah S. Modeling barriers to the adoption of electric vehicles: An Indian perspective. *Energy*, 2021, vol. 237, art. no. 121554. doi: https://doi.org/10.1016/j.energy.2021.121554.

9. Kapeller H., Dvorak D., Šimić D. Improvement and Investigation of the Requirements for Electric Vehicles by the use of HVAC Modeling. *HighTech and Innovation Journal*, 2021, vol. 2, no. 1, pp. 67-76. doi: https://doi.org/10.28991/HIJ-2021-02-01-07.

10. Hariri A.-M., Hejazi M. A., Hashemi-Dezaki H. Investigation of impacts of plug-in hybrid electric vehicles' stochastic characteristics modeling on smart grid reliability under different charging scenarios. *Journal of Cleaner Production*, 2021, vol. 287, art. no. 125500. doi: https://doi.org/10.1016/j.jclepro.2020.125500.

11. León R., Montaleza C., Maldonado J.L., Tostado-Véliz M., Jurado F. Hybrid Electric Vehicles: A Review of Existing Configurations and Thermodynamic Cycles. *Thermo*, 2021, vol. 1, no. 2, pp. 134-150. doi: https://doi.org/10.3390/thermo1020010.

12. Llopis-Albert C., Palacios-Marqués D., Simón-Moya V. Fuzzy set qualitative comparative analysis (fsQCA) applied to the adaptation of the automobile industry to meet the emission standards of climate change policies via the deployment of electric vehicles (EVs). *Technological Forecasting and Social Change*, 2021, vol. 169, art. no. 120843. doi: https://doi.org/10.1016/j.techfore.2021.120843.

13. Deb N., Singh R., Bai H. Transformative Role of Silicon Carbide Power Electronics in Providing Low-cost Extremely Fast Charging of Electric Vehicles. *2021 IEEE Fourth International Conference on DC Microgrids (ICDCM)*, 2021, pp. 1-6. doi: https://doi.org/10.1109/ICDCM50975.2021.9504653.
14. Ambuhl D. *Energy Management Strategies for Hybrid Electric Vehicles*. Doctoral dissertation. ETH/ Measurement and Control Laboratory, 2009. 145 p. doi: https://doi.org/10.3929/ethz-a-005902053.
15. Sundstrom O. *Optimal Control and Design of Hybrid Electric Vehicles*. Doctoral dissertation. ETH Zurich Chalmers University of Technology, 2009. 169 p. doi: https://doi.org/10.3929/ethz-a-005902040.
16. Bowles P., Peng H., Zhang X. Energy management in a parallel hybrid electric vehicle with a continuously variable transmission. *Proceedings of the 2000 American Control Conference*, 2000, vol. 1, pp. 55-59 doi: https://doi.org/10.1109/ACC.2000.878771.
17. Stromberg E. *Optimal Control of Hybrid Electric Vehicles*. Vehicular Systems, Dept. of Electrical Engineering, Linkoping University, 2003. 56 p.
18. Chan-Chiao Lin, Huei Peng, Grizzle J.W., Jun-Mo Kang. Power management strategy for a parallel hybrid electric truck. *IEEE Transactions on Control Systems Technology*, 2003, vol. 11, no. 6, pp. 839-849. doi: https://doi.org/10.1109/TCST.2003.815606.
19. Barsali S., Miulli C., Possenti A. A Control Strategy to Minimize Fuel Consumption of Series Hybrid Electric Vehicles. *IEEE Transactions on Energy Conversion*, 2004, vol. 19, no. 1, pp. 187-195. doi: https://doi.org/10.1109/TEC.2003.821862.
20. Beck R., Richert F., Bollig A., Abel D., Saenger S., Neil K., Scholt T., Noreikat K.-E. Model Predictive Control of a Parallel Hybrid Vehicle Drivetrain. *Proceedings of the 44th IEEE Conference on Decision and Control*, 2005, pp. 2670-2675. doi: https://doi.org/10.1109/CDC.2005.1582566.
21. Yang Y., Pei H., Hu X., Liu Y., Hou C., Cao D. Fuel economy optimization of power split hybrid vehicles: A rapid dynamic programming approach. *Energy*, 2019, vol. 166, pp. 929-938. doi: https://doi.org/10.1016/j.energy.2018.10.149.
22. He D., Zou Y., Wu J., Zhang X., Zhang Z., Wang R. Deep Q-Learning Based Energy Management Strategy for a Series Hybrid Electric Tracked Vehicle and Its Adaptability Validation. *2019 IEEE Transportation Electrification Conference and Expo (ITEC)*, 2019, pp. 1-6. doi: https://doi.org/10.1109/ITEC.2019.8790630.
23. Yang R., Yang X., Huang W., Zhang S. Energy Management of the Power-Split Hybrid Electric City Bus Based on the Stochastic Model Predictive Control. *IEEE Access*, 2021, vol. 9, pp. 2055-2071. doi: https://doi.org/10.1109/ACCESS.2020.3047113.
24. Serrao L., Onori S., Rizzoni G. A Comparative Analysis of Energy Management Strategies for Hybrid Electric Vehicles. *Journal of Dynamic Systems, Measurement, and Control*, 2011, vol. 133, no. 3, art. no. 031012. doi: https://doi.org/10.1115/1.4003267.
25. Sharma O.P., Onori S., Guezennec Y. Analysis of Pontryagin's Minimum Principle-Based Energy Management Strategy for PHEV Applications. *ASME 2012 5th Annual Dynamic Systems and Control Conference Joint with the JSME 2012 11th Motion and Vibration Conference, DSCC 2012-MOVIC 2012*, vol. 1, pp. 145-150. doi: https://doi.org/10.1115/DSCC2012-MOVIC2012-8699.
26. Yan F., Wang J., Huang K. Hybrid Electric Vehicle Model Predictive Control Torque-Split Strategy Incorporating Engine Transient Characteristics. *IEEE Transactions on Vehicular Technology*, 2012, vol. 61, no. 6, pp. 2458-2467. doi: https://doi.org/10.1109/TVT.2012.2197767.
27. Panday A., Bansal H.O. Energy Management Strategy Implementation for Hybrid Electric Vehicles Using Genetic Algorithm Tuned Pontryagin's Minimum Principle Controller. *International Journal of Vehicular Technology*, 2016, pp. 1-13. doi: https://doi.org/10.1155/2016/4234261.
28. Nedungadi A., Smith R., Masrur A. Quantitative analysis of a hybrid electric HMMWV for fuel economy improvement. *26th Electric Vehicle Symposium 2012, EVS 2012*, vol. 3, pp. 1999-2007.
29. Chen Z., Zhang X., Mi C.C. Slide Mode and Fuzzy Logic Based Powertrain Controller for the Energy Management and Battery Lifetime Extension of Series Hybrid Electric Vehicles. *Journal of Asian Electric Vehicles*, 2010, vol. 8, no. 2, pp. 1425-1432. doi: https://doi.org/10.4130/jaev.8.1425.
30. Zhang X., Mi C.C., Yin C. Active-charging based powertrain control in series hybrid electric vehicles for efficiency improvement and battery lifetime extension. *Journal of Power Sources*, 2014, vol. 245, pp. 292-300. doi: https://doi.org/10.1016/j.jpowsour.2013.06.117.
31. Saeks R., Cox C.J., Neidhoefer J., Mays P.R., Murray J.J. Adaptive control of a hybrid electric vehicle. *IEEE Transactions on Intelligent Transportation Systems*, 2002, vol. 3, no. 4, pp. 213-234. doi: https://doi.org/10.1109/TITS.2002.804750.
32. Fiengo G., Di Fiore C., Lepore D., Vasca F. Auxiliary power unit control for hybrid electric vehicles. *2003 European Control Conference (ECC)*, 2003, pp. 2304-2309. doi: https://doi.org/10.23919/ECC.2003.7085310.
33. Sulaiman N., Hannan M.A., Mohamed A., Ker P.J., Majlan E.H., Wan Daud W.R. Optimization of energy management system for fuel-cell hybrid electric vehicles: Issues and recommendations. *Applied Energy*, 2018, vol. 228, pp. 2061-2079. doi: https://doi.org/10.1016/j.apenergy.2018.07.087.
34. Zhang X., Guo L., Guo N., Zou Y., Du G. Bi-level Energy Management of Plug-in Hybrid Electric Vehicles for Fuel Economy and Battery Lifetime with Intelligent State-of-charge Reference. *Journal of Power Sources*, 2021, vol. 481, art. no. 228798. doi: https://doi.org/10.1016/j.jpowsour.2020.228798.
35. Xiao B., Ruan J., Yang W., Walker P.D., Zhang N. A review of pivotal energy management strategies for extended range electric vehicles. *Renewable and Sustainable Energy Reviews*, 2021, vol. 149, art. no. 111194. doi: https://doi.org/10.1016/j.rser.2021.111194.
36. Ali Moussa M., Derrouazin A., Latroch M., Aillerie M. A hybrid renewable energy production system using a smart controller based on fuzzy logic. *Electrical Engineering & Electromechanics*, 2022, no. 3, pp. 46-50. doi: https://doi.org/10.20998/2074-272X.2022.3.07.
37. Guezi A., Bendaikha A., Dendouga A. Direct torque control based on second order sliding mode controller for three-level inverter-fed permanent magnet synchronous motor: comparative study. *Electrical Engineering & Electromechanics*, 2022, no. 5, pp. 10-13. doi: https://doi.org/10.20998/2074-272X.2022.5.02.

Received 30.08.2022
Accepted 22.10.2022
Published 06.01.2023

Anas Ibrar[1], *Lecturer*,
Sohaira Ahmad[1], *PhD*, *Assistant Professor*,
Ayla Safdar[1], *Lecturer*,
Nazo Haroon[2], *Lecturer*,
[1] Department of Electrical Engineering,
Wah Engineering College, University of Wah, Pakistan,
e-mail: anas.ibrar@wecuw.edu.pk (Corresponding Author);
sohaira.ahmad@wecuw.edu.pk; ayla.safdar@wecuw.edu.pk
[2] Department of Mechatronics Engineering,
Wah Engineering College, University of Wah, Pakistan,
e-mail: nazo.haroon@wecuw.edu.pk

How to cite this article:
Ibrar A., Ahmad S., Safdar A., Haroon N. Efficiency enhancement strategy implementation in hybrid electric vehicles using sliding mode control. *Electrical Engineering & Electromechanics*, 2023, no. 1, pp. 10-19. doi: https://doi.org/10.20998/2074-272X.2023.1.02

UDC 621.314 https://doi.org/10.20998/2074-272X.2023.1.03

M. Guergah, K. Nebti, S.E. Rezgui, H. Benalla, D. Ould-Abdeslam

Power quality enhancement using active power filter five-level cascade H-bridge under unbalanced and distorted grid

Introduction. *To improve the power quality of a supply system, the total harmonic distortion (THD) is the most important parameter in the quantification of harmonics caused by nonlinear loads. In practice, it must be less than 5 %. The novelty of the proposed work consists in the use of a cascaded five level active filter, when the converter consisting of six H-bridge pairs, each one includes four transistors.* ***Purpose***. *To increase the efficiency of this filter, two techniques for quantification of harmonic currents are proposed, first the PQ-theory which is simple but can only be used in case of a balanced grid, and second the synchronous reference frame theory (SFR-theory), which is capable of creating harmonic current not only in an unbalanced grid, but also in an unbalanced and distorted beam.* ***Methods***. *Using the control techniques, the harmonic current is extracted from load current and considered as a reference. The constructed current should follow this reference.* ***Results***. *The estimation of the active and reactive powers is based on the measurement of the currents crossing the load and the network voltages, these powers are used to determine the shape of the harmonic (reference) current. Using the PI regulator, the output current of the five-level inverter follows the reference current perfectly. The inverters output current is injected into the grid to eliminate harmonic currents.* ***Practical value***. *In practice, the harmonic distortion rate THD is the most widely used criterion for criticizing the waveform of the currents and judging the quality of the energy involved. For currents on the source side, the THD is considered acceptable if it is less than 5 %, in our proposal the THD is 0.85 % with the PQ-theory and 2.34 % with SFR-theory, so it is optimal.* References 11, figures 23.

Key words: **multilevel active power filter, total harmonic distortion, instantaneous active and reactive power, harmonic currents, synchronous reference frame theory.**

Вступ. *Для поліпшення якості електроенергії у системі електропостачання загальне гармонічне спотворення (ЗГС) є найважливішим параметром кількісної оцінки гармонік, викликаних нелінійними навантаженнями. На практиці вона має бути меншою за 5 %. Новизна запропонованої роботи полягає у використанні каскадного п'ятирівневого активного фільтра, коли перетворювач складається з шести пар Н-мостів, кожна з яких включає чотири транзистора.* ***Мета***. *Щоб підвищити ефективність цього фільтра, пропонуються два методи кількісного визначення гармонійних струмів: по-перше, PQ-теорія, яка проста, але може використовуватися лише у разі збалансованої сітки, і, по-друге, теорія синхронної системи відліку (теорія SFR). , який здатний створювати гармонійний струм не тільки в несиметричній сітці, а й у несиметричному та спотвореному пучку.* ***Методи***. *Використовуючи методи управління, гармонійний струм витягується зі струму навантаження і розглядається як опорний. Побудований струм повинен слідувати за цим посиланням.* ***Результати***. *Оцінка активної та реактивної потужностей заснована на вимірюванні струмів, що проходять через навантаження, та мережевих напруг, за цими потужностями визначається форма гармонійного (опорного) струму. При використанні ПІ-регулятора вихідний струм п'ятирівневого інвертора точно відповідає опорному струму. Вихідний струм інвертора подається до мережі для усунення гармонійних струмів.* ***Практична цінність***. *Насправді коефіцієнт гармонійних спотворень ЗГС є найбільш широко використовуваним критерієм для критики форми хвилі струмів та оцінки якості задіяної енергії. Для струмів на стороні джерела ЗГС вважається прийнятним, якщо він менше 5 %, за нашою пропозицією ЗГС становить 0,85 % з PQ-теорією і 2,34 % з SFR-теорією, тому він є оптимальним.* Бібл. 11, рис. 23.

Ключові слова: **багаторівневий фільтр активної потужності, повні гармонічні спотворення, миттєва активна та реактивна потужності, гармонічні струми, синхронна теорія системи відліку.**

Introduction. The use of power electronics equipment like large and small household appliances, computer and telecommunications equipment, lighting equipment, medical devices, monitoring and control instruments, presents a real problem because they degrade the quality of electrical energy, besides the environmental pollution due to the difficulty of recycling their electronic waste.

This equipment affects the delivered power quality by modifying the reactive power with the generated harmonic currents, which disturb the rest of the receivers connected to the same electrical network. This can take many forms, starting with significant line losses, saturation in distribution transformers, and may even interfere with communication systems.

Many techniques are available to reduce harmonics with many disadvantages such as electromagnetic interference, risk of resonance, fixed compensation and bulkiness [1, 2].

The active power filter improves the shape of the current, adjusts the reactive power as a result of the suppression of the different harmonic levels caused by the nonlinear loads and prevents their propagation toward the network [3, 4].

In the structure of active filters, multilevel converters present significant advantages over traditional two-level converters, namely [5, 6]:

- smaller output voltage step;
- lower harmonic components;
- better electromagnetic compatibility;
- lower switching losses.

In this context, the present work consists in improving the power quality, by reducing the total harmonic distortion, using a three phase cascaded active filter. Each phase contains two H-bridges of 4 power transistors. Hereafter the functioning of this system is outlined.

Design of shunt active power line conditioner (APLC) system. The APLC is controlled in order to draw (supply) a current i_F from (to) the utility, in order to cancel the current harmonics on the network side. In this way, the APLC given by (Fig. 1) is used to eliminate the current harmonics and compensate the reactive power [7].

The nonlinear load current i_L is represented as:

$$i_L(t) = \sum_{n=1}^{\infty} I_n \sin(n\omega t + \phi_n); \quad (1)$$

$$i_L(t) = I_1 \sin(\omega t + \phi_1) + \sum_{n=2}^{\infty} I_n \sin(n\omega t + \phi_n). \quad (2)$$

For harmonic compensation, the active filter must provide the compensation current:

$$i_F(t) = i_L(t) - i_S(t). \quad (3)$$

At that time, the source current i_S will be in phase with the utility voltage and become sinusoidal.

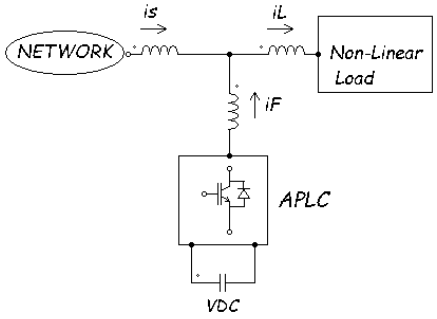

Fig. 1. Block diagram of basic APLC

Active filter structure. The cascaded five-level inverter. In this work, the APLC is a three-phase cascaded multilevel active power inverter. This filter is composed by three pairs of H-bridges; each one consists of 4 power transistors [7]. The design of the filter is shown in Fig. 2.

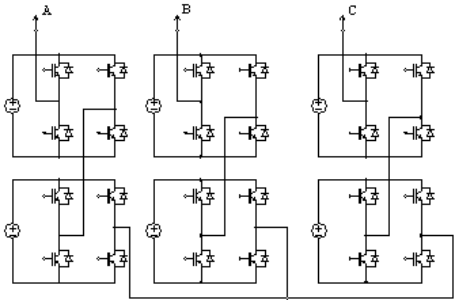

Fig. 2. Cascaded multilevel inverter design

Harmonic powers identification. The identification method chosen in first is called *the method of the real and imaginary instantaneous powers* [8, 9]. It offers the advantage of choosing the disturbance to be compensated with precision, speed and simplicity. The essential feature of this procedure is the reduction of the size of the system to be solved. Indeed, instead of having a system of 6 equations, one will have only to solve a system of four equations. Current and voltage are calculated according to Concordia transformation and given as [10]:

$$\begin{bmatrix} i_\alpha \\ i_\beta \end{bmatrix} = \sqrt{\frac{2}{3}} \begin{bmatrix} 1 & -\frac{1}{2} & -\frac{1}{2} \\ 0 & \frac{\sqrt{3}}{2} & \frac{\sqrt{3}}{2} \end{bmatrix} \begin{bmatrix} i_a \\ i_b \\ i_c \end{bmatrix}; \quad (4)$$

$$\begin{bmatrix} v_\alpha \\ v_\beta \end{bmatrix} = \sqrt{\frac{2}{3}} \begin{bmatrix} 1 & -\frac{1}{2} & -\frac{1}{2} \\ 0 & \frac{\sqrt{3}}{2} & \frac{\sqrt{3}}{2} \end{bmatrix} \begin{bmatrix} v_a \\ v_b \\ v_c \end{bmatrix}. \quad (5)$$

The expressions of the instantaneous real and imaginary load powers are given as follow:

$$\begin{bmatrix} p \\ q \end{bmatrix} = \begin{bmatrix} i_\alpha & i_\beta \\ -i_\alpha & i_\beta \end{bmatrix} \cdot \begin{bmatrix} v_\alpha \\ v_\beta \end{bmatrix}, \quad (6)$$

where p and q contain respectively the harmonic (oscillatory) and continuous terms which can be written as:

$$p = p_c + p_h; \quad q = q_c + q_h. \quad (7)$$

This method is described in detail in the diagram on Fig. 3, 4.

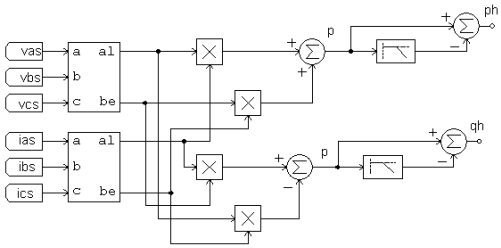

Fig. 3. Building block of calculation of harmonics powers reference

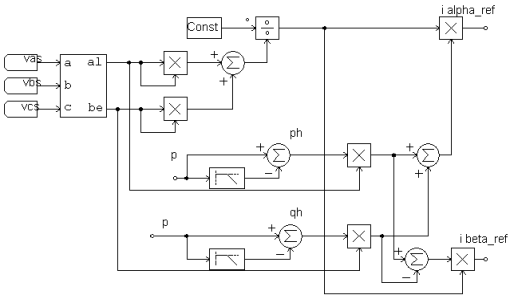

Fig. 4. Building block of the three reference currents calculation

Hereafter, the continuous power component is eliminated in order to preserve only the alternative one, which is related to the required harmonic content. This is feasible by a simple use of a second order low pass filter [4]. This is illustrated by the diagram in Fig. 5.

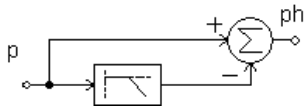

Fig. 5. Harmonic power separation

$$\begin{bmatrix} i_{\alpha ref} \\ i_{\beta ref} \end{bmatrix} = \frac{1}{\left| v_\alpha^2 + v_\beta^2 \right|} \begin{bmatrix} v_\alpha & v_\beta \\ v_\alpha & -v_\beta \end{bmatrix} \cdot \begin{bmatrix} p_h \\ q_h \end{bmatrix}. \quad (8)$$

By a simple use of the reverse Concordia transformation [8] defined by (9), one arrives at the reference current i_{ref}, presented in Fig. 6.

$$\begin{bmatrix} i_{aref} \\ i_{bref} \\ i_{cref} \end{bmatrix} = \sqrt{2/3} \cdot \begin{bmatrix} 1 & 0 \\ -1/2 & \sqrt{3}/2 \\ -1/2 & -\sqrt{3}/2 \end{bmatrix} \cdot \begin{bmatrix} i_{\alpha ref} \\ i_{\beta ref} \end{bmatrix}. \quad (9)$$

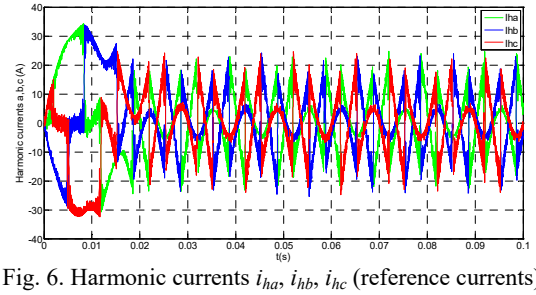

Fig. 6. Harmonic currents i_{ha}, i_{hb}, i_{hc} (reference currents)

Simulation results using theoretical active and reactive powers. The regulation current is realized by using a PI classic regulator as presented in Fig. 7.

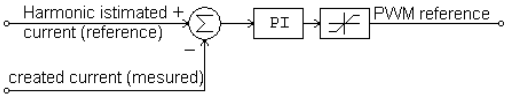

Fig 7.The current regulation scheme

The reference current follows very well the measured harmonic current (Fig. 8).

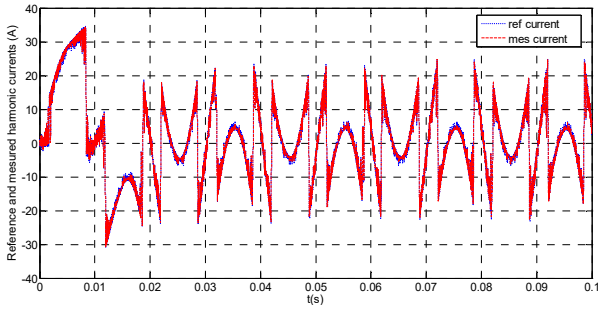

Fig. 8. Reference and measured harmonic currents

Pulse-width modulation (PWM) pulses generation. PWM technique solves the control problem of the commutation frequency while functioning with a fixed frequency, easy to filter downstream from the inverters. The general diagram of the PWM technique is given in Fig. 9.

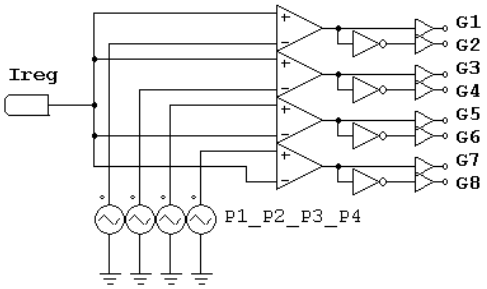

Fig. 9. PWM structure

These triangular signals obtained by the PWM are presented on Fig. 10.

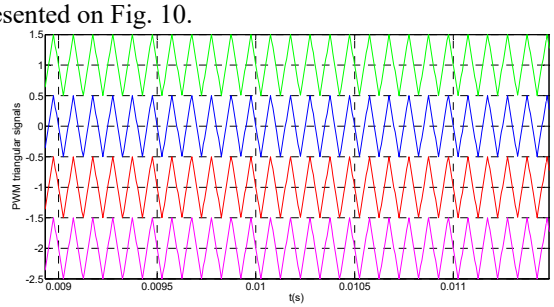

Fig. 10. Super imposed PWM triangular signals (zoom)

Simulation result without filter. In the simulation the model presented in Fig. 11, contain two parts.

Network. It consists of 3 AC voltages having an effective value of 400 V line to line, and a line impedance with L_s = 3mH, R_s = 0.5 Ω, the source frequency is 50 Hz.

Polluting load. It is a 6 diodes bridge, feeding a series *RL* load, where L = 0.1 H and R = 20 Ω.

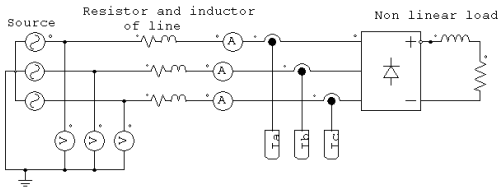

Fig. 11. Simulation model of network and polluting load without filters

The currents polluted by the non-linear load and their spectrum represented respectively in Fig. 12, 13.

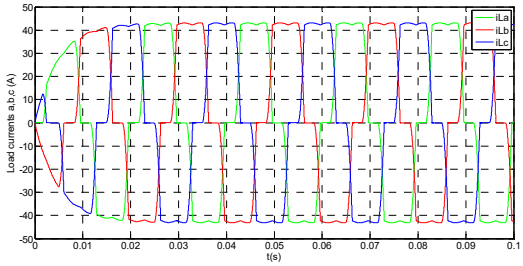

Fig. 12. Polluted load currents without filtering

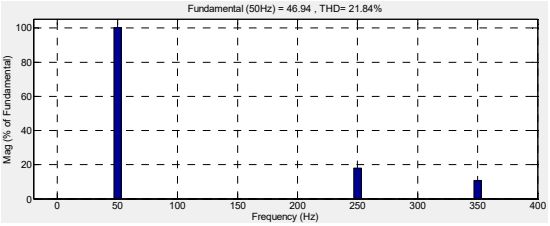

Fig. 13. Spectrum of polluted current i_{sa} without filtering

The cascaded five-level active filter includes 3 pairs of H-bridge, everyone characterized by a compensation DC source of 450 V. This filter is interfaced with the network by an inductive passive filter having L_f = 3 mH, in order to protect the network. Before using this filter the load currents are heavily polluted they have almost the form of a square signal, these are indicated in Fig. 14.

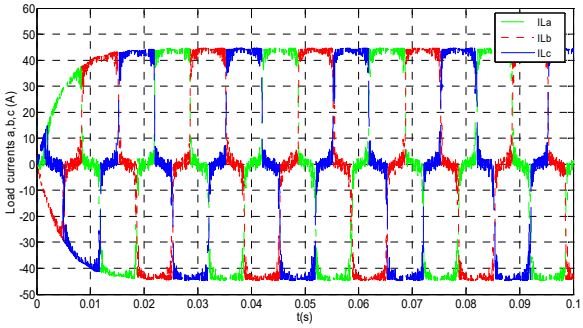

Fig. 14. Load currents

Figure 15 present the filtered source current by a five-level active parallel filter, followed by its harmonic spectrum and the corresponding total harmonic distortion (THD) in Fig. 16.

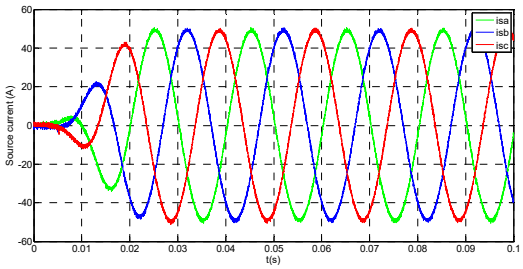

Fig. 15. Filtered source currents

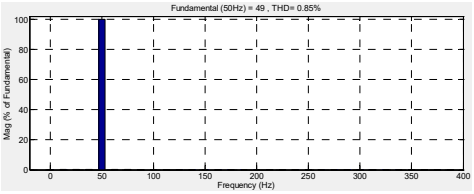

Fig. 16. Spectrum of filtered current i_{sa}

We clearly observe a significant reduction of the secondary spectral peaks, indicating the efficiency of our approach. Indeed, according to the harmonic spectrum and its calculated THD, there is an improvement of the filtering quality. The total harmonic distortion of the current fell from 21.84 % to 0.85 %.

The results obtained demonstrate the efficiency of the theoretical PQ technique for a balanced network, but when the network is unbalanced, the technique cannot sustain these performances. The proof is the unbalanced shape of the currents even after filtering as shown in Fig. 17.

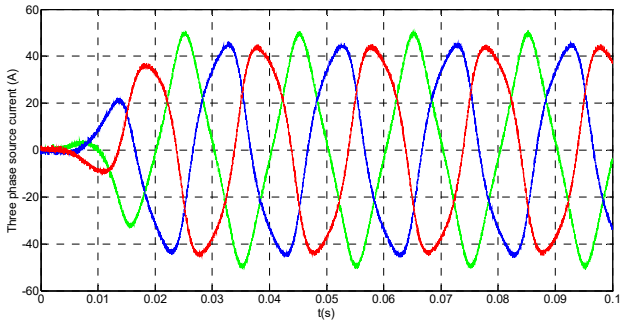

Fig. 17. Three phase current for unbalanced grid using PQ powers theory

An imbalance consists of a 25 % decrease in the voltage of one phase compared to the others.

Synchronous reference frame (SRF) theory. The block diagram of the SRF strategy is given in Fig. 18.

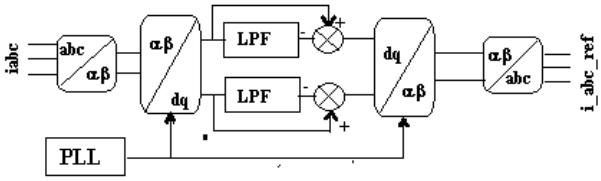

Fig. 18. Block diagram of SRF structure

We use (4) to transform the measured 3 phase current into 2 phase α-β stationary frame, and then the transformation from 2 phase α-β stationary frame to 2 phase d-q rotating frame is given by:

$$\begin{bmatrix} i_d \\ i_q \end{bmatrix} = \begin{bmatrix} \sin\theta & -\cos\theta \\ \cos\theta & \sin\theta \end{bmatrix} \cdot \begin{bmatrix} i_\alpha \\ i_\beta \end{bmatrix}, \tag{10}$$

where i_d and i_q are given by:

$$\begin{bmatrix} i_d \\ i_q \end{bmatrix} = \begin{bmatrix} \overline{i_d} & \tilde{i}_d \\ \overline{i_q} & \tilde{i}_q \end{bmatrix}. \tag{11}$$

The out of low-pass filter gives continuous current component. The inverse transformation the transformation from 2 phase d-q rotating frame to 2 phases α-β-0 stationary frame is given by:

$$\begin{bmatrix} i_{\alpha ref} \\ i_{\beta ref} \end{bmatrix} = \begin{bmatrix} \sin\theta & -\cos\theta \\ \cos\theta & \sin\theta \end{bmatrix}^{-1} \cdot \begin{bmatrix} i_d \\ i_q \end{bmatrix}. \tag{12}$$

The 3-phase compensation currents can be calculated using the same Eq. (9). Finally, the synchronization angle of reference frame is determined using dual second order generalized integrator phase locked loop with prefilter DSOGI-PLL-WPF technique described in [11] (Fig. 19).

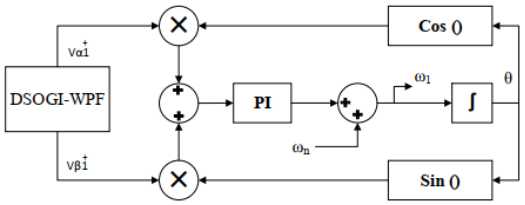

Fig. 19. Synchronization angle determination [11]

Simulation results using SRF theory. In this simulation the grid is unbalanced and also affected by a third rang harmonic applied in the first voltage curve (Fig. 20).

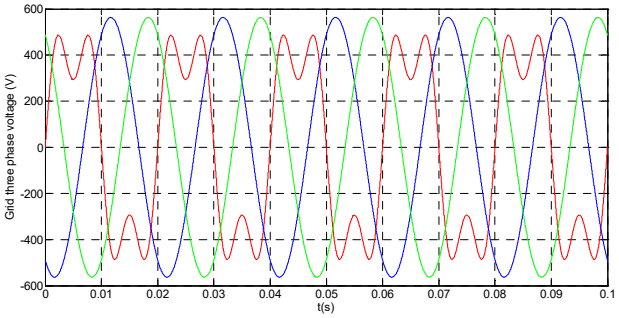

Fig. 20 Three phase voltage for unbalanced and distorted grid

The reference current follows very well the measured harmonic current (Fig. 21).

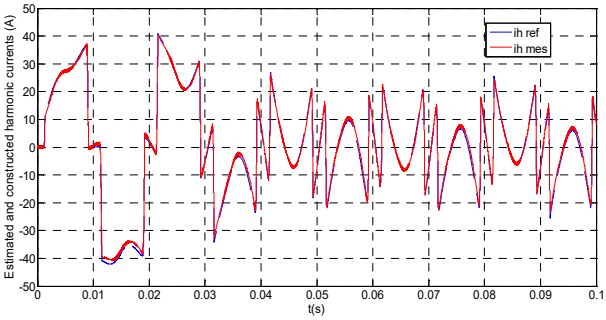

Fig. 21. Reference and measured harmonic currents for SRF

The 3 currents filtered using the SRF and their spectrum are respectively represented in Fig. 22, 23.

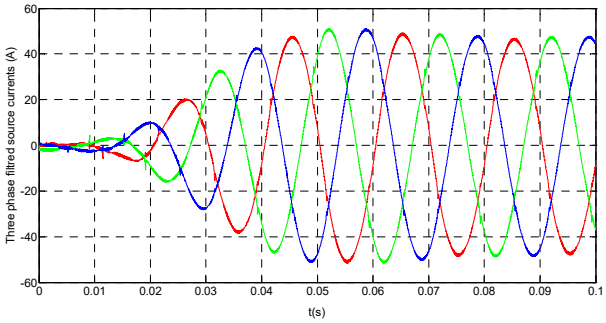

Fig. 22. Three phase filtered source current for unbalanced and distorted grid using SRF

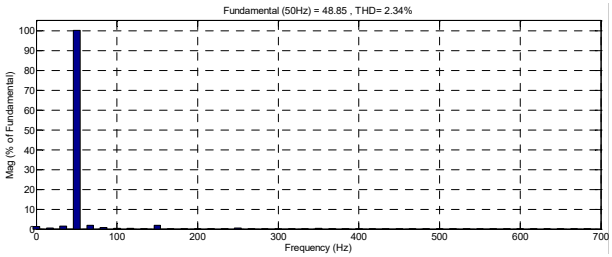

Fig. 23. Spectrum of filtered current i_{sa} of SRF for unbalanced and distorted grid

The unbalanced and distorted grid is considered a critical situation and with a nonlinear load makes the grid very polluted and disturbed. Although the THD is larger comparing with that of the theoretical PQ technique, but under these network conditions it is very acceptable especially that it is still within the allowable range.

Conclusions. In this paper, the elements constituting the structure of a cascaded five-level active filter are presented. At first we presented the structure of the five-level inverter which is the basic element of our study, as well as the PWM technique with superimposed carriers, which offers a precise and fast control of the output quantities of the converter.

To identify harmonic currents, the active and reactive power method is firstly used for balanced grid condition. For unbalanced network PQ theoretical technique is not effective, so we replace it with synchronous reference frame strategy which needs an exact synchronization angle determination. This technique is asily achievable and requires only simple current and voltage sensors.

Compared with the load current THD which is 21.84 %, using the five-level structure, the source current remains slightly infected with noise due to the nonlinear load, the source current THD drops to a value of 2.34 %.

Conflict of interest. The authors declare that they have no conflicts of interest.

REFERENCES

1. Sanjan P.S., Gowtham N., Bhaskar M.S., Subramaniam U., Almakhles D.J., Padmanaban S., Yamini N.G. Enhancement of Power Quality in Domestic Loads Using Harmonic Filters. *IEEE Access*, 2020, vol. 8, pp. 197730-197744. doi: https://doi.org/10.1109/ACCESS.2020.3034734.

2. Das S.R., Ray P.K., Sahoo A.K., Ramasubbareddy S., Babu T.S., Kumar N.M., Elavarasan R.M., Mihet-Popa L. A Comprehensive Survey on Different Control Strategies and Applications of Active Power Filters for Power Quality Improvement. *Energies*, 2021, vol. 14, no. 15, art. no. 4589. doi: https://doi.org/10.3390/en14154589.

3. Fujita H., Akagi H. A practical approach to harmonic compensation in power systems-series connection of passive and active filters. *IEEE Transactions on Industry Applications*, 1991, vol. 27, no. 6, pp. 1020-1025. doi: https://doi.org/10.1109/28.108451.

4. Karuppanan P., Mahapatra K. A novel SRF based cascaded multilevel active filter for power line conditioners. *2010 Annual IEEE India Conference (INDICON)*, 2010, pp. 1-4. doi: https://doi.org/10.1109/INDCON.2010.5712667.

5. Colak I., Kabalci E., Bayindir R. Review of multilevel voltage source inverter topologies and control schemes. *Energy Conversion and Management*, 2011, vol. 52, no. 2, pp. 1114-1128. doi: https://doi.org/10.1016/j.enconman.2010.09.006.

6. Barkati S., Baghli L., Berkouk E.M., Boucherit M.-S. Harmonic elimination in diode-clamped multilevel inverter using evolutionary algorithms. *Electric Power Systems Research*, 2008, vol. 78, no. 10, pp. 1736-1746. doi: https://doi.org/10.1016/j.epsr.2008.03.010.

7. Yin X., Yi H., Yang Z., Zhuo F. Global Configuration Strategy of SAPFs Combined with Comprehensive Evaluation of Power Quality in Distribution Network. *2022 International Conference on Power Energy Systems and Applications (ICoPESA)*, 2022, pp. 430-436. doi: https://doi.org/10.1109/ICoPESA54515.2022.9754415.

8. Seung-Gi Jeong, Myung-Ho Woo. DSP-based active power filter with predictive current control. *IEEE Transactions on Industrial Electronics*, 1997, vol. 44, no. 3, pp. 329-336. doi: https://doi.org/10.1109/41.585830.

9. Buso S., Malesani L., Mattavelli P. Comparison of current control techniques for active filter applications. *IEEE Transactions on Industrial Electronics*, 1998, vol. 45, no. 5, pp. 722-729. doi: https://doi.org/10.1109/41.720328.

10. Afonso J., Couto C., Martins J. Active Filters with Control Based on the p-q Theory. *IEEE Industrial Electronics Society Newsletter*, 2000, vol. 47, no. 3, pp. 5-10. Available at: https://hdl.handle.net/1822/1921 (Accessed 26 April 2022).

11. Kalkoul S., Benalla H., Nabti K., Abdellatif R. An adaptive harmonic compensation strategy for three-phase shunt active power filter based on double second-order generalized integrator with prefilter. *Electrical Engineering & Electromechanics*, 2020, no. 3, pp. 58-64. doi: https://doi.org/10.20998/2074-272X.2020.3.09.

Received 24.05.2022
Accepted 03.08.2022
Published 06.01.2023

Manel Guergah[1], *PhD Student*,
Khalil Nebti[1], *Doctor in Electrical Engineering,*
Salah Eddine Rezgui[1], *Doctor in Electrical Engineering*,
Hocine Benalla[1], *Professor*,
Djaffar Ouid Ould-Abdeslam[2], *Professor*,
[1] Faculty of Technology Sciences,
Brothers Mentouri University Constantine 1, Algeria,
e-mail: guergah_manel26@yahoo.fr (Corresponding Author);
idoor2003@yahoo.fr; rezgui.salaheddine@umc.edu.dz;
benalla.hocine@umc.edu.dz
[2] Laboratory IRIMAS,
Universite de Haute Alsace, Mulhouse, France,
e-mail: djaffar.ould-abdeslam@uha.fr

How to cite this article:
Guergah M., Nebti K., Rezgui S.E., Benalla H., Ould-Abdeslam D. Power quality enhancement using active power filter five-level cascade H-bridge under unbalanced and distorted grid. *Electrical Engineering & Electromechanics*, 2023, no. 1, pp. 20-24. doi: https://doi.org/10.20998/2074-272X.2023.1.03

UDC 621.314 https://doi.org/10.20998/2074-272X.2023.1.04

A. Mimouni, S. Laribi, M. Sebaa, T. Allaoui, A.A. Bengharbi

Fault diagnosis of power converters in a grid connected photovoltaic system using artificial neural networks

Introduction. *The widespread use of photovoltaic systems in various applications has spotlighted the pressing requirement for reliability, efficiency and continuity of service. The main impediment to a more effective implementation has been the reliability of the power converters. Indeed, the presence of faults in power converters that can cause malfunctions in the photovoltaic system, which can reduce its performance.* ***Novelty.*** *This paper presents a technique for diagnosing open circuit failures in the switches (IGBTs) of power converters (DC-DC converters and three-phase inverters) in a grid-connected photovoltaic system.* ***Purpose.*** *To ensure supply continuity, a fault-diagnosis process is required throughout all phases of energy production, transfer, and conversion.* ***Methods.*** *The diagnostic approach is based on artificial neural networks and the extraction of features corresponding to the open circuit fault of the IGBT switch. This approach is based on the Clarke transformation of the three-phase currents of the inverter output as well as the calculation of the average value of these currents to determine the exact angle of the open circuit fault.* ***Results.*** *This method is able to effectively identify and localize single or multiple open circuit faults of the DC-DC converter IGBT switch or the three-phase inverter IGBT switches.* References 26, tables 4, figures 8.

Key words: **grid connected photovoltaic system, artificial neural network, power converters, open circuit failure of IGBT, fault detection.**

Вступ. *Широке використання фотоелектричних систем у різних застосуваннях висунуло на перший план нагальні вимоги до надійності, ефективності та безперервності обслуговування. Основною перешкодою для ефективнішого застосування була надійність силових перетворювачів. Справді, наявність несправностей у силових перетворювачах може спричинити збої в роботі фотоелектричної системи, що може знизити її продуктивність.* ***Новизна***. *У цій статті представлена методика діагностики обриву кола в перемикачах (IGBT) силових перетворювачів (перетворювачів постійного струму та трифазних інверторів) у фотоелектричній системі, підключеній до мережі.* ***Мета***. *Для забезпечення безперервності постачання потрібен процес діагностики несправностей на всіх етапах виробництва, передачі та перетворення енергії.* ***Методи***. *Діагностичний підхід заснований на штучних нейронних мережах та вилучення ознак, що відповідають обриву кола IGBT-перемикача. Цей підхід ґрунтується на перетворенні Кларка трифазних струмів на виході інвертора, а т акож розрахунку середнього значення цих струмів для визначення точного кута обриву кола.* ***Результати***. *Цей метод дозволяє ефективно ідентифікувати та локалізувати одиночні або множинні несправності розімкнутого кола IGBT-перемикача DC-DC перетворювача або IGBT-перемикача трифазного інвертора.* Бібл. 26, табл. 4, рис. 8.

Ключові слова: **фотогальванічна система, підключена до мережі, штучна нейронна мережа, силові перетворювачі, відмова IGBT при обриві кола, виявлення несправностей.**

Introduction. Conventional energy resources remain strategic for energy production, but meeting the world's growing energy needs will be a major challenge in the near future. This is in line with an imminent global energy shortage situation, as well as the depletion of reserves of such energy resources in a way that is dangerous for future generations. At the same time, the use of these energy sources poses a significant environmental risk to the future of our planet due to the release of greenhouse gases. As a result, producing electrical energy from clean, non-polluting, and renewable sources has become a global necessity and a topic of interest in our societies [1, 2].

During the past decade, photovoltaic (PV) energy has become a reliable source of energy, which is based on the conversion of solar radiation into electrical power. In the last decade, solar energy has proliferated and now promises to play a leading role in the current energy transition. The cumulative capacity of the PV installations around the world has increased to reach more than 500 GW [3].

Photovoltaic systems technologies, including power converters, have reached the stage where they can be used in stand-alone, grid-connected or hybrid power systems. In recent years, the evolution of PV systems studies has led to the design of efficient systems [4]. Despite of all this evolution, no system is immune to failures. For this reason, a significant deal of effort is now being put into the monitoring and diagnosis of PV systems. One of the parts most prone to faults in a PV system is the power converters, which includes the DC-DC and the three-phase inverter. These faults, which are mainly caused by the degradation of the switch components such as open circuit faults in IGBT's, can decrease performance and even lead to total unavailability of the PV system. As a result, these faults will reduce the productivity of the system [5].

Several researchers have investigated the behavior of power converters in case of an internal fault and have developed diagnostic and identification methods, focusing in particular on the open circuit failure of IGBT switch. In [6, 7], the authors discuss new approaches based entirely on the artificial neural network (ANN) and the Clarke transformation as a detection tool for locating an interrupt fault of the IGBT switch in a three-phase inverter. In [8, 9], new feature extraction approaches using three-phase load currents are proposed, in [9], the diagnostic method used is based on neural network (NN) that has learned from a database derived from the analysis of the three phase currents. Another study based on discrete wavelet transforms (DWT) and NN for fault detection was proposed in [10, 11]. The presented technique allows the identification of single and multiple faults in IGBTs, where the detection mechanism is based on the analysis of the currents. In [12] the Park's vector technique was presented. The principle of this method is based on the conversion of three phase system (I_a, I_b, I_c) into a two-phase system (I_d, I_q). In this case, the Park contour is a circle whose center is the origin. This contour is considered as a simple and interesting reference index, since these deviations indicate the anomalies that can affect the system. The fixed reference frame is used to

evaluate the evolution of currents at the occurrence of open circuits in the inverter. Another diagnostic method proposed in [13-16] is based on calculating the average values of the three phase currents, the absolute mean values are used as primary variables to formulate diagnostic indicators. In [17-20], the authors use fuzzy logic as an expert system for fault detection of open circuit faults in a three-phase inverter, this technique is based on processing and analyzing the load currents. In [21], the author proposes a fault detection technique for three-phase inverters based on monitoring the RMS value and the average values of the three-phase currents.

This paper proposes a technique for detecting and locating the open circuit fault of the IGBT's switches of the power converters in a grid connected photovoltaic system using the ANN assisted by the Clarke transformation. This approach requires the three phase currents (I_a, I_b, I_c) to calculate the Clarke currents as well as the fault angles related to the open circuit faults of the IGBT switch of the DC-DC converter or the three-phase inverter. These features are then fed as inputs into the ANN structure, the resulting output of the ANN is used to identify and locate faults that may exist in the DC-DC converter or the three-phase inverter.

Description of the grid connected photovoltaic system. Figure 1 shows the model of a photovoltaic system connected to the grid through DC/DC boost converter and a three-phase inverter. In this model we have fixed the weather conditions such as incident solar irradiance and temperature.

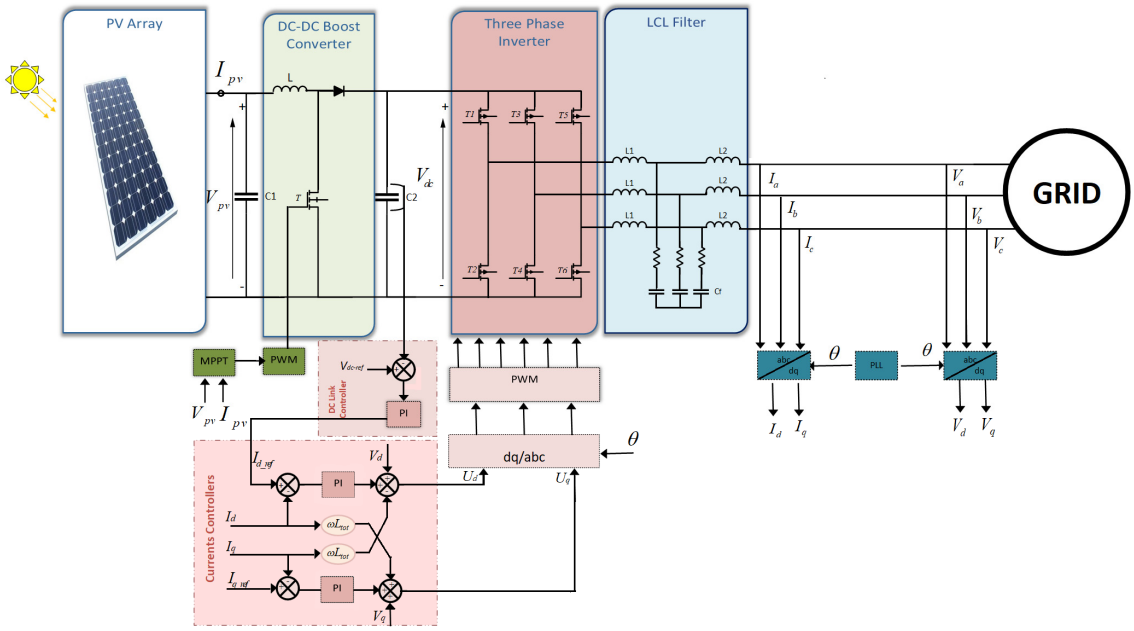

Fig. 1. Grid connected PV system diagram

Photovoltaic cell. The photovoltaic energy results from the direct transformation of rays from the sun into continuous electrical power by means of cells. Thus, to obtain sufficient power, the cells are connected in series and in parallels [2, 22]. The connection between the power source and the distribution grid is provided by a series of power converters. The power stage is an essential element in a photovoltaic system; it is usually formed by a DC-DC converter connected to an inverter via a DC bus.

Implementation of DC side control. A DC-DC boost converter is mainly composed of an inductor L, a switch T, a diode and input capacitance C_1 to smooth the output voltage of the PV panel. It is used to extract the maximum power available at the PV array at any time and transfer it. This converter acts as an interface between two elements. It ensures the transfer of the maximum power supplied by the generator via a control action [3, 23].

A maximum power point tracker (MPPT) control associated with a DC-DC converter, allows a PV array to be operated to produce the maximum of its power whatever the weather conditions (temperature and irradiation), the converter control places the system at the maximum operating point. A power converter controlled by an MPPT will optimize the photovoltaic conversion chain. In this paper a Perturb and Observe algorithm is employed (Fig. 2) because of its simplicity and easy implementation [3, 23].

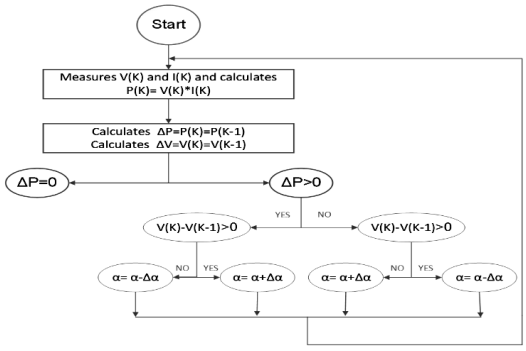

Fig. 2. Flowchart of Perturb and Observe algorithm

Implementation of AC side control. A two level three-phase inverter is used for converting the DC energy into AC energy, where the six switches (T1-T6) are employed in the main circuit of the inverter. The DC bus C_2 is the link between the two converters and its purpose is to act both as a power storage element and a filter [24].

To achieve stable operation of the system, the voltages and currents in the system must be monitored and controlled. This is accomplished by implementing the control part [24, 25].

Figure 1 presents a control strategy for a three-phase inverter connected to grid; this control technique includes two numbers of control loops. Voltage control is provided to maintain the DC link voltage constant; the boost converter is controlled by the duty cycle of the MPPT. Then the voltage measured from the boost V_{dc} is compared to the reference voltage V_{dc-ref}. For the voltage control a PI controller is employed [24, 25].

The three-phase currents of the inverter (I_a, I_b, I_c) and the grid voltages (V_a, V_b, V_c) are transformed into to dq reference frame (I_d, I_q) and (V_d, V_q). To obtain a unit power factor in a grid-connected PV system, the current reference I_{q-ref} is considered to be zero. The output from the voltage controller is the current reference I_{d-ref}. The voltage reference for the PWM is the PI current controller's outputs which are given by [24, 25] in (1):

$$\begin{cases} U_d = V_d - \omega \cdot L_{tot} \cdot i_q + \left(K_p + \dfrac{K_i}{s} \right) \cdot \left(i_{d-ref} - i_d \right); \\ U_q = V_q + \omega \cdot L_{tot} \cdot i_d + \left(K_p + \dfrac{K_i}{s} \right) \cdot \left(i_{q-ref} - i_q \right), \end{cases} \tag{1}$$

where U_d, U_q are the dq desired voltage references; ω is the angular frequency of the grid; K_p, K_i gains of the PI controller; L_{tot} refers to $L_1 + L_2$.

Grid synchronization. One of the most critical issues with grid-connected PV systems is the synchronization between the PV system and the grid. The phase angle θ of the grid voltage vector is the main output of the synchronization algorithm. In this paper it is extracted using phased locked loop. The phase angle used to control the three-phase inverter switches, calculate and control active and reactive power, and convert feedback variables (grid voltage and current) to a reference frame [22, 24].

The fault diagnosis approach. The reliability of power converters has always been a major concern in many power applications such as power generation. It is worth mentioning that these converters are particularly sensitive to faults in their power components IGBT's, which can be broadly can be classified as open circuit faults and short circuit faults. In our work, we focus on the open circuit fault; such a fault can lead to secondary failures in other converter components, which can lead to high repair costs [5].

Figure 3 shows the procedure for diagnosing open circuit failures that may affect the different power converters (DC-DC converter and three-phase inverter) is based on the following steps:

- application of the Clarke transformation on the three-phase currents of the three-phase inverter;
- extraction of information from the Clarke transformation;
- implementation of ANN as diagnosis method;
- identification of open circuit fault of IGBT switch.

For the feature extraction approach, the suggested defect diagnosis system takes into account the inverter output current signals. After applying the Clarke transformation to convert these three-phase currents to two-phase currents, a feature extraction technique is employed to extract the most efficient characteristics of the operating system. The system's characteristics are then determined for various operational scenarios (with and without faults). The values of the feature vectors in distinct fault instances are recorded in a fault table. This table is then used to train the ANN that will be utilized to detect and diagnose open circuit faults in the grid-connected photovoltaic system's power converters.

The extracted characteristics. The system of (2) shows the three phase currents of the inverter output:

$$\begin{cases} I_a = I_{\max} \cdot \sin(\omega \cdot t); \\ I_b = I_{\max} \cdot \sin(\omega \cdot t - 2 \cdot \pi/3); \\ I_c = I_{\max} \cdot \sin(\omega \cdot t + 2 \cdot \pi/3); \end{cases} \tag{2}$$

where $I_{\max}$ is the maximum amplitude of the current.

Applying the Clarke transformation on the system allows us to obtain the system of equation (3) [7]:

$$\begin{cases} i_\alpha = \dfrac{2}{3} \cdot i_a - \dfrac{1}{3} \cdot i_b - \dfrac{1}{3} \cdot i_c; \\ i_\beta = \dfrac{1}{\sqrt{3}} \cdot (i_b - i_c), \end{cases} \tag{3}$$

where i_α, i_β are the Clarke currents.

The average currents in the two axes (α and β) can be calculated using the following equations [7]:

$$\begin{cases} i_{\alpha mean} = \sum_{j=1}^{N} \dfrac{i_\alpha(j)}{length(i_\alpha)}; \\ i_{\beta mean} = \sum_{j=1}^{N} \dfrac{i_\beta(j)}{length(i_\beta)}, \end{cases} \tag{4}$$

where N defines the number of samples.

The calculation of the angle that corresponds to the open circuit fault in each switch is given by [7]:

$$\theta_f = \tan^{-1}\left(\frac{i_{\alpha mean}}{i_{\beta mean}} \right). \tag{5}$$

The range of the angle in each fault condition in the different T_i switches is shown in Table 1 [12, 26].

Table 1

The open circuit angle in each switch of the power converters

State	θ_f	State	θ_f
Healthy	[0, 2π]	T1 and T5	[π/2, 5π/6]
T1	[π/2, 3π/2]]	T1 and T6	[5π/6, 3π/2]
T2	[0, π/2] or [3π/2, 2π]	T2 and T3	[0, π/6] or [3π/2, 2π]
T3	[0, π/6] or [7π/6, 2π]	T2 and T4	[π/6, 2π]
T4	[π/6, 7π/6]	T2 and T5	[0, π/2] or [11π/6, 2π]
T5	[0, 5π/6] or [11π/6, 2π]	T2 and T6	[3π/2, 11π/6]
T6	[5π/6, 11π/6]	T3 and T5	[0, π/6] or [11π/6, 2π]
T	[0, 2π]	T3 and T6	[7π/6, 11π/6]
T1 and T3	[7π/6, 3π/2]	T4 and T5	[π/6, 5π/6]
T1 and T4	[π/2, 7π/6]	T4 and T6	[5π/6, 7π/6]

The architecture of the ANN used. The ANN system is built up of neurons with identical structures that are linked together in a manner comparable to the human nervous system's cells. It consists of a series of layers coupled in such a way that each neuron receives its input from the output of the one before it. The neurons of the input layer are connected only to the next layer while the neurons of the hidden layers have the particularity of being connected to all the neurons of the previous layer and of the next layer [10].

The input layer of our neural network has three neurons ($i_{\alpha mean}$, $i_{\beta mean}$ and θ_f), whose job is to send the input values to the hidden layer, which has 15 neurons, and the output layer, which has six neurons (Fig. 4). The system's intended output is binary (1 or 0).

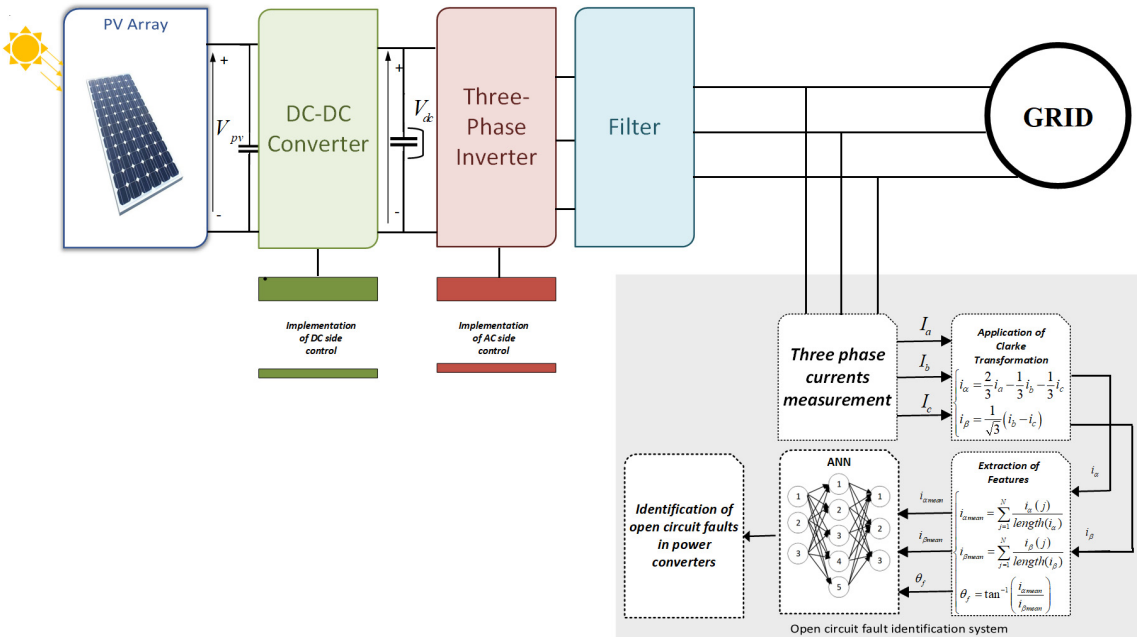

Fig. 3. Diagram of the proposed diagnostic system

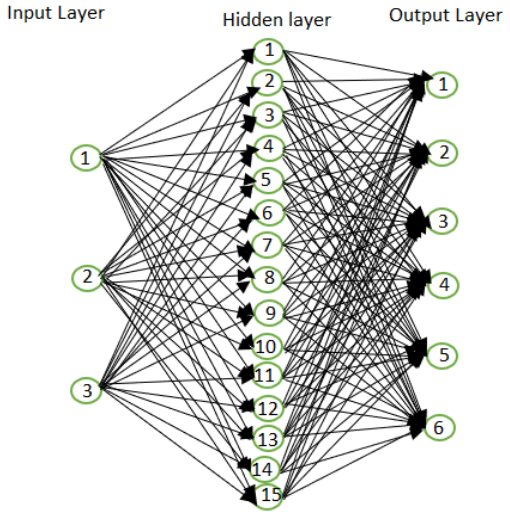

Fig. 4.The architecture of the ANN used

The desired output for the different possible fault cases at the IGBT switches of the two power converters is shown in Table 2.

Table 2

Classification of open circuit faults

State	Output	State	Output
Healthy	[0 0 0 0 0 0]	T1 and T5	[1 0 0 0 1 0]
T1	[1 0 0 0 0 0]	T1 and T6	[1 0 0 0 0 1]
T2	[0 1 0 0 0 0]	T2 and T3	[0 1 1 0 0 0]
T3	[0 0 1 0 0 0]	T2 and T4	[0 1 0 1 0 0]
T4	[0 0 0 1 0 0]	T2 and T5	[0 1 0 0 1 0]
T5	[0 0 0 0 1 0]	T2 and T6	[0 1 0 0 0 1]
T6	[0 0 0 0 0 1]	T3 and T5	[0 0 1 0 1 0]
T	[1 1 1 1 1 1]	T3 and T6	[0 0 1 0 0 1]
T1 and T3	[1 0 1 0 0 0]	T4 and T5	[0 0 0 1 1 0]
T1 and T4	[1 0 0 1 0 0]	T4 and T6	[0 0 0 1 0 1]

Validation of diagnosis method. In this part a validation of the efficiency of the developed method for the detection of the open circuit faults of power switches integrated in the power converters (DC-DC converter and three-phase inverter). A simulation of normal and faulty operation was carried out in MATLAB / Simulink environment. The normal case and all possible fault combinations are manually fed into the system, the ANN is used for the learning process, and the generated code is implemented in our simulation system.

The simulation of the system was carried out using the parameters presented in Table 3.

Table 3

The parameters of the studied system

Parameters	Values
Number of modules in series	15
Number of modules in parallel	16
The desired power, kW	51.156
Capacitor C_1, F	$6.7586 \cdot 10^{-5}$
Capacitor C_2, F	$5.5 \cdot 10^{-3}$
Inductor L, H	$3 \cdot 10^{-3}$
Boost frequency, kHz	5
DC-link voltage, V	700
Inverter frequency, kHz	10
Parameters of LCL filter: L_1, H	$4.1897 \cdot 10^{-4}$
L_2, H	$2.5138 \cdot 10^{-4}$
C_f, F	$5.0886 \cdot 10^{-5}$
Grid frequency, Hz	50

Simulation results. Figure 5 shows the simulation results in the healthy state and in the presence of an open circuit fault. An operation in faulty mode due to an open circuit fault on the IGBT T4 will cause the loss of the negative half-wave of the current of phase B. In another way if there is no opening of the IGBT T4 and T5 will cause a loss of positive alternation in the current of phase C.

The inputs to the system diagnostic block consist of the following characteristics ($i_{\alpha mean}$, $i_{\beta mean}$ and θ_f). The information of each scenario for the healthy case and the defective cases is summarized in Table 4.

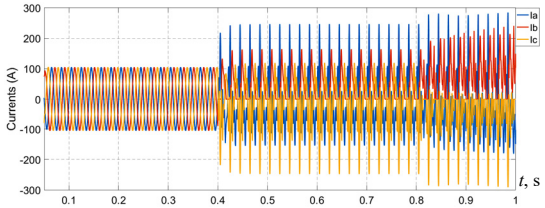

Fig. 5. Three phase currents in healthy and faulty mode

Table 4

Diagnostic indicators values

States	Parameters $i_{\alpha mean}$, $i_{\beta mean}$, θ_f		
Healthy	0.0004039	–0.004703	274.91
T1	–39.14	9.166	166.8
T2	39.17	–9.186	346.8
T3	11.59	–38.45	286.77
T4	–11.6	38.53	106.8
T5	27.52	29.37	46.86
T6	–27.49	–29.43	227
T1 and T3	–16.8	–82.43	258.5
T1 and T4	–96.12	6.134	176.3
T1 and T5	–63.08	55.82	138.5
T1 and T6	–53.36	–80.41	236.4
T2 and T3	96.23	–6.064	356.396
T2 and T4	16.89	82.44	78.42
T2 and T5	53.35	80.32	56.41
T2 and T6	63.04	–55.78	318.45
T3 and T5	79.83	26.65	18.46
T3 and T6	42.88	–86.38	296.4
T4 and T5	–42.68	86.35	116.3
T4 and T6	–79.76	–26.61	198.5
T	–0.003302	–0.000994	196.8

Neural network learning outcomes. Learning is a crucial stage in the deployment of a neural network, in which the network's behavior is modified until the desired behavior is achieved. The software MATLAB was used to do automatic learning until a very small squared error was acquired. The ANN learning base is presented in the form of table. It is represented by classes of vectors, where each class represents a type of functioning (healthy and defective), and each vector is represented by the sampled values.

The best learning performance obtained thanks to a good choice of the ANN structure and after several learning tests. The learning performance of the ANN used is evaluated by the root mean square error. In our case, the ANN reached a value of $9.1656 \cdot 10^{-21}$ after 28 iterations, as shown in Fig. 6.

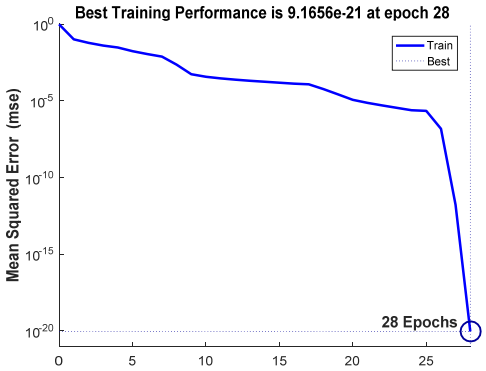

Fig. 6. Performance of the ANN

Once the ANN has been constructed (Fig. 7) and its training has achieved satisfactory performance, we move on to the step of comparing the target outputs to the simulation results. The results of the ANN test are shown below in Fig. 8.

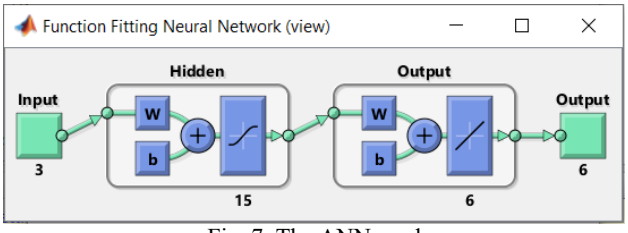

Fig. 7. The ANN used

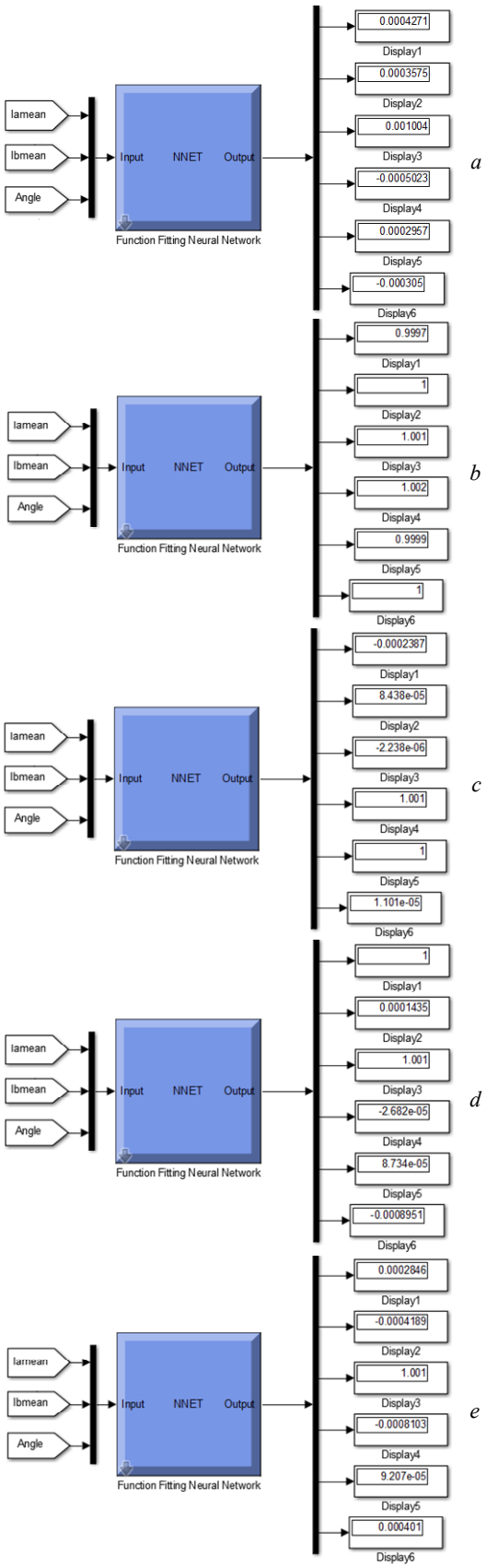

Fig. 8. Simulation results in state: (a) Healthy, (b) Fault in DC-DC Boost Converter, (c) Fault in T4 and T5, (d) Fault in T1 and T3, (e) Fault in T3

According to the results obtained during the test, it can be seen that the results of the ANN used evolve according to the desired results for the different types of operation.

Conclusion. This paper proposes the use of artificial neural networks to classify open circuit faults in IGBTs of power converters in photovoltaic systems. The resulting network has a simple design with an input layer, a decision output layer, and a hidden layer of 15 neurons, as well as graphical outputs that display the learning results. After multiple learning tests, it can be established that a good choice of artificial neural network structure results in greater learning performance. The simulation results, as shown above, demonstrate the reliability and performance of the fault detection and diagnosis system created for the photovoltaic system's power converters.

Conflict of interest. The authors declare that they have no conflicts of interest.

REFERENCES

1. Deshpande S., Bhasme N.R. A review of topologies of inverter for grid connected PV systems. *2017 Innovations in Power and Advanced Computing Technologies (i-PACT)*, 2017, pp. 1-6. doi: https://doi.org/10.1109/IPACT.2017.8245191.

2. Sahraoui H., Mellah H., Drid S., Chrifi-Alaoui L. Adaptive maximum power point tracking using neural networks for a photovoltaic systems according grid. *Electrical Engineering & Electromechanics*, 2021, no. 5, pp. 57-66. doi: https://doi.org/10.20998/2074-272X.2021.5.08.

3. Khan S.A., Mahmood T., Awan K.S. A nature based novel maximum power point tracking algorithm for partial shading conditions. *Electrical Engineering & Electromechanics*, 2021, no. 6, pp. 54-63. doi: https://doi.org/10.20998/2074-272X.2021.6.08.

4. Hu Y., Cao W. Theoretical Analysis and Implementation of Photovoltaic Fault Diagnosis. *In Renewable Energy - Utilisation and System Integration*. InTech. 2016. doi: https://doi.org/10.5772/62057.

5. Bento F., Marques Cardoso A.J. A comprehensive survey on fault diagnosis and fault tolerance of DC-DC converters. *Chinese Journal of Electrical Engineering*, 2018, vol. 4, no. 3, pp. 1-12. doi: https://doi.org/10.23919/CJEE.2018.8471284.

6. Asghar F., Talha M., Kim S.H. Neural Network Based Fault Detection and Diagnosis System for Three-Phase Inverter in Variable Speed Drive with Induction Motor. *Journal of Control Science and Engineering*, 2016, pp. 1-12. doi: https://doi.org/10.1155/2016/1286318.

7. Cherif B.D.E., Bendiabdellah A., Bendjebbar M., Tamer A. Neural Network Based Fault Diagnosis of Three Phase Inverter Fed Vector Control Induction Motor. *Periodica Polytechnica Electrical Engineering and Computer Science*, 2019, vol. 63, no. 4, pp. 295-305. doi: https://doi.org/10.3311/PPee.14315.

8. Boumous Z., Boumous S. New Approach in the Fault Tolerant Control of Three-Phase Inverter Fed Induction Motor. *Engineering, Technology & Applied Science Research*, 2020, vol. 10, no. 6, pp. 6504-6509. doi: https://doi.org/10.48084/etasr.3898.

9. Talha M., Asghar F., Kim S.H. A Matlab and Simulink Based Three-Phase Inverter Fault Diagnosis Method Using Three-Dimensional Features. *The International Journal of Fuzzy Logic and Intelligent Systems*, 2016, vol. 16, no. 3, pp. 173-180. doi: https://doi.org/10.5391/IJFIS.2016.16.3.173.

10. Rohan A., Kim S.H. Fault Detection and Diagnosis System for a Three-Phase Inverter Using a DWT-Based Artificial Neural Network. *The International Journal of Fuzzy Logic and Intelligent Systems*, 2016, vol. 16, no. 4, pp. 238-245. doi: https://doi.org/10.5391/IJFIS.2016.16.4.238.

11. Dhumale R.B., Lokhande S.D. Comparative Study of Fault Diagnostic Methods in Voltage Source Inverter Fed Three Phase Induction Motor Drive. *IOP Conference Series: Materials Science and Engineering*, 2017, vol. 197, art. no. 012006. doi: https://doi.org/10.1088/1757-899X/197/1/012006.

12. Orlowska-Kowalska T., Sobanski P. Simple diagnostic technique of a single IGBT open-circuit faults for a SVM-VSI vector controlled induction motor drive. *Bulletin of the Polish Academy of Sciences Technical Sciences*, 2015, vol. 63, no. 1, pp. 281-288. doi: https://doi.org/10.1515/bpasts-2015-0032.

13. Jian-Jian Z., Yong C., Zhang-Yong C., Anjian Z. Open-Switch Fault Diagnosis Method in Voltage-Source Inverters Based on Phase Currents. *IEEE Access*, 2019, vol. 7, pp. 63619-63625. doi: https://doi.org/10.1109/ACCESS.2019.2913164.

14. Estima J.O., Marques Cardoso A.J. A New Algorithm for Real-Time Multiple Open-Circuit Fault Diagnosis in Voltage-Fed PWM Motor Drives by the Reference Current Errors. *IEEE Transactions on Industrial Electronics*, 2013, vol. 60, no. 8, pp. 3496-3505. doi: https://doi.org/10.1109/TIE.2012.2188877.

15. Estima J.O., Marques Cardoso A.J. A New Approach for Real-Time Multiple Open-Circuit Fault Diagnosis in Voltage-Source Inverters. *IEEE Transactions on Industry Applications*, 2011, vol. 47, no. 6, pp. 2487-2494. doi: https://doi.org/10.1109/TIA.2011.2168800.

16. Wei H., Zhang Y., Yu L., Zhang M., Teffah K. A New Diagnostic Algorithm for Multiple IGBTs Open Circuit Faults by the Phase Currents for Power Inverter in Electric Vehicles. *Energies*, 2018, vol. 11, no. 6, art. no. 1508. doi: https://doi.org/10.3390/en11061508.

17. Yan H., Xu Y., Cai F., Zhang H., Zhao W., Gerada C. PWM-VSI Fault Diagnosis for a PMSM Drive Based on the Fuzzy Logic Approach. *IEEE Transactions on Power Electronics*, 2019, vol. 34, no. 1, pp. 759-768. doi: https://doi.org/10.1109/TPEL.2018.2814615.

18. Chen C.C., Lin Y.H., Ke B.R., Hsue C.W., Hsieh H.C. Fault leg detection for open-circuit faults in PWM voltage-source inverters of renewable energy via the fuzzy logic diagnostic method. *Journal of Technology*, 2017, vol. 32, no. 4, pp. 299-312.

19. Ibem C.N., Farrag M.E., Aboushady A.A. New Fuzzy Logic Based Switch-Fault Diagnosis in Three Phase Inverters. *2020 55th International Universities Power Engineering Conference (UPEC)*, 2020, pp. 1-6. doi: https://doi.org/10.1109/UPEC49904.2020.9209873.

20. He L., Zhao J., Wu F., Yang H. Current residual error analysis based transistor open-circuit fault diagnosis in voltage-source inverter fed induction motor. *2017 12th IEEE Conference on Industrial Electronics and Applications (ICIEA)*, 2017, pp. 1160-1165. doi: https://doi.org/10.1109/ICIEA.2017.8283015.

21. Khelif M.A., Bendiabdellah A., Cherif B.D.E. A Combined RMS-MEAN Value Approach for an Inverter Open-Circuit Fault Detection. *Periodica Polytechnica Electrical Engineering and Computer Science*, 2019, vol. 63, no. 3, pp. 169-177. doi: https://doi.org/10.3311/PPee.13605.

22. Anitha D., Uthra R., Kalaiarasi N. Simulation of grid-connected photovoltaic system with real and reactive power control. *International Journal of Recent Technology and Engineering*, 2019, vol. 8, special issue 1S4, pp. 545-550.

23. Nebti K., Lebied R. Fuzzy maximum power point tracking compared to sliding mode technique for photovoltaic systems based on DC-DC boost converter. *Electrical Engineering & Electromechanics*, 2021, no. 1, pp. 67-73. doi: https://doi.org/10.20998/2074-272X.2021.1.10.

24. Mohamed S.A., Tolba M.A., Eisa A.A., El-Rifaie A.M. Comprehensive Modeling and Control of Grid-Connected Hybrid Energy Sources Using MPPT Controller. *Energies*, 2021, vol. 14, no. 16, art. no. 5142. doi: https://doi.org/10.3390/en14165142.

25. Zorig A., Belkheiri M., Barkat S., Rabhi A. Control of three-level NPC inverter based grid connected PV system. *2015 3rd International Conference on Control, Engineering & Information Technology (CEIT)*, 2015, pp. 1-6. doi: https://doi.org/10.1109/CEIT.2015.7233169.

26. Kim J.-M., Lee K.-B., Lee D.-C., Ko Y.-J. Fault diagnosis of three-parallel voltage-source converter for a high-power wind turbine. *IET Power Electronics*, 2012, vol. 5, no. 7, pp. 1058-1067. doi: https://doi.org/10.1049/iet-pel.2011.0109.

Received 26.05.2022
Accepted 23.08.2022
Published 06.01.2023

Amina Mimouni[1], *PhD Student,*
Saadi Souad Laribi[1], *Doctor of Electrical Engineering,*
Morsli Sebaa[1], *Professor,*
Tayeb Allaoui[1], *Professor of Electrical Engineering,*
Abdelkader Azzeddine Bengharbi[1], *PhD Student,*
[1] Energy Engineering and Computer Engineering (L2GEGI) Laboratory, University of Tiaret,
BP P 78 Zaâroura, 14000, Tiaret, Algeria.
e-mail: amina.mimouni@univ-tiaret.dz (Corresponding Author); souad.laribi@univ-tiaret.dz; m_sebaa@univ-tiaret.dz; tayeb.allaoui@univ-tiaret.dz; bengharbi.aek.azz@univ-tiaret.dz

How to cite this article:
Mimouni A., Laribi S., Sebaa M., Allaoui T., Bengharbi A.A. Fault diagnosis of power converters in a grid connected photovoltaic system using artificial neural networks. *Electrical Engineering & Electromechanics*, 2023, no. 1, pp. 25-30. doi: https://doi.org/10.20998/2074-272X.2023.1.04

UDC 621.314 https://doi.org/10.20998/2074-272X.2023.1.05

E. Parimalasundar, R. Senthil Kumar, V.S. Chandrika, K. Suresh

Fault diagnosis in a five-level multilevel inverter using an artificial neural network approach

Introduction. *Cascaded H-bridge multilevel inverters (CHB-MLI) are becoming increasingly used in applications such as distribution systems, electrical traction systems, high voltage direct conversion systems, and many others. Despite the fact that multilevel inverters contain a large number of control switches, detecting a malfunction takes a significant amount of time. In the fault switch configurations diode included for freewheeling operation during open-fault condition. During short circuit fault conditions are carried out by the fuse, which can reveal the freewheeling current direction. The fault category can be identified independently and also failure of power switches harmed by the functioning and reliability of CHB-MLI. This paper investigates the effects and performance of open and short switching faults of multilevel inverters. Output voltage characteristics of 5 level MLI are frequently determined from distinctive switch faults with modulation index value of 0.85 is used during simulation analysis. In the simulation experiment for the modulation index value of 0.85, one second open and short circuit faults are created for the place of faulty switch. Fault is identified automatically by means of artificial neural network (ANN) technique using sinusoidal pulse width modulation based on distorted total harmonic distortion (THD) and managed by its own. The* ***novelty*** *of the proposed work consists of a fast Fourier transform (FFT) and ANN to identify faulty switch.* ***Purpose.*** *The proposed architecture is to identify faulty switch during open and short failures, which has to be reduced THD and make the system in reliable operation.* ***Methods.*** *The proposed topology is to be design and evaluate using MATLAB/Simulink platform.* ***Results.*** *Using the FFT and ANN approaches, the normal and faulty conditions of the MLI are explored, and the faulty switch is detected based on voltage changing patterns in the output.* ***Practical value.*** *The proposed topology has been very supportive for implementing non-conventional energy sources based multilevel inverter, which is connected to large demand in grid.* References 22, tables 2, figures 17.

Key words: **artificial neural network, fast Fourier transform, multilevel inverter, sinusoidal pulse width modulation, total harmonic distortion.**

Вступ. *Каскадні багаторівневі інвертори H-bridge все частіше використовуються в таких пристроях, як розподільні системи, електричні тягові системи, системи прямого перетворення високої напруги та багато інших. Незважаючи на те, що багаторівневі інвертори містять велику кількість перемикачів, що управляють, виявлення несправності займає значний час. У конфігурації аварійного вимикача увімкнено діод для роботи в режимі вільного ходу в умовах обриву несправності. При короткому замиканні аварійні стани виконуються запобіжником, який може визначити напрямок струму вільного ходу. Категорія несправності може бути визначена самостійно, а також відмова силових вимикачів, що порушує функціонування та надійність каскадних багаторівневих інверторів H-bridge. У цій статті досліджуються наслідки та характеристики обривів та коротких замикань багаторівневих інверторів. Характеристики вихідної напруги 5-рівневого інвертору часто визначаються характерними несправностями перемикача, при цьому при аналізі моделювання використовується значення індексу модуляції 0,85. В імітаційному експерименті значення індексу модуляції 0,85 в місці несправного перемикача створюються односекундні обриви і коротке замикання. Несправність ідентифікується автоматично за допомогою методу штучної нейронної мережі з використанням синусоїдальної широтно-імпульсної модуляції на основі спотвореного повного гармонійного спотворення та керується самостійно.* ***Новизна*** *запропонованої роботи полягає у застосуванні швидкого перетворення Фур'є та штучної нейронної мережі для ідентифікації несправного перемикача.* ***Мета***. *Пропонована архітектура призначена для виявлення несправного комутатора при розмиканні та короткочасних відмовах, що має знизити повне гармонійне спотворення та забезпечити надійну роботу системи. методи. Запропонована топологія має бути спроектована та оцінена з використанням платформи MATLAB/Simulink.* ***Результати***. *Використовуючи підходи швидкого перетворення Фур'є та штучної нейронної мережі, досліджуються нормальні та несправні стани багаторівневих інверторів, і несправний перемикач виявляється на основі моделей зміни напруги на виході.* ***Практична цінність.*** *Запропонована топологія дуже сприятлива для реалізації нетрадиційних джерел енергії на основі багаторівневого інвертора, пов'язаного з великим попитом у мережі.* Бібл. 22, табл. 2, рис. 17.

Ключові слова: **штучна нейронна мережа, швидке перетворення Фур'є, багаторівневий інвертор, широтно-імпульсна модуляція, повні гармонічні спотворення.**

1. Introduction. Multilevel inverters (MLIs) have aroused huge attention in the examination of established manufacturing electric drive organizations in recent days, with the intention of reaching their power quality as well as demands. The key benefits of MLIs are the elimination of harmonic distortion in the output voltage waveform by increasing level capacity, and even the portability of battery packs or fuel including in intervals. Despite the fact that MLIs are an established technology that may be used in engineering applications, the failure of power electronic switches and fault analysis is a new research issue for researchers. It's used in engineering to check the condition of power switches in inverters. The number of levels in the inverter varies, as does the quantity of additional switching devices, increasing the risk of any one of the switches collapsing; hence, any such problem should be addressed at the outset so that the drive and motor processes are not accepted during abnormal situations. To improve system reliability, an effective problem diagnosis system must be implemented.

In [1] had investigated in both moderate and high-power applications of multilevel converters which play a significant role. MLIs come in three typical configurations: diode clamped, flying capacitor, and cascaded H-bridged. The modular design of cascaded H-bridged multilevel inverter (CHB-MLI) characteristics and performance are used to achieve medium voltage and high-performance characteristics. Short and open circuit faults are two types of failures which can occur in power switching devices in CHB-MLIs. Short circuit (SC) problems mostly damage, so protection from SC is required. Artificial neural network (ANN) approaches for SC protection by using high potency fuses and de-saturation method.

In [2] had analyzed open-circuit faults in power switches the device shutting down, and they can go undetected for a long time. This could cause secondary defects in the inverter or other drive components,

culminating in the entire system being shut down and expensive repairs.

In [3] had investigated short-circuit faults in power electronic switches, on the other hand, are extremely damaging and necessitate special precautions to automatically shut down the entire drive. These types of failures must be identified and repaired in a microsecond in order to safeguard analogous semiconductor devices from damage in the converter leg. On the other perspective, extended open circuit fault behaviour of the power converters might cause the entire system. Expertise in fault behaviours, fault prediction, and fault diagnostics will be necessary to keep the MLI system functioning smoothly. The two aspects of power electronic device fault diagnosis are as follows: fault information acquisition, which entails gathering data whenever a failure occurs using a specific fault detection approach; and fault identification and characterization, which rely upon that specific of failure modes to recognize the category. The position of faults is identified by an algorithm which was developed in [4]. In [5] the open circuit fault can be caused by a number of factors, including a damaged inner wire, a transient short-circuits, or a gate driver failure. Over-voltage, over-current, safety component failure, and improper gating signal are some of the causes of SC failure. In [6] authors explained the recurrent neural network-based voltage stability for grid connected solar photovoltaic systems using static synchronous compensator with recurrent neural network. Authors in [7, 8] investigated a number of recent articles on problems such as the creation of inverted pulse width modulation (PWM) method in CHB-MLI systems. In [9] has analyzed fault analysis in inverter and also faults an inverter device is used continuously under abnormal settings, further issues will arise, resulting in severe consequences. Furthermore, the MLI is composed of several switching devices and the entire system is complex in structure, and there are numerous nonlinear impacts. As a result, MLIs need some novel diagnostic strategies which could not deal with nonlinear detection issues but also diagnose and locate faults easily. The device voltage and current of a multilayer inverter might vary based on the part and location of the faults. Some research concentrates on the device output current or voltage to assess fault form and position more quickly and easily, and then used the sample to expand a number of fault diagnosis techniques. Owing to the dangerous effects of SC faults on converter circuits, this type of fault must be detected as soon as possible. It is necessary to remember that certain circuit drivers are already in a position to detect defective switches. Hence considering the value of MV drives on the industry, robust detection mechanisms need to be discussed. In [10] had investigated electrical drives and devices require complex electrical converters to conform to high power requirements. MLI methods have also been tested as an approach to high and low voltage systems. Compared to traditional two-level inverters, MLIs produce major output voltage and low harmonic output current distortion.

The fundamental objectives of the proposed research effort is to develop a high-performance fault detection methodology for evaluating open and SC faults in MLI using enhanced signal processing and soft computing techniques. The fast Fourier transform (FFT) technique and ANN approach are used to evaluate the spectrum properties of output voltage wave forms produced using both modeling and experimental investigations at various fault situations. By using FFT technique, extract salient features such as total harmonic distortion (THD) and harmonic contents of output voltage signal at different fault cases. The performance characteristics of the FFT-ANN model-based fault detection approach for MLIs can be compared to develop an effective fault diagnostic system. These concerns include the identification of switch faults and the monitoring of tolerances because parameters contribute to the reliability of the power converter systems. The validation of proposed model is implemented with the help of open and SC fault voltages and total harmonic distortion.

2. Literature Review. A fault-tolerant method for a CHB inverter was proposed in [11]. Additional versions provide the converter's trustworthy and efficient operation in the event of a failure. The recommended method utilises an additional cross-coupled cascaded H-bridged unit in addition to existing CHB components to preserve output voltage and ensure continuation of function in the event of an open/short-circuit fault.

In [12] was developed an innovative technique of fault diagnostics based on the minimum squares support vector machine using back propagation algorithm. Authors [13] established a digital circuit-based approach for identifying SC problems. The suggested approach detects two types of SC faults: hard switch fault and fault under load; it can be utilised through any switch, independent of its characteristics; and it does not employ artificial intelligence strategies and procedures when inverter function is in progress. Rough sets theory (RST) is used to create the digital diagnostic circuit, which optimizes and specifies a minimal set of variables required to identify problems. When the variables are subjected to RST, a sequence of diagnostic rules is generated. These criteria are implemented using simple logic operations, resulting in a digital diagnostics system.

In [14] had developed a fault diagnostic method for photovoltaic (PV) inverters that allows for various open-circuit fault analyses. In [15] recommended that a fuzzy-based fault detection technique be used to analyse a voltage source inverter supplied three-phase permanent magnet synchronous motor driving. The average current Park's vector approach, which uses phase current information, is used to calculate the fault symptom variables. A fuzzy logic approach is used to process fault symptom variables and recover faulty information from power switches. The suggested fault detection technique can identify and find not only two or more distinct open-circuit problems in switching devices, and moreover periodic failures in power switches, which may enhance the motor drive system's dependability. In a three-phase quasi-Z-source inverter, authors [16] proposed a method for detecting open-circuit failures. The proposed method is confined to Z-source inverters and is based on assessing the impact of shoot-through durations on state variables during switching periods. Defect site identification and open-circuit monitoring are the two steps of the proposed approach. After both steps of the open circuit fault

detection method have been completed, a redundant leg is activated and utilised in lieu of the failed limb. The recommended technique is validated by test results from a low-voltage q-ZSI device.

Authors [17] proposed a signal processing technique for detecting switch open-circuit faults and identifying the individual problematic switch, which will help with servicing and fault-tolerant functioning. The faulty phase and defective switching combination, consisting of the defective component and the switching on its diagonally, was identified using the stator phase currents statistical characteristics.

A fault diagnostic method comprised of multistate data processing through subsection variation analysis lock, and ANN which is created using feature extraction for the output currents of balanced and unbalanced stages. A novel generalized open-switch fault-diagnostic approach was proposed in [18]. In this detection method, defect prediction features are implemented as half-cycle mean bridge voltages for an N-level CHB-MLI, which are computed separately for positive and negative half cycles. Precedent half-cycle averages are utilised to anticipate these averages during open-circuit fault circumstances, which are then compared to observed values to determine the open-circuit fault. This fast detection approach may detect the faulty switch in cascaded inverters with many voltage levels by looking at one structural characteristic of the output voltage. This technique may successfully identify the faulty switch of the cascaded inverter using various level-shifted pulse width modulation methods, variable loading conditions, modulation indexes, and switching frequencies.

Authors [19] presented a novel fault-tolerant control technique for CHB-MLI to increase the greatest achievable voltage under faulty conditions. Instead of bypassing the damaged cell when a semiconductor breaks, this method uses it to generate voltage. Due to the lack of one level of defective cell voltage level, the voltage is decreased to half. In comparison to traditional fault-tolerant techniques, the maximum possible output voltage could be increased for the majority of problematic circumstances. In addition, the defective cell switching mechanism is changed to enhance the output voltage quality. A grid-connected single to three-phase multilevel converter with a fault-tolerant design was proposed in [20]. The induction motor drive can operate even if any of the power semiconductor switches have open circuit faults. A control mechanism on a single active front end converter was used to accomplish this. A separate control method is used to provide the power converter's on-grid fault tolerance capabilities. The control approach employed on a single grid-connected converter enhances the input power factor, resulting in a unity power factor at the source. The voltage control loop adjusts the DC-link voltage to get the command voltage.

The redundancy of the triangular carrier signals is a criterion for expanding sinusoidal pulse width modulation (SPWM) to numerous output voltage levels per phase-leg, according to [21]. The recommended control technique creates suitable modulation patterns for the CHB inverter by modifying a sinusoidal modulating pattern to fit within a single triangle carrier signal range. These frameworks may be used on any level CHB inverter without any further control modifications.

To resolve the insulated gate bipolar transistor (IGBT) open-circuit failure problem of the propulsion inverter in a transmission line power supply system, subsequently, using the IGBT inverter open-circuit fault identification, a simulation model which is based on propulsion inverter structure is constructed, and different switching fault signal waveforms are evaluated. Secondly, the bus voltage magnitude data is poorly represented and turned into a fault signal using direct detection methodology.

The fault-tolerant five-level inverter technique described in [22] for open-end induction motor driving applications uses a single DC connection. One end of the drive is fed by a main inverter, while the other is fed by a supplemental inverter. The proposed approach, in compared to other current inverter systems, allows for five-level inverter operation with little interruption. Furthermore, the design is fault-tolerant in the case that the H-bridge switching devices and the extra two-level inverter fail.

Since these MLIs feature a large number of power semiconductors, the chance of failure is much higher. As a result, identifying potential faults and operating under faulty situations are critical. The identification of a failure might be complex in concept due to the large number of components. MLIs have interesting advantages due to their faulty structure, such as the ability to operate in medium, high voltage, and high-power applications, providing a better voltage waveform with low total harmonic distortion for electric machines applications, output filter elimination, dv/dt transient reduction during commutation, low electromagnetic interference emissions from over voltages, and reduced power loss.

3. Proposed method of fault diagnosis system in MLI. Figure 1 illustrates literally the entire fault detection system set up for identifying defective power semiconductor switches in MLIs, which includes both MLI and fault diagnosis system. The characteristics of output voltage sequences were extracted using the FFT approach. Frequency domain analyses of the terminal voltage patterns are required to construct a significant application assessment method. The FFT approach was used to retrieve distinct attributes from the output voltage signal. Despite the fact that a skilled feature extractor should supply critical data facts more about ANN in the selected area, it was the highest degree of consistency reached within the adaptive intelligence network.

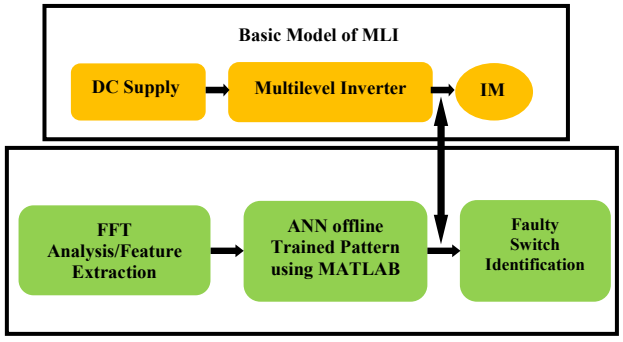

Fig. 1. Proposed fault diagnosis system of MLI

Figure 2 depicts the signal separation of output voltage in terms of harmonics and RMS voltage output. The FFT provides a frequency response representation for any periodic or non-periodic signal. Figure 3 depicts one of the 11th order sample harmonics, as well as THD and V_{rms} values, which are all utilized to extract characteristics from the output signal employing FFT analysis.

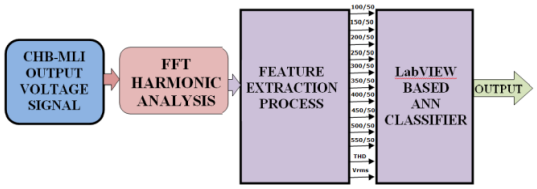

Fig. 2. FFT harmonic analysis of output voltage signal

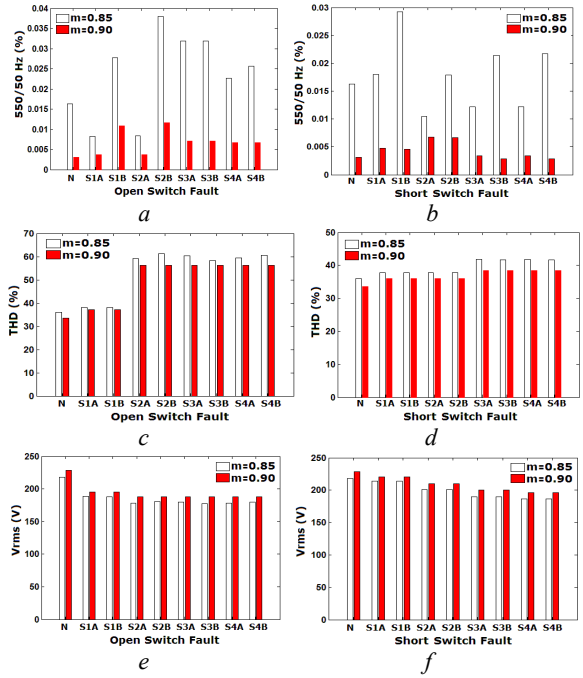

Fig. 3. Representation of FFT investigation during:
a) 11th harmonic with open circuit fault;
b) 11th harmonic with short circuit fault;
c) THD analysis for open circuit fault;
d) THD analysis for short circuit fault;
e) V_{rms} analysis for open circuit fault;
f) V_{rms} analysis for short circuit fault

The FFT provides frequency domain representation of any periodic or non-periodic signal. In general, the Fourier transform (FT) is a generalization of the Fourier series. Instead of sines and cosines, as in a Fourier series, the FT uses exponentials and complex numbers. For a signal or function $f(t)$, the FT is defined as:

$$F(\omega)=\int_{-\infty}^{\infty} f(t)\cdot e^{-j\omega t}\mathrm{d}t\,. \tag{1}$$

The inverse FT is defined as:

$$f(t)=\frac{1}{2\pi}\int_{-\infty}^{\infty} F(\omega)\cdot e^{-j\omega t}\mathrm{d}\omega\,. \tag{2}$$

The expression below is used to calculate THD for an output voltage pattern as:

$$THD=\sqrt{\frac{V_2^{\,2}+V_3^{\,2}+V_4^{\,2}+....+V_n^{\,2}}{V_1}}\,, \tag{3}$$

where V_n is the root means square (RMS) value of the voltage of the n^{th} harmonic; n = 1 is the frequency of the signal. It determines the degree of distortion in a voltage output.

A. Fault classification using ANN techniques. In a multilayer feed forward network, Fig. 4 depicts the error back propagation. The back propagation technique is used to compute the necessary modifications once the network's weights are picked at random. The back propagation algorithm may be separated into four stages in general. The four steps of the back propagation algorithm are feed-forward processing, back propagation to the output layer, back propagation to the hidden layer, and weight changes. The algorithm is disrupted whenever the value of the error function has become reasonably low, i.e., when the error between the actual and planned output is less than a given number (convergence criteria). In this network, the deviation is back-propagated, and the weights and biases are essentially reconfigured using an approach to reduce the mean square error (MSE), which is the mean of all the errors for all sets of inputs and outputs, and is determined as:

$$MSE=\frac{1}{n}\sum_{m}^{n}\left(P_m-Q_m\right). \tag{4}$$

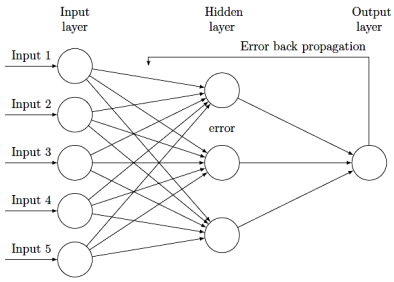

Fig. 4. Back propagation of error in multilayer feed forward network

In this case, P_m and Q_m are the desired and measured outputs for the m^{th} input set, where n is the total number of input sets. The failure detection of MLIs was automated using an ANN in this investigation. The ANN was used to solve the difficulty of detecting the faulty switch in a cascaded MLI. Due to its simple methodology and excellent predictive potential, the multilayer feed forward network with back propagation learning technique has been regarded one of the numerous ANN designs accessible in the literature.

Using the 9 output neurons, the fault is categorized as no fault, S1A to S4A fault, and S1B to S4B fault. The output layer neurons are set up to perform multiple binary training patterns in response to different degradation scenarios.

Network topology, size, and learning rate, number of training sets, convergence criterion, and number of iterations are all essential parameters that influence the neural network's convergence and learning time. The learning rate is known to damp out oscillations to some extent, during the training phase. Higher values of learning rate may result in fast convergence, but it may result in oscillation. The training time of the neural network will rise as the number of training sets and training cycle increases. For improved classification results, an appropriate neural network structure must be found. As a result, in order to arrive at an ideal topology,

the effectiveness of the neural network for varying parameters of the learning rate, training sets, convergence criterion, iterations, and number of neurons in the hidden layer must be examined in depth and assessed.

The majority of processing facilities in the hidden layer and the number of observations is two significant parameters that influence the neural network's functionality. The neural network fails to meet the convergence requirements when the number of hidden layer neurons is fewer than 10. The neural network takes longer to train and meet the convergence requirements when the quantity of hidden layer neurons rises over 24.

The current network achieves convergence criterion at 3800 iterations throughout the training phase. It shows that 3800 iterations are enough for the optimal neural network to be successfully trained. Then 150 more data points were employed for identification testing with modulation indices ranging from 0.8 to 0.95, which is as shown in Fig. 5.

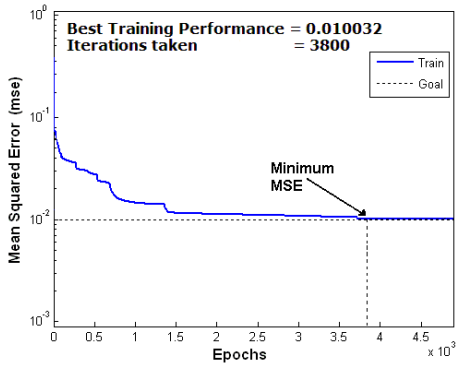

Fig. 5. Identification of best training performance of MSE

As the number of hidden layer neurons exceeds 18, the neural network takes more time to train and adhere to the convergence requirements. The network's mean square error was computed by keeping the step size at 0.1 with 18 hidden layer neurons in order to arrive at an optimal value for the number of epochs. The mean square error values derived from different amounts of hidden layer neurons are shown in Fig. 6 depicts the proposed fault diagnostic system's detection rates for various numbers of hidden layer neurons. As compared to other instances, the device performs better with 18 secret layer neurons. In this context, the overall detection performance for all fault conditions is 100 %, and the device can correctly find the fault in nearly any situation.

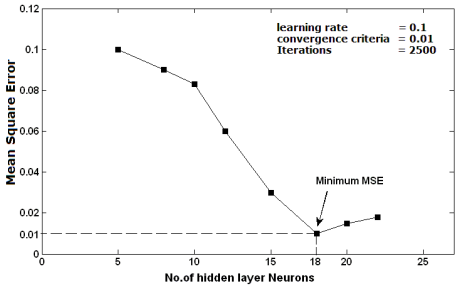

Fig. 6. Investigation of the ANN-MSE at various statistics of hidden layer neurons for 18

B. Fault classification using ANN techniques. Cascaded H-bridged inverter topology consists of a series of H-bridge inverter cells are interconnected to each cell at each point with a different DC voltage configuration. Figure 7 shows that there is a traditional cascaded H-bridged inverter topology with three H-bridged cells attached to the three-phase inductive motor load at each point. The degree of waveforms in the output signal ranges may be calculated using $2N+1$, where N is typically the size of H-bridged cells in the network.

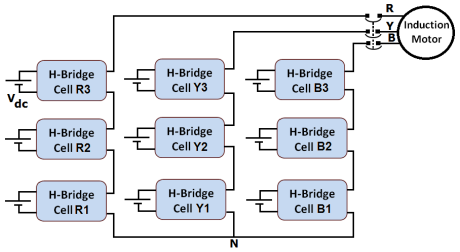

Fig. 7. Structure of traditional three phase cascaded H-bridged inverter topology comprising induction motor

However a three-phase MLI strategy is typically used across drive systems, a single-phase MLI may be used at this point, while a three-phase based fault detection system could be expanded.

Figure 8 shows the schematic single-stage, five-stage voltage output of the CHB-MLI used in existing positions correlated with induction motor load. Induction motor characteristics such as unbalanced stator currents and voltages, torque oscillations, efficiency and torque decreases, overheating, and excessive vibration are all affected if the MLI power semiconductor switches fail. Furthermore, some harmonic components of currents and voltages can be amplified by these motor problems. To achieve good performance, the defective switch must be identified and replaced as quickly as possible. Each IGBT switch is categorized as S1A, S1B, etc. by its cell position. The simulation experiments have been performed using the MATLAB/Simulink tool and Table 1 summarizes the parameters used for the simulation analysis.

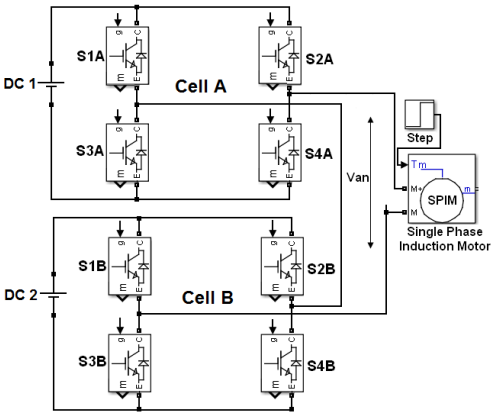

Fig. 8. Single-phase cascaded H-bridged 5-level MLI coupled to the drive system

Table 1

Simulation parameters of five level MLI

Parameters	Values
DC input voltage	115 V
Number of H-bridges	2
No. of switches	4
Output levels	5
Modulation Index	0.85
Carrier frequency	3 kHz
Load	Single phase IM, 0.5 HP, 50 Hz, 230 V

C. Fault classification using ANN techniques. The SPWM switching technique is frequently utilised to create the requisite IGBT transition pulses. The pulse of the triangular carrier is the same as the reference sinusoidal signal when SPWM is resent. As illustrated in Fig. 9; the switching signals are processed using a sinusoidal and triangular signal with a modulation index of 0.85. The technique of SPWM addresses sinusoidal waveform creation by contrasting reference to carrier waves or filtering the pulse output waveform by altering the widths of triangular waveforms. The basic pulse generation circuit for the sine pulse width modulation technique is shown in Fig. 9. Low frequency reference sinusoidal waveforms are compared with high frequency triangular waves, often known as carrier waves. The switching phase is changed when the sine and carrier waves cross is shown in Fig. 10.

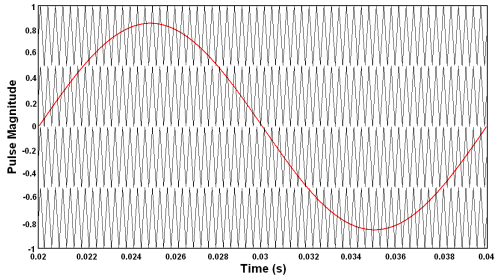

Fig. 9. The sinusoidal reference signal and the triangular carrier signal in PWM are used for modulation index of 0.85 carrier frequency of 3 kHz values

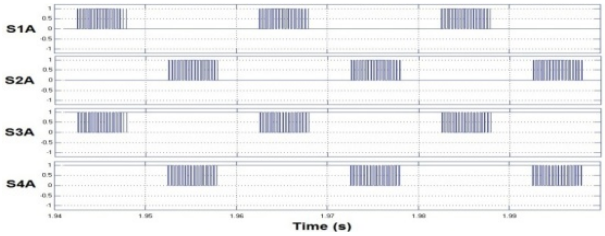

Fig. 10. SPWM based cell A switching pulses are generated by 3 kHz carrier frequency and 0.85 modulation index

Table 2 illustrates the switching patterns of five level cascaded MLI during healthy condition. SPWM based cell A switching pulses are generated by 3 kHz carrier frequency and 0.85 modulation index is shown in Fig. 4.

Table 2

Switching table of five level cascaded MLI

Switching sequences								Voltage levels
Bridge – A				Bridge – B				
S1	S4	S2	S3	S1	S4	S2	S3	
1	1	0	0	1	1	0	0	$+2V_{DC}$
1	1	0	0	0	0	0	0	$+V_{DC}$
0	0	0	0	0	0	0	0	0
0	0	1	1	0	0	0	0	$-V_{DC}$
0	0	1	1	0	0	1	1	$-2V_{DC}$

Mode 1: Five level cascaded H-Bridge inverter switches S1 & S2 – A and S1 & S2 – B are turned on in this mode of operation. $+2V_{DC}$ is the output voltage obtained across the load.

Mode 2: Five level cascaded H-Bridge inverter switches S1 & S2 – A is turned on in this mode of operation. $+V_{DC}$ is the output voltage obtained across the load.

Mode 3: Five level cascaded H-Bridge inverter switches, all the bridge switches are zero, the output voltage obtained across the load is zero.

Mode 4: Five level cascaded H-Bridge inverter switches S3 & S4 – A is turned on in this mode of operation. $+V_{DC}$ is the output voltage obtained across the load.

Mode 5: Five level cascaded H-Bridge inverter switches S3 & S4 – A and S3 & S4 – B are turned on in this mode of operation. $+2V_{DC}$ is the output voltage obtained across the load. The same operation is shown in tabular form above in Table 2.

4. Results and discussion.

A. Open circuit fault analysis and discussion. The primary open circuit failure occurs around 1 s with the bridged cell A switch in S1A to determine the voltage level output before and after the start of the open circuit failure of the MLI. Figure 11 reflects the typical output voltage, amplified view and output current at both the failure of such a single stage cascaded H-bridge inverter topology related to the inductive motor. Related voltages and pulses are sampled at 20 kHz, which is shown in Fig. 11.

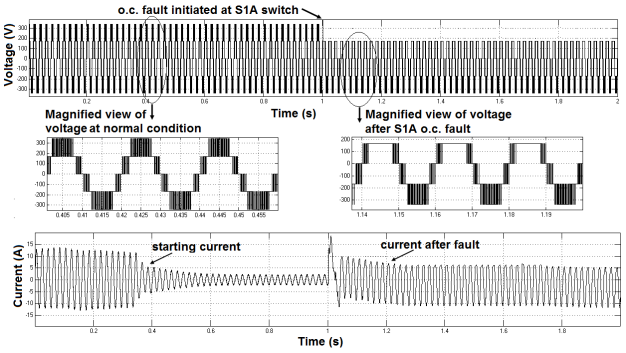

Fig. 11. Voltage and load current pattern of cascaded H-bridged inverter topology with inductive motor before and after S1A switch open circuit fault initialization

Figure 10 displays the typical output waveforms given by the normal and independent open-switch voltage fluctuations of cells A and B according to the basic requirements of the 0.85 modulation index. In the case of open switch fault waveforms, there is a fifty percent clipping at the voltage magnitude level in the positive or negative half of the time as opposed to no fault condition. Figure 11 illustrates the output voltage and current waveforms when an open circuit fault occurs in cell A's S2A switch. Visual examination of voltage and current waveforms reveals that the output voltage amplitude pattern varies significantly for each open circuit fault; however, classifying the sort of fault solely on the load current waveform is difficult. The equivalent load current waveform appears to follow a similar pattern following the onset of an open circuit fault in switches S1A and S2A, making it difficult to differentiate the problematic switch. Figure 12 shows the output voltage and load current waveforms with an induction motor load following an S2A open circuit fault. Figure 13 depicts the typical output voltage waveforms of cells A and B at 0.85 modulation index values under normal, open-switch fault circumstances, respectively. When comparing open switch fault voltage waveforms to no fault conditions, there is a fifty percent clipping in the voltage magnitude level in the positive or negative half cycle. When comparing the output voltage waveforms under open-

switch fault scenarios to the normal state, there is a significant variation in all output voltage patterns. These waveform images clearly depict the fluctuations at each problem instance, which can help to create a fault detection system that is more efficient.

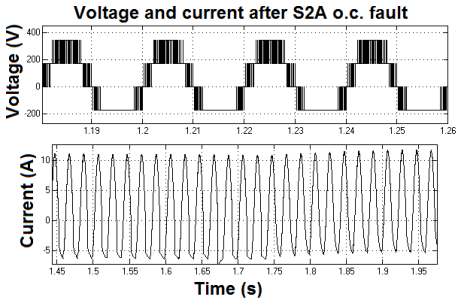

Fig. 12. Voltage and current after S2A open circuit fault

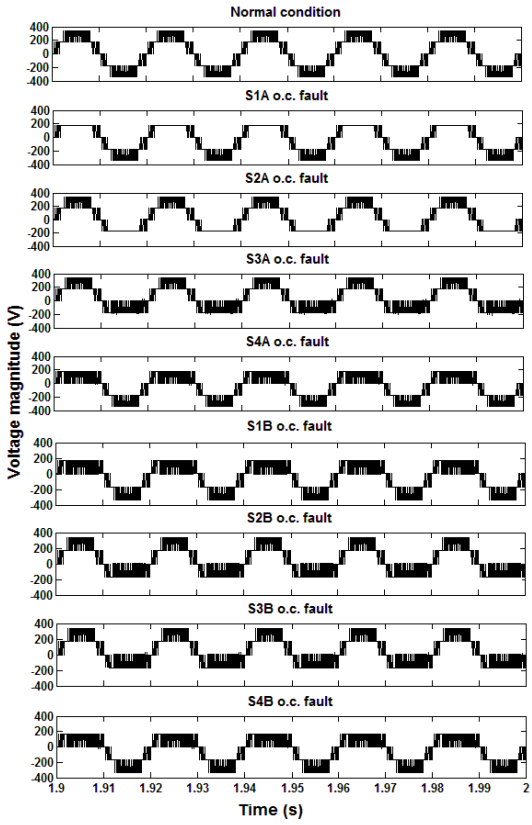

Fig. 13. Output voltage waveforms at normal condition and after open switch fault of Cell A and B

B. Short circuit fault analysis and discussion. The initial short-circuit fault is triggered by one second (1 s) of the H-bridge A S1A switch to consider the pre and post current and voltage series starting the short-circuit fault of the inverter topology. The output displays the normal output voltage and current waveform of the H-bridged multilevel cascaded single-phase inverter. The short circuit fault of S1A is generated at one second (1 s) and Fig. 14 shows the embellished current and voltage waveform and also shows the start of the fault. Figure 15 illustrates a magnified view of the output voltage and load current waveforms with an induction motor load following an S1B short circuit failure. Figure 16 shows the output voltage and load current waveforms with an induction motor load following an S1B short circuit fault. Figure 16 displays the standard output waveforms obtained under the normal and distinct short switch fault conditions of cells A and B at the 0.85 modulation index value respectively. As a consequence, there is a small decrease in the output voltage and in the positive or negative half loop in the case of short switch fault waveform generation. As a result of a detailed inspection of the output voltage waveforms, it has been a significant change in all voltage output patterns in both the open-switch and short-switch voltage fluctuations as opposed to normal conditions. These waveform diagrams explicitly display the variations for each fault situation, which would help encourage the development of a successful fault detecting system.

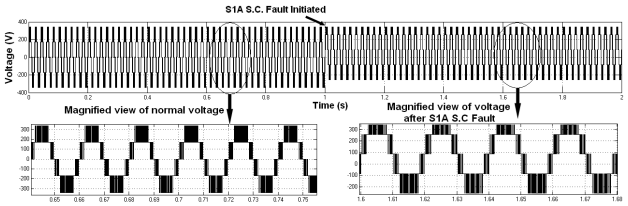

Fig. 14. Output voltage and load current waveform of MLI during short circuit condition

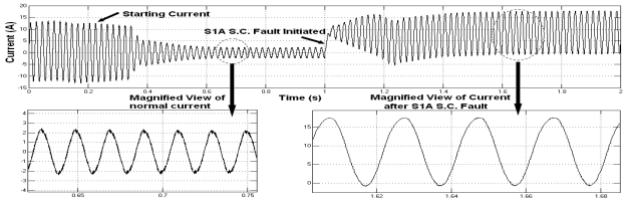

Fig. 15. Magnified view of fault analysis before and after the initiation of S1A short circuit fault with induction motor load m = 0.85. Fault initiated at 1 s

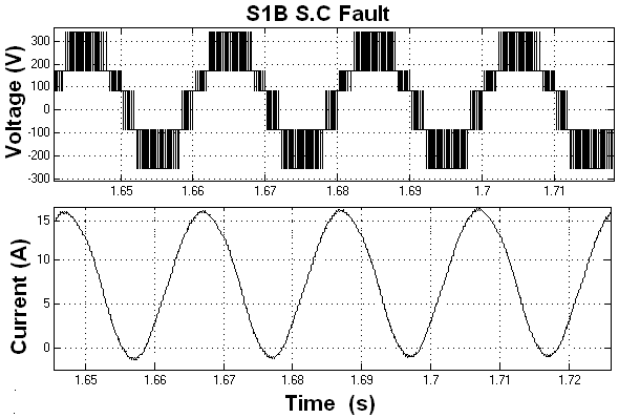

Fig. 16. Output current and voltage waveform of S1B SC fault with induction motor load for the modulation index of 0.85

Figure 15 illustrates visual examination of waveforms reveals that the output voltage pattern varies somewhat for each SC fault; however, classifying the nature of the fault solely on the load current is difficult. The load current pattern of a SC fault in S1A and S1B, for example, is identical, making it difficult to distinguish between the S1 switch faults in H-bridge A and H-bridge B. Furthermore, the type of the load and its changes affect the load current waveform. As a result, it's possible that a switch issue will be misdiagnosed. The output voltage waveform is a crucial parameter to create the fault diagnosis system since it is irrespective of load and has unique patterns for each switch problem. When a SC fault develops in cell B's S1B switch, Fig. 16 depicts the output voltage and current waveforms. Visual examination of voltage and current waveforms indicates

that the output voltage magnitude waveform for each SC fault varies greatly, however diagnosing the fault type purely based on the load current waveform is challenging. Following the commencement of a SC defect in switches S1B and S2B, the equivalent load current waveform seems to follow a similar pattern, making it difficult to differentiate the faulty switch.

Figure 17 depicts the typical output voltage waveforms of cells A and B at 0.85 modulation index values under normal, short-switch fault circumstances, respectively. When comparing short switch fault voltage waveforms to no fault conditions, there is a 50 % clipping in the voltage magnitude level in the positive or negative half cycle. When comparing the output voltage waveforms under short-switch fault scenarios to the normal state, there is a significant variation in all output voltage patterns. These waveform images clearly depict the fluctuations at each problem instance, which can help to create a fault detection system that is more efficient.

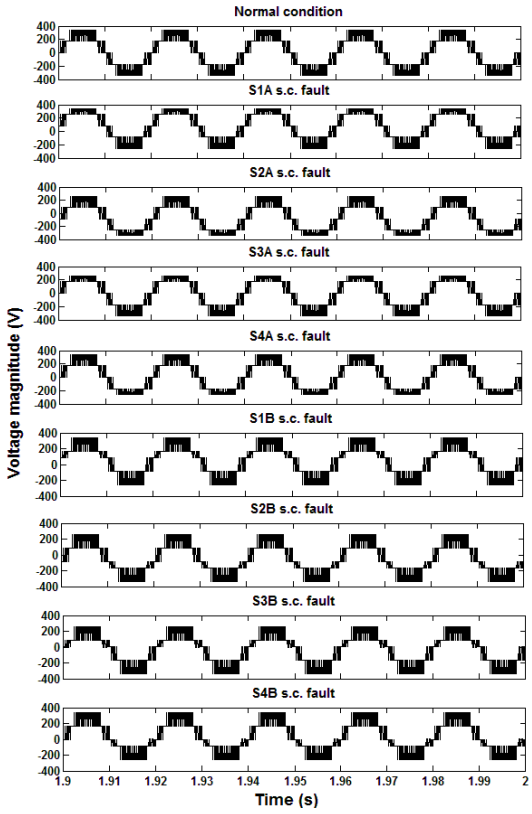

Fig. 17. Voltage output patterns in normal state as well as short circuit fault states of cells A and B

The key properties of the load voltage output waveform are explored utilising simulation under various open-switch and short-switch faulty conditions. Furthermore, major elements such as THD analysis using the FFT technique, as well as an assessment of the MSE at various numbers of hidden layer neurons, are defined to be fed to that back propagation trained ANN. In a cascaded MLI, this suggested fault detection approach could identify each individual fault switch. When compared to the load current pattern, the output voltage waveform at different fault circumstances exhibits distinct patterns, making it easier to discern the nature of the defect via visual observation. THD and harmonic/fundamental ratios up to 11th order harmonics retrieved from the FFT analysis give crucial information regarding the malfunctioning switch of the MLI. For high power applications, the number of levels of MLIs is rising day by day; the suggested system may be tested for 7 level and 9 level inverter system.

5. Conclusions. This paper examines the malfunctioning transition fault diagnosis of a single-phase H-bridged cascaded 5-level inverter topology attached to the inductive motor. Specified output voltage waveform properties are explored through simulation research in various open-switch and short-switch fault conditions. This approach focuses on the similarity of the output voltage and indeed the modulated voltage signal, as well as on the effect of the modification of the multilevel inverters on the discrepancy. Digital filters may be created and implemented in the future for real-time applications while recording the output voltage signal to remove high-frequency noise. The suggested topology is restricted to a five-level multilevel inverter, but it may be expanded to seven, nine, eleven, and more levels. As the number of switches increases, so would the need for identification to locate a faulty switch. Also, the transients detected in the current signal during the open circuit or short circuit faults of the multilevel inverter may be studied and a diagnostic procedure created using this information for 7-level and 9-level inverters.

Conflict of interest. The authors declare that they have no conflicts of interest.

REFERENCES

1. Jahan H.K., Panahandeh F., Abapour M., Tohidi S. Reconfigurable Multilevel Inverter With Fault-Tolerant Ability. *IEEE Transactions on Power Electronics*, 2018, vol. 33, no. 9, pp. 7880-7893. doi: https://doi.org/10.1109/TPEL.2017.2773611.

2. Haji-Esmaeili M.M., Naseri M., Khoun-Jahan H., Abapour M. Fault-Tolerant and Reliable Structure for a Cascaded Quasi-Z-Source DC–DC Converter. *IEEE Transactions on Power Electronics*, 2017, vol. 32, no. 8, pp. 6455-6467. doi: https://doi.org/10.1109/TPEL.2016.2621411.

3. Jalhotra M., Gautam S.P., Kumar L., Gupta S., Chander A.H. Fault Tolerance and Energy Sharing Analysis of a Single Phase Multilevel Inverter Topology. *IECON 2018 - 44th Annual Conference of the IEEE Industrial Electronics Society*, 2018, pp. 1209-1213. doi: https://doi.org/10.1109/IECON.2018.8591853.

4. Amini J., Moallem M. A Fault-Diagnosis and Fault-Tolerant Control Scheme for Flying Capacitor Multilevel Inverters. *IEEE Transactions on Industrial Electronics*, 2017, vol. 64, no. 3, pp. 1818-1826. doi: https://doi.org/10.1109/TIE.2016.2624722.

5. Babaei E., Laali S., Bayat Z. A Single-Phase Cascaded Multilevel Inverter Based on a New Basic Unit With Reduced Number of Power Switches. *IEEE Transactions on Industrial Electronics*, 2015, vol. 62, no. 2, pp. 922-929. doi: https://doi.org/10.1109/TIE.2014.2336601.

6. Praveen Kumar T., Ganapathy S., Manikandan M. Improvement of voltage stability for grid connected solar photovoltaic systems using static synchronous compensator with recurrent neural network. *Electrical Engineering & Electromechanics*, 2022, no. 2, pp. 69-77. doi: https://doi.org/10.20998/2074-272X.2022.2.10.

7. Suresh K., Parimalasundar E. A Modified Multi Level Inverter with Inverted SPWM Control. *IEEE Canadian Journal of Electrical and Computer Engineering*, 2022, vol. 45, no. 2, pp. 99-104. doi: https://doi.org/10.1109/ICJECE.2022.3150367.

8. Suresh K., Parimalasundar E. A novel dual-leg DC-DC converter for wide range DC-AC conversion. *Automatika*, 2022, vol. 63, no. 3, pp. 572-579. doi: https://doi.org/10.1080/00051144.2022.2056809.

9. Suresh K., Parimalasundar E. Design and Implementation of Universal Converter. *IEEE Canadian Journal of Electrical and*

Computer Engineering, 2022, vol. 45, no. 3, pp. 272-278. doi: https://doi.org/10.1109/ICJECE.2022.3166240.
10. Ezhilvannan P., Krishnan S. An Efficient Asymmetric Direct Current (DC) Source Configured Switched Capacitor Multi-level Inverter. *Journal Européen Des Systèmes Automatisés*, 2020, vol. 53, no. 6, pp. 853-859. doi: https://doi.org/10.18280/jesa.530611.
11. Mhiesan H., Wei Y., Siwakoti Y.P., Mantooth H.A. A Fault-Tolerant Hybrid Cascaded H-Bridge Multilevel Inverter. *IEEE Transactions on Power Electronics*, 2020, vol. 35, no. 12, pp. 12702-12715. doi: https://doi.org/10.1109/TPEL.2020.2996097.
12. Cheng Y., Dong W., Gao F., Xin G. Open-circuit fault diagnosis of traction inverter based on compressed sensing theory. *Chinese Journal of Electrical Engineering*, 2020, vol. 6, no. 1, pp. 52-60. doi: https://doi.org/10.23919/CJEE.2020.000004.
13. De Mello Oliveira A.B., Moreno R.L., Ribeiro E.R. Short-Circuit Fault Diagnosis Based on Rough Sets Theory for a Single-Phase Inverter. *IEEE Transactions on Power Electronics*, 2019, vol. 34, no. 5, pp. 4747-4764. doi: https://doi.org/10.1109/TPEL.2018.2861564.
14. Huang Z., Wang Z., Zhang H. Multiple Open-Circuit Fault Diagnosis Based on Multistate Data Processing and Subsection Fluctuation Analysis for Photovoltaic Inverter. *IEEE Transactions on Instrumentation and Measurement*, 2018, vol. 67, no. 3, pp. 516-526. doi: https://doi.org/10.1109/TIM.2017.2785078.
15. Yan H., Xu Y., Cai F., Zhang H., Zhao W., Gerada C. PWM-VSI Fault Diagnosis for a PMSM Drive Based on the Fuzzy Logic Approach. *IEEE Transactions on Power Electronics*, 2019, vol. 34, no. 1, pp. 759-768. doi: https://doi.org/10.1109/TPEL.2018.2814615.
16. Yaghoubi M., Moghani J.S., Noroozi N., Zolghadri M.R. IGBT Open-Circuit Fault Diagnosis in a Quasi-Z-Source Inverter. *IEEE Transactions on Industrial Electronics*, 2019, vol. 66, no. 4, pp. 2847-2856. doi: https://doi.org/10.1109/TIE.2018.2847709.
17. Yang S., Sun X., Ma M., Zhang X., Chang L. Fault Detection and Identification Scheme for Dual-Inverter Fed OEWIM Drive. *IEEE Transactions on Industrial Electronics*, 2020, vol. 67, no. 7, pp. 6112-6123. doi: https://doi.org/10.1109/TIE.2019.2922924.
18. Anand A., Akhil Vinayak B., Raj N., Jagadanand G., George S. A Generalized Switch Fault Diagnosis for Cascaded H-Bridge Multilevel Inverters Using Mean Voltage Prediction. *IEEE Transactions on Industry Applications*, 2020, vol. 56, no. 2, pp. 1563-1574. doi: https://doi.org/10.1109/TIA.2019.2959540.
19. Ouni S., Narimani M., Zargari N.R., Cheng Z. A New Fault-Tolerant Control Method for Cascaded H-Bridge Multilevel Inverter to Increase Maximum Output Voltage. *2019 IEEE Energy Conversion Congress and Exposition (ECCE)*, 2019, pp. 2922-2927. doi: https://doi.org/10.1109/ECCE.2019.8912282.
20. Parimalasundar E., Kumar N.M.G., Geetha P., Suresh K. Performance investigation of modular multilevel inverter topologies for photovoltaic applications with minimal switches. *Electrical Engineering & Electromechanics*, 2022, no. 6, pp. 28-34. doi: https://doi.org/10.20998/2074-272X.2022.6.05.
21. Odeh C.I., Lewicki A., Morawiec M. A Single-Carrier-Based Pulse-Width Modulation Template for Cascaded H-Bridge Multilevel Inverters. *IEEE Access*, 2021, vol. 9, pp. 42182-42191. doi: https://doi.org/10.1109/ACCESS.2021.3065743.
22. Ghosh Majumder M., Rakesh R., Gopakumar K., Umanand L., Al-Haddad K., Jarzyna W. A Fault-Tolerant Five-Level Inverter Topology with Reduced Component Count for OEIM Drives. *IEEE Journal of Emerging and Selected Topics in Power Electronics*, 2021, vol. 9, no. 1, pp. 961-969. doi: https://doi.org/10.1109/JESTPE.2020.2972056.

Received 13.05.2022
Accepted 20.08.2022
Published 06.01.2023

Ezhilvannan Parimalasundar [1], *Associate Professor*,
Ramanathan Senthil Kumar [2], *Assistant Professor,*
Vanitha Selvaraj Chandrika [3], *Professor,*
Krishnan Suresh [4], *Associate Professor*,
[1] Department of Electrical & Electronics Engineering,
Sree Vidyanikethan Engineering College,
Tirupati, AP – 517102, India,
e-mail: parimalasundar.e@vidyanikethan.edu (Corresponding Author);
[2] Department of Electrical and Electronics Engineering,
SRM Institute of Science and Technology,
Chennai, TN – 603203, India,
e-mail: rskrren@gmail.com
[3] Department of Electrical and Electronics Engineering,
KPR Institute of Engineering and Technology,
Coimbatore, TN – 641407, India,
e-mail: mailchandrika@gmail.com
[4] Department of Electrical and Electronics Engineering,
Christ (Deemed to be University), Bangalore, India,
e-mail: sureshk340@gmail.com

How to cite this article:
Parimalasundar E., Senthil Kumar R., Chandrika V.S., Suresh K. Fault diagnosis in a five-level multilevel inverter using an artificial neural network approach. *Electrical Engineering & Electromechanics*, 2023, no. 1, pp. 31-39. doi: https://doi.org/10.20998/2074-272X.2023.1.05

UDC 621.3.022: 621.396.6: 533.93 https://doi.org/10.20998/2074-272X.2023.1.06

M.I. Baranov, S.G. Buriakovskyi, V.V. Kniaziev

A calculation of basic thermophysical, gasodynamic and electropower parameters of electric explosion in the gas environment of a metallic conductor

Goal. *Obtainingand analysis of close analyticalrelationships for the engineering calculation of maximal temperature T_m and pressure P_m in a plasma channel, time t_{ex} of explosion of conductor, active resistance R_c and specific conductivity γ_p of plasma channel, thermal energy entered in conductor W_i and dissipated in the channel W_c and high speed of v_{mw} distribution of shock acoustic wave in the plasma products of electric explosion (EE) in gas of conductor under the action of large puls current (LPC).* ***Methodology.*** *Basis of thermophysics, thermodynamics, theoretical and applied electrical engineering, electrophysics based ontechnique of high-voltage and high pulse currents, basis of high-current electronics, theory of explosion and plasma, measuring technique and electromagnetic compatibility.* ***Results*** *. Close formulas are obtained for the analytical calculation of temperature T_m and pressures P_m in a plasma channel, time t_{ex} of explosion of conductor, active resistance R_c and specific conductivity γ_p of plasma channel, thermal energy entered in conductor W_i and dissipated e in the channel W_c speed v_{mw} of shock acoustic wave in «metallic plasma» at EE in gas of conductor, testing action of LPC in the discharge circuit of high-voltage generator of pulse currents (GPC) with the dissipated energy W_0. It isdemonstrated that at EE in atmospheric air of copper conductor of 110 mm length and radiusof 0.1 mm in the discharge circuit of GPC of the microsecond temporal range ($I_{mc}\approx-190$ кА; $t_{mc}\approx42$ μs; $\omega_c\approx26.18\cdot10^3$ s^{-1}; $W_0\approx121.4$ кJ) levels of temperature T_m, to time of t_{ex} explosion, pressures P_m and speeds ov_{mw} in the area of his explosion can get numeral values: $T_m\approx121.6\cdot10^3$ K, $t_{ex}\approx3.32$ μs; $P_m\approx14.19\cdot10^9$ Pa and $v_{mw}\approx4693$ m/s. The ways of receipt are formulated in the discharge circuit of PIC of «record» (most) values of temperature T_m, pressures P_m and speeds v_{mw}. It is shown that at EE in atmospheric air of the indicated short thin copper conductor the coefficient of the useful use η_c of electric energy W_0 of capacitor battery of GPC arrives at the numeral value of $\eta_c\approx(W_i+W_c)/W_0\approx0.326$ (32.6 %). Arising up in the plasma channel of discharge, initiated EE in gas of conductor, temperature T_m and pressure P_m, time t_{ex} of explosion of conductor, specific conductivity γ_p of channel, thermal energy W_c and speed v_{mw} of shock acoustic wave dissipated in a channel in «metallic plasma» can be certain experimental by a way on results decoding of oscillograms of discharge current $i_c(t)$ and high-voltage of $u_c(t)$ on conductor in the circuit of GPC. A formula is resulted for the close calculation of critical integral of current J_k at EE in gas of conductor from different metals. Executed on powerful GPC high-current experiments were confirmed by substantive provisions offered approach near the analytical calculation of basic parameters of electro-explosive process for the probed conductor.* ***Originality.*** *Offered the engineeringapproach is scientifically grounded for the analytical calculation of the indicated thermophysical, gasodynamic and electroenergy parameters T_m, P_m, t_{ex}, R_c, γ_p, W_i, W_c and v_{mw} at EE in gas of metallic conductor, connected to the discharge circuit of GPC.* ***Practical value.*** *Application in electrophysics practice of the offered engineering approach for calculation in the ciccuit of GPC of basic parameters of electro-explosive process will allow to facilitate labour of workers of scientific laboratories and promote efficiency of work of technicians and engineers during practical realization by them of different electro-explosive technologies.* References 41, tables 1, figures 2.

Key words: **high pulse current, electric explosion of conductor, temperature, pressure, time and energy of explosion, active resistance and specific conductivity of plasma channel, energy entered in conductor and dissipated in plasma channel, speed of shock wave at the explosion of conductor.**

Надані результати інженерного розрахунку температури T_m і тиску P_m в плазмовому каналі, часу t_{ex} вибуху провідника, активного опору R_c і питомої електропровідності γ_p плазми каналу, теплової енергії, що вводиться в провідник W_i та виділяється в каналі W_c, і швидкості v_{mw} розповсюдження ударної акустичної хвилі в «металевій плазмі», що утворюється при електричному вибуху (ЕВ) в газовому середовищі металевого провідника під дією великого імпульсного струму. Показано, що при ЕВ в атмосферному повітрі короткого тонкого мідного провідника в розрядному колі високовольтного генератора імпульсних струмів (ГІС) мікросекундного часового діапазону рівні температури T_m, тиску P_m і швидкості v_{mw} в зоні його вибуху можуть досягати чисельних значень $T_m\approx121{,}6\cdot10^3$ К, $P_m\approx14{,}19\cdot10^9$ Па і $v_{mw}\approx4693$ м/с. Сформульовані електротехнічні шляхи отримання в розрядному колі ГІС з металевим провідником, який вибухає у газовому середовищі, найбільших значень температури T_m, тиску P_m і швидкості v_{mw}. Бібл. 41, табл. 1, рис. 2.

Ключові слова: **великий імпульсний струм, електричний вибух провідника, температура, тиск, час та енергія вибуху, активний опір і питома електропровідність плазмового каналу, енергія, що вводиться в провідник та виділяється в плазмовому каналі, швидкість ударної хвилі при вибуху провідника.**

State and relevance of the problem. Electric explosion (EE) of metal conductors with cross-section S_0 and length l_0 in vacuum, gas and liquid media under the action of high pulse current (HPC) flowing through them of various amplitude-temporal parameters (ATP) has found quite wide practical application both in *scientific* (for example, in the study of the mechanisms of phase transitions of matter [1–5], the phenomena of mass, momentum and energy transfer in extreme conditions, including in the critical modes of nuclear explosions [6, 7], the production of soft X-ray radiation for controlled thermonuclear fusion [8], research of the processes of optical pumping of gas lasers and active media for quantum generators based on metal vapors [9], etc.), as well as *technological* ones (for example, when sputtering thin coatings for microelectronics [10, 11], obtaining highly dispersed conductive powders [12–16], creation fast-acting electric explosive circuit breakers for high-current circuits of high-voltage generators with powerful capacitors and inductive energy storage [17], production of dense high-temperature plasma [18], high-speed power processing and deformation by shock loads of various materials (parts) [19, 20], conducting certification tests of aviation and rocket-space equipment for electromagnetic compatibility and resistance to effects of lightning (first of all, in electrical circuits for introducing current and electromagnetic energy into

objects under test) [21, 22], etc.) purposes. When studying the complex process of EE of metal conductors and the practical implementation of electro-explosive technologies, specialists in the course of their work use both more accurate computational numerical methods of studying the phenomenon of EE of metal conductors in gases and liquids [4, 5, 7, 8] and less accurate engineering analytical methods and models for calculating thermophysical, gas-, electric-, and magnetohydrodynamic processes in continuous media during the occurrence of the specified electrophysical phenomenon [9–15, 23–26]. Here, the known calculation methods and the approximate calculation expressions obtained with their help for the analytical study of the indicated phenomenon of EE of a metal conductor have a significant general drawback: they do not allow providing a comprehensive approach to the simultaneous calculation of the main thermophysical, gas-dynamic, and electrical-power parameters of the EE process of a conductor.

In addition, when establishing the necessary modes of operation of the high-voltage pulse technology (HPT) used in electro-explosive technologies and predicting the effects of the electrophysical effects created by EE of conductors on the processed materials, parts and objects, the engineering and technical personnel needs simplified and convenient in practical application approximate analytical relationships for the calculated assessment of the discharge of powerful capacitive energy storage devices of HPT in the EE of conductors and the plasma channel initiated by it: the maximum levels of temperature T_m, pressure P_m, time t_{ex} of the explosion, active resistance R_c and specific electrical conductivity γ_p of the plasma channel, energy W_i introduced into conductor, and energy W_c released in the plasma channel and the speed v_{mw} of the shock wave in the plasma products of the discharge channel in the gas (liquid). In this regard, obtaining approximate analytical ratios for the engineering complex calculation of the specified parameters T_m, P_m, t_{ex}, R_c, γ_p, W_i, W_c and v_{mw}, characteristic of EE of metallic conductors, is an actual applied scientific and technical problem in the world.

The goal of the paper is to obtain and analyze approximate analytical relationships for the engineering complex calculation of the maximum values of temperature T_m and pressure P_m in the plasma channel, time t_{ex} of the conductor explosion, active resistance R_c and specific electrical conductivity γ_p of the plasma channel, energy W_i introduced into the conductor, and thermal energy W_c released in the plasma channel and the maximum velocity v_{mw} of propagation of the shock acoustic wave in plasma products of EE in the conductor gas under the influence of HPC.

1. Problem deinition. Consider a thin metallic conductor of cylindrical shape located in a gaseous environment under normal atmospheric conditions, along which in its longitudinal direction from a high-voltage pulsed energy source (for example, from a powerful low-inductance capacitor battery) a HPC flows with ATP sufficient to reach in the conductive structure of the conductor with length l_0 and radius r_0 with cross-section $S_0=\pi r_0^2$ the numerical value of the current integral J_k, which is critical for the conductor under study. By the current integral J_k we will understand the well-known integral involving the square of the current density, which is determined by the expression accepted in the works [3, 24, 27] in time t: $J_k = \int_0^{t_{ex}} \delta_k^2(t)dt$, where $\delta_k(t)$ is the critical pulse current density in the conductor that causes sublimation of the metal and overheating of his steam; t_{ex} is the time of onset of EE and the beginning of the spatial spread of the sublimated metal of the conductor and its vapor.

Let us dwell on the use of low-impedance generators of pulse currents (GPC) for EE of the investigated conductor, whose ATP of the discharge current $i_c(t)$ changes in time t according to the law of a decaying sinusoid [9, 10, 19]. We believe that the pulse current density $\delta_k(t)$ is characterized by an almost uniform distribution over the cross-section S_0 of the accepted thin conductor, because for it the thickness of the current skin layer can significantly exceed its radius r_0. We assume that in the pre-explosion state of the sublimated body of a thin conductor, its maximum values of temperature T_m and pressure P_m are uniformly distributed over the cross section of the formed dense «metal plasma» [9, 10], which is located before its high-speed expansion (flight) within the critical section $S_{0c}>S_0$ [20]. We believe that the specified «metal plasma» of the conductor is, in the first approximation, a superheated metal vapor, which refers to highly unsaturated vapors (real gases) with temperature T_m much higher than its boiling point at temperature T_b and high pressure P_m. In this connection, the gas laws known in classical physics can be applied to the «metal plasma» formed after the sublimation of the metal with its highly superheated vapor and their subsequent high-speed expansion (expansion at EE) in the surrounding gas in the considered approximation [28]. We believe that the maximum temperature T_m in the indicated equilibrium «metal plasma», for which the electron temperature practically does not differ from the temperature of its ions and atoms, is determined by the electron temperature, which depends on the amplitude of the longitudinal heat flux density g_m in the cross-section S_0 of the conductor. In the analyzed case, g_m will be determined by the amplitude δ_{mc} of the current density in the conductor and the near-electrode voltage drop U_e in the edge zones of the sublimated body of the conductor [24]. The gas surrounding the investigated conductor with the initial temperature T_a of its material, as well as the «metallic plasma» formed during the EE of its strongly overheated body, are taken as ideal gas environments that correspond to the classical concept of «ideal gas» [10, 28].

Taking into account the normal atmospheric conditions before the EE of the conductor under study, one can use the following basic characteristics of the surrounding source gas medium for the conductor [28]: the gas pressure is $P_a\approx1.013\cdot10^5$ Pa; absolute gas temperature is $T_a\approx273.15$ K; the molar volume of the gas is $V_{Ma}\approx22.41\cdot10^{-3}$ m^3/mol. Taking into account the rapid explosive nature of the thermophysical and gas-dynamic processes occurring during EE of the metal of the conductor (when their duration in time t is up to 0.5 ms

[10]), and the insignificant removal of heat from the EE zone to the radial expansion of the «metal plasma» of the conductor under study [9] we will limit ourselves to the consideration of the flow in the conditions of almost complete thermal insulation of the conductor of the adiabatic process in the local zone around the exploding conductor, with the HPC flowing along it, in which case heat exchange processes between the conductor under study and the gas will not occur in the volume of EE occupied by the cylindrical zone, which surrounds it.

It is necessary, under the assumed assumptions, to obtain calculated relations for estimating the temperature T_m and pressure P_m in the plasma, the time t_{ex} of the conductor explosion, the active resistance R_c and the specific electrical conductivity γ_p of the plasma channel, the energy W_i introduced into the conductor, and the energy W_c released in plasma channel, and the velocity v_{mw} of shock wave propagation in the plasma products of EE of the conductor metal in the gas medium under the influence of HPC.

2. Approximate calculation of the maximum temperature T_m in the plasma channel of the discharge at the gas EE of the conductor. For the engineering calculation of the maximum temperature T_m in the «metal plasma» at EE in the gas environment of the investigated metal conductor with a cross-section S_0 under the action of HPC flowing through it, the following thermophysical relationship can be used [24]:

$$T_m \approx \left[\pi\sigma_c^{-1}U_e(2J_kS_0^{-1} \mid I_{mc} \mid \omega_c)^{1/3}\right]^{1/4}, \qquad (1)$$

where σ_c=5.67·10^{-8} W·(m^2·K^4)$^{-1}$ is the Stefan-Boltzmann constant [28]; U_e is the near-electrode voltage drop in the edge zones of the sublimated conductor, which numerically does not exceed 10 V for base metals used in HPC technology [29]; I_{mc} is the first amplitude of the discharge current $i_c(t)$ in the electrical circuit of the HPC generator, which changes in time t with the circular frequency ω_c and is determined by the electrical parameters of the discharge circuit of the generator; J_k is the critical value of the current integral for a conductor metal with cross-section S_0 [27].

Calculation estimation based on (1) of the value of the highest temperature T_m in the «metal plasma» at EE in air of a short thin copper conductor (l_0 ≈ 110 mm; r_0 ≈ 0.1 mm; S_0 ≈ 3.14·10^{-8} m^2; U_e ≈ 10 V [29]; J_k ≈ 1.95·10^{17} A^2·s·m^{-4} [27]) under the influence of HPC of the microsecond time range (I_{mc}≈−190 kA; ω_c≈26.18·10^3 s^{-1}), experimentally obtained in the conditions of a high-voltage electrophysical laboratory using a GPC with capacitance of C_0≈333 μF and electric energy W_0≈121.4 kJ stored in its powerful capacitor battery (at its charging voltage U_{c0}≈−27 kV) [30] shows that the temperature in this case, it will be approximately equal to T_m ≈121.6·10^3 K. It should be noted that verification by the authors of this temperature by other methods (for example, with the help of appropriate experimental devices) is currently impossible in the conditions of a high-voltage electrophysical laboratory. Let us point out that in [18] at EE in a vacuum of a short thin lithium conductor (l_0 ≈ 10 mm; r_0 ≈ 63.5 μm; S_0≈1.27·10^{-8} m^2; J_k≈0.61·10^{17} A^2·s·m^{-4} [31]; U_e≈5 V [29]), which is connected in the discharge circuit of a high-voltage GPC (I_{mc}≈−45 kA; ω_c≈1.25·10^6 s^{-1}) with nominal electrical energy W_0≈100 kJ, which is stored in its capacitor bank, the maximum temperature T_m ≈113.5·10^3 K was experimentally recorded in the plasma products of EE of this conductor with GPC of the microsecond time range with high frequency of oscillation. The use of (1) to estimate the temperature level T_m in the test case specified in [18] indicates that the numerical value of the temperature will be equal to T_m ≈122.4·10^3 K. As we can see, the approximate results of the numerical calculation by (1) of the maximum temperature T_m in the «metal plasma» during EE of the specified lithium conductor indicate that the calculated data indicated above agree well with the experimental data that were given in [18] and obtained by other EE research methods.

It is interesting to note the fact that during our experimental study [30] of EE in atmospheric air of a thin round copper conductor (l_0≈110 mm; r_0≈0.1 mm), it reached the amplitude of the critical pulse current density δ_{mk}, which is calculated by the following approximate expression:

$$\delta_{mk} \approx (2J_kS_0^{-1} \mid I_{mc} \mid \omega_c)^{1/3}. \qquad (2)$$

From (2) at I_{mc}≈−190·10^3 A and ω_c≈26.18·10^3 s^{-1} [30] for the considered thin copper conductor (l_0 ≈ 110 mm; r_0 ≈ 0.1 mm; S_0 ≈ 3.14·10^{-8} m^2; J_k ≈ 1.95·10^{17} A^2·s·m^{-4} [27]) we find that the amplitude of the critical density δ_{mk} of the sinusoidal current in it will take a numerical value of about δ_{mk} ≈3.95·10^{11} A/m^2. According to the data of the magnetohydrodynamic calculation of EE from [32, 33], this level of current density δ_{mk} will correspond to the high-temperature mode of flow of EE of the conductor.

Calculation data obtained in [32] on the basis of numerical magnetohydrodynamic modeling of the electroexplosive process for metal in vacuum (water) indicate that at high-temperature EE of an aluminum conductor (r_0≈0.1 mm; S_0≈3.14·10^{-2} mm^2; δ_{mk}≈10^{12} A/m^2) regardless of the properties of the environment in which its explosion occurs, the temperature of the «metallic plasma» formed from it reaches a level of up to 8 eV, which corresponds to an absolute temperature of 92.8·10^3 K [27]. The calculated estimation according to the proposed formula (1) for the maximum temperature T_m of the created plasma in the air discharge channel of a powerful high-voltage GPC (I_{mc} ≈ −190 kA; ω_c≈26.18·10^3 s^{-1}) at EE of the specified aluminum conductor (U_e≈8 V [29]; J_k≈0.82·10^{17} A^2·s·m^{-4} [31]) shows that in this case T_m≈107,1·10^3 K. This calculated level of the temperature T_m of the «metal plasma» from that specified in [32] (T_m ≈92.8·10^3 K) differs by almost 13 %. Of course, such a comparison is not entirely correct (here, the initial data for EE were taken by us from different studies). It should not be forgotten that there are very few relevant research results for T_m in the field of EE of conductors. Despite this, for the case under consideration, we can say that formula (1) for T_m works.

It follows from (1) that in order to achieve «record» (highest) levels of absolute temperature T_m in the local zone of EE in a gas environment (vacuum) during the explosion under study, it is necessary to use extremely

thin conductors with the maximum possible value of the critical current integral J_k for them, as well as to use «fast» GPC generators, which are capable of forming on the exploding conductor the maximum possible amplitudes I_{mc} of the first half-waves of the GPC discharge current of nanosecond duration.

Let us point out that experimental numerical values of the critical current integral J_k were given in [27] only for aluminum and copper conductors. Of undoubted practical interest are the calculated data for the current integral J_k for other conductive materials used in HPT and HPC technology for EE of thin metals, when the critical density δ_k of current $i_c(t)$ in them is at least 10^{11} A/m^2.

3. Approximate calculation of the critical current integral J_k at the gas EE of the conductor. Calculation of the numerical value of the critical current integral J_k at EE in the gas of the thin conductor under study can be performed according to the formula [31]:

$$J_k \approx \gamma_{cb} N_0 W_f , \qquad (3)$$

where γ_{cb} is the specific electrical conductivity of the conductor metal at its boiling temperature T_b (during its sublimation) $(\Omega\cdot\text{m})^{-1}$; N_0 is the concentration (density) of atoms (positive ions) in the crystal lattice of the metal of the conductor before the action of HPC on it (m^{-3}); W_f is the thermodynamic work of the release of free electrons from the metal of the conductor before the flow of HPC begins (J).

Equation (3) is based on the results of a theoretical study by the authors of the phenomenon of anomalous thermoelectronic emission of free electrons from the material of the conductor, which during EE is destroyed and loses its metallic conductivity under the action of HPC in the high-current discharge circuit of a powerful high-voltage GPC [31].

Let us point out that the value of γ_{cb} for the main conductor materials can be determined according to the experimentally obtained empirical relations for them given in [34]. The numerical value of the initial concentration (density) of atoms N_0 in the electrically explosive solid metal of the conductor under study with its initial density d_c can be found using the following formula [28]:

$$N_0 = d_c (M_{a0} \cdot 1{,}6606 \cdot 10^{-27})^{-1} , \qquad (4)$$

where M_{a0} is the atomic mass of the metal of the conductor of the density d_c.

The value of the thermodynamic work of output W_f of free electrons from the metal in (3) can be found from [35], where experimental emission data for most metals used in experimental physics, high-current HPT, and HPC technology were given.

Table 1 summarizes the numerical values of the parameters γ_{cb}, N_0, W_f and J_k determined according to (3), (4) taking into account [28, 34–36] for a number of metals used in the study of EE of thin conductors in gaseous media and in the circuits of electrotechnical devices of electroexplosive technologies [9, 10, 20]. From the data in Table 1, it can be seen that the approximate calculated value of the critical current integral J_k for a thin copper conductor ($J_k \approx 1.71\cdot10^{17}$ A$^2\cdot$s$\cdot$m^{-4}) obtained under the accepted assumptions and normal atmospheric conditions according to (3) is approximately 12 % less than its corresponding experimental value in air ($J_k \approx 1.95\cdot10^{17}$ A$^2\cdot$s$\cdot$m^{-4}) at room temperature ($T_a \approx 293.15$ K) [27]. One of the reasons for this may be that the calculated relation (3) does not take into account the influence on the specified thermophysical parameters γ_{cb}, N_0 and W_f of the rapid overheating of the sublimated metal of the conductor (its vapor), which accompanies the high-temperature EE mode in the gas of the conductor placed in the circuit of a powerful high-voltage GPC.

Table 1

Numerical values of parameters γ_{cb}, N_0, W_f, J_k [27, 31, 34, 35]

Metal	Parameter values				
	γ_{cb}, 10^6 $(\Omega\cdot\text{m})^{-1}$ (by [34])	N_0, 10^{28} m^{-3} (by (4))	W_f, 10^{-19} J (by [35])	J_k, 10^{17} A$^2\cdot$ s$\cdot$m^{-4} (by (3))	J_k, 10^{17} A$^2\cdot$ s$\cdot$m^{-4} (by [27])
Copper	2,87	8,43	7,05	1,71	1,95
Aluminum	1,99	6,05	6,81	0,82	1,09
Nickel	0,97	9,10	7,21	0,63	–
Molybdenum	0,65	6,40	6,89	0,28	–
Tungsten	0,50	6,26	7,27	0,23	–

On the other hand, the experimental methods of quantitative determination of the value of the integral J_k are also not without shortcomings and the errors introduced by them in the determination of J_k [32]. The parameters N_0 and W_f in (3) clearly do not depend on the value of γ_{cb}. Therefore, the calculated data of Table 1 for γ_{cb} and J_k clearly demonstrate to us that the smaller the value of the specific electrical conductivity γ_{cb} (the greater the specific electrical resistance of the conductor material) used for EE in the metal in the gas, the smaller the value of the critical current integral J_k necessary for the occurrence of this electrophysical phenomenon will be and accordingly, based on the numerical magnetohydrodynamic model of EE in vacuum (water) of a thin aluminum conductor investigated in [32], the integral of the specific action $h(t)$ of the GPC pulse discharge current with its density $\delta_k(t)$ in this conductor. This, taking into account the theoretical results of works [5, 32], indicates the possibility of using formula (3) for the integral J_k.

4. Approximate calculation of the time t_{ex} of thermal explosion of theconductor in the gas. The calculation estimation of the time t_{ex} of EE in the gas of the investigated metal conductor, which corresponds to the moment of its maximum resistance and peak-like increase in the electric voltage $u_c(t)$, can be carried out according to the expression [30]:

$$t_{ex} \approx 4\left[(2J_k S_0^2)/(\omega_c^2 \mid I_{mc} \mid^2)\right]^{1/3} / 3 . \qquad (5)$$

From (5) for a thin round copper conductor ($l_0 \approx 110$ mm; $r_0 \approx 0.1$ mm; $S_0 \approx 3.14\cdot10^{-8}$ m^2; $J_k \approx 1.95\cdot10^{17}$ A$^2\cdot$s$\cdot$m^{-4} [27]) with the HPC parameters used by us in the discharge circuit of a powerful GPC ($I_{mc} \approx -190$ kA; $\omega_c \approx 26.18\cdot10^3$ s^{-1}), we obtain that $t_{ex} \approx 3.32$ μs. Based on (5), for a given conductor material (a given numerical value of the critical integral J_k), to decrease (increase) the t_{ex} parameter, it is necessary to: decrease (increase) the section S_0 of the conductor and increase (decrease) the circular frequency ω_c of oscillations and the first amplitude I_{mc} of the discharge current in the GPC circuit.

5. Approximate calculation of the maximum pressure P_m in the plasma channel of the discharge at the gas EE of the conductor. Using the well-known equation of state of an ideal gas [28], taking into account the accepted assumptions in a rough approximation that does not take into account the pressure of electrons, for the maximum pressure P_m in the cylindrical zone of the «metal plasma» at EE in the gas environment of a thin metal conductor, we have:

$$P_m \approx \rho_p R_m M_p^{-1} T_m , \quad (6)$$

where R_m =8.314 J/(mol·K) is the universal gas constant [28]; M_p is the molar mass (in kg/mol) of superheated metal vapor with density ρ_p, which occurs before its radial expansion within the critical section $S_{0c}\approx 10S_0$ of the sublimated body of the conductor under study with the initial density d_c of its solid metal.

For the case under consideration, $\rho_p\approx 0.1 d_c$ [20, 23]. Then, taking into account (1) and (6), for the pressure amplitude P_m in the plasma cylindrical channel, which is initiated by EE in the conductor gas, in the final form we obtain the following approximate calculation ratio:

$$P_m \approx 0{,}1 d_c R_m M_p^{-1}\left[\pi\sigma_c^{-1} U_e (2J_k S_0^{-1} \mid I_{mc} \mid \omega_c)^{1/3}\right]^{1/4} . \quad (7)$$

Note that expression (7) corresponds to the approximate calculation model of EE of a metal conductor in gas under conditions where the «metal plasma» within the section of the conductor S_{0c} can be considered as an ideal gas.

From (7) at EE in a gas (for example, in air) of a thin copper conductor ($S_0\approx 3.14\cdot 10^{-8}$ m^2; $d_c\approx 8920$ kg/m^3 [28]; $M_p\approx 63.55\cdot 10^{-3}$ kg/mol [28]; R_m=8.314 J/(mol·K) [28]; $U_e\approx 10$ V [29]; $J_k\approx 1.95\cdot 10^{17}$ A^2·s·m^{-4} [27]), connected in a high-current discharge circuit of the indicated high-voltage GPC ($I_{mc}\approx -190$ kA; $\omega_c\approx 26.18\cdot 10^3$ s^{-1} [30]), we find that the maximum gas-dynamic pressure P_m arising in the local zone of its explosion in the «metal plasma» will be equal to $P_m \approx 14.19\cdot 10^9$ Pa (up to $14\cdot 10^4$ atm [28]). This calculated result for P_m indicates that with EE in the gas environment of thin metal conductors, gas-dynamic pressure of large values can arise in their cross-section S_0. It can be seen from (6), (7) that the pressure value P_m is directly proportional to the temperature level T_m, which is reached in the EE zone of the conductor, and practically does not depend on the parameters of the gas environment in which the EE of the investigated metal conductor takes place. In this regard, in order to achieve «record» (highest) levels of maximum pressure P_m in «metal plasma» at EE in the gas of a thin metal conductor, it is necessary to ensure that the maximum temperature T_m of this plasma is obtained in the zone of this explosion. For this, it is necessary to use the smallest cross-sections S_0 of short metal conductors, as well as «fast» HPC generators, which reproduce in GPC circuits the largest amplitudes I_{mc} and circular frequencies ω_c of their discharge current $i_c(t)$.

6. Approximate calculation of the sublimation energy W_s of the metal at the gas EE of the conductor. The sublimation energy W_s of the conductor substance will be equal to the sum of the energies of its heating Q_{h1} from the initial temperature T_a to the melting temperature T_w, heating Q_{h2} from the melting temperature T_w to the boiling temperature T_b, melting Q_f and vaporization Q_v [28]. For the heating energy Q_{h1}, the formula will be valid:

$$Q_{h1} \approx c_h m_c (T_w - T_a) , \quad (8)$$

where c_h is the specific heat capacity (at constant volume) of the material of the investigated metal conductor of the initial mass $m_c=l_0 S_0 d_c$ [28].

We have the following expression for the heating energy Q_{h2}:

$$Q_{h2} \approx c_h m_c (T_b - T_w) . \quad (9)$$

For the heat of melting of the metal of the conductor Q_f, the following relation will be valid [28]:

$$Q_f = q_f m_c , \quad (10)$$

where q_f is the the specific heat of melting of the material of the cylindrical conductor with its initial absolute temperature $T_a\approx 273.15$ K and the mass $m_c=l_0 S_0 d_c$.

For the heat of vaporization Q_v of the metal of the conductor under study, the expression can be written [28]:

$$Q_v = q_v m_c , \quad (11)$$

where q_v is the specific heat of vaporization of the material of a cylindrical conductor of the mass $m_c=l_0 S_0 d_c$ at its initial absolute temperature $T_a\approx 273.15$ K.

From (8)–(11) for the analyzed short thin cylindrical copper conductor ($l_0 \approx 110$ mm; $r_0 \approx 0.1$ mm; $S_0 \approx 3.14\cdot 10^{-8}$ m^2; $d_c\approx 8920$ kg/m^3; $m_c\approx 0.308\cdot 10^{-4}$ kg; $T_a \approx 273.15$ K; $T_w \approx 1356.15$ K; $T_b \approx 2863.15$ K; $c_h \approx 385$ J/(kg·K); $q_f\approx 2.05\cdot 10^5$ J/kg; $q_v\approx 4.79\cdot 10^6$ J/kg [28]), later used when we conducted high-current experiments ($I_{mc}\approx -190$ kA; $\omega_c\approx 26.18\cdot 10^3$ s^{-1} [30]) on a powerful high-voltage GPC according to its air EE, we find that $W_s \approx (Q_{h1} + Q_{h2} + Q_f + Q_v) \approx 197.4$ J. Note that according to experimental data from [9, 37], the specific sublimation energy q_s for copper is numerically equal to approximately $q_s \approx 4.68\cdot 10^{10}$ J/m^3. In this regard, the refined value of the sublimation energy W_s for the thin copper conductor ($V_0\approx l_0 S_0\approx 34.5\cdot 10^{-10}$ m^3) will be equal to about $W_s\approx 161.5$ J. It can be seen that the calculated and experimental values for the sublimation energy W_s of the indicated copper conductor under study ($l_0\approx 110$ mm; $r_0\approx 0.1$ mm) differ from each other with an error of no more than 18 %. Therefore, we can say that the calculated estimation of the sublimation energy W_s of the copper conductor metal is valid.

7. Approximate calculation of the overheating energy W_{sh} of the sublimated metal at the gas EV of the conductor. The energy of strong overheating W_{sh} of the metal vapor in the discharge plasma channel, which was formed from the sublimated one by discharge current $i_c(t)$, which flows through the conductor in the GPC circuit, its metal and is part of the «metal plasma» of this cylindrical channel, can be estimated by the following expression:

$$W_{sh} \approx (T_m - T_b) c_{vs} m_c , \quad (12)$$

where c_{vs} is the specific heat capacity (at constant volume) of the metal vapor of the sublimated body of the conductor with mass equal to the initial mass $m_c=l_0 S_0 d_c$ of the metal conductor exploding in a gas environment.

From (12) taking into account the accepted assumptions for the investigated thin copper cylindrical conductor ($l_0\approx 110$ mm; $r_0\approx 0.1$ mm; $S_0\approx 3.14\cdot 10^{-8}$ m^2;

d_c≈8920 kg/m^3; m_c≈0.308·10^{-4} kg; T_b≈2863.15 K; c_{vs}≈0.385·10^3 J/(kg·K) [28]; J_k≈1.95·10^{17} A^2·s·m^{-4} [27]; U_e≈10 V [29]) at high-current discharge on the conductor of a powerful high-voltage GPC (I_{mc}≈−190 kA; ω_c≈26.18·10^3 s^{-1}; T_m≈121.6·10^3 K [30]), which explodes electrically in air, we obtain that the sought overheating energy W_{sh} will take a numerical value of about W_{sh} ≈1407.9 J. As can be seen, the calculated value of the overheating energy W_{sh} of the sublimated conductor metal and, accordingly, the metal vapor formed from it, is approximately seven times greater than the calculated sublimation energy W_s≈197 .4 J of copper conductor metal: W_{sh}/W_s≈7.1. According to the theoretical data from [32], obtained on the basis of a complex numerical magnetohydrodynamic model of EE of the metal with current, this indicator for high-temperature EE (T_m≈92.8·10^3 K; δ_{mk}≈10^{12} A/m^2) in vacuum (water) of thin aluminum of the conductor is also approximately W_{sh}/W_s≈7 (without taking into account the energy released during EE, which is introduced into the metal structure of this conductor). In this regard, the approximate results of the estimated energy W_{sh} given by us are valid.

8. Approximate calculation of the energy of the thermal explosion W_{ex} in the gas of the superheated vapor of the metal conductor. Taking into account the accepted assumptions, in the approximate calculation of the energy of the thermal explosion W_{ex} in the gas medium of the highly superheated metal vapor of the metal conductor under study, we use the formulas known in thermodynamics for the work done by the gas during its adiabatic expansion [28]. Using the mode of adiabatic expansion of a highly superheated metal vapor with a gas-dynamic pressure P_m of a sublimated body of a metal conductor with mass of m_c≈$l_0S_0d_c$, in the considered approximation for the work W_{ex} produced by this vapor and, accordingly, the thermal energy released in the surrounding gas by the «metal plasma» that rapidly expands around the conductor in a gaseous medium, the following gas-dynamic relation can be written [28]:

$$W_{ex} \approx l_0 S_0 d_c R_m (M_a + M_p)^{-1} (T_m - T_{ap})(\beta_p - 1)^{-1}, \quad (13)$$

where M_a, M_p are, respectively, the molar mass (in kg/mol) of the initial gas around the conductor (T_a ≈273.15 K) and the metal vapor formed in this gas from its sublimated metal; β_p is the adiabatic index for «metal plasma» in the EE zone; T_{ap} is the temperature that is established in the EE zone of the conductor after the expansion of its highly superheated metal vapor in the gas.

In the general case T_{ap}≠T_a for further calculation estimations according to (13) of the largest values of the thermal explosion energy W_{ex} at EE of a metallic conductor in a gas (for example, in air), we limit ourselves to the particular thermophysical case when T_{ap}≈T_a.

It can be seen from (13) that the thermal explosion energy W_{ex} of the highly overheated metal of the conductor is determined mainly by the mass m_c=$l_0S_0d_c$ of the exploding conductor and the maximum temperature T_m according to (1) in the formed plasma channel of the high-current GPC discharge. As for the adiabatic index β_p for «metallic plasma», taking into account the fact that at EE in the gas of a metallic conductor, this plasma usually contains diatomic gases by its composition (for example, nitrogen N_2, hydrogen H_2 and oxygen O_2, which are part of air), in the first approximation for it in the case of the presence of diatomic gases in the gaseous medium around the conductor, it is possible to take the numerical value of the adiabatic index β_p, which is about β_p≈1.4 [28]. Then from (13) for EE in atmospheric air (T_a≈273.15 K; β_p≈1.4; M_a≈28.97·10^{-3} kg/mol [28]) of the copper conductor (l_0≈110 mm; r_0≈0.1 mm; S_0≈3.14·10^{-8} m^2; d_c≈8920 kg/m^3; m_c≈0.308·10^{-4} kg; J_k≈1.95·10^{17} A^2·s·m^{-4} [27]; U_e≈10 V [29]; M_p≈63.55·10^{-3} kg/mol [28]) in the high-current discharge circuit of a powerful high-voltage GPC (I_{mc} ≈ −190 kA; ω_c ≈ 26.18·10^3 s^{-1} [30]) for R_m = 8.314 J/(mol·K) [28] and T_m≈121,6·10^3 K, we obtain that in this electrophysical case the value of the thermal explosion energy W_{ex} of the conductor under study will be numerically equal to approximately W_{ex}≈838.8 J.

9. Approximate indicators of the process of introducing energy W_i into the structure of the conductor at its gas EE. As is known, the peculiarities of the process of rapid introduction of thermal energy W_i into the crystalline structure of the metal conductor will determine all the thermophysical and thermodynamic characteristics of its next EE both in vacuum and in gas and liquid media [5, 9, 10, 20, 32]. In the studied case of the engineering approach to the gas EE of a thin metal conductor in the high-current discharge circuit of a powerful high-voltage GPC, this process includes the stages of its sublimation, severe overheating, and thermal explosion of the metal vapor of the conductor. For a brief description of these stages above, in sections 2 and 4–8, the corresponding approximate calculation formulas (1) and (5)–(13) were given for determining the maximum temperature T_m of the plasma, the time t_{ex} of the thermal explosion, the maximum pressure P_m, the sublimation energy W_s, the overheating energy W_{sh} and the thermal explosion energy W_{ex} at EE in the accepted gas environment (T_a≈273.15 K; P_a≈1.013·10^5 Pa [28]) of the considered metal conductor. With respect to a short thin copper cylindrical conductor ((l_0≈110 mm; r_0≈0.1 mm; S_0≈3.14·10^{-8} m^2; d_c≈8920 kg/m^3; m_c≈0.308·10^{-4} kg; J_k≈1.95·10^{17} A^2·s·m^{-4} [27]), placed in the high-current discharge circuit of a powerful high-voltage GPC (I_{mc}≈−190 kA; ω_c≈26.18·10^3 s^{-1}; U_{c0}≈−27 kV [30]), it was established by calculation that the thermal energy W_i ≈ (W_s + W_{sh} + W_{ex}) injected into the metal of the conductor in the microsecond time range is numerically about W_i ≈ 2.44 kJ (with a powerful GPC stored in a capacitor battery with capacitance of C_0≈333 μF electrical energy is about W_0≈121.4 kJ [30]). It can be seen that the thermal energy W_i does not exceed 2 % of the electrical energy W_0 of the GPC battery. Such an electrophysical approach to the calculated determination of the energy W_i introduced into the metal structure of the conductor is in full agreement with the first law of classical thermodynamics [28].

10. Approximate calculation of the active resistance R_c of the plasma channel of the discharge at the gas EE of the conductor. After the considered conductor loses its metallic conductivity, which is characterized at the boiling temperature T_b by the specific

electrical conductivity γ_{cb} (see Table 1) [34], strong overheating of the metal vapor, the appearance of radial spread (from the moment of time t_{ex}) of the sublimated metal vapor of the thin conductor [4, 5, 7, 32] and the formation in the local zone of its EE in the gas of a high-temperature «metal plasma» [31], which forms a cylindrical plasma channel of a gas discharge [29], the main part of the stored in the GPC capacitor battery of its electrical energy is «switched on» in the electrophysical process energy W_0. This part of the energy W_0 will be dissipated on the active resistances of the electric circuit of the high-voltage GPC: R_c for the formed plasma cylindrical discharge channel of length l_c and R_k for the current-carrying elements of the GPC discharge circuit [19, 20]. Analytical determination of R_c faces serious technical difficulties. Therefore, later, when calculating R_c numerically, we will limit ourselves to the results of our own experimental studies [37], performed on a low-impedance powerful high-voltage GPC (R_k≈50 mΩ [21]) with a discharge decaying sinusoidal current $i_c(t)$, which was used (see the following section 14) during the experimental study of EE in the atmospheric air of a thin cylindrical conductor (l_0≈110 mm; r_0≈0.1 mm).

In [36, 37], experimentally when using in the discharge circuit of a powerful GPC a decaying sinusoidal current $i_c(t)$ of microsecond duration, the first amplitude of which Imc varied within ±(30–220) kA, the validity of Braginsky formula for the maximum radius r_{mc} of the plasma channel of a spark discharge in atmospheric air initiated by EE of a copper conductor was confirmed [38]:

$$r_{mc} \approx 0{,}093 \cdot |I_{mc}|^{1/3} \cdot t_{mc}^{1/2}, \qquad (14)$$

where t_{mc} is the time (s) corresponding to the first amplitude I_{mc} (A) of the discharge decaying sinusoidal current $i_c(t)$ in the capacitor battery circuit of the high-voltage GPC.

When (14) is valid for the air channel of a spark discharge and the specified conditions of change in a cylindrical plasma channel with length l_c≈l_0 of the ATP of the discharge current $i_c(t)$ of a powerful high-voltage GPC [37], it was established that the minimum running active resistance R_{c0}=R_c/l_c of a high-current plasma of the spark discharge channel in atmospheric air when it is initiated by the exploding thin copper conductor (l_0 ≈ 50 mm; r_0 ≈ 0.1 mm) is numerically R_{c0}≈(0.167±0.005) Ω/m. Knowing R_{c0}, the minimum value of the active resistance R_c of the plasma discharge channel in atmospheric air, formed by the GPC capacitor battery, which is discharged on a thin, exploding metal conductor of length l_0≈l_c, can be found from the relationship: R_c≈$R_{c0}l_c$. At l_c≈110 mm for the minimum active resistance R_c<R_k formed in the high-current discharge circuit of the GPC (I_{mc}≈−190 kA; ω_c≈$26.18 \cdot 10^3$ s^{-1} [30]) of the plasma discharge channel that initiates EE in air of the short thin round copper conductor (l_0≈110 mm; r_0≈0.1 mm), we get the following numerical value for R_c: R_c≈18.37 mΩ.

11. Approximate calculation of the specific electrical conductivity γ_p of the plasma channel of the discharge at the gas EE of the conductor. From the classical electrical engineering formula for R_c of a conductor with radius r_{mc}, taking into account (14) and the minimum linear active resistance R_{c0} of initiated EE in the gas of the conductor of the plasma cylindrical discharge channel in the GPC electric circuit, we obtain the formula for the engineering estimation of the maximum specific electrical conductivity γ_p of its plasma:

$$\gamma_p \approx 36{,}8(R_{c0} \cdot |I_{mc}|^{2/3} \cdot t_{mc})^{-1}. \qquad (15)$$

From (15) at the studied EE in atmospheric air (T_a≈273.15 K; P_a≈$1.013 \cdot 10^5$ Pa [28]) of a thin copper conductor (l_0≈110 mm; r_0≈0.1 mm), which is connected in a high-current discharge GPC high-voltage capacitor bank circuit (I_{mc}≈−$190 \cdot 10^3$ A; t_{mc}≈$42 \cdot 10^{-6}$ s; ω_c≈$26.18 \cdot 10^3$ s^{-1}; U_{c0}≈−27 kV [30]) for R_{c0}≈0.167 Ω/m the specific electrical conductivity γ_p of the plasma cylindrical channel with length l_c≈110 mm, which occurs in this case, turns out to be numerically equal to γ_p≈1587.6 $(\Omega \cdot m)^{-1}$. This calculated value of γ_p is in good agreement with the corresponding experimental data of γp for «metallic plasma» given in [9, 10, 37].

12. Approximate calculation of the energy W_c released in the plasma channel of the discharge at the gas EE of the conductor. At EE in the gaseous medium of the metal conductor of length l_0 under consideration, through it and the cylindrical channel of length l_c≈l_0 formed by this explosion with «metal plasma» in the high-current GPC circuit of the capacitive type, a discharge decaying sinusoidal current $i_c(t)$ flows, which is described in time t by the following dependence [6, 36]:

$$i_c(t) = \pm k_c I_{mc} \cdot \exp(-\delta_c t) \cdot \sin(\omega_c t), \qquad (16)$$

where δ_c, ω_c are, respectively, the attenuation coefficient and the circular frequency of oscillations of the discharge current of the powerful GPC; k_c = $[\exp(-\delta_c/\omega_c \operatorname{arcctg}\delta_c/\omega_c) \cdot \sin(\operatorname{arcctg}\delta_c/\omega_c)]^{-1}$ is the dimensionless normalizing coefficient.

On the active resistance R_c of the plasma cylindrical channel of the spark discharge of length l_c≈l_0, initiated by EE in the gaseous medium of a thin metal conductor of length l_0, in the accepted high-current circuit of the high-voltage GPC of the capacitor type with pulsed sinusoidal current $i_c(t)$ according to (16), thermal energy W_c will be released, which is calculated according to the following electrotechnical formula:

$$W_c \approx l_0 R_{c0} k_c^2 I_{mc}^2 \int_0^\infty e^{-2\delta_c t} \sin^2(\omega_c t) dt. \qquad (17)$$

After integration in (17) for the thermal energy W_c released in the plasma discharge channel formed in the GPC circuit due to EE in the metal conductor gas, we obtain finally:

$$W_c \approx l_0 R_{c0} k_c^2 I_{mc}^2 \delta_c^{-1} [1 + (\delta_c / \omega_c)^2]^{-1} / 4. \qquad (18)$$

According to (18), at EE in the atmospheric air of the short copper conductor (l_0≈110 mm; r_0≈0.1 mm) and the plasma channel of the spark discharge initiated by it (l_c≈l_0≈110 mm; R_{c0}≈0.167 Ω/m [37]) in the high-current circuit of a powerful high-voltage GPC (I_{mc}≈−190 kA; δ_c≈$14.39 \cdot 10^3$ s^{-1}; ω_c≈$26.18 \cdot 10^3$ s^{-1}; k_c≈2.05 [30]) in the indicated channel with «metallic plasma» thermal energy W_c will release, numerically equal to W_c≈37.2 kJ. This energy W_c in sum with the thermal energy W_i≈2.44 kJ introduced into the investigated explosive copper conductor (l_0≈110 mm; r_0≈0.1 mm) is approximately (W_c + W_i) ≈ 39.6 kJ. Then the ratio of the sum of thermal

energies (W_c + W_i) to the electrical energy W_0≈121.4 kJ [30] stored in the GPC capacitor battery will be numerically equal to (W_i + W_c)/W_0≈0.326. Therefore, it can be said that in the considered electric circuit with the use of a powerful high-voltage GPC of the capacitor type (C_0≈333 μF; U_{c0}≈−27 kV; W_0≈121.4 kJ [30]) for the practical implementation of the EE process in the atmospheric air of the short copper conductor (l_0≈110 mm; r_0≈0.1 mm) the efficiency η_c≈(W_i + W_c)/W_0 of the electrical energy of the GPC capacitor bank is numerically η_c≈0.326 (32.6 %). This indicator η_c turned out to be smaller than the similar indicator η_c ≈ 57.1 %, typical for the use of the same powerful high-voltage GPC when forming a similar copper conductor of a plasma channel of an underwater discharge in its discharge circuit based on EE in technical water [39]. The reason for this is the greater value of the active resistance R_c≈$R_{c0}l_c$ of the underwater plasma discharge channel compared to the gas discharge channel [20, 39]. It follows from (1) and (18) that both the temperature T_m of the plasma channel and the energy W_c released in it can be determined from the oscillogram of the discharge current $i_c(t)$ of the GPC at EE in the conductor gas.

13. Approximate calculation of the maximum velocity v_{mw} of the shock acoustic wave at the gas EE of the conductor. In the analyzed electrophysical case, the expression for the maximum velocity v_{mw} of propagation of theshock acoustic wave in plasma products formed from EE in the gas medium of the investigated metal conductor can be represented in the following form [28, 40]:

$$v_{mw} \approx 0{,}5(\beta_p+1)\left[\beta_p R_m T_m/(M_a+M_p)\right]^{1/2}. \quad (19)$$

When obtaining (19), we used the known relationship between the shock wave velocity v_{mw} and the velocity of expansion v_{ex} of a highly overheated metal vapour of a conductor behind the shock wave front [27, 40]: v_{mw}≈0,5(β_p+1)v_{ex}. In the studied case, it is assumed that the velocity v_{ex} corresponds to the velocity of a sound wave in a dense «metal plasma» formed at the initial stage of EE in the gas of a metal conductor [10, 28]. It can be seen that the value of v_{mw} is directly proportional to the level of the temperature indicator $T_m^{1/2}$.

From (19) at EE in air with normal atmospheric conditions (T_a≈273.15 K; β_p≈1.4; M_a≈28.97·10^{-3} kg/mol; R_m = 8.314 J/(mol·K) [28]) of the short copper conductor (l_0 ≈ 110 mm; r_0 ≈ 0.1 mm; S_0 ≈ 3.14·10^{-8} m^2; J_k ≈ 1.95·10^{17} A^2·s·m^{-4} [27]; M_p ≈ 63.55·10^{-3} kg/mol [28]), connected in the high-current discharge circuit of a high-voltage GPC (I_{mc}≈−190 kA; ω_c≈26.18·10^3 s^{-1}; T_m≈121.6·10^3 K), it turns out that the velocity of the shock acoustic wave v_{mw} acquires a numerical value of approximately v_{mw}≈4693 m/s. This estimated calculated value of the velocity v_{mw} of the gas-dynamic shock wave at EE in the atmospheric air of a thin copper conductor corresponds to the velocity as a shock wave from the EE of a copper wire with radius of 75 μm with HPC propagating in distilled water at speed of approximately 4.3·10^3 m/s (at thus, the pressure amplitude in the water near the exploding wire reaches the level of 6.5·10^9 Pa or 6.42·10^4 atm) [8], as well as the detonation wave in «slow» solid explosive explosives [41]. In this regard, the EE phenomenon in gas environments of thin metal conductors can be used in electrodetonators when detonating ammunition with both conventional and nuclear explosives [40, 41].

14. Results of experiments for air EE of the thin cylindrical conductor. To verify some of the calculation results obtained above for EE in the gaseous medium of thin metal conductors, corresponding experiments were performed for EE in the atmospheric air of the thin copper conductor (l_0 ≈ 110 mm; r_0 ≈ 0.1 mm; S_0 ≈ 3.14·10^{-8} m^2). Here, a low-impedance high-voltage GPC with a powerful capacitor battery was used as a source of electrical energy, characterized by the following nominal electrical parameters [22, 30]: C_0≈333 μF; U_{c0}≈±50 kV; W_0≈416 kJ.

Figures 1, 2 show the combined in time t oscillograms of the discharge decaying sinusoidal current $i_c(t)$ of the indicated GPC (curve 1; I_{mc}≈−190 kA; δ_c≈14.39·10^3 s^{-1}; ω_c≈26.18·10^3 s^{-1}; t_{mc}≈42 μs; k_c≈2.05) and pulsed peak-like voltage $u_c(t)$ (curve 2; $u_{mc}(t_{ex})$≈−28.17 kV; t_{ex}≈3.2 μs [30]) at air EE of the short thin copper conductor (l_0≈110 mm; r_0≈0.1 mm) in a high-current discharge circuit of a powerful high-voltage GPC (U_{c0}≈−27kV; W_0≈121.4 kJ) at a horizontal scale of 5 and 50 μs/division.

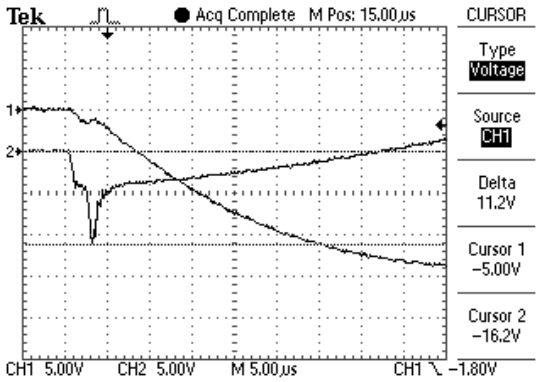

Fig. 1. Combined oscillograms of current $i_c(t)$ (curve of channel 1) and voltage $u_c(t)$ (curve of channel 2) in the high-current circuit of a powerful high-voltage GPC at EE in atmospheric air of the thin copper conductor (l_0=110 mm; r_0=0.1 mm; t_{ex}≈3.2 μs [30]) (vertical scale for current – 50 kA/division; vertical scale for voltage – 12.6 kV/division; horizontal scale – 5 μs/division)

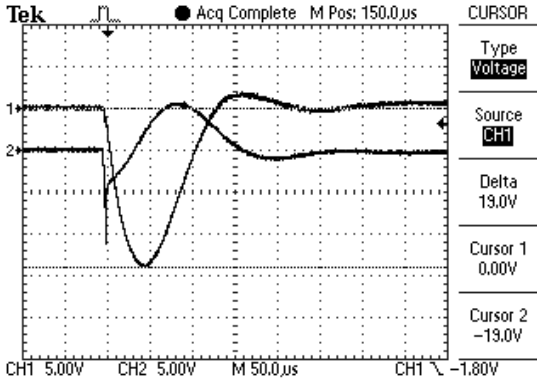

Fig. 2. The same as in Fig. 1 combined oscillograms of the discharge current $i_c(t)$ (curve of channel 1; I_{mc}≈−190 kA; δ_c≈14.39·10^3 s^{-1}; ω_c≈26.18·10^3 s^{-1}; T_c≈2π/ω_c≈240 μs [30]) and voltage $u_c(t)$ (curve of channel 2) in the high-current circuit of a powerful high-voltage GPC at EE in the atmospheric air of the thin copper conductor (l_0=110 mm; r_0=0.1 mm; t_{ex}≈3.2 μs) but with horizontal scale – 50 μs/division

When conducting experimental studies of air EE of the specified thin copper conductor, the coaxial measuring shunt of the ShK-300 type, the capacitive voltage divider of the EPN-100 type, and the Tektronix TDS 1012 digital oscilloscope [30] were used, which passed the state metrological inspection.

From the oscillograms of the discharge current $i_c(t)$ (curve 1) and the voltage $u_c(t)$ on the exploding copper conductor (curve 2), it should be noted that in this case the experimental time t_{ex} of the thermal explosion of the conductor in question, which occurs at the front of the first half-wave of the discharge current $i_c(t)$, is approximately $t_{ex}\approx3.2$ μs (when its value is $t_{ex}\approx3.32$ μs calculated by (5)).

It can be seen that for the t_{ex} parameter, the discrepancy between its calculated and experimental values does not exceed 4 %. These data indicate the efficiency and reliability of the applied calculation approach to the determination of the t_{ex} parameter when describing the electrophysical process of EE in the gas environment of the round thin metal conductor.

In addition, given according to Fig. 1, 2 experimental data for the ATP of the discharge current $i_c(t)$ together with the experimental results from [36, 37] for the electrophysical parameters R_{c0} and r_{mc} indirectly indicate the validity of the calculated estimations according to (1), (7), (14), (15) and (18), respectively, of the parameters T_m, P_m, R_c, γ_p and W_c at the EE in atmospheric air of the copper conductor ($l_0\approx110$ mm; $r_0\approx0.1$ mm) connected in the electric circuit of a powerful high-voltage GPC.

Conclusions.

1. The proposed electrophysical approach to the analytical complex calculation of the main parameters of the EE in the gas medium of a thin metal conductor allows to determine with engineering accuracy such thermophysical, gas-dynamic and electrical parameters of a given explosion as: the maximum temperature T_m and the pressure P_m in the plasma channel, the time t_{ex} of the explosion of the conductor, the active resistance R_c and the specific electrical conductivity γ_p of the plasma channel, the thermal energy W_i introduced into the conductor and the thermal energy W_c released in the channel, and the maximum velocity v_{mw} of the propagation of the shock acoustic wave in the «metal plasma» from EE in the gas of a thin metal conductor under electrothermal action of the HPC.

2. It was found that at the EE in the atmospheric air of the thin copper conductor ($l_0\approx110$ mm; $r_0\approx0.1$ mm), which is connected in the discharge circuit of a capacitor battery of a powerful high-voltage GPC of the microsecond time range ($I_{mc}\approx-190$ kA; $\delta_c\approx14.39\cdot10^3$ s^{-1}; $\omega_c\approx26.18\cdot10^3$ s^{-1}; $t_{mc}\approx42$ μs; $U_{c0}\approx-27$ kV; $W_0\approx121.4$ kJ), the specified parameters of the electroexplosive process in its circuit take the following approximate numerical values: $T_m\approx121.6\cdot10^3$ K; $P_m\approx14.19\cdot10^9$ Pa; $t_{ex}\approx3.32$ μs; $R_c \approx 18.37$ mΩ; $\gamma_p \approx 1587.6$ (Ω·m)$^{-1}$; $W_i \approx 2.44$ kJ; $W_c \approx 37.2$ kJ; $v_{mw} \approx 4693$ m/s.

3. As part of the further development of the engineering approach to the analytical complex calculation of the above-listed main parameters of the electro-explosive process in the discharge circuit of the GPC, the relationship (3) is given for the approximate calculation of the values of the critical current integral J_k at the EE in the gaseous medium of thin metal conductors with the most widely used in the field of experimental physics HPT and electro-explosive technologies with conductive materials (see Table 1).

4. It is shown that such parameters of the electric explosion process as the maximum temperature T_m and the highest pressure P_m in the plasma channel, the time t_{ex} of the conductor explosion, the specific electrical conductivity γ_p of the plasma channel, the thermal energy W_i introduced into the metal conductor, and the thermal energy W_c released in the channel, do not depend on the properties of the gas in which the EE of the investigated metal conductor takes place.

5. At the EE in the gas environment of a thin metal conductor connected in the discharge circuit of a powerful high-voltage GPC, the temperature T_m and the pressure P_m, the time t_{ex} of the conductor explosion, the specific electrical conductivity γ_p of the plasma channel, the thermal energy W_c released in the channel, and the velocity v_{mw} of the wave in the explosion zone, occurring in the discharge plasma channel, can be determined by (1), (5), (7), (15), (18) and (19) on the basis of deciphering the oscillograms of the discharge current $i_c(t)$ and voltage $u_c(t)$ in the electrical circuit of the GPC.

6. The thermal energy $W_i\approx2.44$ kJ, which is introduced into the investigated short thin copper conductor ($l_0\approx110$ mm; $r_0\approx0.1$ mm), which is connected in the high-current discharge circuit of the indicated powerful high-voltage GPC, at its EE in atmospheric air, does not exceeds 2 % of the electrical energy $W_0\approx121.4$ kJ stored in the capacitor bank of this GPC.

7. In the analyzed electrical circuit of the practical implementation of the phenomenon of high-temperature EE in the atmospheric air of the studied short thin copper conductor ($l_0\approx110$ mm; $r_0\approx0.1$ mm), the thermal energy released in the plasma channel $W_c\approx37.2$ kJ together with the energy introduced into the conductor $W_i \approx2.44$ kJ, ensures the achievement of the efficiency η_c of the electrical energy of the capacitor bank of the powerful high-voltage GPC $W_0\approx121.4$ kJ, which is numerically equal to approximately $\eta_c\approx0.326$ (32.6 %).

8. The high-current experiments performed with the help of a powerful high-voltage GPC confirmed the main provisions of the proposed engineering approach to the analytical complex calculation of the specified parameters of the electro-explosive process in a gaseous medium with normal atmospheric conditions and showed that the difference between the calculated according to (5) and the experimental data for the explosion time t_{ex} of the copper conductor ($l_0\approx110$ mm; $r_0\approx0.1$ mm) does not exceed 4 %.

Acknowledgment. The work was carried out with the support of the Ministry of Education and Science of Ukraine (Project DB No. 0121U109546).

Conflict of interest. The authors of the article declare that there is no conflict of interest.

REFERENCES

1. Abramova K.B., Zlatin N.A., Peregud B.I. MGD – instability of liquid and hard conductors. Destruction of

conductors an electric current. *Journal of experimental and theoretical physics,* 1975, vol. 69, no. 6(12), pp. 2007-2021. (Rus).
2. Lebedev S.V. About the mechanism of electric explosion of metal. *High Temperature*, 1980, vol. 18, no. 2, pp. 273-279. (Rus).
3. Lebedev S.V., Savvatimskiy A.I. Metals in the process of the rapid heating of high-slay an electric current. *Successes physical sciences*, 1984, vol. 144, no. 2, pp. 215-250. (Rus).
4. Vorob'ev V.S., Eronin A.A., Malyshenko S.P. Phase Explosion of Conductor with Current. *High Temperature*, 2001, vol. 39, no. 1, pp. 97-103. doi: https://doi.org/10.1023/A:1004182800475.
5. Oreshkin V.I., Khishchenko K.V., Levashov P.R., Rousskikh A.G., Chaikovskii S.A. Strata formation at fast electrical explosion of cylindrical conductors. *High Temperature*, 2012, vol. 50, no. 5, pp. 584-595. doi: https://doi.org/10.1134/S0018151X12050148.
6. Kvarckhava I.F., Bondarenko V.V., Plyutto A.P., Chernov A.A. Oscillographic determination of energy of electric explosion wires. *Journal of Experimental and Theoretical Physics*, 1956, vol. 31, no. 5 (11), pp. 745-751. (Rus).
7. Rousskikh A.G., Baksht R.B., Labetskii A.Y., Oreshkin V.I., Shishlov A.V., Chaikovskii S.A. Electric explosion of fine tungsten wires in vacuum. *Plasma Physics Reports*, 2004, vol. 30, no. 11, pp. 944-952. doi: https://doi.org/10.1134/1.1825130.
8. Rousskikh A.G., Oreshkin V.I., Labetsky A.Y., Chaikovsky S.A., Shishlov A.V. Electrical explosion of conductors in the high-pressure zone of a convergent shock wave. *Technical Physics*, 2007, vol. 52, no. 5, pp. 571-576. doi: https://doi.org/10.1134/S1063784207050064.
9. Stolovich N.N. *Elektrovzryvnye preobrezovateli energii* [The electro-explosive transformers of energy]. Minsk, Science and Technique Publ., 1983. 151 p. (Rus).
10. Burtsev V.A., Kalinin N.V., Luchinskiy A.V. *Elektricheskiy vzryv provodnikov i ego primenenie v elekrophizicheskih ustanovkah* [The electric explosion of conductors and his application in electrophysics options]. Moscow, Energoatomizdat Publ., 1990. 288 p. (Rus).
11. Boguslavsky L.Z., Sinchuk A.V., Nazarova N.S., Ovchinnikova L.E. Electrical explosion of conductors for the production of nanoscale carbides and the deposition of functional nanocoatings. *Electronic Processing of Materials*, 2019, vol. 55, no. 5, pp. 10-23. doi: https://doi.org/10.5281/zenodo.3522291.
12. Yavorovskiy N.A. Receipt of ultradispersible powders the method of electric explosion. *Russian Physics Journal*, 1994, vol. 37, no. 4, pp. 111-136.
13. Lerner M.I. Formation of nanosize phase at the electric explosion of conductors. *Russian Physics Journal*, 2006, vol. 49, no. 6, pp. 91-95.
14. Lerner M.I., Svarovskaya N.V., Psakhie S.G., Bakina O.V. Production technology, characteristics, and some applications of electric-explosion nanopowders of metals. *Nanotechnologies in Russia*, 2009, vol. 4, no. 11-12, pp. 741-757. doi: https://doi.org/10.1134/S1995078009110019.
15. Baranov M.I. Receipt of dispersible materials with the micronic, submicrometer and nanostructural particles of matter at the electric explosion of thin metallic econductors. *Electrical Engineering & Electromechanics*, 2012, no. 4, pp. 45-49.
16. Boguslavskii L.Z., Vinnichenko D.V., Nazarova N.S., Adamchuk Yu.O., Chushchak S.V., Kozyrev S.S. Control of the process of electrodischarge synthesis of nanocarbon from gaseous hydrocarbons on metal surfaces. *Surface Engineering and Applied Electrochemistry*, 2019, vol. 55, no. 3, pp. 274-279. doi: https://doi.org/10.3103/S1068375519030037.
17. Mesiats G.A. *Impul'snaia energetika i elektronika* [Pulsed power and electronics]. Moscow, Nauka Publ., 2004. 704 p. (Rus).
18. Rouse K. The maximum temperature of a wire explosion in a vacuum. *In book trans. with Eng. Electric explosion of conductors*. Moscow, Mir Publ., 1965, pp. 43-46. (Rus).
19. Dashuk P.N., Zayents S.L., Komel'kov V.S., Kuchinskiy G.S., Nikolayevskaya N.N., Shkuropat P.I., Shneerson G.A. *Tehnika bol'shih impul'snyh tokov i magnitnyh polej* [The technique of large pulsed currents and magnetic fields]. Moscow, Atomizdat Publ., 1970. 472 p. (Rus).
20. Gulyy G.A. *Nauchnye osnovy razrjadno-impul'snyh tehnologij* [Scientific basis of the discharge-pulse tehnologies]. Kiev, Naukova Dumka Publ., 1990. 208 p. (Rus).
21. Baranov M.I., Buriakovskyi S.G., Rudakov S.V. The tooling in ukraine of model tests of objects of energy, aviation and space-rocket engineering on resistibility to action of pulsed current of artificial lightning. *Electrical Engineering & Electromechanics*, 2018, no. 4, pp. 45-53. doi: https://doi.org/10.20998/2074-272X.2018.4.08.
22. Baranov M.I., Buriakovskyi S.G., Hrytsenko A.S., Kostiuk V.A. Results of investigations of thermal resistibility of prototypes of aluminum alloy panels of fuel tank of airplane to direct action of normalized components of artificial lightning current. *Electrical Engineering & Electromechanics*, 2019, no. 6, pp. 29-38. doi: https://doi.org/10.20998/2074-272X.2019.6.04.
23. Barakhvostov S.V., Bochkarev M.B., Volkov N.B., Nagaev K.A., Tarakanov V.P., Tkachenko S.I., Chingina E.A. Ultrafast electric explosion of microconductors: plasma channel structure and optical characteristics. *Scientific Herald of Uzhhorod University. Series «Physics»*, 2011, no. 30, pp. 63-68.
24. Baranov M.I., Rudakov S.V. Approximate calculation of basic characteristics of plasma at the air electric explosion of metal conductor. *Electrical Engineering & Electromechanics*, 2017, no. 6, pp. 60-64. doi: https://doi.org/10.20998/2074-272X.2017.6.09.
25. Wu J., Li X., Li M., Li Y., Qiu A. Review of effects of dielectric coatings on electrical exploding wires and Z pinches. *Journal of Physics D: Applied Physics*, 2017, vol. 50, no. 40, art. no. 403002. doi: https://doi.org/10.1088/1361-6463/aa86a1.
26. Sarathi R., Reddy R.S., Tavarmani R.S., Okamoto A., Suematsu H., Selvam P., Kamachi Mudali U., Kamaraj M. Investigation of Nano-Molybdenum Carbide Particle Produced by Wire-Explosion Process. *IEEE Transactions on Plasma Science*, 2015, vol. 43, no. 10, pp. 3470-3475. doi: https://doi.org/10.1109/TPS.2015.2426019.
27. Knopfel' G. *Sverkhsil'nye impul'snye magnitnye polia* [Ultra strong pulsed magnetic fields]. Moscow, Mir Publ., 1972. 391 p. (Rus).
28. Kuhling H. *Spravochnik po fizike* [Handbook of Physics]. Moscow, Mir Publ., 1982. 520 p. (Rus).
29. Rayzer Yu.P. *Fizika gazovogo razrjada* [Physics of gas discharge]. Moscow, Nauka Publ., 1987. 592 p. (Rus).
30. Baranov M.I., Lysenko V.O. The main characteristics of an electric explosion of a metallic conductor at high impulse currents. *Elektrichestvo*, 2013, no. 4, pp. 24-30. (Rus).
31. Baranov M.I. Analytical calculation of critical values of integral of current for parent metals, applied in the technique of large impulsive currents at the electric explosion of conductors. *Technical Electrodynamics*, 2008, no. 6, pp. 14-17. (Rus).
32. Oreshkin, V.I., Barengol'ts, S.A. & Chaikovsky, S.A. Numerical calculation of the current specific action integral at the electrical explosion of wires. *Technical Physics*, 2007, vol. 52, no. 5, pp. 642-650. doi: https://doi.org/10.1134/S1063784207050179.
33. Zhigalin A.S., Russkikh A.G., Oreshkin V.I., Chaykovskiy S.A., Ratakhin N.A., Baksht P.B. Experimental research of the strata formation during electrical explosion of foils in vacuum. *Russian Physics Journal*, 2015, vol. 58, no. 9-2, pp. 113-117.
34. Stolovich N.N., Minitskaya N.S. *Temperaturnye zavisimosti teplofizicheskikh svoistv nekotorykh metallov* [Temperature

dependences of thermophysical properties of some metals]. Minsk, Science and Technique Publ., 1975. 160 p. (Rus).
35. Fomenko V.S. *Emissionnye svoistva materialov. Spravochnik* [Emission properties of materials. Directory]. Kyiv, Naukova Dumka Publ., 1981. 339 p. (Rus).
36. Baranov M.I. *Izbrannye voprosy elektrofiziki. Monografiya v 4kh tomakh. Tom 2, Kn. 1: Teoriia elektrofizicheskikh effektov i zadach* [Selected topics of Electrophysics. Monograph in 4 Vols. Vol.2, Book 1. A theory of electrophysical effects and tasks]. Kharkiv, NTU «KhPI» Publ., 2009. 384 p. (Rus).
37. Baranov M.I., Koliushko G.M., Lysenko V.O. Experimental determination of active resistance and conductivity of heavy-current plasma channel in the discharge chain of generator impulsive components of current of artificial lightning. *Electrical Engineering & Electromechanics*, 2011, no. 3, pp. 51-55. (Rus).
38. Lozanskiy E.D., Firsov O.B. *Teoriia iskry* [Theory of spark]. Moscow, Atomizdat Publ., 1975. 272 p. (Rus).
39. Baranov M.I., Lysenko V.O. Basic descriptions of heavy-current plasma channel of submarine electric discharge. *Elektrichestvo*, 2012, no. 4, pp. 2-8. (Rus).
40. Zel'dovich Ja.B., Rayzer Yu.P. *Fizika udarnykh voln i vysokotemperaturnykh gidrodinamicheskikh iavlenii* [Physics of shock waves and high-temperature hydrodynamic phenomena]. Moscow, Science Publ., 1966. 686 p. (Rus).
41. Orlova E.Yu. *Khimiia i tekhnologiia brizantnykh vzryvchatykh veshchestv* [Chemistry and technology of brizant explosives]. Leningrad, Chemistry Publ., 1981. 312 p. (Rus).

Received 22.02.2022
Accepted 15.08.2022
Published 06.01.2023

M.I. Baranov[1], *Doctor of Technical Science, Professor,*
S.G. Buriakovskyi [1], *Doctor of Technical Science, Professor,*
V.V. Kniaziev[1], *Candidate of Technical Science, Leader Research Scientist,*
[1] Research and Design Institute «Molniya»
of National Technical University «Kharkiv Polytechnic Institute»,
e-mail: baranovmi@kpi.kharkov.ua (Corresponding Author);
sergbyr@i.ua; knyaz2@i.ua

How to cite this article:
Baranov M.I., Buriakovskyi S.G., Kniaziev V.V. A calculation of basic thermophysical, gasodynamic and electropower parameters of electric explosion in the gas environment of a metallic conductor. *Electrical Engineering & Electromechanics*, 2023, no. 1, pp. 40-50. doi: https://doi.org/10.20998/2074-272X.2023.1.06

UDC 621.3 https://doi.org/10.20998/2074-272X.2023.1.07

M.A. Hessad, Z. Bouchama, S. Benaggoune, K. Behih

Cascade sliding mode maximum power point tracking controller for photovoltaic systems

Introduction. *Constant increases in power consumption by both industrial and individual users may cause depletion of fossil fuels and environmental pollution, and hence there is a growing interest in clean and renewable energy resources. Photovoltaic power generation systems are playing an important role as a clean power electricity source in meeting future electricity demands.* ***Problem****. All photovoltaic systems have two problems; the first one being the very low electric-power generation efficiency, especially under low-irradiation states; the second resides in the interdependence of the amount of the electric power generated by solar arrays and the ever changing weather conditions. Load mismatch can occur under these weather varying conditions such that maximum power is not extracted and delivered to the load. This issue constitutes the so-called maximum power point tracking problem.* ***Aim.*** *Many methods have been developed to determine the maximum power point under all conditions. There are various methods, in most of them based on the well-known principle of perturb and observe. In this method, the operating point oscillates at a certain amplitude, no matter whether the maximum power point is reached or not. That is, this oscillation remains even in the steady state after reaching the maximum power point, which leads to power loss. This is an essential drawback of the previous method. In this paper, a cascade sliding mode maximum power point tracking control for a photovoltaic system is proposed to overcome above mentioned problems.* ***Methodology.*** *The photovoltaic system is mainly composed of a solar array, DC/DC boost converter, cascade sliding mode controller, and an output load. Two sliding mode control design strategies are joined to construct the proposed controller. The primary sliding mode algorithm is designed for maximum power point searching, i.e., to track the output reference voltage of the solar array. This voltage is used to manipulate the setpoint of the secondary sliding mode controller, which is used via the DC-DC boost converter to achieve maximum power output.* ***Results.*** *This novel approach provides a good transient response, a low tracking error and a very fast reaction against the solar radiation and photovoltaic cell temperature variations. The simulation results demonstrate the effectiveness of the proposed approach in the presence of environmental disturbances.* References 23, table 1, figures 11.
Key words: **renewable energy, photovoltaic system, maximum power point tracking, DC-DC boost converter, sliding mode control.**

Вступ*. Постійне збільшення енергоспоживання як промисловими, так і індивідуальними користувачами може призвести до виснаження запасів викопного палива та забруднення навколишнього середовища, тому зростає інтерес до чистих та відновлюваних джерел енергії. Фотоелектричні системи виробництва електроенергії відіграють важливу роль як екологічно чисте джерело електроенергії для задоволення майбутніх потреб в електроенергії.* ***Проблема****. Усі фотоелектричні системи мають дві проблеми; по-перше, дуже низька ефективність вироблення електроенергії, особливо в умовах низького опромінення; друга полягає у взаємозалежності кількості електроенергії, що виробляється сонячними батареями, та постійно мінливих погодних умов. У цих погодних умовах, що змінюються, може відбутися невідповідність навантаження, так що максимальна потужність не буде витягнута і передана в навантаження. Ця проблема є так званою проблемою відстеження точки максимальної потужності.* ***Мета****. Було розроблено безліч методів визначення точки максимальної потужності за будь-яких умов. Існують різні методи, здебільшого засновані на відомому принципі збурення та спостережень. У цьому методі робоча точка коливається з певною амплітудою, незалежно від того, досягнуто точку максимальної потужності чи ні. Тобто це коливання залишається навіть у стійкому стані після досягнення точки максимальної потужності, що призводить до втрати потужності. Це значний недолік попереднього способу. У цій статті для подолання вищезазначених проблем пропонується каскадне керування відстеженням точки максимальної потужності в режимі ковзання для фотоелектричної системи.* ***Методологія****. Фотоелектрична система в основному складається з сонячної батареї, перетворювача постійного струму, що підвищує, каскадного контролера ковзного режиму та вихідного навантаження. Дві стратегії проєктування керування ковзним режимом об'єднані для побудови пропонованого контролера. Алгоритм первинного ковзного режиму призначений для пошуку точки максимальної потужності, тобто для відстеження вихідної опорної напруги сонячної батареї. Ця напруга використовується для управління уставкою вторинного контролера ковзного режиму, який використовується через перетворювач постійного струму, що підвищує, для досягнення максимальної вихідної потужності.* ***Результати****. Цей новий підхід забезпечує хорошу перехідну характеристику, низьку помилку відстеження та дуже швидку реакцію на сонячне випромінювання та коливання температури фотогальванічного елемента. Результати моделювання демонструють ефективність пропонованого підходу за наявності збурень довкілля.* Бібл. 23, табл. 1, рис. 11.
Ключові слова: **відновлювана енергія, фотогальванічна система, відстеження точки максимальної потужності, DC-DC підвищувальний перетворювач, керування ковзним режимом.**

Introduction. Due to the increasing energy demands and environmental protection requirements, renewable and sustainable energy resources are becoming an important part of power generation. Photovoltaic (PV) systems are one of the most promising renewable sources since they exhibit many merits such as availability, cleanness, little maintenance and no noise pollution. Thus, the power generation from PV systems will keep increasing in the future electrical power grid and microgrid systems as well [1-5]. However, PV systems present notable disadvantages, such as a very low electric-power generation efficiency, especially under low-irradiation states; an interdependence of the amount of the electric power generated by solar arrays and changing weather conditions [2-7].

To harvest a maximum amount of energy available under all environmental operating conditions, maximum power point tracker (MPPT) is an important component in a PV system that enables to extract maximum power at maximum power point (MPP). PV systems have nonlinear configurations, which require a robust control scheme for a practical operating environment. Therefore, an efficient MPPT algorithm which considers the nonlinear nature of the plant is necessary and is addressed in this paper.

Many papers have addressed this issue using nonlinear approaches such as backstepping technique [8], perturbation and observation (P&O) method [9], incremental conductance approach (InC) [10, 11] and sliding mode control (SMC) schemes [12, 13]. In most of

these approaches, the MPP to track the reference voltage is obtained based on P&O method, InC approach and constant voltage technique (CV) [7, 14, 15]. However, in quickly changing meteorological circumstances, both of these strategies fail [7, 14, 15]. In this paper to improve the operation of the PV system, both power-voltage and characteristic curve of a PV array are analysed and a new MPPT algorithm based on SMC is proposed.

Sliding mode technique provides a robust control law driving system states to a predesigned attractor and on to the operating equilibrium point. The main advantage of this approach is that once system states reach the attractor, the system dynamics remain insensitive to a class of parameter variation and disturbances, which are typical in solar systems. Consequently, some solutions based on this approach have been proposed to provide good performance in attenuating the oscillations of the output voltage and to ensure the tracking of the reference provided by the MPPT algorithm [16, 17]. However, these solutions do not guarantee the existence of the sliding mode throughout the entire operating range.

The **objective** of this work is to develop an improved sliding mode based maximum power point tracking (SMC-MPPT) controller that takes into account all the elements required to ensure the PV system's desired operation, namely, a robust controller that can follow the reference provided by an MPPT algorithm in the presence of environmental disturbances.

The proposed approach ensures a stable sliding regime over the system's desired operating range, while also providing the convergence time and PV voltage overshoot required by an MPPT algorithm. The simulation results demonstrate the efficiency of the improved sliding mode MPPT controller in the presence of environmental disturbances.

Design of cascade sliding mode controller. This work presents an improved procedure of designing a sliding mode MPPT controller for PV systems, which forces the PV voltage to follow a reference provided by an external MPPT algorithm and attenuates the disturbances caused by the climatic changes. A DC-DC boost converter constituting the heart of the MPPT is inserted between the PV module and its load to achieve optimum power transfer, such a scheme with a resistive load is illustrated in Fig. 1. The converter is used to regulate the PV output voltage (v_{pv}) in order to extract as much power as possible from the PV module.

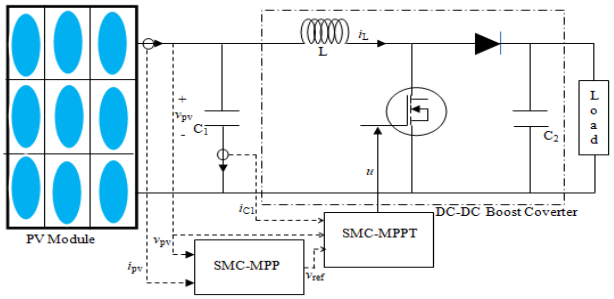

Fig. 1. Block diagram of PV system using cascade SMC-MPPT control

Where the output PV voltage v_{pv} and the output PV current i_{pv} are measured from PV array and sent to the sliding mode maximum power point searching algorithm (SMC-MPP), which generates the reference maximum power voltage v_{ref}. Then, the reference voltage is given to the SMC-MPPT controller the maximum power tracking.

Design of SMC-MPP controller. The maximum power at any operation point can be performed in an easy way if the SMC is used to generate the reference output voltage by imposing the following sliding equation.

$$\sigma = \frac{dP_{pv}}{dv_{pv}} = i_{pv} + v_{pv}\frac{di_{pv}}{dv_{pv}} = 0\,, \qquad (1)$$

where σ is the sliding mode surface; P_{pv} is the output PV power.

If (1) is satisfied, the PV array operates at its maximum power point (MPP) and reference voltage v_{ref} is generated.

Now consider the characteristic curve of the PV system as shown in Fig. 2, the SMC-MPP method can be designed according to the following steps.

Step 1. As shown in Fig. 2 the sliding mode surface has a positive value in region A, this conduct to a negative value of its derivative, i.e. $\dot{\sigma} \prec 0$ to ensure the local reachability condition $\sigma\dot{\sigma} \prec 0$ of the existence SMC operation [18]. From this analysis, SMC-MPP controller increase v_{pv} from v_1 to v_{ref} to track the MPP. Thus $\dot{v}_{pv}$ must be a positive value.

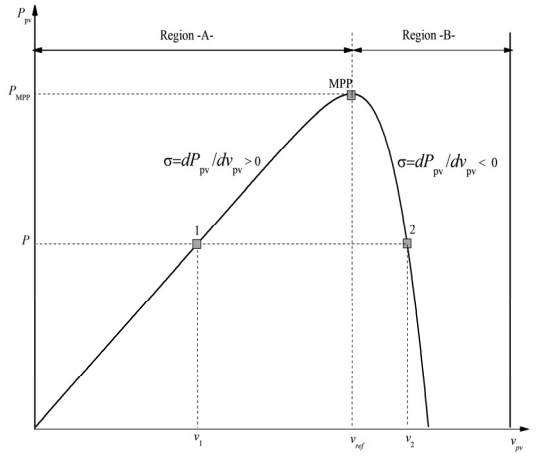

Fig. 2. Power-voltage characteristic curve of a PV system

Step 2. In this case, the sliding mode surface has a negative value as shown in Fig. 3 (region B), this conduct to a positive value of its derivative, i.e. $\dot{\sigma} \succ 0$ to ensure the local reachability condition of the existence SMC operation [18]. Due to this analysis, SMC-MPP controller decrease v_{pv} from v_1 to v_{ref} to track the MPP. Thus $\dot{v}_{pv}$ must be a negative value.

Now, define the output of the SMC-MPP controller as v_{ref}, then combining steps (1) and (2), leads to (2):

$$\dot{v}_{ref} = -\dot{\sigma}\,. \qquad (2)$$

Thus, the control law of the proposed SMC-MPP controller can be designed as

$$v_{ref} = -\int \dot{\sigma}\, dt\,. \qquad (3)$$

Based on the exponential reaching law [18], the equation in (3) can also be written as:

$$v_{ref} = \int \left(k\,\sigma + \eta\ \mathrm{sgn}(\sigma)\right) dt\,, \qquad (4)$$

where η and k are the positive constants.

With sliding mode control law (4), MPP reference voltage can be generated under various weather conditions.

Design of SMC-MPPT controller. The proposed controller has advantages over existing solutions which rely on the linearization of the dynamics of the internal current loop, since the chosen sliding surface S is a linear combination of the input capacitor current and the error of PV voltage

$$S = \lambda_1 \left(v_{PV} - v_{ref} \right) + \lambda_2 \, i_{C_1} , \tag{5}$$

where λ_1 and λ_2 are the constants.

The main advantage of this approach is voltage regulation v_{pv} without additional regulators based on linearized models. A good alternative to define the behavior of PV voltage is to include both the error with respect to the reference voltage given by a SMC-MPP algorithm and the voltage derivative in the expression of the sliding surface. The voltage derivative can be obtained by measuring the current of the input capacitor i_{C1}.

This work is based on the choice of a sliding surface S given in (5), which makes it possible to explore the stability of the PV voltage in presence of climatic changes. The dynamic behavior of the DC-DC converter is modeled by (6), (7):

$$i_{C_1} = C_1 . \frac{dv_{PV}}{dt} = i_{PV} - i_L ; \tag{6}$$

$$v_L = L \frac{di_L}{dt} = v_{PV} - v_{C2} \left(1 - u \right) , \tag{7}$$

where C_1, L and v_{C2} are respectively the output capacitance, inductance and the output voltage of the boost converter; i_L is the inductor current; v_L is the inductor voltage and u is the control signal.

The PV current i_{pv} can be modeled by the simplified single diode model given by (8) [19]:

$$i_{PV} = i_{SC} - I_R \left(e^{\alpha v_{PV}} - 1 \right) . \tag{8}$$

where i_{SC} is the short-circuit current; I_R is the saturation current of the diode; α is the thermal voltage which depends on the temperature of the panel [20], knowing that the short-circuit current is approximately proportional to the irradiance E [21]:

$$i_{SC} = K_S \, E . \tag{9}$$

The design of sliding mode regulators supports the desired performance in a systematic way. It also requires fulfilling three conditions: transversality, equivalent control and reachability [18, 19, 22, 23].

Transversality condition. The derivative of the function S with respect to time is given by (10):

$$\begin{aligned} \frac{dS}{dt} = \frac{d\, v_{PV}}{dt} \left(\lambda_1 + \lambda_2 \frac{d\, i_{PV}}{d\, v_{PV}} \right) - \lambda_1 \frac{d\, v_{ref}}{dt} + \\ + \lambda_2 \frac{d\, i_{SC}}{dt} - \lambda_2 \left(\frac{v_{PV} - v_{C2} \left(1 - u \right)}{L} \right) . \end{aligned} \tag{10}$$

By differentiating (10) versus u, we have:

$$\frac{d \dfrac{dS}{dt}}{du} = - \frac{\lambda_2 \, v_{C2}}{L} \neq 0 , \tag{11}$$

since v_{C2} and L are both positive, the transversality condition is then satisfied if the parameter $\lambda_2 \neq 0$.

Equivalent control condition. The equivalent control u_{eq} is a continuous function which is used to maintain the variable to be controlled on the sliding surface. It is obtained thanks to the invariance conditions of the sliding surface. For the DC-DC converter, the correct range is given by $0 \prec u_{eq} \prec 1$

$$d \frac{dS}{dt} = 0 \quad \rightarrow \; 0 < u_{eq} < 1 . \tag{12}$$

By replacing u by u_{eq} in (12), while respecting the inequality given in (11), we obtain:

$$\begin{aligned} 0 < u_{eq} = \frac{L}{v_{C2}} \left[\left(\frac{\lambda_1}{\lambda_2} + A \right) \frac{d\, v_{PV}}{dt} - \frac{\lambda_1}{\lambda_2} \frac{d\, v_{ref}}{dt} \right] \\ + \frac{L}{v_{C2}} \frac{d\, i_{SC}}{dt} - \frac{v_{PV}}{v_{C2}} + 1 < 1 \end{aligned} \tag{13}$$

where:

$$A = - I_R \, \alpha \, e^{\alpha v_{pv}} . \tag{14}$$

Considering that the system is maintained on the sliding surface $S = 0$, equation (15) obtained from (5) and (6) describes the dynamics of the sliding mode, which can be analyzed in the Laplace domain as indicated by (14):

$$i_{C_{in}} = C_1 \frac{d\, v_{PV}}{dt} = - \frac{\lambda_1}{\lambda_2} \left(v_{PV} - v_{ref} \right) ; \tag{15}$$

$$\frac{V_{PV}(s)}{V_{ref}(s)} = \frac{1}{\dfrac{\lambda_2 . C_1}{\lambda_1} s + 1} . \tag{16}$$

Equation (16) shows the existence of an equivalent pole $-\lambda_1/\lambda_2 C_1$. Therefore, λ_1 and λ_2 must be of the same sign to ensure the stability of the system.

Reachability conditions. These conditions allow the sliding surface to have a dynamic of convergence towards zero. As discussed in the previous section, the proposed approach design requires a negative value for the parameter λ_2; thus, the existence condition in (11) is positive, imposing the reachability conditions (17), (18):

$$\lim_{S \to 0^-} \left. \frac{d\, S}{dt} \right|_{u=1} = \left. \frac{d\, S}{dt} \right|_{u=1, \; S=0} > 0 ; \tag{17}$$

$$\lim_{S \to 0^+} \left. \frac{d\, S}{dt} \right|_{u=0} = \left. \frac{d\, S}{dt} \right|_{u=0, \; S=0} < 0 . \tag{18}$$

The value of u is imposed for each condition: $u = 1$ for $S \prec 0$ and $u = 0$ for $S \succ 0$ [18, 23]. Substituting (10) in (17) and (18), leads to (19) and (20) which confirm that the condition $S\dot{S} \prec 0$ is satisfied:

$$\begin{aligned} \lim_{S \to 0^-} \frac{d\, S}{dt} = \frac{d\, v_{PV}}{dt} \left(\lambda_1 + \lambda_2 \, A \right) - \lambda_1 \frac{d\, v_{ref}}{dt} + \\ + \lambda_2 \frac{d\, i_{SC}}{dt} - \lambda_2 \left(\frac{v_{PV}}{L} \right) > 0 ; \end{aligned} \tag{19}$$

$$\begin{aligned} \lim_{S \to 0^+} \frac{d\, S}{dt} = \frac{d\, v_{PV}}{dt} \left(\lambda_1 + \lambda_2 \, A \right) - \lambda_1 \frac{d\, v_{ref}}{dt} + \\ + \lambda_2 \frac{d\, i_{SC}}{dt} - \lambda_2 \left(\frac{v_{PV} - v_b}{L} \right) < 0 . \end{aligned} \tag{20}$$

Simulation results. In order to test and compare the performance of the proposed SMC-MPPT algorithm to the conventional P&O algorithm, the PV solar system is modeled and implemented in MATLAB/Simulink software.

The Simulink PV system model shown in Fig. 3 was selected to assess the performance and the effectiveness of the proposed controller SMC-MPPT. Specification parameters PV power generation are given in Table 1.

Table 1

PV system specifications

Parameter	Value
Maximum output power P_{max}, W	85
Maximum voltage V_{PMM}, V	18
Maximum current I_{PMM}, A	4.72
Open circuit voltage V_{OC}, V	22.1
Short circuit current I_{SC}, A	5
Temperature coefficient of V_{OC}, %·°C^{-1}	–0.8
Temperature coefficient of I_{SC}, %·°C^{-1}	0.00065

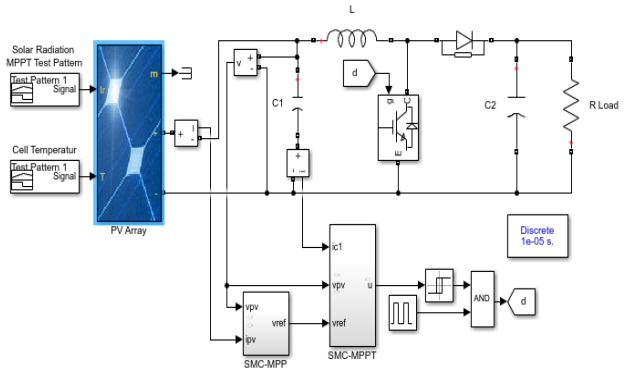

Fig. 3. Simulink PV system model

A comparative study with strictly identical simulation parameters is carried out. The PV system consists of a typical PV generator BP585, a DC-DC boost converter and a load. The input voltage of the DC-DC converter is set to 18 V, the inductance value is equal to 22.5 mH, the input capacitor is set to 132 µF, the output capacitor is equal to 66 µF and the output resistive load is set to 12 Ω. In DC-DC converter applications, hysteresis comparators are commonly used to implement the proposed controller. To limit the switching frequency, a hysteresis band (h) must be introduced to the sliding surface [22, 23]. As a result, the sliding surface's limits will be:

$$-\frac{h}{2} \le S \le \frac{h}{2}. \qquad (21)$$

Equation (22) which is derived from inequalities (17), (18) shows this constraint:

$$S \le -\frac{h}{2} \rightarrow u = 1 \wedge S \ge \frac{h}{2} \rightarrow u = 0. \qquad (22)$$

Several simulations were carried out taking into account variations in climatic conditions, namely irradiance and temperature. Obtained results are presented for a period of 1 s. Each figure presents a comparison of the characteristics of the PV system governed by the cascade SMC and P&O approaches. Zooming was carried out at two different locations, the first at the beginning of the profile to illustrate the response time and the second to show the oscillations around the MPP.

Case 1: variable temperature. A variable temperature is used with a constant irradiance equal to 1000 W/m^2.

It can be noted from Fig. 5–7, that the response times are approximately 2 ms and 17.5 ms. During the transient regime, we notice that the trajectory of the PPM obtained by applying the cascade SMC control is better than that obtained with the P&O. In steady state, the P&O oscillates around the PPM between 81.75 W and 84.45 W as shown in Fig. 4.

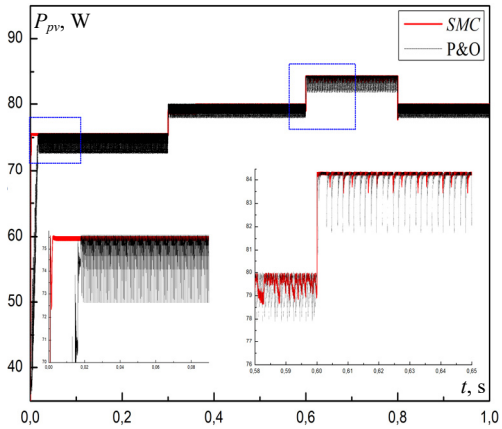

Fig. 4. PV power evolution for case 1

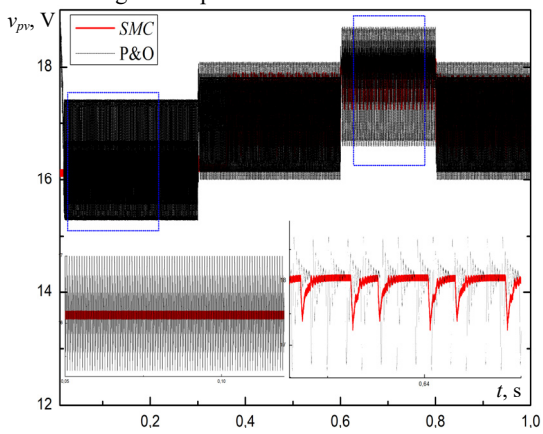

Fig. 5. PV voltage evolution for case 1

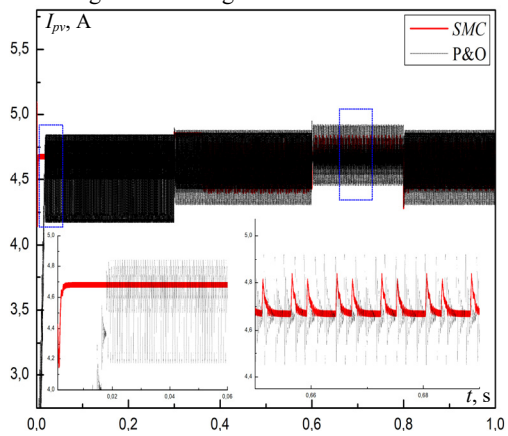

Fig. 6. PV current evolution for case 1

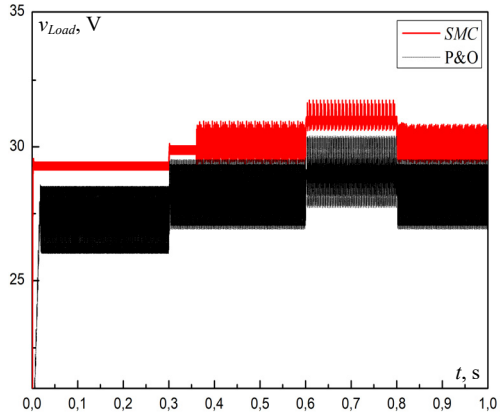

Fig. 7. Load voltage evolution for case 1

Case 2: variable irradiance. To validate the effectiveness of the proposed approach, another robustness test was carried out where a trapezoidal irradiance profile was chosen (the temperature is set to 25 °C). The simulation results as given in Fig. 8–11 show that the P&O method exhibits poor performance in its dynamic response. With a constant increase in irradiance in the form of a positive slope, the P&O method fails to follow the true path of the MPP thus causing losses of power and energy. Under decreasing variation in irradiation, the same monitoring problem is observed. In addition, in static mode the power of the PV constantly oscillates around MPP.

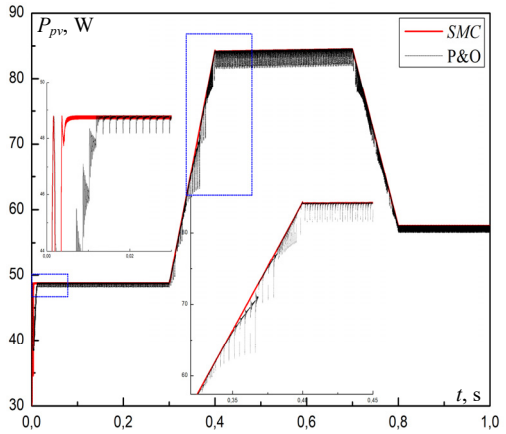

Fig. 8. PV power evolution for case 2

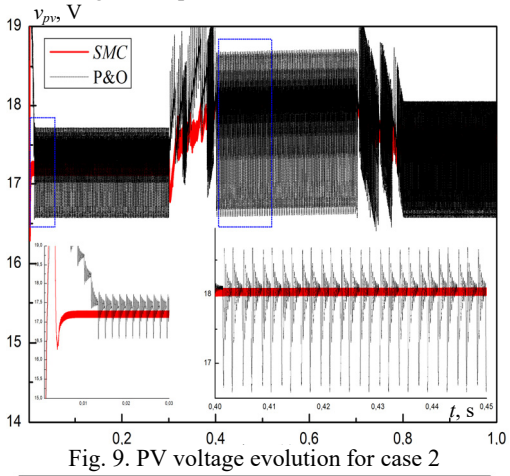

Fig. 9. PV voltage evolution for case 2

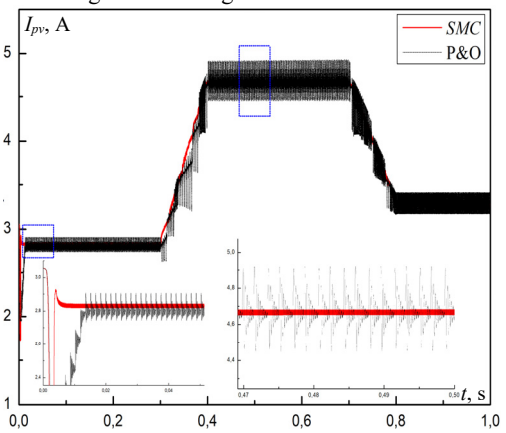

Fig. 10. PV current evolution for case 2

Unlike the P&O algorithm, the proposed approach reveals remarkable performance in all irradiance conditions. The SMC controller perfectly follows the MPP trajectory as shown in the zoomed parts where the tracking of the MPP is perfect and the minimization of power oscillation in static regime is effective.

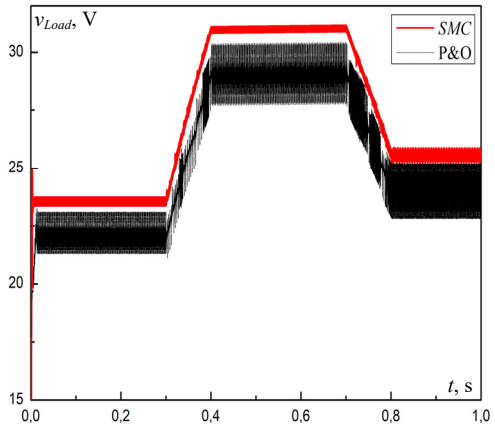

Fig. 11. Load voltage evolution for case 2

Conclusion. The study reported in this paper focused on the control of a solar system that uses a DC-DC boost converter to supply electrical clean power. An advanced procedure for the designation of a sliding mode based maximum power point tracking control for photovoltaic systems has been proposed. This control ensures maximum power point operation and robustness to irradiance and temperature fluctuations, as well as reducing oscillations at the converter's output voltage. The simulation results made it possible to demonstrate the performance and robustness of the proposed control law.

Conflict of interest. The authors declare that they have no conflicts of interest.

REFERENCES

1. Wu Libo, Zhao Zhengming, Liu Jianzheng. A Single-Stage Three-Phase Grid-Connected Photovoltaic System With Modified MPPT Method and Reactive Power Compensation. *IEEE Transactions on Energy Conversion*, 2007, vol. 22, no. 4, pp. 881-886. doi: https://doi.org/10.1109/TEC.2007.895461.

2. Janardhan G., Surendra Babu N.N.V., Srinivas G.N. Single phase transformerless inverter for grid connected photovoltaic system with reduced leakage current. *Electrical Engineering & Electromechanics*, 2022, no. 5, pp. 36-40. doi: https://doi.org/10.20998/2074-272X.2022.5.06.

3. Muthubalaji S., Devadasu G., Srinivasan S., Soundiraraj N. Development and validation of enhanced fuzzy logic controller and boost converter topologies for a single phase grid system. *Electrical Engineering & Electromechanics*, 2022, no. 5, pp. 60-66. doi: https://doi.org/10.20998/2074-272X.2022.5.10.

4. Saeed H., Mehmood T., Khan F.A., Shah M.S., Ullah M.F., Ali H. An improved search ability of particle swarm optimization algorithm for tracking maximum power point under shading conditions. *Electrical Engineering & Electromechanics*, 2022, no. 2, pp. 23-28. doi: https://doi.org/10.20998/2074-272X.2022.2.04.

5. Balakishan P., Chidambaram I.A., Manikandan M. Improvement of power quality in grid-connected hybrid system with power monitoring and control based on internet of things approach. *Electrical Engineering & Electromechanics*, 2022, no. 4, pp. 44-50. doi: https://doi.org/10.20998/2074-272X.2022.4.06.

6. Chandramouli B., Vijayaprabhu A., Arun Prasad D., Kathiravan K., Udhayaraj N., Vijayasanthi M. Design of single switch-boosted voltage current suppressor converter for uninterrupted power supply using green resources integration. *Electrical Engineering & Electromechanics*, 2022, no. 5, pp. 31-35. doi: https://doi.org/10.20998/2074-272X.2022.5.05.

7. Nebti K., Lebied R. Fuzzy maximum power point tracking compared to sliding mode technique for photovoltaic systems based on DC-DC boost converter. *Electrical Engineering & Electromechanics*, 2021, no. 1, pp. 67-73. doi: https://doi.org/10.20998/2074-272X.2021.1.10.
8. Behih K., Attoui H. Backstepping Terminal Sliding Mode MPPT Controller for Photovoltaic Systems. *Engineering, Technology & Applied Science Research*, 2021, vol. 11, no. 2, pp. 7060-7067. doi: https://doi.org/10.48084/etasr.4101.
9. Sera D., Mathe L., Kerekes T., Spataru S.V., Teodorescu R. On the Perturb-and-Observe and Incremental Conductance MPPT Methods for PV Systems. *IEEE Journal of Photovoltaics*, 2013, vol. 3, no. 3, pp. 1070-1078. doi: https://doi.org/10.1109/JPHOTOV.2013.2261118.
10. Huynh D.C., Dunnigan M.W. Development and Comparison of an Improved Incremental Conductance Algorithm for Tracking the MPP of a Solar PV Panel. *IEEE Transactions on Sustainable Energy*, 2016, vol. 7, no. 4, pp. 1421-1429. doi: https://doi.org/10.1109/TSTE.2016.2556678.
11. Kok Soon Tey, Mekhilef S. Modified Incremental Conductance Algorithm for Photovoltaic System Under Partial Shading Conditions and Load Variation. *IEEE Transactions on Industrial Electronics*, 2014, vol. 61, no. 10, pp. 5384-5392. doi: https://doi.org/10.1109/TIE.2014.2304921.
12. Chiu C.-S., Ouyang Y.-L., Ku C.-Y. Terminal sliding mode control for maximum power point tracking of photovoltaic power generation systems. *Solar Energy*, 2012, vol. 86, no. 10, pp. 2986-2995. doi: https://doi.org/10.1016/j.solener.2012.07.008.
13. Moutaki K., Ikaouassen H., Raddaoui A., Rezkallah M. Lyapunov Function Based Control for Grid-Interfacing Solar Photovoltaic System with Constant Voltage MPPT Technique. *Advances in Intelligent Systems and Computing*, 2019, vol. 912, pp. 210-219. doi: https://doi.org/10.1007/978-3-030-12065-8_20.
14. Chung H.S.-H., Tse K.K., Hui S.Y.R., Mok C.M., Ho M.T. A novel maximum power point tracking technique for solar panels using a SEPIC or Cuk converter. *IEEE Transactions on Power Electronics*, 2003, vol. 18, no. 3, pp. 717-724. doi: https://doi.org/10.1109/TPEL.2003.810841.
15. Patel H., Agarwal V. Maximum Power Point Tracking Scheme for PV Systems Operating Under Partially Shaded Conditions. *IEEE Transactions on Industrial Electronics*, 2008, vol. 55, no. 4, pp. 1689-1698. doi: https://doi.org/10.1109/TIE.2008.917118.
16. Siew-Chong Tan, Lai Y.M., Tse C.K. General Design Issues of Sliding-Mode Controllers in DC–DC Converters. *IEEE Transactions on Industrial Electronics*, 2008, vol. 55, no. 3, pp. 1160-1174. doi: https://doi.org/10.1109/TIE.2007.909058.
17. Levron Y., Shmilovitz D. Maximum Power Point Tracking Employing Sliding Mode Control. *IEEE Transactions on Circuits and Systems I: Regular Papers*, 2013, vol. 60, no. 3, pp. 724-732. doi: https://doi.org/10.1109/TCSI.2012.2215760.
18. Slotine J.J.E, Li W. *Applied nonlinear control*. Englewood Cliffs, NJ, Prentice Hall, New Jersey, 1991. 461 p.
19. Wang A., Jia X., Dong S. A New Exponential Reaching Law of Sliding Mode Control to Improve Performance of Permanent Magnet Synchronous Motor. *IEEE Transactions on Magnetics*, 2013, vol. 49, no. 5, pp. 2409-2412. doi: https://doi.org/10.1109/TMAG.2013.2240666.
20. Petrone G., Ramos-Paja C.A. Modeling of photovoltaic fields in mismatched conditions for energy yield evaluations. *Electric Power Systems Research*, 2011, vol. 81, no. 4, pp. 1003-1013. doi: https://doi.org/10.1016/j.epsr.2010.12.008.
21. Bianconi E., Calvente J., Giral R., Mamarelis E., Petrone G., Ramos-Paja C.A., Spagnuolo G., Vitelli M. A Fast Current-Based MPPT Technique Employing Sliding Mode Control. *IEEE Transactions on Industrial Electronics*, 2013, vol. 60, no. 3, pp. 1168-1178. doi: https://doi.org/10.1109/TIE.2012.2190253.
22. Shah M.S., Mahmood T., Ullah M.F. Power quality improvement using ultra capacitor based dynamic voltage restorer with real twisting sliding mode control. *Electrical Engineering & Electromechanics*, 2022, no. 1, pp. 59-63. doi: https://doi.org/10.20998/2074-272X.2022.1.08.
23. Sira-Ramirez H. Sliding motions in bilinear switched networks. *IEEE Transactions on Circuits and Systems*, 1987, vol. 34, no. 8, pp. 919-933. doi: https://doi.org/10.1109/TCS.1987.1086242.

Received 24.07.2022
Accepted 16.11.2022
Published 06.01.2023

Mohammed Amine Hessad [1], *PhD Student,*
Ziyad Bouchama[2,3], *PhD, Associate Professor,*
Said Benaggoune[1], *Professor,*
Khalissa Behih[4], *PhD, Associate Professor,*
[1] LSTEB Laboratory, Department of Electrical Engineering, Mostefa Ben Boulaïd University of Batna 2, Batna, Algeria,
e-mail: mouh_tech@hotmail.fr; s.benaggoune@univ-batna2.dz
[2] Department of Electromechanical Engineering, Mohamed El Bachir El Ibrahimi University of Bordj Bou Arreridj, Algeria,
e-mail: ziyad.bouchama@univ-bba.dz (Corresponding Author)
[3] QUERE Laboratory, Department of Electrical Engineering, Ferhat Abbas University of Setif 1, Setif, Algeria,
e-mail: ziad.bouchama@univ-setif.dz
[4] LSI Laboratory, Department of Electrical Engineering, Ferhat Abbas University of Setif 1, Setif, Algeria,
e-mail: khalissabehih@univ-setif.dz

How to cite this article:
Hessad M.A., Bouchama Z., Benaggoune S., Behih K. Cascade sliding mode maximum power point tracking controller for photovoltaic systems. *Electrical Engineering & Electromechanics*, 2023, no. 1, pp. 51-56. doi: https://doi.org/10.20998/2074-272X.2023.1.07

UDC 621.3 https://doi.org/10.20998/2074-272X.2023.1.08

A. Khatir, Z. Bouchama, S. Benaggoune, N. Zerroug

Indirect adaptive fuzzy finite time synergetic control for power systems

Introduction. *Budget constraints in a world ravenous for electrical power have led utility companies to operate generating stations with full power and sometimes at the limit of stability. In such drastic conditions the occurrence of any contingency or disturbance may lead to a critical situation starting with poorly damped oscillations followed by loss of synchronism and power system instability. In the past decades, the utilization of supplementary excitation control signals for improving power system stability has received much attention. Power system stabilizers (PSS) are used to generate supplementary control signals for the excitation system in order to damp low-frequency oscillations caused by load disturbances or short-circuit faults.* ***Problem.*** *Adaptive power system stabilizers have been proposed to adequately deal with a wide range of operating conditions, but they suffer from the major drawback of requiring parameter model identification, state observation and on-line feedback gain computation. Power systems are nonlinear systems, with configurations and parameters that fluctuate with time that which require a fully nonlinear model and an adaptive control scheme for a practical operating environment. A new nonlinear adaptive fuzzy approach based on synergetic control theory which has been developed for nonlinear power system stabilizers to overcome above mentioned problems.* ***Aim.*** *Synergetic control theory has been successfully applied in the design of power system stabilizers is a most promising robust control technique relying on the same principle of invariance found in sliding mode control, but without its chattering drawback. In most of its applications, synergetic control law was designed based on an asymptotic stability analysis and the system trajectories evolve to a specified attractor reaching the equilibrium in an infinite time. In this paper an indirect finite time adaptive fuzzy synergetic power system stabilizer for damping local and inter-area modes of oscillations for power systems is presented.* ***Methodology.*** *The proposed controller design is based on an adaptive fuzzy control combining a synergetic control theory with a finite-time attractor and Lyapunov synthesis. Enhancing existing adaptive fuzzy synergetic power system stabilizer, where fuzzy systems are used to approximate unknown system dynamics and robust synergetic control for only providing asymptotic stability of the closed-loop system, the proposed technique procures finite time convergence property in the derivation of the continuous synergetic control law. Analytical proofs for finite time convergence are presented confirming that the proposed adaptive scheme can guarantee that system signals are bounded and finite time stability obtained.* ***Results.*** *The performance of the proposed stabilizer is evaluated for a single machine infinite bus system and for a multi machine power system under different type of disturbances. Simulation results are compared to those obtained with a conventional adaptive fuzzy synergetic controller.* References 20, table 1, figures 9.

Key words: **adaptive fuzzy systems, synergetic control theory, finite time convergence, power system stabilizer, multi-machine power system.**

Вступ. *Бюджетні обмеження у світі, жадібному до електроенергії, змушують комунальні підприємства експлуатувати станції, що генерують, на повну потужність, а іноді і на межі стабільності. У таких різких умовах виникнення будь-якої позаштатної ситуації або збурення може призвести до виникнення критичної ситуації, що починається з погано згасаючих коливань з подальшою втратою синхронізму та нестійкістю енергосистеми. В останні десятиліття велика увага приділялася використанню додаткових сигналів, керуючих збудження, для підвищення стійкості енергосистеми. Стабілізатори енергосистеми (СЕС) служать для вироблення додаткових сигналів керування системою збудження з метою гасіння низькочастотних коливань, спричинених збуреннями навантаження або короткими замиканнями.* ***Проблема***. *Адаптивні стабілізатори енергосистем були запропоновані для того, щоб адекватно справлятися з широким діапазоном робочих умов, але вони страждають від основного недоліку, що полягає в необхідності ідентифікації моделі параметрів, спостереження за станом та обчислення коефіцієнта посилення зворотного зв'язку в режимі реального часу. Енергетичні системи є нелінійними системами з конфігураціями та параметрами, які змінюються з часом, що потребує повністю нелінійної моделі та схеми адаптивного управління для практичного операційного середовища. Новий нелінійний адаптивно-нечіткий підхід, заснований на синергетичній теорії управління, розроблений для нелінійних стабілізаторів енергосистем для подолання вищезазначених проблем.* ***Мета***. *Теорія синергетичного управління успішно застосовувалася під час проєктування стабілізаторів енергосистем. Це найбільш перспективний надійний метод управління, заснований на тому ж принципі інваріантності, що і в ковзному режимі управління, але без його недоліку, пов'язаного з вібрацією. У більшості своїх програм синергетичний закон управління був розроблений на основі аналізу асимптотичної стійкості, і траєкторії системи еволюціонують до заданого атрактора, що досягає рівноваги за нескінченний час. У статті подано непрямий адаптивний нечіткий синергетичний стабілізатор енергосистеми з кінцевим часом для гасіння локальних та міжзонових мод коливань енергосистем.* ***Методологія.*** *Пропонована конструкція регулятора заснована на адаптивному нечіткому управлінні, що поєднує синергетичну теорію управління з атрактором кінцевого часу та синтезом Ляпунова. Удосконалюючи існуючий стабілізатор адаптивної нечіткої синергетичної енергосистеми, де нечіткі системи використовуються для апроксимації динаміки невідомої системи та надійного синергетичного управління тільки для забезпечення асимптотичної стійкості замкнутої системи, запропонований метод забезпечує властивість збіжності за кінцевий час при виведенні безперервного синергетичного закону керування. Наведено аналітичні докази збіжності за кінцевий час, що підтверджують, що запропонована адаптивна схема може гарантувати обмеженість сигналів системи та отримання стійкості за кінцевий час.* ***Результати***. *Працездатність пропонованого стабілізатора оцінюється для одномашинної системи з нескінченними шинами і багатомашинної енергосистеми при різних типах збурень. Результати моделювання порівнюються з результатами, отриманими за допомогою звичайного нечіткого адаптивного синергетичного регулятора.* Бібл. 20, табл. 1, рис. 9.

Ключові слова: **адаптивні нечіткі системи, синергетична теорія управління, збіжність за кінцевий час, стабілізатор енергосистеми, багатомашинна енергосистема.**

Introduction. Power systems are one of the most complex and nonlinear systems, with configurations and parameters fluctuating with time thus require a fully nonlinear model and an adaptive control scheme for adequate and sound operating environment [1-4]. Therefore, guaranteeing system stability for all operating condition is a major concern for utility companies. It is a recognized fact that hindering low frequency oscillations often occur in power networks upon advent of

perturbations and power system stabilizers (PSS) have been developed to suppress them and to enhance overall system dynamic stability. PSS are used to generate supplementary control signals for the excitation system in order to damp low-frequency oscillations during disturbances [3-5]. Adaptive stabilizers have been proposed to provide better dynamic performance over a wide range of operating conditions [3, 4], but they suffer from the major drawback of requiring parameter model identification, state observation and on-line feedback gain computation. However, a nonlinear adaptive fuzzy approach based on synergetic control theory (SC) has been developed for nonlinear power system stabilizers [6, 7] to overcome above mentioned problems.

Synergetic control, a powerful tool for nonlinear system control [8-12] is a most promising robust control approach relying on the same principle of invariance found in sliding mode control, but devoid of its shortcoming: inherent chattering. Its robustness and its ease in implementation have put forth this recent control technique. Synergetic control has been successfully applied in the design of power system stabilizers [6-8]. In most of these papers, synergetic control law was designed based on an asymptotic stability analysis in which system trajectories reach the equilibrium point in infinite time. Several papers have proposed a so called terminal approach resulting in a finite time convergence based on terminal attractor techniques [13-15]; it is evident that reducing the time required in reaching the equilibrium point reinforces convergence as well as dwarfs disturbance impacts.

In the present paper, the first contribution lies in investigating the efficiency and robustness of indirect finite time adaptive fuzzy synergetic PSS (ITFSC-PSS) to control partially known or unknown systems and the second one consists in determining a new dynamic evolution of the synergetic attractor, such that system trajectories evolve to a specified attractor reducing the time required in reaching the equilibrium point and reinforcing the convergence as well as faster attenuation of disturbances. A nonlinear power system model consisting of a single machine connected to an infinite bus and a nonlinear multi-machine power system model, are used to assess performance and effectiveness of the proposed controllers. Performances obtained with the proposed ITFSC-PSS are compared to those obtained using an indirect adaptive fuzzy synergetic power system stabilizer (IFSC-PSS) [6], under different operating conditions.

Synergetic power system stabilizer. In order to design the power system stabilizer proposed in this paper, a power system dynamics can be expressed in a canonical form given in [6, 7, 16, 17], using speed variation $\Delta\omega_i = \omega_i - \omega_{0i}$ and the accelerating power $\Delta P_i = P_{mi} - P_{ei}$ as measurable input variables to the PSS. The synchronous machine system model can be represented in the following non linear state-space equations form [8, 16, 17]:

$$\begin{cases} \Delta\dot{\omega}_i = \dfrac{1}{2H_i}\Delta P_i \\ \Delta\dot{P}_i = f_i\left(\Delta\omega_i, \Delta P_i\right) + g_i\left(\Delta\omega_i, \Delta P_i\right)u_i \end{cases} \quad (1)$$

where ω_i is the angular speed in per units; P_{ei} is the delivered electrical power; P_{mi} is the mechanical input power treated as a constant in the excitation controller design and H_i is the per unit machine inertia constant; u_i is the necessary control signal to be designed, i.e. the PSS output; f_i (.) and g_i (.) are the nonlinear functions with g_i (.) $\neq 0$ in the controlled region.

It has been assumed that two nonlinear functions can be found from system dynamics analysis [6, 7, 16, 17]. In generic terms, the equation set (1) for the i^{th} generator is:

$$\begin{cases} \dot{x}_1 = \Delta\dot{\omega} = \dfrac{1}{2H}x_2 \\ \dot{x}_2 = \Delta\dot{P} = f\left(x_1, x_2\right) + g\left(x_1, x_2\right)u \end{cases} \quad (2)$$

Synthesis of a synergetic controller begins with a choice of a state variables function called a macro-variable:

$$\sigma = \lambda x_1 + x_2; \qquad \lambda \succ 0. \quad (3)$$

Desired dynamic evolution of the macro-variable can be designer chosen such as (4):

$$\dot{\sigma} + \tau\sigma = 0, \quad (4)$$

where τ is the positive constant imposing a designer chosen speed convergence to the desired manifold.

Differentiating the macro-variable (3) along (2) leads to (5):

$$\begin{aligned} \dot{\sigma} &= \lambda\dot{x}_1 + \dot{x}_2 \\ &= \frac{\lambda}{2H}x_2 + \left(f\left(x_1, x_2\right) + g\left(x_1, x_2\right)u\right) \end{aligned} \quad (5)$$

Combining equations (4) and (5), leads to (6):

$$\frac{\lambda}{2H}x_2 + f\left(x_1, x_2\right) + g\left(x_1, x_2\right)u = -\tau\sigma. \quad (6)$$

Solving for the control law u, leads to (7):

$$u = -\left(\frac{\lambda}{2H}x_2 + f\left(x_1, x_2\right) + \tau\sigma\right)\left(g\left(x_1, x_2\right)\right)^{-1}. \quad (7)$$

The power system under synergetic control stabilizer (7) has an asymptotic stability and its trajectories converge to the equilibrium point in infinite time. Therefore, robust operating conditions may not be satisfied and even slight disturbances can destabilize the system. To improve robust tracking and finite time convergence, a terminal synergetic controller leading to fast response and more robust performance is proposed.

Finite time synergetic power system stabilizer. In this new approach, aiming to reinforce robustness and better tracking, a reformulation of the dynamic evolution of the macro-variable (4) is adopted by defining a new nonlinear functional equation given in (8).

$$\dot{\sigma} + \tau\ \sigma^{n/m} + \alpha\sigma = 0 \quad , \quad (8)$$

where $\alpha > 0$ is the constant and n, m are the odd positive integers.

It can be derived that the time to reach the equilibrium $\sigma = 0$ is [13-15]:

$$t^* = \frac{1}{\alpha\left(1 - m/n\right)}\ln\frac{\alpha\left|\sigma(0)\right|^{1-n/m} + \tau}{\tau}, \quad (9)$$

where t^* is the finite expressing a finite time convergence as opposed to the asymptotic infinite time convergence to the attractor $\sigma = 0$ resulting in the previous scheme.

This approach inspired from sliding mode techniques [13-15] will be used to express the finite time synergetic control law u. Using (5), (8), the synergetic control law is then obtained as:

$$u=-\left(\begin{array}{c}\alpha\sigma+\dfrac{\lambda}{2H}x_2+f\left(x_1,x_2\right)\\ +\tau\sigma^{n/m}\end{array}\right)\left(g\left(x_1,x_2\right)\right)^{-1}. \quad (10)$$

Equation (10) is used in the design of a synergetic power system stabilizer which assures finite time stability of the system, in which $\sigma = 0$ is guaranteed in finite time

Stability and robustness analysis. Under the control law (10) and macro-variable design constraint (8), the state trajectories of the power system (2) can be driven onto the manifold $\sigma = 0$ in a finite time (9) thus ensuring finite time stability.

Theorem 1 [13-15]: suppose that there exists a positive definite continuous function $v(t)$ with positive real numbers ρ, β and $0 < \gamma < 1$, such that $v(t)$ satisfies the differential inequality:

$$\dot{v}(t)\le-\rho v(t)-\beta v^{\gamma}(t)\ . \quad (11)$$

Then the positive definite continuous function $v(t)$ will converge to the origin in finite time given by:

$$t_f=\frac{1}{\rho(1-\gamma)}\ln\frac{\rho\left|v(0)\right|^{1-\gamma}+\beta}{\beta}. \quad (12)$$

Proof: let's consider Lyapunov function candidate: $v = \sigma^2 / 2$, where σ defined as in (3). Then the time derivative of v leads to:

$$\dot{v}=\sigma\dot{\sigma}=\sigma\left(\frac{\lambda}{2H}x_2+\left(f\left(x_1,x_2\right)+g\left(x_1,x_2\right)u\right)\right). \quad (13)$$

Substituting (10) into (13), one can obtain

$$\dot{v}\le-\tau\ \sigma^{1+n/m}-\alpha\sigma^2\ . \quad (14)$$

Using (11), (14) becomes

$$\dot{v}\le-\tau\,2^{(1+n/m)/2}v^{(1+n/m)/2}-2\alpha v\ . \quad (15)$$

Defining constants: ρ and β as: $\rho = 2\alpha$ and $\beta = \tau\cdot 2^{(1+n/m)/2}$, if the parameter $\gamma = (1+n/m)/2$ is chosen such that $0<(1+n/m)/2<1$, therefore, (15) can be further simplified as:

$$\dot{v}\le-\beta v^{\gamma}-\rho v\ . \quad (16)$$

Thus according to Theorem 1, the stability of the power system (1) is guaranteed and the state trajectories can be driven onto the manifold $\sigma = 0$ in a finite time t^* given in (9). Therefore, $\sigma = 0$ is achieved in finite time, and the proof is complete. However, power system parameters for nonlinear functions are not well known and imprecise; therefore it is difficult to implement the control law (10) for unknown nonlinear system model. A fuzzy logic system will now be used to address this latter issue.

Finite time adaptive fuzzy synergetic power system stabilizer. The control law (10) for power system (1) can be modified as:

$$u=-\left(\alpha\sigma+\frac{\lambda}{2H}x_2+f\left(x\right)+\tau\sigma^{n/m}\right)\left(g\left(x\right)\right)^{-1}. \quad (17)$$

In a practical real case where $f(x)$ and $g(x)$ are unknown functions, they are replaced by their fuzzy estimates [6, 7, 16, 17]:

$$\hat{f}(x/\theta_f)=\theta_f^T\xi(x)\,; \quad (18)$$

$$\hat{g}(x/\theta_g)=\theta_g^T\xi(x)\,, \quad (19)$$

where $\xi(x)$ is the fuzzy basis functions defined as:

$$\xi_l(\underline{x})=\frac{\prod_{i=1}^{n}\mu_{F_i^l}(x_i)}{\sum_{l=1}^{M}\left(\prod_{i=1}^{n}\mu_{F_i^l}(x_i)\right)}, \quad (20)$$

where $\mu_{F_i^l}(x_i)$ is the membership function value of x_i in labels of fuzzy sets F_i^l in $U=\prod_{i=1}^{n}U_i\in R^n$ and the parameters vectors θ_f and θ_g of the fuzzy logic systems (18) and (19), can be continuously updated as [6, 7, 16, 17]:

$$\dot{\theta}_f=\eta_1\sigma\xi(x)\,; \quad (21)$$

$$\dot{\theta}_g=\eta_2\sigma\xi(x)\,u\,, \quad (22)$$

where η_1 and η_2 are the positive constants that will be used as learning rates in the adaptation procedure.

It is to be noted that the approximation issue has been addressed in great details in [18] where the universal approximation theorem is used to prove that fuzzy systems can approximate any continuous real function on a compact set to any arbitrary accuracy, while fuzzy rules are derived based on experts' recommendations. Therefore the new control law is rewritten as:

$$u=-\left(\begin{array}{c}+\alpha\sigma+\dfrac{\lambda}{2H}x_2+\hat{f}\left(x/\theta_f\right)\\ +\tau\sigma^{n/m}\end{array}\right)\left(\hat{g}\left(x/\theta_g\right)\right)^{-1}. \quad (23)$$

The power system models shown in Fig. 1, Fig. 5 are used to evaluate performance of the terminal adaptive fuzzy synergetic stabilizer (23) and results obtained are compared with a IFSC-PSS [6]. Different operating conditions are used in a simulation study and results are given and discussed in the next section.

Simulation results. The basic function of a PSS is to damp power oscillations that occur upon perturbations such as sudden change of loads or in the event of short-circuit occurrence. In this study, we will investigate the performance of the proposed power system stabilizer as it is applied to both single machine infinite-bus and multi-machine power systems. The success of the proposed PSS, with the single-machine infinite-bus case, motivates us to test its capability on a multi-machine model.

Application to the single-machine infinite bus model. A simplified schematic diagram of a single-machine infinite-bus system, which illustrates the position of a PSS, has been shown in Fig. 1.

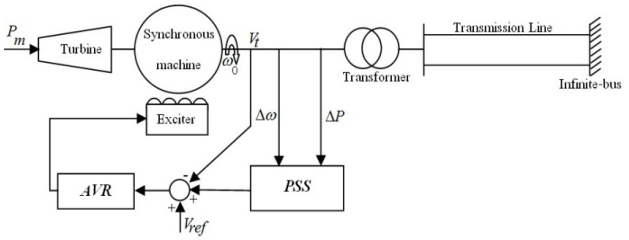

Fig. 1. Single-machine infinite-bus power system

The power system consists of a synchronous machine connected to an infinite bus through a transformer, a double transmission line and automatic voltage regulator (AVR) is represented by a four order model [3, 4]. The power system equations and parameters can be found in [4]. When the power system is operating

with a leading power factor, the stability margin is reduced and, thus, the PSS faces adverse operating conditions. This scenario is now considered and power system simulation is carried out under the following severe fault cases:

Case 1. 0.2 p.u. disturbance in mechanical torque occurring at $t = 1$ s.

Faster oscillations damping occurs, as can be seen in Fig. 2, for the ITFS-PSS than for the traditional fuzzy synergetic stabilizer IFSC-PSS under a mechanical torque disturbance. A larger control effort is solicited by FFSPSS but only as a transient that rapidly dies out as opposed to its counterpart.

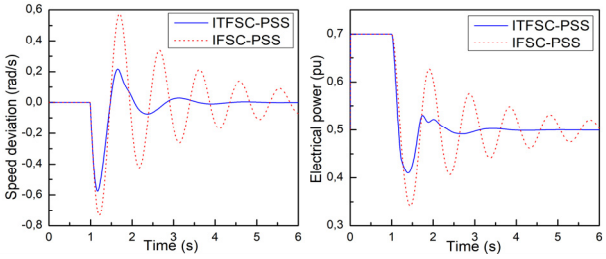

Fig. 2. System response for case 1

Case 2. Three-phase fault to ground on the transmission line occurring at $t = 1$ s with 0.06 s duration.

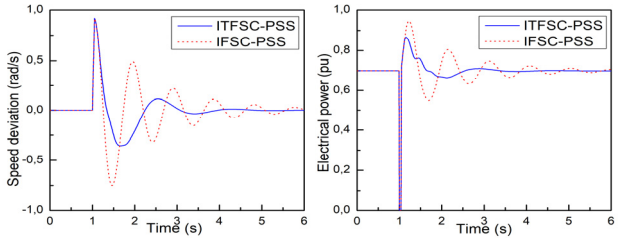

Fig. 3. System response for case 2

Even in the case of severe three-phase short circuit , the proposed controller effectively exhibits and confirms superior performance in improving finite time convergence of the system responses as clearly shown in Fig. 3, compared to IFSC-PSS.

Case 3. 0.1 p.u. step increase in reference voltage applied at $t = 1$ s.

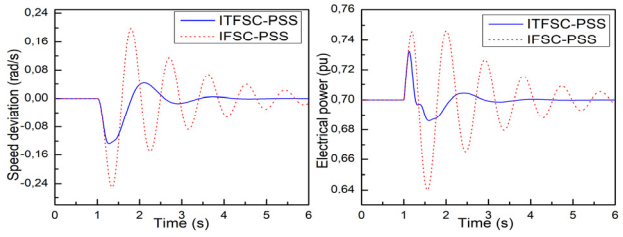

Fig. 4. System response in case 3

Simulation results show that the output responses of the IFSC-PSS are considerably affected by the step change in reference voltage as shown in Fig. 4, while oscillations are rapidly damped with the use of proposed PSS. It can be easily concluded that the latter achieves better robustness and has satisfactory time response under these types of disturbance and uncertainties over its presented counterpart.

Application to the multi-machine model. In this study, the three-machine nine-bus power system shown in Fig. 5 is considered. Details of the system data are given in [3, 4]. To identify the optimum location of PSS's in multi-machine power system the participation factor method [19] and the sensitivity of PSS effect method [20] were used. Both methods result indicate that G2 and G3 are the optimum location for installing PSS's in WSCC system. To assess the effectiveness and robustness of the proposed method over a wide range of loading conditions, three different cases designated as nominal, lightly and heavily loading are considered. The generator and system loading levels at these cases are given in Table 1.

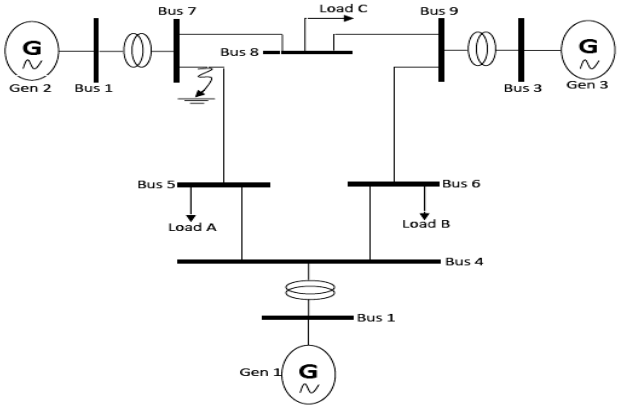

Fig. 5. Multi machine power system

Table 1

Loading operating conditions for the system (in p.u)

	Nominal		Heavy		Light	
Gen	*P*	*Q*	*P*	*Q*	*P*	*Q*
G1	0.72	0.27	2.1	1.09	0.36	0.16
G2	1.63	0.07	1.92	0.56	0.80	0.11
G3	0.85	0.11	1.28	0.36	0.45	0.20
Load	*P*	*Q*	*P*	*Q*	*P*	*Q*
A	1.25	0.50	2.0	0.80	0.65	0.55
B	0.9	0.30	1.80	0.60	0.45	0.35
C	1.0	0.35	1.50	0.60	0.50	0.25

The performance of the proposed controller under transient conditions is verified by applying a 6-cycle three-phase fault at $t = 1$ s, on bus 7 at the end of line 5-7 [4]. The fault is cleared by permanent tripping of the faulted line. System response under the nominal, lightly and heavily loading conditions are shown in Figs. 7-9. Figure 6 shows the system response without PSS. It is clear that the system response without PSS is highly oscillatory and eventually becomes unstable.

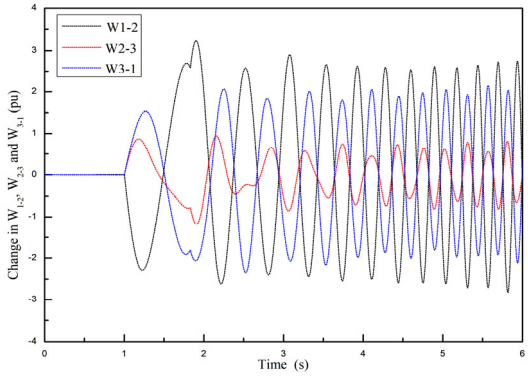

Fig. 6. Response of $W_{1\text{-}2}$, $W_{2\text{-}3}$ and $W_{3\text{-}1}$ in nominal operating condition without PSS

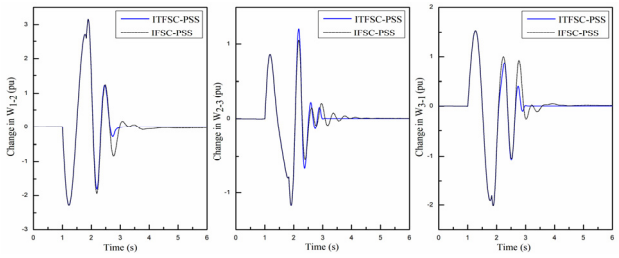

Fig. 7. Response of $W_{1\text{-}2}$, $W_{2\text{-}3}$ and $W_{3\text{-}1}$ in nominal operating condition

It is evident from the results in Figs. 7-9, that the damping of the low frequency oscillations in IFSC-PSS requires more time and has more oscillations before the speed deviation response is stabilized. The indirect adaptive fuzzy synergetic PSS improves the damping of oscillations in the change of operating conditions.

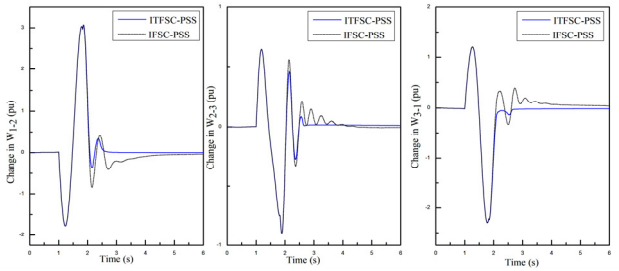

Fig. 8. Response of $W_{1\text{-}2}$, $W_{2\text{-}3}$ and $W_{3\text{-}1}$ in heavy operating condition

However, the superiority performance is clear with the proposed controller. The proposed controller provides significantly better damping enhancement in the power system oscillations. It is possible to observe that the overshoot and the settling time are reduced.

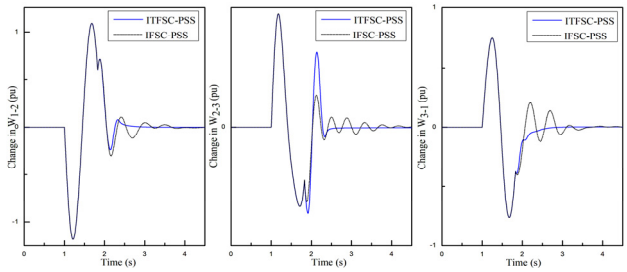

Fig. 9. Response of $W_{1\text{-}2}$, $W_{2\text{-}3}$ and $W_{3\text{-}1}$ in light operating condition

Conclusion. An indirect finite time adaptive fuzzy synergetic power system stabilizer has been presented and its performance evaluated by simulation using nonlinear power system models. Furthermore results have been compared to simple adaptive fuzzy synergetic PSS showing the pre-eminence of the proposed approach in both time response and steady-state performance. Despite the critical conditions, power systems considered have been subjected to the overall performance using the indirect adaptive finite time fuzzy synergetic power system stabilizer shows remarkable fast suppression of undesirable oscillations.

Conflict of interest. The authors declare that they have no conflicts of interest

REFERENCES

1. Chappa H., Thakur T. A novel load shedding methodology to mitigate voltage instability in power system. *Electrical Engineering & Electromechanics*, 2022, no. 3, pp. 63-70. doi: https://doi.org/10.20998/2074-272X.2022.3.09.

2. Zahra S.T., Khan R.U., Ullah M.F., Begum B., Anwar N. Simulation-based analysis of dynamic voltage restorer with sliding mode controller at optimal voltage for power quality enhancement in distribution system. *Electrical Engineering & Electromechanics*, 2022, no. 1, pp. 64-69. doi: https://doi.org/10.20998/2074-272X.2022.1.09.

3. Anderson P.M., Fouad A.A. *Power System Control and Stability*. IEEE Press, New York, 1993.

4. Kundur P. *Power System Stability and Control*. McGraw-Hill Inc., 1994.

5. Anwar N., Hanif A., Ali M.U., Zafar A. Chaotic-based particle swarm optimization algorithm for optimal PID tuning in automatic voltage regulator systems. *Electrical Engineering & Electromechanics*, 2021, no. 1, pp. 50-59. doi: https://doi.org/10.20998/2074-272X.2021.1.08.

6. Bouchama Z., Harmas M.N. Optimal robust adaptive fuzzy synergetic power system stabilizer design. *Electric Power Systems Research*, 2012, vol. 83, no. 1, pp. 170-175. doi: https://doi.org/10.1016/j.epsr.2011.11.003.

7. Bouchama Z., Essounbouli N., Harmas M.N., Hamzaoui A., Saoudi K. Reaching phase free adaptive fuzzy synergetic power system stabilizer. *International Journal of Electrical Power & Energy Systems*, 2016, vol. 77, pp. 43-49. doi: https://doi.org/10.1016/j.ijepes.2015.11.017.

8. Jiang Z. Design of a nonlinear power system stabilizer using synergetic control theory. *Electric Power Systems Research*, 2009, vol. 79, no. 6, pp. 855-862. doi: https://doi.org/10.1016/j.epsr.2008.11.006.

9. Benbouhenni H., Lemdani S. Combining synergetic control and super twisting algorithm to reduce the active power undulations of doubly fed induction generator for dual-rotor wind turbine system. *Electrical Engineering & Electromechanics*, 2021, no. 3, pp. 8-17. doi: https://doi.org/10.20998/2074-272X.2021.3.02.

10. Bouchama Z., Khatir A., Benaggoune S., Harmas M.N. Design and experimental validation of an intelligent controller for DC–DC buck converters. *Journal of the Franklin Institute*, 2020, vol. 357, no. 15, pp. 10353-10366. doi: https://doi.org/10.1016/j.jfranklin.2020.08.011.

11. Behih K., Saadi S., Bouchama Z. Hyperchaos synchronization using T-S fuzzy model based synergetic control theory. *International Journal of Intelligent Engineering and Systems*, 2021, vol. 14, no. 6, p. 588-595. doi: https://doi.org/10.22266/ijies2021.1231.52.

12. Mahgoun M.S., Badoud A.E. New design and comparative study via two techniques for wind energy conversion system. *Electrical Engineering & Electromechanics*, 2021, no. 3, pp. 18-24. doi: https://doi.org/10.20998/2074-272X.2021.3.03.

13. Zerroug N., Harmas M.N., Benaggoune S., Bouchama Z., Zehar K. DSP-based implementation of fast terminal synergetic control for a DC–DC Buck converter. *Journal of the Franklin Institute*, 2018, vol. 355, no. 5, pp. 2329-2343. doi: https://doi.org/10.1016/j.jfranklin.2018.01.004.

14. Zak M. Terminal attractors in neural networks. *Neural Networks*, 1989, vol. 2, no. 4, pp. 259-274. doi: https://doi.org/10.1016/0893-6080(89)90036-1.

15. Xu S.S., Chen C., Wu Z. Study of non singular fast terminal sliding-mode fault-tolerant control. *IEEE Transactions on Industrial Electronics*, 2015, vol. 62, no. 6, pp. 3906-3913. doi: https://doi.org/10.1109/TIE.2015.2399397.

16. Hossein-Zadeh N., Kalam A. An indirect adaptive fuzzy-logic power system stabiliser. *International Journal of Electrical Power & Energy Systems*, 2002, vol. 24, no. 10, pp. 837-842. doi: https://doi.org/10.1016/S0142-0615(01)00093-X.

17. Saoudi K., Harmas M.N. Enhanced design of an indirect adaptive fuzzy sliding mode power system stabilizer for multi-machine power systems. *International Journal of Electrical Power & Energy Systems*, 2014, vol. 54, pp. 425-431. doi: https://doi.org/10.1016/j.ijepes.2013.07.034.

18. Wang L.X. Stable adaptive fuzzy control of nonlinear systems. *IEEE Transactions on Fuzzy Systems*, 1993, vol. 1, no. 2, pp. 146-155. doi: https://doi.org/10.1109/91.227383.
19. Hsu Y.-Y., Chen C.-L. Identification of optimum location for stabiliser applications using participation factors. *IEE Proceedings C Generation, Transmission and Distribution*, 1987, vol. 134, no. 3, pp. 238-244. doi: https://doi.org/10.1049/ip-c.1987.0037.
20. Zhou E.Z., Malik O.P., Hope G.S. Theory and method for selection of power system stabilizer location. *IEEE Transactions on Energy Conversion*, 1991, vol. 6, no. 1, pp. 170-176. doi: https://doi.org/10.1109/60.73804.

Received 25.06.2022
Accepted 12.09.2022
Published 06.01.2023

Abdelfatah Khatir[1], *PhD Student,*
Ziyad Bouchama[2,3], *PhD, Associate Professor,*
Said Benaggoune[1], *Professor,*
Nadjat Zerroug[2], *PhD, Associate Professor,*
[1] LSTEB Laboratory, Department of Electrical Engineering, Mostefa Ben Boulaïd University of Batna 2, Batna, Algeria,
e-mail: abdelfatah.khatir@univ-bba.dz;
s.benaggoune@univ-batna2.dz
[2] QUERE Laboratory, Department of Electrical Engineering, Ferhat Abbas University of Setif 1, Setif, Algeria,
e-mail: ziad.bouchama@univ-setif.dz (Corresponding Author);
nadjatzerroug@univ-setif.dz
[3] Department of Electromechanical Engineering, Mohamed El Bachir El Ibrahimi University of Bordj Bou Arreridj, Algeria,
e-mail: ziyad.bouchama@univ-bba.dz

How to cite this article:
Khatir A., Bouchama Z., Benaggoune S., Zerroug N. Indirect adaptive fuzzy finite time synergetic control for power systems. *Electrical Engineering & Electromechanics*, 2023, no. 1, pp. 57-62. doi: https://doi.org/10.20998/2074-272X.2023.1.08

UDC 621.3 https://doi.org/10.20998/2074-272X.2023.1.09

Ch. Sathish, I.A. Chidambaram, M. Manikandan

Intelligent cascaded adaptive neuro fuzzy interface system controller fed KY converter for hybrid energy based microgrid applications

Purpose. *This article proposes a new control strategy for KY (DC-DC voltage step up) converter. The proposed hybrid energy system fed KY converter is utilized along with adaptive neuro fuzzy interface system controller. Renewable energy sources have recently acquired immense significance as a result of rising demand for electricity, rapid fossil fuel exhaustion and the threat of global warming. However, due to their inherent intermittency, these sources offer low system reliability. So, a hybrid energy system that encompasses wind/photovoltaic/battery is implemented in order to obtain a stable and reliable microgrid. Both solar and wind energy is easily accessible with huge untapped potential and together they account for more than 60 % of yearly net new electricity generation capacity additions around the world.* ***Novelty.*** *A KY converter is adopted here for enhancing the output of the photovoltaic system and its operation is controlled with the help of a cascaded an adaptive neuro fuzzy interface system controller.* ***Originality.*** *Increase of the overall system stability and reliability using hybrid energy system fed KY converter is utilized along with adaptive neuro fuzzy interface system controller.* ***Practical value.*** *A proportional integral controller is used in the doubly fed induction generator based wind energy conversion system for controlling the operation of the pulse width modulation rectifier in order to deliver a controlled DC output voltage. A battery energy storage system, which uses a battery converter to be connected to the DC link, stores the excess power generated from the renewable energy sources. Based on the battery's state of charge, its charging and discharging operation is controlled using a proportional integral controller. The controlled DC link voltage is fed to the three phase voltage source inverter for effective DC to AC voltage conversion. The inverter is connected to the three phase grid via an LC filter for effective harmonics mitigation. A proportional integral controller is used for achieving effective grid voltage synchronization.* ***Results.*** *The proposed model is simulated using MATLAB/Simulink, and from the obtained outcomes, it is noted that the cascaded adaptive neuro fuzzy interface system controller assisted KY converter is capable of maintaining the stable operation of the microgrid with an excellent efficiency of 93 %.* References 21, table 1, figures 20.

Key words: **photovoltaic system, hybrid energy system, proportional integral controller, adaptive neuro fuzzy interface system controller.**

Мета*. У цій статті пропонується нова стратегія управління перетворювачем КУ (підвищення напруги постійного струму). Пропонована гібридна енергетична система, що живиться перетворювачем КУ, використовується разом із контролером системи адаптивного нейро-нечіткого інтерфейсу. Відновлювані джерела енергії останнім часом набули величезного значення внаслідок зростання попиту на електроенергію, швидкого виснаження викопного палива та загрози глобального потепління. Однак через властиву їм уривчастість ці джерела забезпечують низьку надійність системи. Таким чином, гібридна енергетична система, що включає енергію вітру/фотоелектричних елементів/акумулятору, реалізована для отримання стабільної і надійної мікромережі. Як сонячна, так і вітрова енергія доступні з величезним невикористаним потенціалом, і разом вони забезпечують понад 60 % щорічного чистого приросту нових потужностей з виробництва електроенергії в усьому світі.* ***Новизна****. Перетворювач КУ використовується тут для підвищення вихідної потужності фотоелектричної системи, і його робота керується за допомогою каскадного контролера системи з адаптивним нейро-нечітким інтерфейсом.* ***Оригінальність****. Підвищення загальної стабільності та надійності системи за допомогою гібридної енергетичної системи, що живиться перетворювачем КУ і використовується разом з контролером системи з адаптивним нейро-нечітким інтерфейсом.* ***Практична цінність****. Пропорційний інтегральний контролер використовується в системі перетворення енергії вітру на основі асинхронного генератора з подвійним живленням для управління випрямлячою роботою з широтно-імпульсною модуляцією для забезпечення регульованої вихідної напруги постійного струму. Акумуляторна система накопичення енергії, в якій використовується акумуляторний перетворювач для підключення до кола постійного струму, зберігає надмірну потужність, що виробляється з відновлюваних джерел енергії. Залежно від стану заряду акумулятора, процес його зарядки і розрядки контролюється за допомогою пропорційного інтегрального контролера. Керована напруга кола постійного струму подається на трифазний інвертор джерела напруги для ефективного перетворення постійної напруги змінну. Інвертор підключений до трифазної мережі через LC-фільтр для ефективного придушення гармонік. Пропорційний інтегральний регулятор використовується для досягнення ефективної синхронізації напруги мережі.* ***Результати****. Запропонована модель змодельована з використанням MATLAB/Simulink, і з отриманих результатів випливає, що каскадний адаптивний нейро-нечіткий інтерфейс із системним контролером та перетворювачем КУ здатний підтримувати стабільну роботу мікромережі з чудовим ККД 93 %.* Бібл. 21, табл. 1, рис. 20.

Ключові слова: **фотогальванічна система, гібридна енергетична система, пропорційний інтегральний контролер, системний контролер з адаптивним нейро-нечітким інтерфейсом.**

Introduction. The increasing energy demand and awareness about the harmful consequences of carbon emissions from fossil fuels have intensified the need for infusion of clean and sustainable sources of energy that includes wind, solar, biomass and fuel cell into electrical systems. Among these, solar and wind power, in particular have grown at an incredible rate during the last decade. Since, both are non-polluting, abundantly available and generate power closer to load centers [1]. The widespread integration of renewable energy sources (RESs) into the utility AC grid causes voltage fluctuations and protection issues [2]. As a result, the utility grid's reliability, security and quality are highly affected. To subdue the effect of these issues, a new concept called microgrid has been developed for future electrical power systems. Microgrid is an interconnected network of Distributed sources of energy, loads and energy storage systems (ESS) that operates in either grid connected mode or islanded mode [3, 4]. Microgrids are basically categorized as AC, DC and hybrid microgrid on the basis of the voltages and currents used [5]. The voltage output from a photovoltaic (PV) is basically a low DC voltage and it fluctuates with the varying weather conditions and solar irradiance, hence a DC-DC converter is considered to be crucial for the conversion of the low voltage to a

high voltage [6]. Different DC-DC converters like boost [7], buck-boost [8], Cuk [9], SEPIC [10] and so on are used with the PV system for the purpose of executing effective DC-DC conversion process.

By using efficient control techniques, the efficiency of the converter is significantly improved with the reduction of total harmonic distortion, settling time, peak overshoot issues and steady state error. The control techniques are categorized into two major types, which are conventional control and intelligent control [11]. The conventional control technique like PI controller is simple in design and effectively controls the DC quantities. However, this controller suffers from certain drawbacks like nonzero steady state error, poor performance during sudden load variations and excessive integration of distributed energy resources in microgrid. Additionally, for the system's operation, an accurate mathematical model is required. Artificial neural network (ANN), fuzzy logic controller (FLC), and neuro fuzzy systems are examples of intelligent control approaches. When compared to conventional PI controller, these techniques are more reliable and efficient as they enhance a system's dynamic performance without the requirement of an accurate mathematical model of the system. One of the most frequently used approach in microprocessor-based control system is FLC because its working is not affected by the fluctuations in operating points and PV parameters. However, it is an error prone and time-consuming approach as it works on the basis of membership functions and rule base. ANN, which is made up of a group of simple processing interconnected neurons, replicates the human learning approach. Here, the learning process is complicated and focused on a number of methods. Moreover, it is too difficult to create a mathematical model that incorporates all of these methods. The adaptive network based fuzzy inference system (ANFIS) is a neuro fuzzy system that combines ANN and FLC characteristics. Here, the parameters and structure of a fuzzy inference system are identified and tuned using neural learning rules solely with the given data [12-15].

In [16], both doubly fed induction generator (DFIG) based wind energy conversion system (WECS) and solar PV system are integrated into the microgrid for providing seamless power supply. The two most common types of wind turbines utilised for wind energy extraction are variable-speed and fixed-speed wind turbines. Fixed speed wind turbines are simple in operation, but generation of high-power losses has limited their application. Variable-speed wind turbines with DFIG are broadly utilized due to the several advantages they provide, including lower acoustic noise, lower converter ratings, excellent energy efficiency and minimum power loss.

The stability, resiliency and efficiency of the electric power grid are greatly improved by using a proper ESS. Some of the most essential tasks of the ESSs are to store the surplus energy generated from the RESs, to smoothen the variations that result from the non-linear quality of the RES, to heighten the flexibility and security of the power system [17-19]. For the sake of minimizing the DC voltage fluctuations, a bidirectional DC-DC converter is implemented for interfacing the ESS to the DC bus [20, 21].

A hybrid wind/PV/battery based microgrid is designed in this research work. The non-linear output from the PV is stabilized using cascaded ANFIS assisted KY converter (KY is the name given to this converter by the first letters of both authors **K**.I. Haw, **Y**.T. You). The output from the DFIG based WECS is stabilized using PI controller. The excess power from both PV and WECS is stored in battery energy storage system (BESS), which acts as a secondary power source in the absence of power supply from primary sources. The interfacing of battery to the microgrid is accomplished using a battery converter and the state of charge (SOC) of the battery is managed using a PI controller. The effective grid synchronisation is also achieved by the control of 3φ voltage source inverter (VSI) using the PI controller. The performance of the designed hybrid microgrid in enhancing the voltage stability is examined using MATLAB simulations.

Proposed system description. The PV system's output is generally low, so a KY converter is implemented for boosting the solar panels output voltage. The output of the converter is not stable and experience incessant fluctuations due to the intermittency of the PV system so the cascaded ANFIS controller is chosen for stabilizing the converter output. The error signal obtained by comparing the actual DC voltage output $V_{DC_{act}}$ of the converter to the reference voltage $V_{DC_{ref}}$ is fed to cascaded ANFIS controller. The reference signal generated from the controller is provided to the PWM generator for the purpose of generating PWM pulses. The resultant pulses control the switching action of the converter so as to produce a stable output. Figure 1 illustrates the block diagram of proposed hybrid energy based microgrid. In the WECS, the wind turbine produces mechanical energy by conversion of the kinetic energy of the wind, whereas the DFIG produces electrical energy by conversion of mechanical energy. The obtained electrical energy is AC, hence the conversion of AC voltage to DC voltage is carried out using a pulse width modulation (PWM) rectifier. The output power of the WECS fluctuates with the changing wind speed, so the PI controller is used for stabilizing the voltage output of the PWM rectifier.

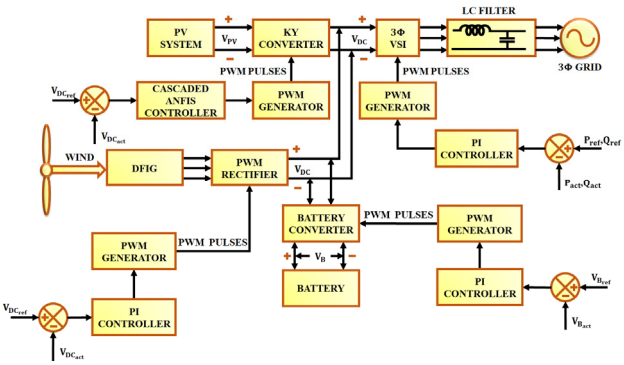

Fig. 1. Proposed hybrid energy based microgrid

The error obtained by analogising the actual DC voltage $V_{DC_{act}}$ of the PWM rectifier with the reference voltage $V_{DC_{ref}}$ is supplied to the PI controller. The control signal generated by the PI controller is supplied into the PWM generator for the generation of PWM pulses. These pulses control the switching operation of the rectifier so as to generate a controlled DC output. The

error signal produced by comparing the actual DC voltage output $V_{B_{act}}$ of the battery with the reference voltage $V_{B_{ref}}$ is provided to the PI controller. The controller generates a control signal, which is fed to the PWM generator for generating PWM pulses. These pulses control the switching operation of the battery converter for providing a constant DC supply. The 3φ VSI, which converts the DC output voltage of the converter into AC voltage, is connected to the 3φ grid through an LC filter.

Proposed system modelling.

a) Solar PV modeling. The solar cell is the most essential component of a PV system that generates DC voltage when exposed to sun light based on the phenomenon of PV effect. A PV panel consists of many solar cells, which are linked in parallel and series, with the parallel connection expansion increasing the current and the series connection expansion increasing the voltage. A PV array is made up of many PV panels. Figure 2 illustrates the equivalent circuit of a PV cell.

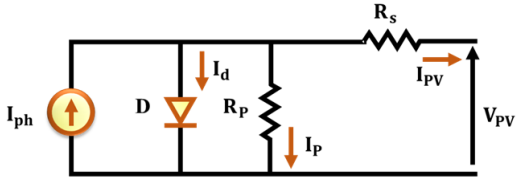

Fig. 2. Equivalent circuit of PV cell

By applying Kirchchoff's current law

$$I_{PV} = I_{ph} - I_d - I_P, \tag{1}$$

where

$$I_d = I_o \cdot \left[\exp\left(\frac{V_{PV} + I_{PV} \cdot R_S}{n \cdot v} \right) - 1 \right], \tag{2}$$

$$I_p = \left(\frac{V_{PV} + I_{PV} \cdot R_S}{R_P} \right), \tag{3}$$

$$I_{PV} = I_{ph} - I_o \cdot \left[\exp\left(\frac{V_{PV} + I_{PV} \cdot R_S}{n \cdot v} \right) - 1 \right] - \frac{V_{PV} + I_{PV} \cdot R_S}{R_P}, \tag{4}$$

where I_{PV} is the PV output current that flows through the series resistance R_S; V_{PV} is the PV output voltage; I_{ph} is the photo generated current; I_d is the diode saturation current; I_o is the reverse saturation current; I_P is the current that flows through the shunt resistance R_P; n is the number of series connected solar PV cells; v is the junction thermal voltage; a is the diode ideality constant; q is the electron charge ($1.602 \cdot 10^{-19}$ C); k is the Boltzmann constant ($1.381 \cdot 10^{-23}$ J/K); T is the temperature of p-n junction.

The PV panel's open circuit voltage is:

$$V_{OC} = \frac{a \cdot k \cdot T}{q} \log_n \left(\frac{I_{ph}}{I_d} + 1 \right). \tag{5}$$

b) KY converter. KY converter is a voltage boosting converter, which has low output voltage ripple. This converter has the same properties as that of the buck converter and has rapid transient load response. It comprises of two power switches S_1 and S_2, a diode VD, an output capacitor C, an energy transferring capacitor C_b, an output inductor L and a load resistance R. The terms v_o and v_{pv} represent the output and input voltage respectively. The i_{pv} specifies the input current and i denotes the current flowing through L. The voltage across C_b is denoted as v_{pv} as the voltage across C_b completely follows the input voltage v_{pv}. Figure 3 presents the equivalent structure of KY converter. The two different modes of operation of KY converter are illustrated in Fig. 4.

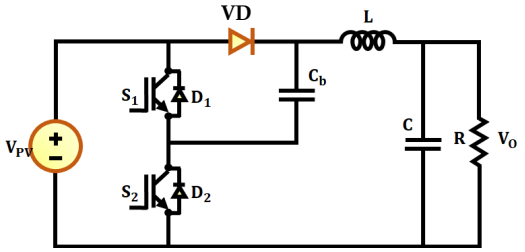

Fig. 3. Circuit diagram of KY converter

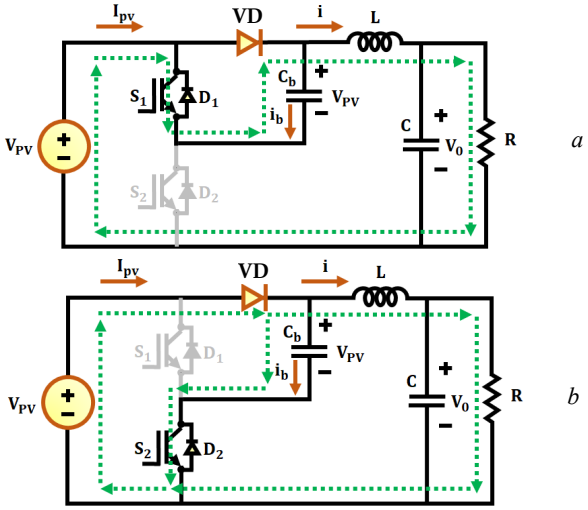

Fig. 4. KY converter operating modes: *a*) mode 1; *b*) mode 2

Mode 1. At this stage, the power switch S_1 is switched ON, whereas the power switch S_2 is switched OFF. On subtracing the output voltage v_o from the sum of voltage v_{pv} across C_b and input voltage v_{pv}, the magnitude of voltage across the inductor L is determined. The inductor L is magnetized in this mode. As a result, the differential equations are:

$$L \cdot \frac{\partial i}{\partial t} = 2 \cdot v_{pv} - v_o; \quad C \cdot \frac{\partial v_o}{\partial t} = i - \frac{v_o}{R}; \quad i_{PV} = i. \tag{6}$$

Mode 2. At this stage, the power switch S_1 is switched OFF, whereas the power switch S_2 is switched ON. During this mode, the demagnetisation of inductor L takes place. On subtracing the output voltage v_o from voltage v_{pv} across C_b, the magnitude of voltage across the inductor L is determined. As a result, the differential equations are:

$$L \cdot \frac{\partial i}{\partial t} = v_{pv} - v_o; \quad C \cdot \frac{\partial v_o}{\partial t} = i - \frac{v_o}{R}; \quad i_{PV} = i + i_b. \tag{7}$$

where i_b is the current of energy transferring capacitor.

The relationship between v_{pv} and v_o is represented as follows:

$$\frac{v_o}{v_{pv}} = 1 + D, \tag{8}$$

where D is the duty cycle.

The intermittent nature of the solar energy has a huge impact on the KY converter output, so it fluctuates and remains unstable. The operation of the converter is made more efficient by using cascaded ANFIS controller.

c) ANFIS controller. ANFIS is a versatile intelligent control technique, which is first introduced by Jang in the year 1993, combines both the ANN and fuzzy inference system (FIS).To deal with non-linear functions, a system is transformed into if-then rules using ANFIS. The structure of ANFIS controller comprises of five different layers, which are fuzzification layer, rule layer, normalization layer, defuzzification layer and output layer as represented in Fig. 5. Here, the two inputs to the ANFIS structure are *a* and *b*, while the output is *f*.

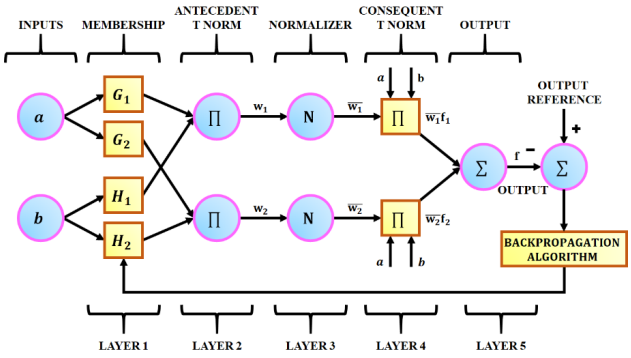

Fig. 5. ANFIS structure

The Sugeno FIS-based ANFIS if-then rule configuration is as follows:

rule 1: if *a* is G_1 and *b* is H_1; then $f_1 = p_1 \cdot a + q_1 \cdot b + r_1$;

rule 2: if *a* is G_2 and *b* is H_2; then $f_2 = p_2 \cdot a + q_2 \cdot b + r_2$;

The design parameters for training process are p_i, q_i and r_i, where i = 1, 2. The fuzzy sets are represented by the terms G_1 and H_1.

In the initial layer, the membership functions for each of the specified input data are developed. The membership functions of the adaptive nodes of this layer are given by:

$$O_{1,i} = \mu_{Gi}(a),\ i = 1,2; \tag{9}$$

$$O_{1,i} = \mu_{Hj}(b),\ i = 1,2; \tag{10}$$

where the membership grades for fuzzy set (G_1, G_2, H_1 and H_2) are represented as $\mu_{Gi}(a)$ and $\mu_{Hj}(b)$.

The second layer consists of circular nodes that are labeled as π. This layer multiplies the input signals as shown in the following mathematical expression

$$O_{2,i} = w_i = \mu_{Gi}(a) \times \mu_{Hj}(b),\ i = 1,2; \tag{11}$$

where the term w_i specifies the firing strength of node *i*.

The third layer is the normalization layer, which consists of circular nodes that are labeled as *N*. The output of the second layer is normalised in this layer, as given below:

$$O_{3,i} = \overline{w}_l = \frac{w_i}{w_1 + w_2},\quad i = 1, 2, \tag{12}$$

where $\overline{w}_l$ specifies the normalized firing strengths.

The third layer output is simplified in the fourth layer and the result is given by:

$$O_{4,i} = \overline{w}_l \cdot f_i = \overline{w}_l \cdot \left(p_i \cdot g + q_i + r_i\right),\quad i = 1, 2, \tag{13}$$

where $\{p_i, q_i, r_i\}$ represents the parameter set and the term $\overline{w}_l$ specifies the output of the third layer.

The summing of all the inputs is carried out in the final layer. This layer consists of only one node, which is labeled as Σ. The overall result is given as:

$$O_{5,i} = \sum_{i=1}^{2} \overline{w}_l \cdot f_i = \frac{w_1 \cdot f_1 + w_2 \cdot f_2}{w_1 + w_2}. \tag{14}$$

The parameters of first and fourth layer are known as premise and consequent parameters, respectively. The first layer parameters are tuned by back propagation approach, while the fourth layer parameters are tuned by least square approach. These two approaches improve the system's accuracy and speed of convergence, hence the learning ability of ANFIS is better.

d) Cascaded ANFIS controller. The conventional ANFIS method has certain limitations like computational complexity and the curse of dimensionality. These limitations are overcome by using cascaded ANFIS method, which is an extension of conventional ANFIS. It comprises of two important modules namely, pair selection module and training module. The flow chart of cascaded ANFIS is represented in Fig. 6,*a*.

Pair selection module. The overall procedure of the pair selection module is illustrated in Fig. 6,*b*. Here, ANFIS structure with two inputs and one output is used to find the best matching pair from the input variables. In this module, sequential feature selection process is carried out and the matching pair is obtained as the final outcome. To go through all two pair combinations, a nested loop is used. The term NI in Fig. 6,*b* specifies the number of input variables. The chosen inputs for the system are $input_i$ and $input_j$. The value of root mean square error (RMSE), which is represented as E_p is computed and saved for comparing with the prior value of RMSE (E_{prev}). The matching pair is extracted by checking the lowest RMSE value at the conclusion of second loop. The training phase begins after the pairs have been chosen.

Train model module. The train model module also uses the ANFIS model with two inputs similar to the pair selection module. It receives the matching pairs from the pair selection module as input, and outputs are produced for each set of inputs provided. When the target error is reached, the process is completed; otherwise, the next iteration is performed. The operational flowchart of training module is presented in Fig. 7.

Consider X_1, X_2, X_3 and X_4 as the input variables of optimization problem:

$$\text{Input} = \{X_1, X_2, X_3, X_4\}. \tag{15}$$

The four input variables form pairs with the best match in the pair selection module as specified below:

$$Input_{pairs} = \{X_1, X_3\}, \{X_2, X_1\}, \{X_3, X_4\}, \{X_4, X_1\}. \tag{16}$$

For each input pair, ANFIS model with two inputs are used to generate two outputs namely, $RMSE_i$ and Y_i:

$$RMSE = \sqrt{\overline{(A-P)^2}}\ ; \tag{17}$$

$$RMSE_{A,P} = \left[\sum_{i=1}^{N} \frac{(O_{Ai} - O_{Pi})^2}{N}\right]^{\frac{1}{2}}, \tag{18}$$

where the actual results and predicted results are specified as *A* and *P*, respectively; *N* is the sample size.

The output *f* is:

$$f = \frac{w_1}{w_1 + w_2} \cdot f_1 + \frac{w_2}{w_1 + w_2} \cdot f_2 + \frac{w_3}{w_2 + w_3} \cdot f_3 + \frac{w_4}{w_3 + w_4} \cdot f_4 . \tag{19}$$

The initial iteration comes to an end after the determination of *RMSE* and *Y*. The *RMSE* and goal error are compared before moving on to the next iteration. The outputs obtained from the first iteration are Y_1, Y_2, Y_3 and Y_4, which are used as inputs for the second iteration.

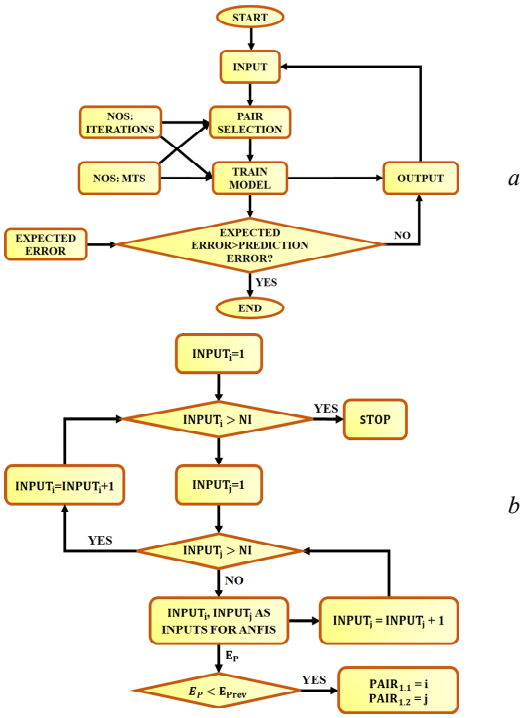

Fig 6. Flow chart of cascaded ANFIS (*a*) and pair selection module (*b*)

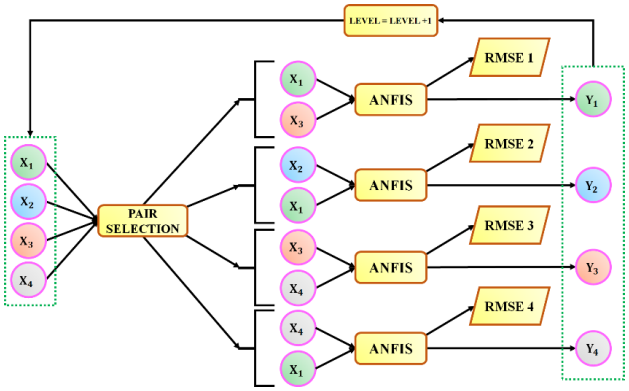

Fig. 7. Structure of training module

e). Grid voltage synchronization using PI controller. Voltage control and current control are the two different types of control techniques adopted for controlling the 3φ VSI. In case of voltage controlled VSI, the phase angle between grid voltage and the inverter voltage output is used to establish power flow control, where as in case current controlled VSI, the reactive and active components of the injected current to the grid are controlled by the use of PWM approach. The current control technique provides quick response and is less sensitive to grid voltage distortion and voltage phase shifts. The voltage control technique is sensitive to small phase errors and when the grid voltage is distorted, significant harmonic currents occur. As a result, the current control technique is highly preferred for controlling the operation of grid connected inverter. Among different current control techniques, the PI controller is widely adopted approach for compensating current errors as it provides quick steady state response, minimum current ripple and stable switching frequency. Figure 8 illustrates the process of grid voltage synchronization using PI controller.

The PI controller minimizes the error, which is determined by comparing the actual output current of the inverter with the reference grid current. The proportional

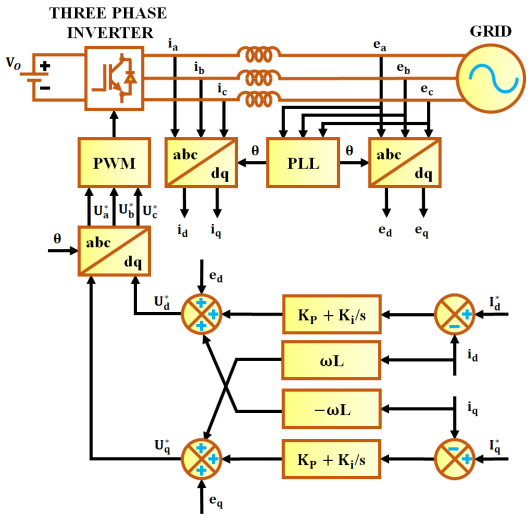

Fig. 8. A synchronous PI controller-based grid voltage synchronization

constant K_P and the integral constant K_I are the two different parameters that are involved in the calculation procedure of the controller. Here both proportional and integral operation takes place. In case of proportional operation, the error e is multiplied with the gain K_P, whereas in case of integral operation, the error e is integrated and then multiplied with gain K_I. At the end of both operations, the steady state error is totally minimized and the reference signal is generated in a short span of time. This controller is capable of working with both stationary reference frame (αβ) and synchronous reference frame (dq). Here the PI controller is used in dq reference frame for achieving effective grid voltage synchronization.

The grid-connected inverter's output voltage in the synchronous (dq) frame is calculated using the inverter's mathematical model, as shown below:

$$\begin{bmatrix} u_d \\ u_q \end{bmatrix} = L \cdot \frac{\mathrm{d}}{\mathrm{d}t}\begin{bmatrix} i_d \\ i_q \end{bmatrix} + R \cdot \begin{bmatrix} i_d \\ i_q \end{bmatrix} + \omega \cdot L \cdot \begin{bmatrix} -i_q \\ i_d \end{bmatrix} + \begin{bmatrix} e_d \\ e_q \end{bmatrix}, \quad (20)$$

where u_d and u_q are the Park transformation components of the inverter output; e_d and e_q are the Park transformation components of the grid voltage; R, L are the resistance and inductance between the grid and the grid connected inverter, respectively; ω is the angular frequency of the grid.

The structure of synchronous PI controller for grid tied inverter is illustrated in Fig. 8. The current vector components indicated in the synchronous reference frame (dq) are compensated using two PI controllers One PI controller compares I_d and I_d^*, while the other compares I_q and I_q^* and generate errors that are minimized to zero. The power factor and output power are regulated by varying the q-axis and d-axis currents.

f) DFIG based WECS. The wind turbine produces mechanical energy by conversion of the kinetic energy of the wind. The developed mechanical power is:

$$P_m = \frac{1}{2} \cdot C_p(\lambda, \beta) \cdot \pi \cdot r^2 \cdot \rho \cdot V_w^3, \quad (21)$$

where C_p is the power coefficient; λ is the tip speed ratio; β is the pitch angle; r is the radius of wind turbine, m; ρ is the air density, kg/m^3; V_w is the wind speed, m/s.

Figure 9 illustrates the direct interfacing of the stator to the grid, while a grid-side converter (GSC) and rotor-

side converter (RSC) are used for interfacing the rotor to the grid. The control of DC link voltage in between the two converters is performed by the GSC. The reactive power required by DFIG for magnetization is provided by RSC. A PWM rectifier converts the AC voltage generated by the DFIG to DC voltage. An error signal is produced when the actual DC voltage $V_{DC_{act}}$ of the PWM rectifier is compared to the reference voltage $V_{DC_{ref}}$. The error thus obtained is given as input to the PI controller. In the PI controller, proportional and integral action takes place and the error is eliminated. The PWM generator receives the control signal generated by the PI controller and generates PWM pulses. The switching operation of the rectifier is monitored using these pulses in order to generate a steady and controlled DC output voltage V_{DC}.

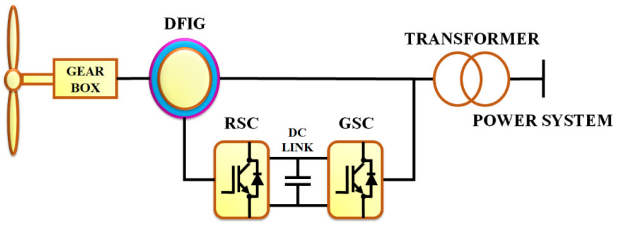

Fig. 9. DFIG based WECS

g) PI controller based BESS. The actual battery voltage $V_{B_{act}}$ and the reference voltage $V_{B_{ref}}$ are compared to find the steady state error *e*. This error is fed into the PI controller, which performs both proportional and integral control operations and generates the control signal *u* as shown below:

$$u = K_P \cdot e + K_I \cdot \int e dt \,. \tag{22}$$

The circuit diagram of PI controller based BESS is illustrated in Fig. 10. The PWM generator generates PWM pulses based on the control signal, which is obtained from the PI controller. The resultant PWM pulses controls the duty cycle of the battery converter in order to enable buck as well as boost mode of operation. The battery is charged during the buck mode of operation and discharged during the boost mode of operation.

Results and discussions. A hybrid energy based microgrid is designed with PV, WECS and BESS for getting a reliable power supply in this work. By adopting cascaded ANFIS controller and PI controllers the overall system voltage stability is maintained. The performance of the proposed hybrid energy based microgrid is analysed by using MATLAB simulation and the results are obtained as specified below. The specifications of the solar panel, WECS, converters, BESS and load are mentioned in Table 1.

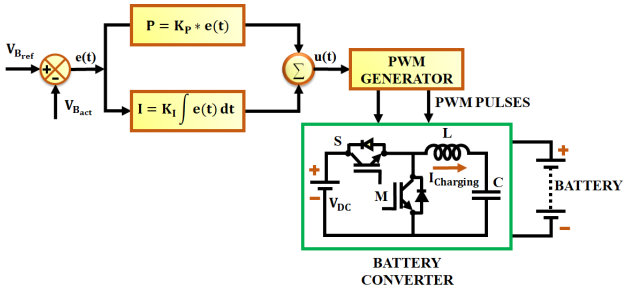

Fig. 10. PI controller for BESS

Table 1

Solar panel, WECS, KY converter, BESS, battery converter and load specifications

PV Panel	
Parameters	Ratings
Peak power	10 kW
No. of solar PV panels	750 W, 13 panels
Short circuit voltage V_{SC}	12 V
Short circuit current I_{SC}	62.5 A
Open circuit voltage V_{OC}	22.6 V
No. of series connected solar cells	36
WECS	
No. of wind turbines	1
Power	10 kW
Voltage	575 V
Speed range	4–16 m/s
KY converter	
L	4 mH
C_b	22 μF
C	1000 μF
Switching frequency	10 kHz
BESS	
Capacity	100 A·h
No. of battery units	5.12 V
Battery converter	
L	1 mH
C	1000 μF
Switching frequency	10 kHz
Load	
Capacity	5 kW

The waveforms that indicate the magnitude of voltage and current obtained from the PV panel is illustrated in Fig. 11. The panel voltage experiences a slight rise at 0.2 s and maintained constant, while the PV panel output current is constantly maintained at 25 A after 0.1 s. However, the effects of the variations in operating condition are seen on the panel output current, which also happens to be the converter's input.

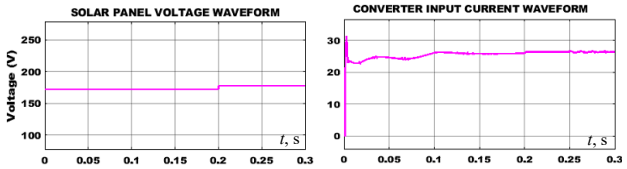

a *b*

Fig. 11. Solar panel: output voltage (*a*); output current (*b*)

The KY converter output voltage and current settles quickly after undergoing incessant fluctuations at 0.15 s and 0.1 s respectively due to the application of cascaded fuzzy controller as illustrated in Fig. 12. Thus, the adopted cascaded fuzzy assisted KY converter displays a remarkable performance in stabilizing and enhancing the PV output within a short period of time.

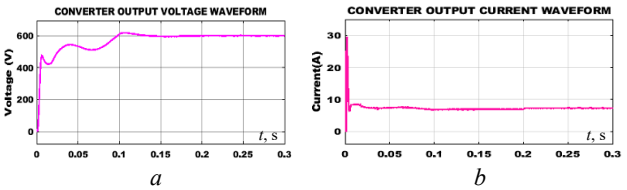

a *b*

Fig. 12. KY converter:
output voltage (*a*); output current waveform (*b*)

In Fig. 13,*a* the output voltage of the DFIG is around 550 V with slight fluctuations owing to the wind energy intermittency. The output voltage of the PWM rectifier undergoes a sudden rise at the beginning and gradually settles down at 0.15 s with the implementation of PI controller as seen in Fig. 13,*b*. The output of the PI controller based PWM rectifier is constant and remains distortion free.

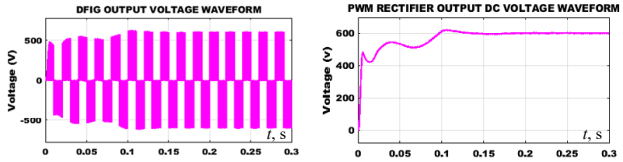

a *b*

Fig. 13. Output voltage waveform of DFIG (*a*) and PWM rectifier (*b*)

The battery voltage and current waveforms are illustrated in Fig. 14,*a* and Fig. 14,*b* respectively. The SOC of the battery is about 60 % as indicated in Fig. 14,*c*. When the SOC of the battery is below 60 %, the battery converter executes battery charging by operating in buck mode. When the SOC of the battery is above 60 %, the battery converter executes battery discharging by operating in boost mode. From the figure, it is evident that the battery voltage and current initially suffers from fluctuations and becomes stable within a short period due to the application of PI controller.

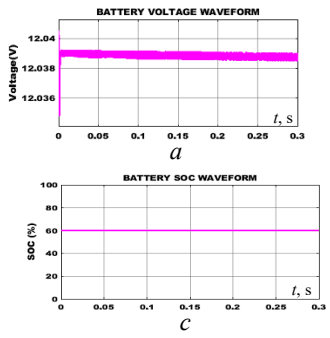

a *b* *c*

Fig. 14. Waveforms of battery: *a* – voltage; *b* – current; *c* – SOC

Figure 15 presents the waveforms that indicate the magnitude of the real and reactive power. The magnitude of reactive power gradually increases and becomes stable at a value of 5400 W at 0.03 s. The magnitude of reactive power is –50 VAr from 0.1 s.

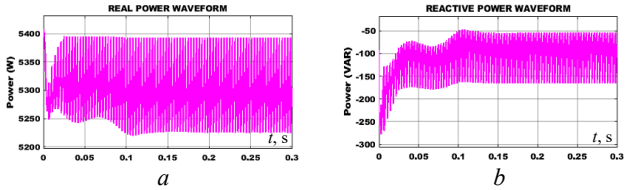

a *b*

Fig. 15.Waveforms of real power (*a*) and reactive power (*b*)

The waveforms that represent the grid voltage and current are seen in Fig. 16. Both the grid voltage and grid current are stable without fluctuations with the effective grid voltage synchronization achieved by PI controller. The magnitude of grid voltage is maintained at 230 V and the magnitude of grid current is maintained at 10 A.

The voltage gain and efficiency of different DC-DC converters are compared with KY converter in Fig. 17,*a* and Fig. 17,*b* respectively. From Fig. 17,*a*, it is clear that the voltage gain of KY converter is 1:10 and it is comparatively higher than the other four conventional DC-DC converters. The efficiency of cascaded ANFIS controller assisted KY converter is about 93 %, which is higher than the efficiency of other 4 conventional DC-DC converters as represented in Fig. 17,*b*.

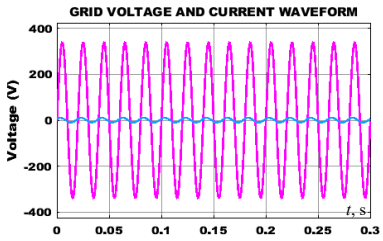

Fig. 16. Waveform of grid voltage and current

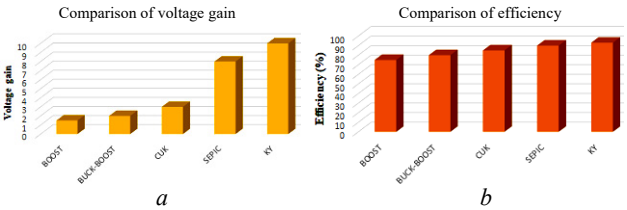

a *b*

Fig. 17. Comparison of voltage gain (*a*) and efficiency (*b*) of various DC-DC converters

Hardware implementation is represented in Fig. 18. In Fig. 19, 20 the oscillograms of voltages for KY converter, which got from experiments, are shown.

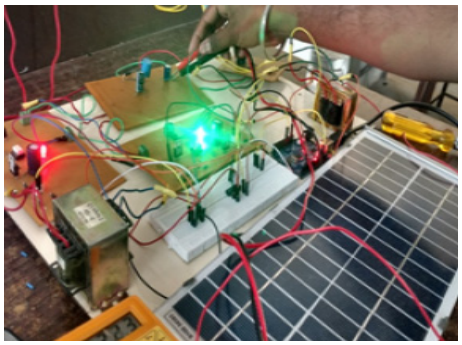

Fig. 18. Hardware setup

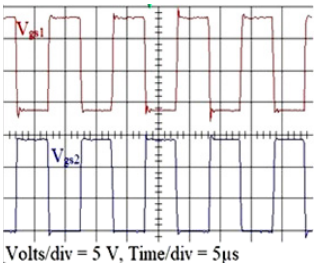

Fig. 19. Gating pulses of S1 and S2

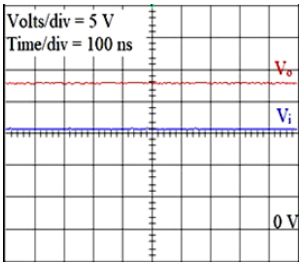

Fig. 20. V_o and V_i of KY converter

Conclusions.

A hybrid energy based microgrid that combines renewable energy sources like photovoltaic system and wind energy conversion system is designed for the purpose of heightening the overall system stability and reliability. The KY converter, which is connected to the output side of the photovoltaic system, enhances its output voltage with reduced switching loss. The operation of the converter is optimized with the assistance of cascaded adaptive neuro fuzzy interface system controller. A proportional integral controller is used to stabilize the output of the doubly fed induction generator based wind energy conversion system. The battery energy storage system, which is interfaced with

the microgrid through a battery converter, ensures consistent supply of power. The state of charge of the battery is monitored and controlled with the help of a proportional integral controller. The adopted control approach of cascaded adaptive neuro fuzzy interface system assisted KY converter operates with an impressive efficiency of 93 %.

Conflict of interest. The authors declare that they have no conflicts of interest

REFERENCES

1. Mosaad M.I., Ramadan H.S.M., Aljohani M., El-Naggar M.F., Ghoneim S.S.M. Near-Optimal PI Controllers of STATCOM for Efficient Hybrid Renewable Power System. *IEEE Access*, 2021, vol. 9, pp. 34119-34130. doi: https://doi.org/10.1109/ACCESS.2021.3058081.

2. Ali Moussa M., Derrouazin A., Latroch M., Aillerie M. A hybrid renewable energy production system using a smart controller based on fuzzy logic. *Electrical Engineering & Electromechanics*, 2022, no. 3, pp. 46-50. doi: https://doi.org/10.20998/2074-272X.2022.3.07.

3. Kumar D., Zare F., Ghosh A. DC Microgrid Technology: System Architectures, AC Grid Interfaces, Grounding Schemes, Power Quality, Communication Networks, Applications, and Standardizations Aspects. *IEEE Access*, 2017, vol. 5, pp. 12230-12256. doi: https://doi.org/10.1109/ACCESS.2017.2705914.

4. Farrokhabadi M., Konig S., Canizares C.A., Bhattacharya K., Leibfried T. Battery Energy Storage System Models for Microgrid Stability Analysis and Dynamic Simulation. *IEEE Transactions on Power Systems*, 2018, vol. 33, no. 2, pp. 2301-2312. doi: https://doi.org/10.1109/TPWRS.2017.2740163.

5. Lotfi H., Khodaei A. AC Versus DC Microgrid Planning. *IEEE Transactions on Smart Grid*, 2017, vol. 8, no. 1, pp. 296-304. doi: https://doi.org/10.1109/TSG.2015.2457910.

6. Praveen Kumar T., Ganapathy S., Manikandan M. Improvement of voltage stability for grid connected solar photovoltaic systems using static synchronous compensator with recurrent neural network. *Electrical Engineering & Electromechanics*, 2022, no. 2, pp. 69-77. doi: https://doi.org/10.20998/2074-272X.2022.2.10.

7. Errouissi R., Al-Durra A., Muyeen S.M. A Robust Continuous-Time MPC of a DC–DC Boost Converter Interfaced With a Grid-Connected Photovoltaic System. *IEEE Journal of Photovoltaics*, 2016, vol. 6, no. 6, pp. 1619-1629. doi: https://doi.org/10.1109/JPHOTOV.2016.2598271.

8. Jedari Zare Zadeh M., Fathi S.H. A New Approach for Photovoltaic Arrays Modeling and Maximum Power Point Estimation in Real Operating Conditions. *IEEE Transactions on Industrial Electronics*, 2017, vol. 64, no. 12, pp. 9334-9343. doi: https://doi.org/10.1109/TIE.2017.2711571.

9. De Morais J.C. dos S., De Morais J.L. dos S., Gules R. Photovoltaic AC Module Based on a Cuk Converter With a Switched-Inductor Structure. *IEEE Transactions on Industrial Electronics*, 2019, vol. 66, no. 5, pp. 3881-3890. doi: https://doi.org/10.1109/TIE.2018.2856202.

10. Tey K.S., Mekhilef S., Seyedmahmoudian M., Horan B., Oo A.T., Stojcevski A. Improved Differential Evolution-Based MPPT Algorithm Using SEPIC for PV Systems Under Partial Shading Conditions and Load Variation. *IEEE Transactions on Industrial Informatics*, 2018, vol. 14, no. 10, pp. 4322-4333. doi: https://doi.org/10.1109/TII.2018.2793210.

11. Tey K.S., Mekhilef S. Modified Incremental Conductance Algorithm for Photovoltaic System Under Partial Shading Conditions and Load Variation. *IEEE Transactions on Industrial Electronics*, 2014, vol. 61, no. 10, pp. 5384-5392. doi: https://doi.org/10.1109/TIE.2014.2304921.

12. Ali M.S., Wang L., Alquhayz H., Rehman O.U., Chen G. Performance Improvement of Three-Phase Boost Power Factor Correction Rectifier Through Combined Parameters Optimization of Proportional-Integral and Repetitive Controller. *IEEE Access*, 2021, vol. 9, pp. 58893-58909. doi: https://doi.org/10.1109/ACCESS.2021.3073004.

13. Seidi Khorramabadi S., Bakhshai A. Critic-Based Self-Tuning PI Structure for Active and Reactive Power Control of VSCs in Microgrid Systems. *IEEE Transactions on Smart Grid*, 2015, vol. 6, no. 1, pp. 92–103. doi: https://doi.org/10.1109/TSG.2014.2354651.

14. Ali M., Tariq M., Lodi K.A., Chakrabortty R.K., Ryan M.J., Alamri B., Bharatiraja C. Robust ANN-Based Control of Modified PUC-5 Inverter for Solar PV Applications. *IEEE Transactions on Industry Applications*, 2021, vol. 57, no. 4, pp. 3863-3876. doi: https://doi.org/10.1109/TIA.2021.3076032.

15. Hannan M.A., Ghani Z.A., Hoque M.M., Ker P.J., Hussain A., Mohamed A. Fuzzy Logic Inverter Controller in Photovoltaic Applications: Issues and Recommendations. *IEEE Access*, 2019, vol. 7, pp. 24934-24955. doi: https://doi.org/10.1109/ACCESS.2019.2899610.

16. Garcia P., Garcia C.A., Fernandez L.M., Llorens F., Jurado F. ANFIS-Based Control of a Grid-Connected Hybrid System Integrating Renewable Energies, Hydrogen and Batteries. *IEEE Transactions on Industrial Informatics*, 2014, vol. 10, no. 2, pp. 1107-1117. doi: https://doi.org/10.1109/TII.2013.2290069.

17. Puchalapalli S., Tiwari S.K., Singh B., Goel P.K. A Microgrid Based on Wind-Driven DFIG, DG, and Solar PV Array for Optimal Fuel Consumption. *IEEE Transactions on Industry Applications*, 2020, vol. 56, no. 5, pp. 4689-4699. doi: https://doi.org/10.1109/TIA.2020.2999563.

18. Byrne R.H., Nguyen T.A., Copp D.A., Chalamala B.R., Gyuk I. Energy Management and Optimization Methods for Grid Energy Storage Systems. *IEEE Access*, 2018, vol. 6, pp. 13231-13260. doi: https://doi.org/10.1109/ACCESS.2017.2741578.

19. Li X., Wang S. Energy management and operational control methods for grid battery energy storage systems. *CSEE Journal of Power and Energy Systems*, 2021, vol. 7, no. 5, pp. 1026-1040. doi: https://doi.org/10.17775/CSEEJPES.2019.00160.

20. Fan F., Kockar I., Xu H., Li J. Scheduling framework using dynamic optimal power flow for battery energy storage systems. *CSEE Journal of Power and Energy Systems*, 2022, vol. 8, no. 1, pp. 271-280. doi: https://doi.org/10.17775/CSEEJPES.2020.03710.

21. Gangatharan S., Rengasamy M., Elavarasan R.M., Das N., Hossain E., Sundaram V.M. A Novel Battery Supported Energy Management System for the Effective Handling of Feeble Power in Hybrid Microgrid Environment. *IEEE Access*, 2020, vol. 8, pp. 217391-217415. doi: https://doi.org/10.1109/ACCESS.2020.3039403.

Received 07.06.2022
Accepted 23.08.2022
Published 06.01.2023

Chindam Sathish[1], *Research Scholar*,
Ilanji Akilandam Chidambaram[1], *Professor,*
Mani Manikandan[2], *Professor,*
[1] Annamalai University,
Chidambaram, Tamil Nadu, 608002, India,
e-mail: chindam.satish@jits.ac.in (Corresponding Author);
driacdm@gmail.com
[2] Jyothishmathi Institute of Technology and Science,
Karimnagar, Telangana, 505481, India,
e-mail: cm.manikandan@gmail.com

How to cite this article:
Sathish Ch., Chidambaram I.A., Manikandan M. Intelligent cascaded adaptive neuro fuzzy interface system controller fed KY converter for hybrid energy based microgrid applications. *Electrical Engineering & Electromechanics*, 2023, no. 1, pp. 63-70. doi: https://doi.org/10.20998/2074-272X.2023.1.09

UDC 621.3 https://doi.org/10.20998/2074-272X.2023.1.10

P. Venkatesh, N. Visali

Investigations on hybrid line stability ranking index with polynomial load modeling for power system security

Introduction. *In recent years, numerous non-renewable and renewable energies are connected to the grid to meet the demand. Also, transient variation with loads poses the shortcomings for generating units, transmission and distribution networks. In this regard, the study on choice of suitable load modelling is essential to predict the system characteristics. The aspect of the research design is a ZIP load model, which, when combined with contingency criteria and constant-impedance, constant-current, and constant-power loads, produces realistic and long-term load representations.* ***Purpose.*** *The proposed technique, infers the single transmission line outage for obtaining the contingency ranking to ensure the system behavior.* ***Methods.*** *The proposed mathematical model with hybrid line stability ranking index has been used for observing the stability analysis with and without considering unified power flow controller.* ***Results****. The power system involves many unpredictable conditions or contingency conditions like single transmission line outage, double transmission line outage, generator outage and load variations. This paper mainly focuses on the single transmission line outage for obtaining the contingency ranking.* ***Practical value.*** *The recommended stability analysis has been very beneficial in establishing a secure transmission power system.* References 19, tables 8, figures 3.
Key words: **hybrid line stability ranking index, power system security, unified power flow controller.**

Вступ*. Останніми роками для задоволення попиту до мережі підключається безліч невідновлюваних і відновлюваних джерел енергії. Крім того, перехідна зміна навантаження створює недоліки для генеруючих установок, передаючих та розподільчих мереж. У зв'язку з цим дослідження з метою вибору відповідного моделювання навантаження має важливе значення для прогнозування характеристик системи. Одним із аспектів побудови дослідження є модель навантаження ZIP, яка у поєднанні з критеріями непередбачених обставин та навантаженнями з постійним імпедансом, постійним струмом та постійною потужністю дає реалістичні та довгострокові уявлення навантаження.* ***Мета****. Пропонований метод передбачає відмову однієї лінії передачі для отримання рейтингу непередбачених обставин для забезпечення поведінки системи.* ***Методи****. Запропонована математична модель із рейтинговим індексом стійкості гібридної лінії використовувалася для спостереження за аналізом стійкості з урахуванням та без урахування уніфікованого контролера перетікання потужності.* ***Результати****. Енергосистема включає безліч непередбачуваних умов або непередбачених обставин, таких як відключення однієї лінії передачі, відключення подвійної лінії передачі, відключення генератора і коливання навантаження. Ця робота присвячена відключенню однієї лінії електропередачі для отримання рейтингу непередбачених обставин.* ***Практична цінність****. Рекомендований аналіз стабільності виявився дуже корисним під час створення надійної системи передачі електроенергії.* Бібл. 19, табл. 8, рис. 3.
Ключові слова: **індекс стійкості гібридної лінії, безпека енергосистеми, єдиний контролер потоку потужності.**

1. Introduction. Multilevel electricity is necessity of the maximum elementary condition of the contemporary world. Hence, safeguarding the safety of the power system is identical important. The major goal of power system security is to deliver consistent power to the clients short of disruption, harm to the user utilizations, and financial process of the power system. But such a power system is also disposed to numerous problems like the transmission line outage, the generator outage, the rapid increase in load demand, the loss of a transformer, etc. which are known as contingencies. Power system safety is one of the keys stimulating errands in the power system. The gears of blackouts due to contingency in the power system are fetching extra frequent in new times. It causes substantial losses to the industries and gravely disturbs the daily life of a common man. Thus, it is significant to accept a precise and active measure to stop the propagation of contingency to other lines which is the major cause of the blackout. Contingency analysis is used for fast guessing the system stability right after the outage or any abnormal conditions. The purpose of the contingency plan is to ascertain the change within the device's functioning, which can occur after the fault element is removed. Large violations inline flow may end in single line outages which may cause cascading effects of the outages and may also cause overloading on the other lines. If such overload results from a line outage there's an immediate essential for the regulator action to be taken. Therefore, contingency analysis is one of the prime important tasks to be met by the power system planners and operation engineers. Several steady-state and dynamic contingency ranking methods are used for contingency screening [1, 2].

Load models may be used to predict how loads will respond to changes in voltage or frequency. It's important to choose a load model that is easy to understand and can appropriately represent a variety of load response situations while executing. In this study, the effects of steady-state and polynomial load models are examined. This model is less precise than the polynomial load model because it depicts a combination of three different sorts of features in a single load. It is possible to express resistive loads, induction motor loads, and variable-frequency loads in a polynomial load model by using the constant impedance, the constant current, and the constant power. As a result, the polynomial load model is more accurate since it accurately depicts load [3].

During any disturbances in the system, the stability of the system becomes vulnerable and there is a high risk of moving towards global instability or total collapse, or even blackout if preventive actions are not taken quickly. When installed and calibrated properly, flexible AC transmission system (FACTS) devices may alleviate several power system problems including contingency. FACTS devices have shown good performance in solving the contingency issues of the power systems. An index-based strategy for placing FACTS devices is found to be extremely precise and computationally efficient. Static and dynamic analyses of the system are both possible using this tool. The two most affected parameters due to contingency in a transmission system are line loading and voltage stability. The line overload index and voltage stability index must be combined to estimate system stress under emergency situations. Line stability index is easier to calculate, takes less time, and can identify weak buses [4, 5].

Unified power flow controller (UPFC) is the most adaptable and versatile FACTS device [6, 7] due to its use of both series and parallel inverters connected by a shared DC connection. FACTS devices are placed on the most severe line to reduce the severity of the line. A hybrid stability ranking index has been used for contingency ranking. The position of the UPFC is recommended to be on the line with the greatest chance of severity. UPFC is tuned for providing compensation [8]. The proposed method is implemented and tested on IEEE 14 and IEEE 118 bus system.

In this paper, section 1 briefs the polynomial load model or ZIP (constant impedance *Z*, constant current *I*, constant active power *P*) modelling and other existing modeling. Section 2 gives an overview of the contingency ranking approach and represents the contingency ranking process in a flowchart. Section 3 gives an overview of the steady-state and polynomial load model used to analyse the contingency. The developed mathematical model incorporated with Newton-Raphson method is used for analysing the stability of the system. Section 4 explains a hybrid line stability index, which is used to assess the stability of the lines between two buses. According to the value of this index the lines which are under stressed conditions can be identified. Section 5 explains the algorithm used for ranking the contingency in the power system is explained. Section 6 gives an overview of the UPFC. It is placed in the most severe line and simulated to provide compensation. Section 7 shows the results obtained for load modelling and then the results obtained while performing single line outages are shown. From these results, the most critical lines are identified and compensated. The results obtained before compensation and after compensation are compared and section 8 reviews the complete effort done and concludes the study. It clarifies the robustness and usefulness of the slants accessible in this paper.

2. Contingency ranking approach. Contingency analysis is a fit know function in modern energy management systems. Contingency analysis of system may be a main movement in power grid planning and process. Generally, an outage of single line or transformer may lead to overloads in other branches and also cause sudden system voltage rise or drop [9]. The power system security can be analyzed by ranking the contingencies based on the severity of the contingency. It consists of three basic steps to make the analysis easier [10, 11]. The three steps are contingency creation, contingency selection, and contingency evaluation.

Contingency creation.

It involves of all set of likely contingencies that may arise in a power system. This step consists of generating contingency lists.

Contingency selection.

In this step severe contingencies are selected from the list that leads to the bus voltage and power edge ruins. Least severe contingencies are eliminated to minimize the contingency list. It uses line stability index to find the sternness of contingencies.

Contingency evaluation.

It is the utmost weighty step which embraces essential control and safety actions in order to lessen the effect of contingency. There are various types of contingencies such as line outage, bus outage and transformer outage. Line outage is analyzed in this paper as it is the most occurred contingency in the system (Fig. 1).

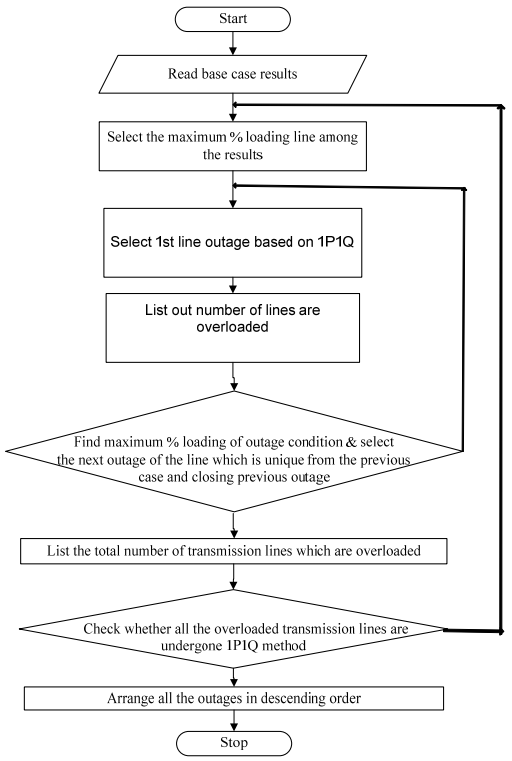

Fig. 1. Flowchart for outages according to their priority

3. Load modelling. Contingency occur mainly due sudden increase or decrease of loads. Load modelling plays a major role in analyzing various types of loads. Load modelling refers to the mathematical illustration of the connection between the power and the voltage in a load bus. It has a significant impact on power system studies [12-14]. Two types of load models are considered in this project for analyzing the contingency – steady state load model and polynomial load model.

3.1 Steady state load model. Steady state load model is also known as constant load model [15]. The active and reactive power equations in this model are represented as

$$P_i = \sum_{j=1}^{n} V_i Y_{ij} V_j \cos\left(\theta_{ij} + \delta_j - \delta_i\right); \quad (1)$$

$$Q_i = -\sum_{j=1}^{n} V_i Y_{ij} V_j \sin\left(\theta_{ij} + \delta_j - \delta_i\right), \quad (2)$$

where P_i and Q_i be the active and reactive power diagonal and off-diagonal elements of active power and reactive power are developed.

3.2 Polynomial load model. Polynomial load model is also known as ZIP load model. *Z* represents constant impedance, *I* represent constant current and *P* represents constant power. The active and reactive power equations in this model are represented in (3), (4). At bus-*i*:

$$P_i = \left[\sum_{j=1}^{n} V_i Y_{ij} V_j \cos\left(\delta_{ij} + \theta_j - \theta_i\right)\right]\left[P_1 V_i^2 + P_2 V_i + P_3\right]. \quad (3)$$

$$Q_i = \left[-\sum_{j=1}^{n} V_i Y_{ij} V_j \sin\left(\delta_{ij} + \theta_j - \theta_i\right)\right]\left[P_1 V_i^2 + P_2 V_i + P_3\right]. \quad (4)$$

At bus-*j*:

$$P_j = \left[\sum_{i=1}^{n} V_j Y_{ji} V_i \cos\left(\delta_{ji} + \theta_i - \theta_j\right)\right]\left[P_1 V_j^2 + P_2 V_j + P_3\right]; \quad (5)$$

$$Q_j = \left[-\sum_{i=1}^{n} V_j Y_{ji} V_i \sin\left(\delta_{ji} + \theta_i - \theta_j\right) \right] \left[P_1 V_j^2 + P_2 V_j + P_3 \right], \quad (6)$$

where P_i, P_j and Q_i, Q_j are the active and reactive power values at buses i and j; V_i, V_j are the nodal voltage values at buses i and j respectively; δ_{ij} is the angle voltage of unit i and j; Y_{ji} is the admittances of the line; P_1, P_2 and P_3 represents the ZIP load parameters.

The diagonal and off-diagonal elements of active power and reactive power at bus-i and bus-j are developed. These load models are incorporated with Newton-Raphson power flow solution method. Newton-Raphson method is used as it is faster, more reliable; results are accurate and quadratic type convergence. Jacobian matrix is formed using the developed diagonal and off-diagonal elements. The Jacobian matrix springs the linear connection between the small vagaries in voltage magnitude and phase angle with the small vagaries in real and reactive power as:

$$\begin{bmatrix} \Delta P \\ \Delta Q \end{bmatrix} = \begin{bmatrix} J_1 & J_2 \\ J_3 & J_4 \end{bmatrix} \begin{bmatrix} \Delta\delta \\ \Delta|V| \end{bmatrix}, \quad (7)$$

where J_1, J_2, J_3 and J_4 are the Jacobean matrix of Newton-Rapson method. The variance between the programmed and the designed values known as power residual is given in (8), (9)

$$\Delta P_i^k = P_i^{sch} - P_i^k; \quad (8)$$

$$\Delta Q_i^k = Q_i^{sch} - Q_i^k. \quad (9)$$

The new estimates for voltage angle and voltage magnitude are shown in (10), (11):

$$\delta_i^{k+1} = \delta_i^k - \Delta\delta_i^k; \quad (10)$$

$$\left|V_i^{k+1}\right| = \left|V_i^k\right| - \left|\Delta V_i^k\right|. \quad (11)$$

These two load models are applied to IEEE 118 bus system for analyzing the behavior of the loads. Line stability index gives support to find most severe lines.

4. Hybrid line stability ranking index (HLSRI) for contingency ranking. To derive the HLSRI we first consider the line stability index (LSI or L_{mn}) and the fast voltage stability index (FVSI). We then showed that the FVSI is a calculation of the L_{mn} and proceed to derive the HLSRI for better precision and speed. L_{mn} index is given in (12) [16]:

$$L_{mn} = \frac{4XQ_n}{\left[V_m \sin(\theta - \delta)\right]^2} \le 1, \quad (12)$$

where $\delta = \delta_m - \delta_n$; V_m is the voltage magnitude; X is the reactance of the transmission line.

The FVSI is derived from L_{mn} when the voltage angle difference between sending and receiving end is assumed to be very small (i.e., $\delta = 0$). Then FVSI is show in (13):

$$FVSI = \frac{4Q_n \cdot (|Z^2|)}{\left[|V_m|^2 \cdot X\right]} \le 1, \quad (13)$$

where Q_n is the reactive power at receiving end; Z is the impedance of the line; X is the reactance of the line.

We therefore propose to combine (13) and (14) into a single equation to compute a HLSRI rendering to a switching function β, as shown in (14). Each value of δ computed from the load-flow program is tested against a threshold value δ_C to determine whether β is 1 or 0. The proposed index is formed by combining (12) and (13) into one to produce a HLSRI show in (14) that gain more accuracy and fastness with improved line stability. The HLSRI is given as formulation of FVSI:

$$HLSRI = \frac{4XQ_n}{\left[V_m\right]^2} \left[\frac{|Z|^2}{X_{Line}} \beta - \frac{XQ_n}{\left[\sin(\theta - \delta)\right]^2} (\beta - 1) \right] \le 1, \quad (14)$$

where $\beta = \begin{cases} 1 & \delta < \delta_C \\ 0 & \delta \ge \delta_C \end{cases}$,

where δ is used as modifier; β is used as switching function.

When HLSRI is less than 1, the system is stable or HLSRI is approached to one, then the system is unstable.

Table 1 shows the proposed index value in ZIP load model without contingency of IEEE 14 test system. It has 5 generator buses (PV), 9 load buses (PQ) and 20 interconnected lines or branches. Various indices value with proposed index as shown in the Table 1.

Table 1

Comparison between indices values of proposed index with LSI and FVSI

S. no	From	To	Index		
			LSI	FVSI	HLSRI
1	1	2	0.0286	0.0287	0.0287
2	2	3	0.0259	0.0259	0.0259
3	2	4	0.0004	0.0004	0.0004
4	1	5	0.008	0.008	0.008
5	2	5	0.0026	0.0026	0.0026
6	3	4	0.011	0.011	0.011
7	4	5	0.0067	0.0067	0.0067
8	5	6	0.0159	0.0159	0.0159
9	4	7	0.0618	0.0616	0.0618
10	7	8	0.0425	0.0425	0.0425
11	4	9	0.0406	0.0406	0.0406
12	7	9	0.0022	0.0022	0.0022
13	9	10	0.0083	0.0083	0.0083
14	6	11	0.037	0.037	0.037
15	6	12	0.0662	0.0663	0.0663
16	6	13	0.0114	0.0114	0.0114
17	9	14	0.0456	0.0455	0.0455
18	10	11	0.2916	0.264	0.264
19	12	13	0.0097	0.0098	0.0098
20	13	14	0.0507	0.0509	0.0509

From the Table 1 it is evidence that, instead of using two individual line indexes, the proposed HLSRI values are very close to the other indices and more accuracy.

5. Power system contingency ranking algorithm is shown below.

Stage 1. Recite the given system line data and the bus data.

Stage 2. Without seeing the line contingency perform the load flow analysis for the base case.

Stage 3. Simulate a line outage or line contingency i.e. removing a line proceeding to the next step.

Stage 4. Load flow analysis is done for this specific outage then calculation of the active power flow is done in the lasting lines and value of $P_{\max}$ is also calculated.

Stage 5. Subsequently for the exact line contingency, voltages of all the load buses are designed.

Stage 6. Then HLSRI is being calculated which indicates the voltage collapse.

Stage 7. Stages 3 to 6 for all the line voltages is repeated to obtain HLSRI.

Stage 8. Contingencies are ranked based on the sternness of the contingency.

The proposed HLSRI is investigated with IEEE 14 bus system with contingency (single line outage) as shown in Fig. 2.

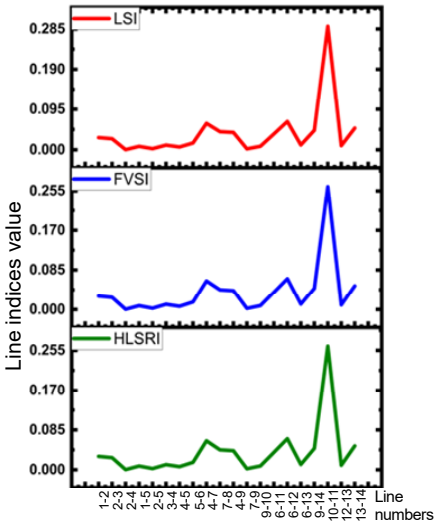

Fig. 2. Proposed index value with LSI and FVSI using contingency

From Fig. 2 the proposed index gives more accuracy and fastness in the stability value in the contingency when compared to others. First five ranks considered as most critical lines, and rank 6 to 16 considered as semi critical and ranks 17 to 20 considered as non-critical line, so in this paper most critical lines are analyzed with compensation to maintain the system stable and secure. Table 2 illustrates the data of tuned UPFC devices placed at critical location for compensation in contingency. Figure 2 shows the comparison between proposed index with others when line no. 4-7 gets outage then severity of the lines along with ranking shown in Table 2.

Table 2

Tuned UPFC devices placed at critical location for compensation in contingency

Rank	From	To	V_m, p.u	P, MW	Q, MVAr	P_{losses}, MW	Q_{losses}, MVAr
1	10	11	1.026	14.62	11.14	2.37	–27.22
2	6	12	1.12	26.16	24.57	5.53	–19.47
3	13	14	1.083	16.43	19.4	2.14	–24.12
4	9	14	1.034	14.22	12.52	2.00	–24.12
5	6	11	1.12	23.29	–6.67	6.59	–20.86

The above analysis is also carried out for IEEE 118 test system with different percentage of loadings in contingency analysis.

6. Unified power flow controller. A FACTS device plays a vital role in controlling power and enhancing the working volume of existing lines. Basic purpose of the parallel inverter is to supply real power required by the series inverter through the common DC link. The parallel inverter can also grip or produce controllable reactive power as shown in Fig. 3 [17, 18].

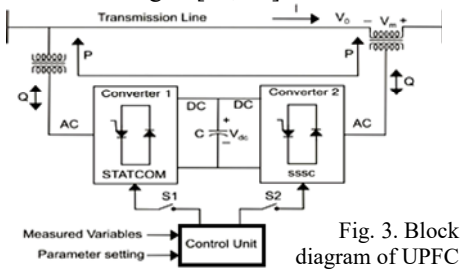

Fig. 3. Block diagram of UPFC

The active and reactive power equation of the UPFC [19] is developed with ZIP load model as shown in:

$$P_i = \left\{\left[\frac{-2R_{se}rV_i^2\cos\gamma}{R_{se}+X_{se}}\right]+\left[\frac{rV_i^2X_{se}\sin\gamma}{R_{se}^2+X_{se}^2}\right]-\left[\frac{R_{se}r^2V_i^2}{R_{se}^2+X_{se}^2}\right]-\right.$$
$$\left.-\left[\frac{rV_iV_jX_{se}\sin(\theta_i+\gamma-\theta_j)}{R_{se}^2+X_{se}^2}\right]+\left[\frac{rV_iV_jR_{se}\cos(\theta_i+\gamma-\theta_j)}{R_{se}^2+X_{se}^2}\right]\right\}\times \quad (15)$$
$$\times\left\{P_1V_i^2+P_2V_i+P_3\right\};$$

$$Q_i = \left[\frac{-rV_iV_j}{R_{se}^2+X_{se}^2}\right]\cdot\left\{X_{se}\cos\gamma-R_{se}\sin\gamma\right\}\cdot\left\{P_1V_i^2+P_2V_i+P_3\right\}; \quad (16)$$

$$P_j = \left[\frac{rV_iV_j}{R_{se}^2+X_{se}^2}\right]\cdot\left\{R_{se}\cos(\theta_i+\gamma-\theta_j)+X_{se}\sin(\theta_i+\gamma-\theta_j)\right\}\times \quad (17)$$
$$\times\left\{P_1V_i^2+P_2V_i+P_3\right\};$$

$$Q_j = \left[\frac{rV_iV_j}{R_{se}^2+X_{se}^2}\right]\cdot\left\{X_{se}\cos(\theta_i+\gamma-\theta_j)-R_{se}\sin(\theta_i+\gamma-\theta_j)\right\}\times \quad (18)$$
$$\times\left\{P_1V_i^2+P_2V_i+P_3\right\},$$

where P_i, P_j, Q_i, Q_j are the active and reactive power at i^{th} and j^{th} bus; R_{se} and X_{se} are the resistance and reactance of the line.

The crosswise and off-diagonal elements are developed. By using this developed mathematical model, MATLAB program is developed and used for compensating the most severe lines.

7. Results and discussion. In this paper, the IEEE 14 test bus system shown for 100 % loading along with compensation as shown in Table 2.

From the below Table 3, it shows the power flows without UPFC compensation for 100 % loading (which find with the help of proposed index).

Table 3

Results of ZIP load modeling for 100 % loading

Rank	From	To	P, MW	Q, MVAr	V_m, p.u	P_{losses}, MW	Q_{losses}, MVAr
	ZIP load modeling						
1	70	74	17.1	14.03	0.99	107.8	1758
2	71	72	15.1	–10.14	0.996	137.8	1758
3	24	72	–3.02	–4.11	1	137.8	1758
4	24	70	–11.0	–7.45	1	137.8	1758
5	92	100	32.0	–13.30	0.99	137.8	1758
	Z load modeling alone						
1	70	74	18.6	21.06	0.99	144.9	–1729
2	71	72	20.0	–11.19	1.001	144.9	–1729
3	24	72	–7.7	–2.87	1	144.9	–1729
4	24	70	–16.0	–7.14	1	144.9	–1729
5	92	100	32.0	–13.3	0.99	144.9	–1729
	I load modeling alone						
1	70	74	17.21	14.03	0.99	137.6	1760
2	71	72	15.06	–10.1	0.996	137.6	1760
3	24	72	–2.94	–4.13	1	137.6	1760
4	24	70	–10.92	–7.46	1	137.6	1760
5	92	100	31.30	–13.2	0.99	137.6	1760
	P load modeling						
1	70	74	16.77	14.15	0.99	133.0	–1775
2	71	72	9.92	–8.96	0.996	133.0	–1775
3	24	72	2.13	–5.40	1	133.0	–1775
4	24	70	–5.55	–7.67	1	133.0	–1775
5	92	100	30.86	–13.1	0.99	133.0	–1775

IEEE 118 bus test system which consists of 1 slack bus, 69 load buses, 48 generator buses and 179 transmission lines is simulated using MATLAB for ZIP load modeling and individual Z, I, P load modeling and following results are obtained for different loading conditions without contingency. Tables 4 and 5 shows the ZIP and individual Z, I, P load model with 100 % and 150 % of loading for the critical lines without contingency.

At a time, single line outage is performed, and the stability is analysed on IEEE 118 bus system by observing the standards of voltage profile, active and reactive power flows and total power loss. All the lines are graded affording to the values of a HLSRI. Among 179 ranks, 1 to 8 ranks are identified as most critical lines

and the below tables shows the results for these 8 most critical lines obtained while performing contingency and shows the results obtained after compensating the most critical lines.

Table 4

Results of ZIP, *Z*, *I*, *P* load modeling for 100 % loading with contingency

Rank	From	To	HLSRI	V_m, p.u	*P*, MW	*Q*, MVAr	P_{losses}, MW	Q_{losses}, MVAr
ZIP load modelling								
1	70	74	1.086	0.99	25	8	139.60	–1732
2	71	72	0.965	0.99	15	20	140.54	–1734
3	24	72	0.847	1.01	7	3	140.08	–1737
4	24	70	0.759	1.01	7	3	151.89	–1675
5	92	100	0.542	1	10	8	140.34	–1732
Z load modelling alone								
1	70	74	1.065	1	138.09	17	145.14	–1723
2	71	72	0.999	0.99	66	20	144.53	–1719
3	24	72	0.843	1.01	7	3	144.21	–1723
4	24	70	0.758	1.01	7	3	158.43	–1652
5	92	100	0.537	1	10	8	145.05	–1718
I load modelling alone								
1	70	74	1.086	1	25	8	138.09	–1752
2	71	72	0.96	0.99	66	20	137.47	–1750
3	24	72	0.848	1.01	7	3	137.34	–1754
4	24	70	0.76	1.01	7	3	148.85	–1692
5	92	100	0.532	1	10	6	137.84	–1747
P load modelling alone								
1	70	74	1.102	1	25	8	138.09	–1752
2	71	72	0.93	0.99	66	20	137.47	–1750
3	24	72	0.858	1.01	7	3	137.34	–1754
4	24	70	0.766	1.01	7	3	148.85	–1692
5	92	100	0.522	1	10	10	137.84	–1747

Table 5

Results of ZIP, *Z*, *I*, *P* load modeling for 150 % loading

Rank	From	To	*P*, MW	*Q*, MVAr	V_m, p.u	P_{losses}, MW	Q_{losses}, MVAr
	ZIP load modeling						
1	70	74	5.179	–4.58	0.95	861.6	616.43
2	71	72	163.36	–33.4	0.969	861.6	616.43
3	24	72	–123.6	44.32	1	861.6	616.43
4	24	70	–142.77	52.42	1	861.6	616.43
5	92	100	–223.27	433.0	0.98	861.6	616.43
	Z load modeling alone						
1	70	74	–350.31	254.3	0.95	544.3	307.91
2	71	72	9131.19	1890	6.72	544.3	307.91
3	24	72	–308.57	724.0	1	544.3	307.91
4	24	70	12.218	2.207	1	544.3	307.91
5	92	100	–223.2	433.0	0.98	544.3	307.91
	I load modeling alone						
1	70	74	5.246	–4.606	0.95	862.8	2622.87
2	71	72	163.3	–33.492	0.969	862.8	2622.87
3	24	72	–123.6	44.35	1	862.8	2622.87
4	24	70	–142	52.45	1	862.8	2622.87
5	92	100	22.46	–11.906	0.98	862.8	2622.87
	P load modeling alone						
1	70	74	7.975	–5.4015	0.95	695.3	1615.45
2	71	72	138.394	–34.067	0.971	695.3	1615.45
3	24	72	–104.80	34.238	1	695.3	1615.45
4	24	70	–123.65	38.692	1	695.3	1615.45
5	92	100	22.305	–8.7145	0.99	695.3	1615.45

Table 6 and 7 shows the values for HLSRI of ZIP load model with 100 % and 150 % loading with contingency. Table 8 shows the ZIP load model with compensation for the critical lines which is ranked from 1 to 8 with different percentage of loading.

In Table 6, $|r|$ denotes ratio of sending end voltage and injected voltage; γ is the angle between the voltages.

Table 6

Results of ZIP, *Z*, *I*, *P* load modeling for 100 % loading with UPFC compensation

Rank	From	To	*r*	γ	V_m, p.u	*P*, MW	*Q*, MVAr	P_{losses}, MW	Q_{losses}, MVAr
ZIP load modelling									
1	70	74	0.1	10	0.96	41.8	88.3	130	–1777
2	71	72	0.1	15	0.96	21.5	36.2	132	–1778
3	24	72	0.1	10	0.96	14.2	45.8	132	–1777
4	24	70	0.3	20	0.96	16.6	75.9	131	–1767
5	92	100	0.1	1	0.96	40.5	19.9	133	–1774
Z load modelling									
1	70	74	0.1	5	0.96	40.5	81.49	132	–1778
2	71	72	0.1	10	0.96	21.0	37.47	132	–1779
3	24	72	0.1	6	0.96	14.4	46.31	132	–1779
4	24	70	0.8	120	0.96	156.	36.28	125	–1677
5	92	100	0.7	5	0.96	33.8	–5.57	133	–1775
I load modelling									
1	70	74	0.1	5	0.96	40.4	81.51	132	–1778
2	71	72	0.1	5	0.96	19.0	38.27	132	–1778
3	24	72	0.1	2	0.96	12.6	47.03	132	–1778
4	24	70	0.8	120	0.96	15.6	36.28	125	–1677
5	92	100	0.5	5	0.96	32.0	–10.1	133	–1775
P load modelling									
1	70	74	0.1	5	0.96	32.4	82.12	135	–1766
2	71	72	0.1	10	0.96	17.3	37.34	133	–1772
3	24	72	0.1	5	0.96	8.11	48.01	134	–1771
4	24	70	0.8	120	0.96	15.6	36.44	125	–1677
5	92	100	0.5	5	0.96	35.9	2.52	132	–1776

From the results it is clear that the values of the transmission line parameters are improved after compensation compared to before compensation. For example, between buses 70 and 74 when performing load modelling, results are active power 17.184 MW, reactive power 14.0386 MVAr, voltage profile 0.99, total system loss 107.815 MW and when contingency is created the results are active power 25 MW, reactive power 8 MVAr, voltage profile 0.99, total system loss 139.60 MW and finally after providing compensation results are active power 41.878 MW, reactive power 88.37 MVAr, voltage profile 0.96, total system loss 130.43 MW. This shows that after providing compensation voltage profile is maintained, active power flow is increased, reactive power flow is maintained, and the total system losses are condensed and hence the system is maintained stable.

Table 7

Results of ZIP, *Z*, *I*, *P* load modeling for 150 % loading with contingency

Rank	From	To	HLSRI	V_m, p.u	*P*, MW	*Q*, MVAr	P_{losses}, MW	Q_{losses}, MVAr
ZIP load modelling								
1	69	75	7.78	0.97	54	200	896	2833
2	69	77	3.95	0.97	54	200	904	2846
3	70	74	2.00	1	66	120	1649	6692
4	24	70	1.82	0.99	10.5	4.5	1550	6188
5	76	77	1.20	0.91	70.5	16.5	915	2925
I load modelling alone								
1	69	75	6.81	0.97	54	200	864	2641
2	69	77	3.70	0.97	54	200	872	2653
3	70	74	1.88	1	66	120	644	1654
4	24	70	1.35	0.99	10.5	4.5	1649	6692
5	75	77	1.16	0.95	102	40.5	950	3712
P load modelling alone								
1	69	75	4.22	0.97	54	200	695	1626
2	69	77	2.33	0.97	54	200	702	1636
3	70	74	1.20	1	66	120	644	1654
4	24	70	0.96	0.99	10.5	4.5	914	2729
5	75	77	0.93	0.95	102	40.5	745	2358

Table 8

Results of ZIP, *Z*, *I*, *P* load modeling for 150 % loading with UPFC compensation

Rank	From	To	*r*	Gamma	V_m, p.u	*P*, MW	*Q*, MVAr	P_{losses}, MW	Q_{losses}, MVAr
ZIP load modelling									
1	69	75	0.1	10	0.95	437	83.6	689	1565
2	69	77	0.1	10	0.95	587	125	692	1562
3	70	74	0.2	5	0.95	30.5	59.6	692	1599
4	24	70	0.1	15	0.95	–128	63.2	692	1593
5	76	77	0.5	15	0.95	67	417	735	1726
I load modelling									
1	69	75	0.1	1	0.95	430	84	688	1564
2	69	77	0.1	4	0.95	581	124	690	1559
3	70	74	0.6	75	0.95	322	194	651	1356
4	24	70	0.4	68	0.95	–63.5	68	661	1385
5	75	77	0.5	77	0.95	234	63	676	1453
P load modelling									
1	69	75	0.4	20	0.95	620	303	700	1504
2	69	77	0.3	65	0.95	768	214	722	1558
3	70	74	0.2	20	0.95	59	132	689	1584
4	24	70	0.1	10	0.95	–128	63	692	1592
5	75	77	0.5	33	0.95	158	171	708	1610

8. Conclusions. The proposed index is applied for IEEE 14, 118 test system and mathematical model of steady state and polynomial load models (ZIP) are developed and analyzed with the IEEE test system by in view of the single line outage at a time. IEEE 118 test system is analyzed for various percentages of ZIP load model for contingency with and without compensation. A hybrid line stability ranking index shows the most critical lines in the system for which compensation is provided by placing unified power flow controller with proper tuned. Based on the outcomes it is apparent that the stress level is reduced, and the system is maintained stable and healthy by providing suitable compensation at suitable location.

Conflict of interest. The authors declare that they have no conflicts of interest

REFERENCES

1. Mishra A., Kumar G.V.N. A risk of severity based scheme for optimal placement of interline power flow controller using composite index. *International Journal of Power and Energy Conversion*, 2017, vol. 8, no. 3, pp. 257-275. doi: https://doi.org/10.1504/IJPEC.2017.10003636.

2. Venkatesh P., Visali N. Assessment of Power System Security Using Contingency Analysis. *International Journal of Control and Automation*, 2019, vol. 12, no. 5, pp. 25-32. doi: https://doi.org/10.33832/ijca.2019.12.5.03.

3. Venkateswaran J., Manohar P., Vinothini K.., Shree B.T.M., Jayabarathi R. Contingency analysis of an IEEE 30 bus system. *2018 3rd IEEE International Conference on Recent Trends in Electronics, Information & Communication Technology (RTEICT)*, 2018, pp. 328-333. doi: https://doi.org/10.1109/RTEICT42901.2018.9012509.

4. Angadi R.V., Daram S.B., Venkataramu P.S. Contingency Analysis of Power System using Big Data Analytic Techniques. *2020 5th International Conference on Computing, Communication and Security (ICCCS)*, 2020, pp. 1-7. doi: https://doi.org/10.1109/ICCCS49678.2020.9276796.

5. Arif A., Wang Z., Wang J., Mather B., Bashualdo H., Zhao D. Load Modeling – A Review. *IEEE Transactions on Smart Grid*, 2018, vol. 9, no. 6, pp. 5986-5999. doi: https://doi.org/10.1109/TSG.2017.2700436.

6. Seshapalli S.R. Analysis of Hybrid Power Flow Controller using Static load model under Contingency Screening. *2019 IEEE International Conference on Clean Energy and Energy Efficient Electronics Circuit for Sustainable Development (INCCES)*, 2019, pp. 1-6. doi: https://doi.org/10.1109/INCCES47820.2019.9167709.

7. Asawa S., Al-Attiyah S. Impact of FACTS device in electrical power system. *2016 International Conference on Electrical, Electronics, and Optimization Techniques (ICEEOT)*, 2016, pp. 2488-2495. doi: https://doi.org/10.1109/ICEEOT.2016.7755141.

8. Chorghade A., Kulkarni Deodhar V.A. FACTS Devices for Reactive Power Compensation and Power Flow Control – Recent Trends. *2020 International Conference on Industry 4.0 Technology (I4Tech)*, 2020, pp. 217-221. doi: https://doi.org/10.1109/I4Tech48345.2020.9102640.

9. Suresh K., Parimalasundar E. A Modified Multi Level Inverter with Inverted SPWM Control. *IEEE Canadian Journal of Electrical and Computer Engineering*, 2022, vol. 45, no. 2, pp. 99-104. doi: https://doi.org/10.1109/ICJECE.2022.3150367.

10. Sairam S., Daram S.B. Contingency Ranking in a Power Transmission System using ZIP Load Modeling. *UPB Scientific Bulletin, Series C: Electrical Engineering and Computer Science*, 2020, vol. 82, no. 1, pp. 205-220.

11. Ding T., Li C., Yan C., Li F., Bie Z. A Bilevel Optimization Model for Risk Assessment and Contingency Ranking in Transmission System Reliability Evaluation. *IEEE Transactions on Power Systems*, 2017, vol. 32, no. 5, pp. 3803-3813. doi: https://doi.org/10.1109/TPWRS.2016.2637060.

12. Suresh K., Parimalasundar E. Design and Implementation of Universal Converter. *IEEE Canadian Journal of Electrical and Computer Engineering*, 2022, vol. 45, no. 3, pp. 272-278. doi: https://doi.org/10.1109/ICJECE.2022.3166240.

13. Ram S.S., Daram S.B., Venkataramu P.S., Nagaraj M.S. Analysis of ZIP Load Modeling in Power Transmission System. *International Journal of Control and Automation*, 2018, vol. 11, no. 7, pp. 11-24. doi: https://doi.org/10.14257/ijca.2018.11.7.02.

14. Suresh K., Parimalasundar E. A novel dual-leg DC-DC converter for wide range DC-AC conversion. *Automatika*, 2022, vol. 63, no. 3, pp. 572-579. doi: https://doi.org/10.1080/00051144.2022.2056809.

15. Chappa H., Thakur T. A novel load shedding methodology to mitigate voltage instability in power system. *Electrical Engineering & Electromechanics*, 2022, no. 3, pp. 63-70. doi: https://doi.org/10.20998/2074-272X.2022.3.09.

16. Ezhilvannan P., Krishnan S. An Efficient Asymmetric Direct Current (DC) Source Configured Switched Capacitor Multi-level Inverter. *Journal Européen Des Systèmes Automatisés*, 2020, vol. 53, no. 6, pp. 853-859. doi: https://doi.org/10.18280/jesa.530611.

17. Yari S., Khoshkhoo H. Assessment of line stability indices in detection of voltage stability status. *2017 IEEE International Conference on Environment and Electrical Engineering and 2017 IEEE Industrial and Commercial Power Systems Europe (EEEIC / I&CPS Europe)*, 2017, pp. 1-5. doi: https://doi.org/10.1109/EEEIC.2017.7977454.

18. Goutham N.S., Dr. Mohd. Z. A. Ansari. Determination of Optimal Location of FACTS Devices for Power System Restoration Including Load Flow and Contingency Analysis, *International Journal of Engineering Research & Technology (IJERT)*, 2017, vol. 5, no. 18, pp. 1-4. doi: https://doi.org/10.17577/IJERTCONV5IS18004.

19. Praveen Kumar T., Ganapathy S., Manikandan, M. Improvement of voltage stability for grid connected solar photovoltaic systems using static synchronous compensator with recurrent neural network. *Electrical Engineering & Electromechanics*, 2022, no. 2, pp. 69-77. doi: https://doi.org/10.20998/2074-272X.2022.2.10.

Received 25.06.2022
Accepted 12.09.2022
Published 06.01.2023

Peruthambi Venkatesh[1], *Research Scholar*,
Nagalamadaka Visali[1], *Professor*,
[1] Department of Electrical & Electronics Engineering,
JNTUA College of Engineering (Autonomous) Ananthapuramu,
Ananthapuramu-515002, Andhra Pradesh, India,
e-mail: venkateshp.engg@gmail.com (Corresponding Author);
nvisali.eee@jntua.ac.in

How to cite this article:
Venkatesh P., Visali N. Investigations on hybrid line stability ranking index with polynomial load modeling for power system security. *Electrical Engineering & Electromechanics*, 2023, no. 1, pp. 71-76. doi: https://doi.org/10.20998/2074-272X.2023.1.10

UDC 621.316.9 https://doi.org/10.20998/2074-272X.2023.1.11

D.G. Koliushko, S.S. Rudenko, A.N. Saliba

Determination of the scope of the experimental-calculation method for measuring the touch voltage

*The work is devoted to the improvement of methods for determining the normalized parameters of the grounding system (GS) of operating power stations and substations. The **aim** of the work is determination of the scope of the experimental-calculated method for measuring the touch voltage, depending on short-circuit (SC) current value for the given dimensions of the GS and the type of soil. **Methodology**. The study analyzed the non-linear effect of the SC current value on the touch voltage, taking into account such factors as the GS size and the soil type. The calculation used statistical data on the GS size and the characteristics of the soil obtained by monitoring the GS state of 585 operating electrical substations with a voltage class of 110-750 kV using the induction method and the method of vertical soil sounding, respectively. For the calculation, a mathematical model of a non-equipotential GS located in a three-layer semiconductor space with plane-parallel boundaries was used, this model was developed using the method of integro-differential equations. **Results**. To determine the scope of the method, in this work it is proposed to use the linearity criterion, which is determined due to the ratio of the constant of reduced touch voltage to the current value. The example shows the method for determining the threshold minimum and maximum values of the measuring current of the soil, in the range between which the measurements by experimental-calculated methods are impossible. A table of threshold current values has been formed and recommendations have been developed on the possibility of using experimental-measuring methods for determining the touch voltage depending on the GS size and soil characteristics.* References 22, tables 3, figures 7.

Key words: **electrical substations, grounding system, modeling of the electromagnetic processes, touch voltage, soil characteristics, short-circuit.**

Метою роботи є визначення області застосування експериментально-розрахункового методу вимірювання напруги дотику в залежності від значення струму короткого замикання для заданих розмірів заземлювального пристрою (ЗП) та типу ґрунту. В дослідженні було проаналізовано нелінійний вплив величини струму КЗ на напругу дотику з урахуванням таких факторів як розмір ЗП та тип ґрунту. Для розрахунку була використана математична модель нееквіпотенційного ЗП, розташованого у тришаровому напівпровідному просторі з плоско-паралельними границями поділу, що була розроблена за допомогою методу інтегро-диференційних рівнянь. Для визначення області застосування методу в роботі запропоновано використовувати критерій лінійності, який визначається через відношення сталої приведеної напруги дотику до поточного значення. Сформовано таблицю значень порогових струмів та розроблено рекомендації щодо можливості використання експериментально-вимірювальних методів визначення напруги дотику в залежності від розміру ЗП та характеристик ґрунту. Бібл. 22, табл. 3, рис. 7.

Ключові слова: **електрична підстанція, заземлювальний пристрій, моделювання електромагнітних процесів, напруга дотику, характеристики ґрунту, коротке замикання.**

Problem. The grounding system (GS) of power stations and substations is a branched complex system of horizontal ground electrodes and vertical electrodes. The main purpose of the GS is to ensure the electrical safety of both the operating personnel of the power facility and unauthorized persons, as well as the reliable operation of the equipment.

In all regulatory documents, electrical safety at a power facility is characterized by the value of the touch voltage (U_t). In Ukraine, the permissible value of U_t is regulated by [1], in the European Union it is regulated by [2]. Swiss standards [3, 4], as well as Austrian [5] generally meet European Union requirements.

The method of electromagnetic diagnostics (EMD) has become widespread for determining the GS current state of operating power facilities. It involves the implementation of three stages [6]: the experimental stage, the calculation stage, and the stage of developing recommendations for reconstruction aimed at bringing the GS in line with the requirements of the current regulatory documents to further perform the main functions.

Over past 20 years specialist of Research & Design institute «Molniya» was diagnosis of 585 objects with a voltage class of 110-750 kV (operating power stations, substations of energy systems, mining and processing plants, factories, oil pumping stations, etc.), and it was found that the design of 97 % before reconstruction of GS was not meet the requirements of regulatory documents , and for more than 75 % it was exceeds the allowable values of the touch voltage [7], which can to severe post-accident consequences and poses a threat to the safety of people and animals.

A number of factors that significantly affect the value of the touch voltage were determined in [8]: the design of the GS, the electrophysical characteristics of the soil (EPC) and the resistance of the base at the place of maintenance of the equipment, etc. In this work, we will consider in detail the dependence of the touch voltage on the value of the ground fault current.

Analysis. According to the method of determining the touch voltage, three methods can be distinguished: experimental, calculated, and experimental-calculated.

The experimental method for measuring the touch voltage is carried out in the field on an operating object directly at a short-circuit (SC) current. It is dangerous, expensive and can be justified only in isolated cases in exceptional situations; therefore, it is practically not used.

The calculated method is based on the results of the GS EMD: the current structural state [9], additional experimental characteristics of the GS for assessing the adequacy of the calculation model [10, 11], and the EPC found using vertical electrical sounding (VES) [12]. The advantages of the method are the ability to determine the normalized parameters of the GS in all modes with a real SC current on all equipment with high accuracy (94 %), as well as checking the effectiveness of the developed recommendations [9]. In addition, the calculation programs

take into account the geometric, electrical and magnetic parameters of ground electrodes. The disadvantages of the calculated method are the laboriousness of the work to determine the initial data (the actual state of the GS, the carrying out of the VES, etc.), the need for specialized expensive devices and software, as well as highly qualified scientific and technical personnel.

The experimental-calculated method has received the greatest distribution both in Ukraine and in the world. His varieties and analysis are considering in sufficient detail in [13]. The general principle is to measure U_t while simulating a SC mode on substation equipment. With the help of a sinusoidal current generator, a voltage is applied to the circuit (see Fig. 1) with a frequency close to the industrial one, but different from it and its harmonics. The current measuring electrode C is on distance L_C, which is, as a rule, 2–3 times greater than the diagonal GS (D). In this case, the current value in the circuit I_m is fixed using an ammeter A, and the measured touch voltage U_m is fixed using a voltmeter V connected in parallel with the resistor R_B, simulating the resistance of the human body (usually equal to 1000 Ω). The horizontal distance L_p from the contact point to the plate is assumed to be 0,8 m [1, 9] or 1,0 m [14, 15]. As a potential electrode P imitating two human feet, a plate with a contact surface of 25×25 cm^2 is used, which is loaded with a weight of at least 25 kg. To simulate the most unfavorable seasonal conditions, the place of potential electrode installation is moistened.

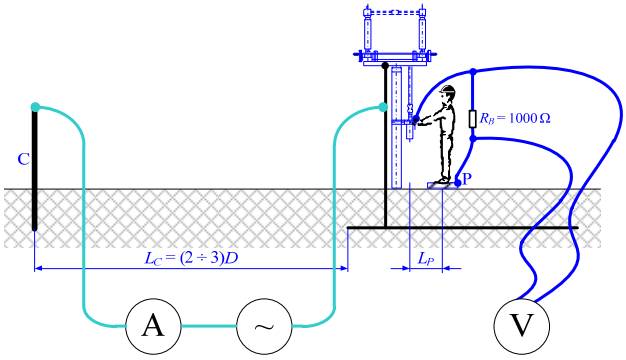

Fig. 1. The measurement circuit of touch voltage

In Ukraine and other countries of near and far abroad, a method of measuring at a low current value (up to 10 A) with subsequent reduction of the measured touch voltage in proportion to the real SC current has become widespread [9]:

$$U_t = U_m \frac{I_{SC}}{I_m}, \qquad (1)$$

where I_{SC} is the SC current calculated according to the energy system data.

In the international standard IEEE [15], the determination of the touch voltage is performed at a current of 0,1–0,2 kA (method of current input or high current method), after which the measured values of the touch voltage are found by expression (1). In [16], it is indicated that a value ~ 0,1 kA is necessary to ensure the best signal-to-noise ratio. Thus, none of the analyzed sources considered the issue of the influence of the SC current value on the normalized parameters of the GS when carrying out the measurements.

In Ukraine, as in some other countries, the GS of power stations and substations are made of hot-rolled steel (coated or uncoated). When high currents of a single phase-to-earth fault (their value for power facilities in Ukraine can reach up to 60 kA) [17] flow by the elements of GS, the inductive component of the self-resistance of the ground electrodes is not a constant, which is explained by the nonlinear dependence of the magnetic permeability of steel on the strength of the magnetic field around, hence the magnitude of the current flowing through the ground electrode (see Fig. 2). It is assumed that the nonlinear dependence is more pronounced at low and medium currents.

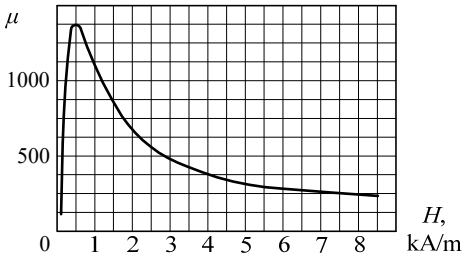

Fig. 2. The dependence of the magnetic permeability μ on magnetic field strength for steel BSt3SP (Fe37-3FN) [16]

Because of the type of dependence, it can be argued that the influence of the SC current or measuring current on the value of the normalized GS parameters is non-linear. Thus, the disadvantage of the experimental-calculated method for determining the touch voltage is the methodological error, which is associated with the neglect of the dependence of the magnetic permeability of the ground electrode material on the flowing current.

In addition, such measurements require the installation of a measuring electrode in the zone of zero potential, the distance to which L_C in 2-3 diagonals of the GS D (see Fig. 1) is valid only for homogeneous soil, for a two-layer soil such a distance can be in the range of 3-40 diagonals, as indicated by the data given in [14, 18, 19]. In conditions of dense buildings or developed infrastructure, this is almost impossible to achieve. Also, during a short-circuit, as a rule, part of the current flows in the neutral, which is not taken into account when measuring by this method. This component of the methodological measurement error is considered in detail in [8].

Nevertheless, there are current values at which magnetic saturation of the GS elements occurs and the dependence of the touch voltage on the SC current can be considered linear, and the GS resistance can be considered as a constant. In addition, the ascending part of the dependence in Fig. 2 is conditionally linear.

Thus, it can be assumed that there are such values of the measuring current and SC current for which expression (1) will be valid. At the same time, the main factors that affect the limit values of the above currents are the parameters that are individual for each power facility: the size of the GS and the EPC of the soil.

The aim of the work is determination of the scope of the experimental-calculated method for measuring the touch voltage, depending on SC current value for the given dimensions of the GS and the type of soil.

Research materials.

It is known that there are four types of VES curves, each of which is characterized by the ratio of the

resistivity of the layers: Q – $\rho_1 > \rho_2 > \rho_3$; A – $\rho_1 < \rho_2 < \rho_3$; H – $\rho_1 > \rho_2 < \rho_3$; K – $\rho_1 < \rho_2 > \rho_3$. Taking into account the previously obtained statistical distribution of EPC [20], it is advisable to carry out the study for the data given in Table 1.

Table 1

Typical EPC of the soil

Soil type	ρ_1, Ω×m	ρ_2, Ω×m	ρ_3, Ω×m	h_1, m	h_2, m
Q	100	50	10	0,8	6,3
H	100	50	100	0,8	6,3
K	10	100	10	0,8	6,3
A	10	50	100	0,8	6,3

As part of the GS EMD of 585 power facilities of Ukraine with a voltage class of 110-750 kV, the distribution of the GS size S was obtained (see Fig. 3,*a*) and it was determined that its value varies in the range from 122 m^2 to 436158 m^2.

This approximately corresponds to the GS size from 11 m × 11 m to 660 m × 660 m. Figure 3,*b* shows the distribution of the SC current value for the selected database. The database of SC was formed on the basis of responses to requests to operating organizations, similarly to [17]. In this case, the current value is in the range from 0,74 kA to 59,995 kA, and the median is 8,47 kA. In Fig. 3,*a*,*b*: *f* is the number of energy facilities as a percentage of all selected ones.

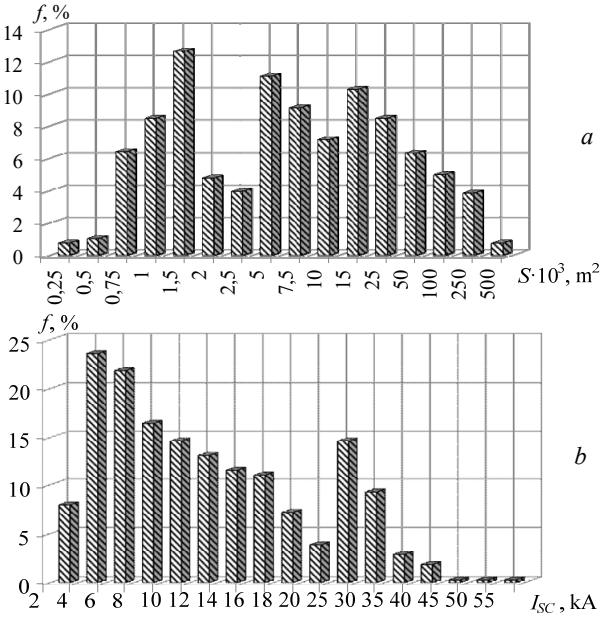

Fig. 3. The number of energy facilities as a percentage: *a* – GS size distribution of; *b* – SC current distribution

To carry out the study, the range of GS size S is [30×30; 156×156] m^2 was chosen, and the value of the SC current I_{SC} is [0,2; 20] kA, which allows covering about 75 % of cases. For the calculation, a mathematical model of a non-equipotential GS located in a three-layer semiconductor space with plane-parallel separation boundaries was used, developed using the method of integro-differential equations [10, 11, 21]. The determination of the normalized parameters was carried out for the specified current ranges, while the GS was located at a depth of 0,5 m, the size of its cell was 6 m × 6 m, and the cross section was ∅14 mm.

It should be noted that the dependence of the touch voltage value or the reduced touch voltage on the SC current is inconvenient for analysis, since visually the curves look close to straight lines (see Fig. 4), which does not allow determining the linear section of the dependence for direct recalculation using the expression (1).

Current and voltage are generally vector values. According to the theorem on the linear dependence of vectors, vectors will be linearly dependent if and only if at least one of them is a linear combination of others [22]. As can be seen from Fig. 4, there are the following SC current values, starting from which the reduced touch voltage $U'_t = U_t / I_{SC}$ is almost constant (U'_{tconst}). Therefore, to determine the range at which the touch voltage can be considered linearly dependent on the SC current, it is proposed to use the linearity criterion K_{con}, the value of which should be less than the engineering error of 10 %:

$$K_{con} = \left(\frac{U'_{ti}}{U'_{const}} - 1 \right) \times 100\% < 10\% . \qquad (2)$$

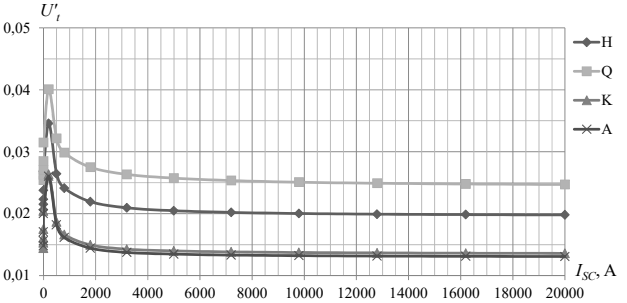

Fig. 4. The dependence of reduced touch voltage on the SC current for the steel GS, S = (156×156) m^2 and soil (Table 1)

As a result of the calculations, a number of dependences of the values of the GS normalized parameters on three factors were obtained: the SC current value, the GS size, and the soil type (see Table 1). For example, Table 2 shows the characteristic points of such a dependence for the area S = (30×30) m^2. As a steady value of the reduced touch voltage, we consider one that does not change with increasing current. For example, for soil type A and GS with 30×30 m^2, U'_{tconst} = 0,025 V/A.

The data obtained indicate that there are intervals before and after the threshold values of the currents $I_{\min}$ and $I_{\max}$, respectively, where the criterion K_{con} is less than 10 %, therefore, a directly proportional recalculation can be applied. Based on the calculated data, it is possible to construct a family of curves for the corresponding areas. Their general view is shown in Fig. 5.

It should be noted that the use of other values of specific resistances, sizes of GS and sizes of GS cells can affect the absolute values of the calculated parameters, but does not change the general appearance of the curves.

Consider the method for finding the values of the currents $I_{\min}$ and $I_{\max}$ using the example of GS with an area of 30×30 m^2. Fig. 6 shows the ascending and descending part of the curves for different soil types. In Table 2 (soil type K) we find that with an increase in current from 0,05 A to 0,50 A, the coefficient K_{con} increases from 1,188 % to 10,163 %, therefore, the corresponding current value determined by interpolation for K_{con} = 10 % can be considered as the lower limit of applying the techniques of linear recalculation for GS of the specified area and soil type: $I_{\min}$ = 0,48 A.

Table 2

The dependence of the calculated GS parameters on the SC current

SC current I_{SC}, A	Voltage on the GS U_G, V	Touch voltage U_t, V	Reduced touch voltage U'_t	Linearity criterion K_{con}, %	Voltage on the GS U_G, V	Touch voltage U_t, V	Reduced touch voltage U'_t	Linearity criterion K_{con}, %
	Soil type K				**Soil type A**			
0,05	0,02	0,0017	0,035	1,188	0,0421	0,0013	0,025	1,758
0,10	0,04	0,0035	0,035	2,361	0,0842	0,0026	0,026	3,496
0,30	0,12	0,0109	0,036	6,467	0,2531	0,0081	0,027	9,598
0,35	0,15	0,0128	0,037	7,431	0,2954	0,0096	0,027	10,983
0,45	0,188	0,017	0,037	9,302	0,38	0,01	0,028	13,603
0,50	0,209	0,019	0,038	10,163	0,42	0,01	0,028	14,851
16,0	7,012	0,934	0,058	71,286	13,840	0,805	0,050	103,30
54,0	23,55	2,99	0,055	62,509	46,63	2,55	0,047	90,985
549,3	230,2	20,7	0,038	10,431	465,2	15,7	0,029	15,590
686,0	286,9	25,2	0,037	7,870	580,3	19,0	0,028	11,811
843,8	352,3	30,6	0,036	6,196	713,1	22,8	0,027	9,299
2000,0	830,9	69,6	0,035	2,038	1686,0	51,0	0,026	3,092
3041,8	1262,0	104,7	0,034	0,956	2562,0	76,4	0,025	1,517
20000	8279,0	681,9	0,034	0,000	16830	494,9	0,025	0,000
	Soil type Q				**Soil type H**			
0,05	0,03	0,013	0,256	0,118	0,0645	0,0100	0,201	0,150
0,10	0,06	0,026	0,256	0,274	0,1290	0,0201	0,201	0,349
6,8	4,174	1,836	0,272	6,541	8,825	1,467	0,217	8,504
16,0	9,974	4,426	0,277	8,353	21,000	3,551	0,222	10,803
31,3	19,490	8,646	0,277	8,371	41,020	6,937	0,222	10,826
54,0	33,55	14,81	0,274	7,426	70,760	11,860	0,220	9,650
2000,0	1202,0	512,4	0,256	0,353	2581,0	402,4	0,201	0,449
4920,8	2953,0	1257,0	0,255	0,058	6345,0	986,8	0,201	0,119
5488,0	3293,0	1402,0	0,255	0,065	7076,0	1100,0	0,200	0,069
16200	9716,0	4136,0	0,255	0,003	20880	3245,0	0,200	0,004
20000	11990,0	5106,0	0,255	0,000	25780	4006,0	0,200	0,000

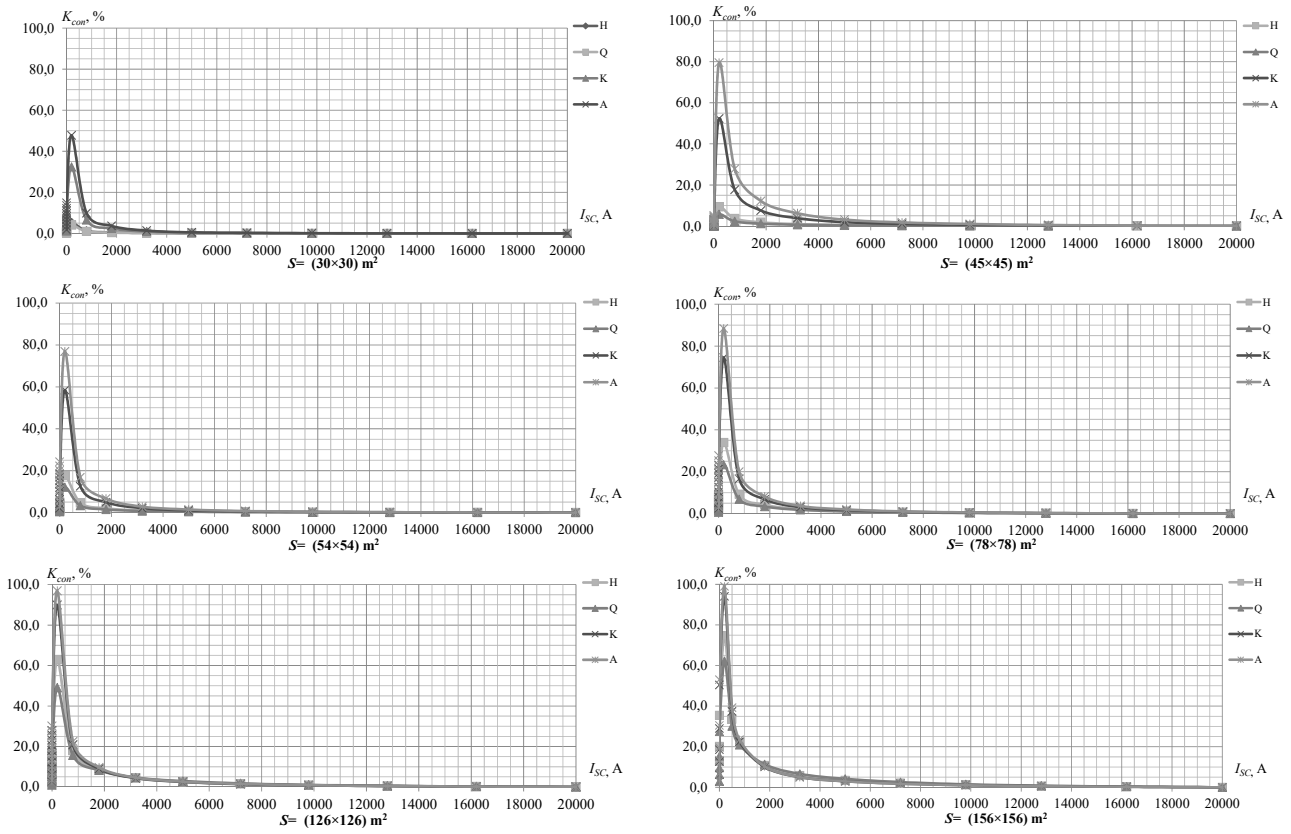

Fig. 5. The dependence of the linearity criterion on the current simulating a SC for a GS of a given area for different soil types

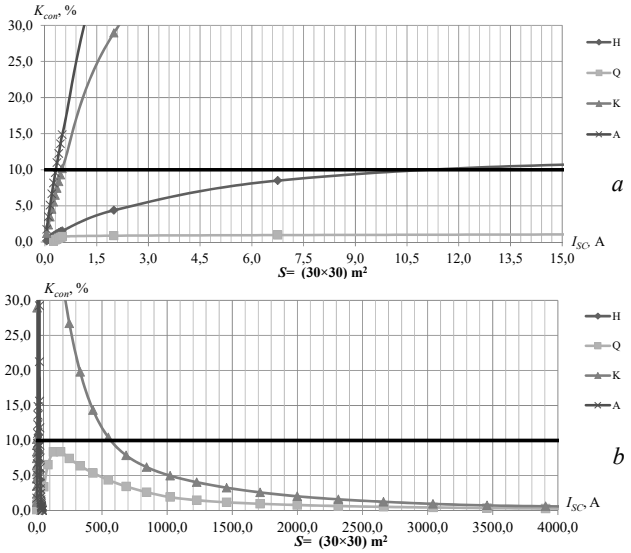

Fig. 6. The dependence of the linearity criterion K_{con} on the current simulating a SC: *a* – ascending; *b* – descending

Then follows the non-linearity section caused by the dependence of the magnetic permeability of the ground electrode material on the magnetic field strength and, accordingly, on the SC current (see Fig. 2). Starting from the value of 16 A, the value of the criterion K_{con} passes to the descending part, and at a current of approximately 550 A, it crosses the 10 % boundary, then gently decreases to 0. Thus, in this case, we accept $I_{\max} = 550$ A.

Similarly, the corresponding values of the boundaries of the currents $I_{\min}$ and $I_{\max}$ were found for all soil types and the considered sizes of the GS. The data obtained are summarized in Table 3.

Table 3

Threshold current values for using the experimental-calculated method for determining the touch voltage

GS area S, m^2	Low current method $I_{\max}$, A				High current method $I_{\min}$, A			
	H	Q	K	A	H	Q	K	A
30×30	12,7	–	0,48	0,32	32	–	550	800
45×45	12,1	–	0,4	0,3	149	–	600	820
54×54	3,5	100	0,25	0,17	525	350	900	1050
78×78	0,6	25	0,19	0,16	900	650	1050	1400
126×126	0,27	0,39	0,16	0,15	1500	1300	1700	1800
156×156	0,24	0,3	0,13	0,13	1900	2000	1800	1850

In Table 3 for soil type Q and GS areas 30×30 m^2 and 45×45 m^2 the lines with the sign «–» mean that there are no restrictions on the measuring current, because in all cases, the linearity criterion is less than 10 %.

The obtained dependencies form the limits of application of the experimental-calculated method for determining the touch voltage, because the criterion for the possibility of linear recalculation allows the possibility of measurement under the following condition:

$$I_m \le I_{\min} \quad \text{or} \quad I_m \ge I_{\max}. \qquad (3)$$

That is, for GS with an area of 30×30 m^2 located in soil type A, the measuring current must meet the following requirements: $I_{\min} \le 0{,}32$ A and $I_{\max} \ge 800$ A.

The use of a measuring current of more than 800 A threatens sensitive microprocessor technology, expensive high-voltage equipment, and the relay protection system.

Provided that all soil types are covered and for considered dimensions of GS substation, the measurement requires a current with a value of at least 2000 A. The use of such a current for the considered soil types with the resistance of the feet $R_f = 100$ Ω and GS with $S = 156\times156$ m^2 will lead to a touch voltage from 219 V up to 495 V (you can get the indicated values from the graph in Fig. 4 by multiplying the corresponding current value by the reduced touch voltage). Furthermore, such a current is dangerous.

In addition, it follows from this that a proportional recalculation of the touch voltage value measured by the low current method for GS of arbitrary size with an arbitrary soil type is possible only for substations in which the SC current will exceed 2000 A.

The use of the experimental-calculated method with a low current value is acceptable for GS with the area 30×30 m^2 and 45×45 m^2 located in the soil type Q, and for the IEEE method – GS with the area 30×30 m^2 and 45×45 m^2 for soil types H and Q and 54×54 m^2 – for soil type Q.

The carrying out measurements using the low current method, even for GS with the area $S = 30\times30$ m^2, requires a measuring current not exceeding 0,32 A (to cover all possible soil types). Such a current, subject to the resistance of the feet $R_f = 100$ Ω, creates a touch voltage not exceeding 8,1 mV (type A), and for large substations, the value of U_m will be even less. Taking into account that measurements are carried out at an operating power facility, with electric field strength of up to 30 kV/m and a measuring current with a frequency close to the industrial one, there are only two options for determining the touch voltage:

- the use of an experimental-calculated method using the existing fleet of instruments for some soil types and GS sizes, according to the restrictions given in Table 3 and expression (3), or the creation of new instruments that can measure U_m with a value of less than a few millivolts at a frequency close to the industrial one, in a complex electromagnetic environment;
- the use of the calculated method based on the data obtained using the GS EMD with the verification of the adequacy of the calculated model [10].

An alternative is relevant to develop devices with the ability to measure units of millivolts, provided that they operate at a frequency close to an industrial one and external electric field strength of up to 30 kV/m for determining the touch voltage by using the experimental-calculated method.

It should be noted that such dependence is not observed for GS made of a diamagnetic or paramagnet, which makes it possible to use the experimental-calculated method for measuring the touch voltage for GS made, for example, of copper (see Fig. 7) without restrictions.

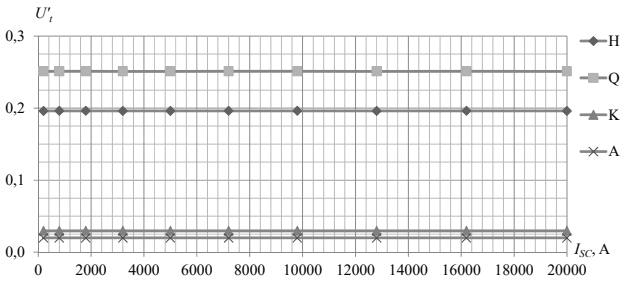

Fig. 7. The dependence of the reduced touch voltage value on the SC current for GS made of a copper at $S = (30\times30)$ m^2 and given soil parameters from Table 1

Conclusions.

1. For the first time, it was proposed to set the minimum and maximum threshold values of the measuring current for determine of the scope application of the experimental-calculated method for measuring the touch voltage. It has been proved that a proportional recalculation of the measured touch voltage value is possible only for the GS of substations, in which the SC current will exceed 2000 A.

2. It was found that using of the experimental-calculated method for GS made of steel (or other ferromagnetic material) with:

- low measuring current is limit for GS with the area 45×45 m^2 (and less) located in soil type Q;
- high measuring current (IEEE method) is limit for GS with the area 30×30 m^2 and 45×45 m^2 for soil types H and Q, 54×54 m^2 – for soil type Q.

3. Determining the touch voltage by the experimental-calculated method for GS of other sizes located in soil types H and Q, as well as soil types K and A types with the modern level of instruments is impossible with an error of less than 10 %.

Conflict of interest. The authors declare that they have no conflicts of interest

REFERENCES

1. *Rules of the device electroinstallations. General rules*. Kharkiv, Minenergovugillya Ukrayiny Publ., 2017. 760 p. (Ukr).

2. *BS EN 50522:2010. Earthing of power installations exceeding 1 kV a.c*. London, BSI, 2012. 104 p. doi: https://doi.org/10.3403/30191665.

3. *Verordnung über elektrische Starkstromanlagen (Starkstromverordnung).* Bern, Der Schweizerische Bundesrat, 2016. 34 p. (Ger).

4. *Erdungshandbuch Regelwerk: Technik Eisenbahn. D RTE 27900*. Bern, Verband öffentlicher Verkehr, 2014. 49 p. (Ger).

5. *Errichtung von elektrischen Anlagen mit Nennspannungen bis 1000 V ~ und 1500 V = Teil 1: Begriffe und Schutz gegen elektrischen Schlag (Schutzmaßnahmen). (ÖVE/ÖNORM E 8001-1)*. Vienna, Österreichisches Normungsinstitut, 2010. 138 p. (Ger).

6. Koliushko D.G., Rudenko S.S. Analysis of methods for monitoring of existing energy objects grounding devices state at the present stage. *Electrical Engineering & Electromechanics*, 2019, no. 1, pp. 67-72. doi: https://doi.org/10.20998/2074-272X.2019.1.11.

7. Koliushko D.G., Koliushko G.M., Rudenko S.S. Statistical analysis according grounding grid the power stations and substations for of normalized parameters. *Energy and Electrification*, 2015, no. 6, pp. 3-7. (Rus).

8. Koliushko D.G., Rudenko S.S. The factors of the influence on the touch voltage from the review of the development of recommendations for the reconstruction of the grounding device. *Technical Electrodynamics*, 2019, no. 3, pp. 29-36. doi: https://doi.org/10.15407/techned2019.03.029. (Ukr).

9. *Test and control devices, electrical grounding. Standard instruction. SOU 31.2-21677681-19:2009*. Kyiv, Minenergovugillya Ukrayiny Publ., 2010. 54 p. (Ukr).

10. Koliushko D.G., Rudenko S.S. Experimental substantiation of the calculation procedure of normalized parameters of grounding device based on the three-layer soil model. *Electrical Engineering & Electromechanics*, 2018, no. 1, pp. 66-70. doi: https://doi.org/10.20998/2074-272X.2018.1.11.

11. Koliushko D.G., Rudenko S.S. Determination the electrical potential of a created grounding device in a three-layer ground. *Technical Electrodynamics*, 2018, no. 4, pp. 19-24. doi: https://doi.org/10.15407/techned2018.04.019. (Rus).

12. Calixto W.P., Neto L.M., Wu M., Yamanaka K., da Paz Moreira E. Parameters Estimation of a Horizontal Multilayer Soil Using Genetic Algorithm. *IEEE Transactions on Power Delivery*, 2010, vol. 25, no. 3, pp. 1250-1257. doi: https://doi.org/10.1109/TPWRD.2010.2040845.

13. Kostić V.I., Raičević N.B. An alternative approach for touch and step voltages measurement in high-voltage substations. *Electric Power Systems Research*, 2016, vol. 130, pp. 59-66. doi: https://doi.org/10.1016/j.epsr.2015.08.023.

14. *IEEE Std 80-2013 Guide for Safety in AC Substation Grounding*. New York, IEEE, 2013. 226 p. doi: https://doi.org/10.1109/IEEESTD.2015.7109078.

15. *IEEE Std 81-2012 Guide for Measuring Earth Resistivity, Ground Impedance, and Earth Surface Potentials of a Grounding System.* New York, IEEE, 2012. 74 p. doi: https://doi.org/10.1109/IEEESTD.2012.6392181.

16. Koliushko D.G. *Improving the diagnostics of grounding devices of electric power facilities.* PhD dissertation. Kharkiv, NTU «KhPI», 2003. 172 p. (Ukr).

17. *Letter No. 02-45-09/1875 NEC «Ukrenergo» Donbasska ES*, 19.04.2005, Chief Engineer of Donbass Power Plant S.A. Kardashev. (Rus).

18. M. Telló, D. S. Gazzana, G. A. D. Dias, R. C. Leborgne, A. S. Bretas. New methodology to measure the grounding grid resistance of substations applying short distance among electrodes. *Proc. 20th Int. Conf. Comput. Electromagn. Fields*, Montreal, Canada, 2015, pp. 1-4.

19. Koliushko D.G., Rudenko S.S., Asmolova L.V., Tkachova T.I. Determination of the soil sounding depth for the earthing resistance calculation of substations 35 kV. *Electrical Engineering & Electromechanics*, 2020, no. 1, pp. 52-55. doi: https://doi.org/10.20998/2074-272X.2020.1.08.

20. Koliushko D.G., Rudenko S.S., Koliushko G.M. Analysis of electrophysical characteristics of grounds in the vicinity electrical substation of Ukraine. *Electrical Engineering & Electromechanics*, 2015, no. 3, pp. 67-72. doi: https://doi.org/10.20998/2074-272X.2015.3.10.

21. Rezinkina M.M. Simulation of electric fields in the presence of rods with rounded upper ends. *Technical Physics*, 2015, vol. 60, no. 3, pp. 337-343. doi: https://doi.org/10.1134/S1063784215030238.

22. Friedberg S., Insel A., Spence L. *Linear Algebra*. London, Pearson, 4th Edition, 2003. pp. 48-49.

Received 03.08.2022
Accepted 12.10.2022
Published 06.01.2023

D.G. Koliushko[1]*, PhD, Senior Research Scientist,*
S.S. Rudenko[1]*, PhD, Senior Research Scientist,*
A.N. Saliba[2]*, General Manager, Postgraduate Student,*
[1] National Technical University «Kharkiv Polytechnic Institute», 2, Kyrpychova Str., Kharkiv, Ukraine, 61002,
e-mail: nio5_molniya@ukr.net (Corresponding Author)
[2] TMC Group, Beirut, Horsh Tabet, Sin el Fil, Lebanon,
e-mail: abdel.nour.saliba@gmail.com

How to cite this article:
Koliushko D.G., Rudenko S.S., Saliba A.N. Determination of the scope of the experimental-calculation method for measuring the touch voltage. *Electrical Engineering & Electromechanics*, 2023, no. 1, pp. 77-82. doi: https://doi.org/10.20998/2074-272X.2023.1.11

Матеріали приймаються за адресою:
Кафедра "Електричні апарати", НТУ "ХПІ", вул. Кирпичева, 2, м. Харків, 61002, Україна
Електронні варіанти матеріалів по e-mail: a.m.grechko@gmail.com

Довідки за телефонами: +38 067 359 46 96 Гречко Олександр Михайлович

Передплатний індекс: 01216